Terahertz quantum cascade laser application in local oscillator development

Rui Dong

Submitted in accordance with the requirements for the degree of
Doctor of Philosophy

The University of Leeds
Institution of Microwave and Photonics
School of Electronic and Electrical Engineering

August 2016

The candidate confirms that the work submitted is his own, except where work which has formed part of jointly-authored publications has been included. The contribution of the candidate and the other authors to this work has been explicitly indicated below. The candidate confirms that appropriate credit has been given within the thesis where reference has been made to the work of others. Further details of the jointly-authored publications and the contributions of the candidate and the other authors to the work should be included below this statement.

Chapter 5.2

Valavanis A; Han YJ; Brewster N; Dean P; Dong R; Bushnell L; Oldfield M; Zhu JX; Li LH; Davies AG (2015) Mechanically robust waveguide-integration and beam shaping of terahertz quantum cascade lasers. Electronics Letters, 51 (12), pp. 919-921.

I am response for the measurement and data processing under guidance of Valavanis A and Dean P.

Chapter 6.3 and chapter 3

Dong R; Valavanis A; Han Y; Kundu I; Oldfield M; Brewster N; Li L; Li C; Zhu J; Bushnell L (2015) Waveguide-integrated terahertz-frequency quantum cascade lasers for detection of trace-gas species IRMMW-THz 2015-40th International Conference on Infrared, Millimeter, and Terahertz Waves

I fabricated the QCLs and characterized them. And the waveguide integrated device characterization and data processing. And write the paper. All those work are helped or guided by Valavanis A, Dean P. and Linfield. E.

Chapter 5.2.4.3 and chapter 6.3

Valavanis A; Henry M; Han Y; Auriacombe O; Dong R; Rawlings T; Li LH; Oldfield M; Brewster N; Davies AG Feedhorn-integrated THz QCL Local Oscillators For The LOCUS Atmospheric Sounder Proceedings of the 41st International Conference on Infrared, Millimeter and Terahertz Waves.

I fabricated the devices and characterized them and participated in the system setup. I also measure the gas spectroscopy in the Lab. I processed the gas spectroscopy data under guidance of Valavanis A and Dean P.

All the work are under Edmund Linfield’s guidance.

This thesis is dedicated to my family. Without your endless support throughout my life, I would never have the chance to explore the wonderful world no matter life or research.

Acknowledgements

First of all, I want to give my sincere gratitude to my supervisor professor Edmund Linfield the person who brings me here and gives me guide all through my PhD project. He teaches not only the knowledge and skill in the Lab but also the methods of handling problems of research and life. I couldn’t finish this project without his encouragement and help during the past 4 years. Thanks for your patience all over the years. You always make sure that I understand what happened during the project and what I need to do in the future. I am really happy to be guided by you. Thank you for everything I achieved, Edmund.

My sincere thanks all goes to Alex Valavanis. Thanks for all your help during the project. Whenever I need help in the Lab or during the data analyse, you always the first choice I made. The patience you show during the project is really impressive and I am gratitude to that kindness. Thanks for your valuable suggestions all through my research. I am happy to work with you and enjoying those happy days in the Lab. Without your help I couldn’t arrive here today.

I also want to thanks Paul Dean, Giles Davies, John Cunningham, Iman Kundu and Jay for their valuable suggestions during all the supervision meetings. All my work in the Lab are contributed by your excellent Lab coordination. You always provide immediate help whenever I need. Thanks for all your help in and out of the Lab.

I must give my thanks to Lianhe Li, Jingxuan Zhu, Yingjun Han, Li Chen, Jingbo Wu, Binbin Hong and Kun Meng. You give me help not only for my work but also my life. Without your encouragement, I couldn’t even finish the work during those hard days. You always provide useful advice to my life and my work here. I must thank you for all the things you have done during the 4 years. Thanks for your interesting talks and discussion after work. Thanks for your blessings and wishes during the Chinese traditional festivals.

Then I want to thank the people I work and study with. We share the office and always work together in the Lab. Thanks so much for your company. I will

never forget those happy days with you Reshma, Jay, Dave, Siddhant Victor and Manoj.

I want thank you for your company. My honey Lily Yuan. Your sacrifices and gives too much during the past year, my most stressful time. Your smile and encouragement always cheer me up no matter how difficult the situation is. I can’t image what kind of days I would experience if you are not there. I love you.

I want to give my biggest thanks to my family. Thank you so much, 爸爸妈妈. Your tremendous support and sacrifice all through my life makes me who I am now. I have no words but I love you to describe my gratitude.

I need to express my gratitude to my Chinese family. Chuanlin Wang, Liang Wang, Fangfang Li, Qing Lan, Li Zhang, Weibing Li, Wei Fu and Rui Yu. We have so many good days in Leeds. Living with you makes me less homesick. Life after work is also part of my research and you contribute it a lot. Best wishes for your future life in Leeds. I also want to thank Junfan Lin, Xixing Hua, Leigang Cao, Bing Hou, Hongseng Peng, Hongmiao Wang, Qiang Liu, Peng Bao Jiacheng Yao Xujun Luo and Xiaoxu Li for playing badminton and basketball together. Those sports make me always positive and confident in my life. I am sure that helps me a lot during the research.

I have to give my thanks to China Scholarship Council (CSC)-Leeds Scholarship for fund my research and study in University of Leeds.

Abstract

Terahertz (THz) quantum cascade lasers (QCLs) are high-quality THz sources in terms of power (>1W) and compact size, and the application of THz QCLs has been widely investigated. Spectroscopy is one of the most widespread application for THz QCLs. The project presented in this thesis is an application of THz quantum cascade laser.

The project is focused on development of a local oscillator (LO system) aimed to be used in Earth observation. A single mode THz QCL which produces continuous-wave signals is designed, fabricated and characterized. In order to improve the performance of the LO (THz QCL), it is integrated within a waveguide block, which is more mechanically robust than a normal packed QCL and a significant improvement in beam profile was obtained by the integration with little change in the electrical and thermal performance.

Next, the detector (Schottky diode detector) use in the application was investigated in terms of heterodyne detection and detection calibration. The heterodyne signal from the Schottky diode detector was used to study a Fabry–Perot (FP) QCL, whose neighbouring FP modes are coupled into the Schottky diode detector. The investigation gives a QCL emission linewidth and thermal equilibrium speed of the THz QCL. QCLs are used to calibrate a new Schottky diode detector designed by Rutherford Appleton Laboratory (RAL), which gives a 3.67 THz room temperature cut-off frequency.

Lastly, spectroscopy with the THz QCL is carried out. A single mode CW lasing QCL and a photomixer are used in this application. The system gives a clear demonstration of methanol spectroscopy. Different partial pressure and absolute pressure of methanol are investigated. The measured result is backed by the simulation result from a JPL database. The measured result also proves the possibility of obtaining absorption linewidth broadening by increase methanol pressure. The noise level of the system is also investigated, which gives a detection limitation of 6.0×10^{18} molecules in the 73 cm long gas cell that can be detected for the system.

Key words: Terahertz, quantum cascade lasers, single mode source, spectroscopy, and Schottky diode detector

List of publications

Edmund Linfield, Alexander Valavanis, Yin Han, Lian, Li, Jing, Zhu, Rui Dong, Paul Dean, A.G. Davies, N. Brewster, L. Bushnell, M. Oldfield, Brain Ellison (2016), Terahertz frequency quantum cascade lasers for use as waveguide-integrated local oscillator, In 10th European Conference on Antennas and Propagation (EuCAP) April 2016, Davos, Switzerland.

Dong R; Valavanis A; Han Y; Kundu I; Oldfield M; Brewster N; Li L; Li C; Zhu J; Bushnell L (2015) Waveguide-integrated terahertz-frequency quantum cascade lasers for detection of trace-gas species IRMMW-THz 2015-40th International Conference on Infrared, Millimeter, and Terahertz Waves.

Valavanis A; Henry M; Han Y; Auriacombe O; Dong R; Rawlings T; Li LH; Oldfield M; Brewster N; Davies AG Feedhorn-integrated THz QCL Local Oscillators For The LOCUS Atmospheric Sounder Proceedings of the 41st International Conference on Infrared, Millimeter and Terahertz Waves.

Bulcha BT; Hesler JL; Valavanis A; Drakinskiy V; Stake J; Dong R; Zhu JX; Dean P; Li LH; Davies AG (2015) Phase locking of a 2.5 THz quantum cascade laser to a microwave reference using THz Schottky mixer IRMMW-THz 2015 - 40th International Conference on Infrared, Millimeter, and Terahertz Waves.

Rui, D, Valavanis, A, Han, Y, Kundu, I, Brewster, N, Lianhe, L, Chen, L, Jingxuan, Zhu, Bushnell, L, Ellison, B.N, Dean, P, Linfield, H.E, Davies, G.A (2015) Waveguide-integrated terahertz-frequency quantum cascade lasers for trace-gas detection application. In: UK Semiconductors 201, 1-2 July 2015, Sheffield, UK.

Valavanis A; Han YJ; Brewster N; Dean P; Dong R; Bushnell L; Oldfield M; Zhu JX; Li LH; Davies AG (2015) Mechanically robust waveguide-integration and beam shaping of terahertz quantum cascade lasers. Electronics Letters, 51 (12), pp. 919-921.

Valavanis A; Han YJ; Brewster N; Dean P; Dong R; Bushnell L; Oldfield M; Zhu JX; Li LH; Davies, AG, Ellison, BN and Linfield, EH waveguide-integrated

Terahertz quantum cascade lasers for use as local oscillators. In: 36th ESA Antenna workshop, 06-09 Oct 2015, ESTEC, Noordwijk, The Netherlands.

Table of Contents

List of Tables

List of Figures

List of Abbreviations

AC – Alternating current

AlGaAs – Aluminium-Gallium-Arsenide

GaAs – Gallium-Arsenide

BTC – Bound-to-continuum

CW – continuous wave

DBR − distributed Bragg resonator

DC – Direct current

DFB − distributed feedback

EBL− Electron beam lithography

FIB – Focused ion beam

FP – Fabry-Pérot

FTIR – Fourier transform infrared

FWHM – Full width at half maximum

IV – Current-Voltage

JPL – Jet Propulsion Laboratory

LIA − lock-in amplifier

LIV – Lasing power – current

LO – Local oscillator

MBE – Molecular beam epitaxy

N_2 – Nitrogen

NASA – The National Aeronautics and Space Administration

PA – Photoconductive Antenna

PLs − photonic lattices

PM – Photomixer

PMMA – poly (methyl methacrylate)

QCL − quantum cascade laser

R* − Responsivity

RP – Resonant phonon

SEM – Scanning electron microscopy

SNR – Signal noise ratio

TDs – Time domain spectroscopy

THz – Terahertz

TPX – Polymethylpentene

UV – Ultra-violet

Chapter 1Introduction

1.1 Earth Observation

Earth Observation aims to study the dynamic status of Earth in terms of its physical, chemical and biological systems. Common methods include the use of remote sensing instruments, installed on satellites in a range of different orbits. Earth Observation has become increasingly important because of the impact of modern civilization on the planet, such as climate change caused by greenhouse gas emissions.

A range of passive and active remote sensing techniques are commonly used in Earth observation. In general terms, passive sensing techniques analyse radiation that has been reflected, transmitted or emitted by the object of investigation, whereas active sensing techniques illuminate the object with radiation with well-known spectral characteristics, and analyse the reflected or transmitted signal. Common passive sensing techniques analyse the spectrum of transmitted solar radiation, which is extremely broadband, and therefore it has been possible to develop remote sensing techniques across a wide range of frequency bands, including visible light [1], infrared [2], microwave [3] and ultraviolet radiation [4].

Microwave and infrared (IR) technologies have been proven effective methods for Earth observation. Microwave detectors are commonly used in water, ice, and cloud observations [3], whereas greenhouse gases are usually studied using IR detectors. One example is the Aqua Earth-observing satellite mission, whose payload includes the Atmospheric Infrared Sounder (AIRS), and the Advanced Microwave Sounder Unit (AMSU-A) instruments. The infrared detector gives information about CO, CO_2 and methane.

Climate change is an important and timely topic of Earth observation. The mesosphere and lower thermosphere (MLT) regions of the Earth's atmosphere (55−90 km and 90–150 km from ground respectively) form the "gateway" between the Earth's atmosphere and the near-space environment. In this region, ultraviolet radiation and particles from the sun collide with the upward energy from the lower atmosphere [5]. Key molecular species (including O, O_2, O_3, H and OH^-) are very important for the energetic balance in this region, as shown in Figure 1-1 [6]. The temperature of this region is balanced by O_2 and O_3 UV absorption ($2O_3$+ UV radiation→$3O_2$) [7], and chemical interactions involving O and H ($H+O_3 \rightarrow OH+O_2$ and $OH+O \rightarrow O_2+H$) [8]. CO and NO in this area act as atmospheric coolant and indicator of Solar particle reaction respectively [9].

The temperature in the MLT is balanced through radiation and absorption of energy these interactions. The influence of human activity on this radiative balance can be determined by studying the molecular species in this atmospheric region.

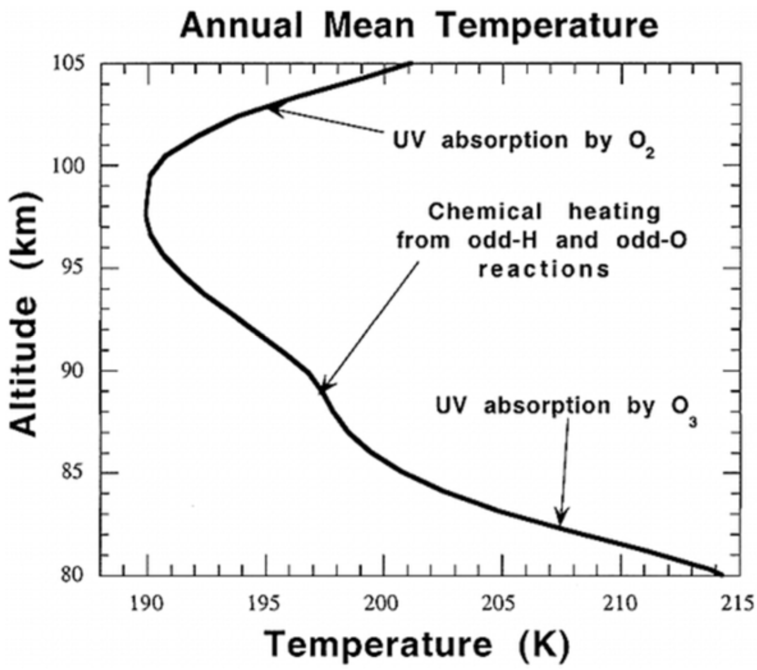

Figure 1-1 Averaged temperature of MLT over both diurnal and annual cycles

[2]. Three different regions are identified to show the roles played by O and H.

Although small molecules, such as O, OH, CO and NO are very important components of the MLT, traditional method as infrared can only indirectly detect them by study higher order harmonic components of their emission spectrum [10]. They can only be directly observed via their emission lines within the terahertz (1−5 THz) band of the electromagnetic spectrum [9]. Conversely, infrared detection schemes may only obtain the higher order harmonic components of the emission spectrum, which have much broader linewidth compared to the sharp fundamental THz lines of these species. In order to have a good resolution, altitude across the MLT region need to be measured. This can be done either by an aeroplane or a limb sounder which is much cheaper than multi-fly of aeroplane. As such, THz instrumentation installed in a satellite has the potential to enable the first direct global mapping of these key MLT species. The following sections describe the properties of THz radiation, a review of THz system components (with a focus on their satellite compatibility), and the architecture of a proposed satellite mission (*LOCUS*) to study the MLT using THz radiometers.

1.2 Terahertz radiation

The terahertz-frequency (THz) radiation band lies between the infrared and microwave regions of the electromagnetic spectrum [11], spanning from 300 GHz to 3 THz (1 mm to 0.1 mm wavelength) as shown in Figure 1-2 [12].

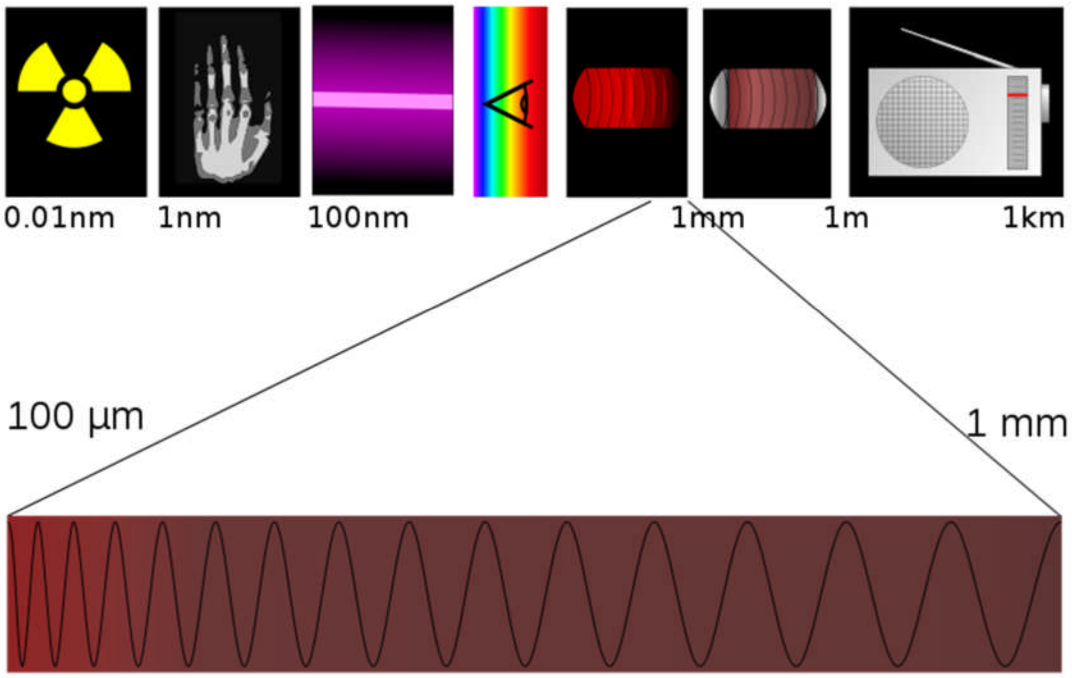

Figure 1-2 Terahertz radiation

[12]

THz radiation shares a number of properties with microwave-frequency radiation, which underpin a wide range of potential terrestrial and satellite-based applications. These properties include the ability to penetrate non-conducting materials (including clothing, paper, cardboard, wood, masonry, plastic, ceramics and biological tissues), although the penetration depth is typically less than that of microwave radiation [11]. This enables applications including the detection of concealed weapons [13]. Another characteristic of THz radiation is that it is non-ionizing due to its relatively low photonic energy. This enables potential applications in biomedical imaging [14], security [15] and non-destructive evaluation of samples [16], without the ionization risks associated with *X*-rays. Due to its longer wavelength, images of objects formed using THz radiation lack resolution, when compared with infrared and visible imaging techniques. However, the relatively long wavelength provides the possibility of obtaining a deeper background than optical cameras. 2D [17] & 3D [18] imaging with THz radiation is another extensive research field. The frequency of THz radiation is significantly higher than traditional microwaves, potentially enabling high-data-rate communications [19].

As stated in Section 1.1, another important property of terahertz radiation is that many gas absorption lines occur in this region. For instance, water vapour, which is abundant in the Earth's atmosphere, has a very broad absorption band within the terahertz region. Many molecules, ions and atoms such as methanol, water, OH^-, CH^-, O and so on, exhibit THz emission spectrum [20]. This property makes THz radiation useful for the detection and spectroscopy of a wide range of chemicals [9]. However, the significant water absorption also limits the scope of terrestrial applications of THz radiation, such as the length of communications links and the tissue penetration depth for biological sensing.

Spectral analysis in the THz band has historically been challenging, as the well-established instrumentation used in millimetre wavelength technology is typically limited to frequencies below ~1 THz [3]. Conversely, the generation of coherent THz radiation using bulk semiconductor lasers is not possible since the required phonon energy is significantly lower than the material bandgap [21]. New devices and techniques are, therefore, required to detect and emit radiation in this range, and these will be discussed in Section 1.3. However, some detection methods developed for higher wavelength instrumentation, such as Fourier transform infrared spectroscopy (FTIR) [22] and energy measurement using bolometers, are also suitable for use in the terahertz region.

1.3 THz sources

This section, and the next, review a range of THz system components, and evaluate their suitability for use in satellite instrumentation.

Active and passive THz remote sensing systems commonly require a high-quality THz source. In the case of radiometry systems, a local oscillator (LO) is required: i.e., a stable, narrowband THz source, which provides a local frequency reference. For satellite applications, this source must be small in terms of both weight and volume, and must also have low power consumption. It also needs to be stable and mechanically robust.

There are many methods used to generate THz radiation including thermal sources, vacuum electronic devices, solid-state electronic devices, lasers, laser pumped sources and mechanical excitation techniques. This section gives an overview of THz sources based on these principles. These sources are evaluated against the indicative specifications of THz LOs for satellite applications. These include the need for a compact size, large continuous-wave output power, high enough operation temperature and narrow spectral linewidths.

1.3.1 Thermal THz sources

A black body can emit electromagnetic radiations with a range of wavelengths at a given temperature T when the system achieves thermal equilibrium, which can be described by Planck's law [23].

Mercury lamps and electrically-heated silicon carbide (SiC) rods are common thermal THz sources used in the laboratory environment [24, 25]. Thermal sources operated at around 1650 K correspond to emission between 0.5 and 0.8 THz [24]. The operation temperature would be increased to even higher if a THz radiation above 2 THz is needed.

1.3.2 Vacuum electronic sources

In order to generate THz frequency radiation in vacuum based electronics, a high-energy electron beam is injected into a resonant cavity or waveguide.

The energy is transferred from the kinetic energy of the electron beam to an electromagnetic wave [27].

The three main types of device that use this technique are Gyrotrons [26-31], backward wave oscillators (BWOs) [32-36], and free electron lasers (FEL) [37]. The FEL can operate over a large bandwidth, ranging from microwave to *X*-rays. BWOs are usually very large and complex, and require high voltage and thus water cooling systems. These features make vacuum electronic sources unsuitable for satellite applications. However, the output power and the frequencies achievable make them attractive sources for terrestrial research applications. Powers as high as 50 mW at 300 GHz and several mW at 1 THz have been reported [38]. Work is currently being done to make these smaller and more convenient for use in micro-fabrication and micro-assembly technologies [38]. Extended-interaction klystrons [39] and synchrotrons [40] also use vacuum electronic sources using similar principles as BWOs and FELs.

1.3.3 Solid-State Sources

Resonant tunnelling diodes (RTDs), Gunn diodes [41], transferred electron devices (TEDs), tunnel diodes and avalanche diodes are all solid-state sources based on the properties of two dimensional electron-gases. Among them, Gunn, tunnel diodes and RTDs are diode based. Gunn diode sources have been the subject of extensive research and consequently have been successfully used as commercial millimetre-wave and THz sources [42]. Field effect transistors, such as high electron mobility transistors (HEMTs), can also be used to generate THz radiation. Those devices can give relatively high frequencies compared with three-dimensional electron-gas solid-state THz sources such as heterojunction bipolar transistors (HBTs).

Due to the transit time of carriers through semiconductor junctions, electronic solid-state sources are only effective in the low-frequency range, typically below 500 GHz [43]. The power available from these devices tends to be inversely proportional to the output frequency [43]. Electronic solid-state oscillators suffer from physical scaling issues, metallic wall losses and the need for high magnetic and electric fields, as well as high electron current densities as the frequency is increased [43]. In some aspects, traditional three dimensional electron gas devices are more desirable, as they can provide better low noise performance and wideband amplifier applications.

Frequency multiplication techniques are also widely used for THz generation. THz frequency multipliers consist of a nonlinear device, such as a Schottky diode, and a lower frequency generator, which usually outputs microwave signals. The nonlinear devices generate harmonics of the input signal. A filter is then employed to select the required frequency, removing the unwanted fundamental frequency and outputting the harmonics. Commonly used multipliers include doublers, which output twice the frequency of the input, or triplers which output three times of the frequency of the input. These THz sources are widely researched and applied to achieve high frequency signals [44-46].

Most solid state sources are compact and fulfil the LO requirement, in terms of weight and volume. However, the power output of these devices is small compared with other sources at high frequencies beyond 2 THz.

1.3.4 Laser pumped sources

A laser source is used as an incident pump to generate terahertz radiation in this approach. The driving laser can be operated in either continuous wave (CW) or pulsed mode.

Photomixers is commonly used sources that employ CW visible or infrared lasers to generate THz radiation. This is discussed in Chapter 6 in detail. In a photomixer, the wavelength of the laser used is dependent on the bandgap of the material used to fabricate the photomixer [47]. Photomixers are fabricated using low-temperature-grown Gallium Arsenide (LT-GaAs). When pumped by a pair of infrared diode lasers, coherent CW THz radiation is generated with a frequency bandwidth up to 5 THz [47-48]. The principle of THz generation using photomixers is presented in Section 6.3.1 .

A related technique exists, in which ultrafast pulsed lasers are used to generate terahertz radiation from photoconductive switches [49] or non-linear crystals [50]. As the incident photon energy is greater than the bandgap of the semiconductor, electron–hole pairs are generated, and a bias across the device causes the carriers to accelerate. The acceleration and eventual recapture of these carriers in the timescale of picosecond provides the source of pulsed terahertz radiation.

Non-linear crystals for use in terahertz generation include lithium niobate [51], gallium selenide [52]. When quasi-phase matched with GaAs [53], these will generate a second order harmonic when they are irradiated by infrared or visible lasers. $LiNbO_3$ is widely used as the target, which is always pumped by ns-Nd:YAG lasers. This process will yield coherent, tuneable, and unidirectional THz radiation but high power emission can only be realized through efficient output coupling [51].

The laser-pumped THz source can give as high as several mW THz power. But the conversion efficiencies from pump power are very low, less than 1% [54]. And this can't fulfil the low power consumption requirement of LO used in satellites.

1.3.5 Gas lasers

THz gas lasers can be realised by irradiating a gas using a CO_2 pump-laser [55]. When the gas within the cavity is excited by a CO_2 laser, a molecular state inversion of the gas as rotation and vibration states achieved. The lasing obtained when those states inversion jump to the equilibrium states again. The emitted radiations' photon energy is the energy difference between those states. A large span of emission frequencies is possible, (0.1 to 8 THz [55]) by changing the gas filling the cavity. It is common to achieve 1−20mW of THz power for laser pump powers of 20-100mW [56-58]. The methanol line, which is located at 2522.78 GHz, is known to provide the most output power [56-58]. Recently, a compact gas laser, with the dimensions of 75×30×10 cm^3 and a weight of 20 kg was reported, through which 30mW power at 2.5 THz was obtained [59].

However, the application of this type of laser is also limited by the fact that it is hard to achieve continuously tuneable broadband THz emission, as with photomixers. Furthermore, the power of this type of laser is relatively low compared with that of quantum cascade lasers. Considering the requirement of satellite instrumentation, gas laser is too heavy and large to be installed.

1.3.6 Quantum cascade lasers

The first THz semiconductor lasers were developed in 2002 [60]. These THz quantum cascade lasers (QCLs) are based on quantum wells (typically $GaAs/Al_xGa_{1-x}As$), which are grown using molecular-beam epitaxy (MBE) [61]. QCLs have better beam profiles [62], comparably higher power [63, 64] and they are more compact than other sources, such as photomixers.

Within a traditional diode laser, the frequency of radiated emission is determined by the transition between the conduction band and the valence band edges. Electrons are injected into the active layer through a forward biased *p–n* junction and radiation is emitted when the electrons recombine with the hole. As such, the band gap of the material determines the radiated wavelength. Since both types of carrier (electrons and holes) are involved in the lasing mechanism, these are referred to bipolar lasers. However, the mechanisms governing a QCL are different. In this instance, the lasing transition relies on only one type of carrier (i.e., electrons in the conduction band only) and thus QCLs are referred to as unipolar lasers. Electrons cascade down a potential “staircase”, sequentially emitting photons at each step. The steps consist of coupled quantum wells in which the population inversion between discrete conduction band states is achieved by control of the tunnelling and scattering rates through bandstructure engineering [65].

In QCLs the emission wavelength is determined by the lasing transition, which itself is dictated by the energy levels in the quantum wells. By varying the thickness of the layers in the heterostructure, the emission frequency can be varied from the mid-infrared region [69] of the electromagnetic spectrum to the THz [60].

The first QCL was developed for 4.2 µm mid-infrared emission [65] in 1994 and the first THz QCL, lasing at 4.4 THz with a peak power of 2.4 mW, was realized in 2002 [60] by implementing a novel waveguide design. Since this point, much process has been made, investigating novel active region and waveguide designs, with the aim of achieving higher working temperatures, extending the frequency range, and improving the beam profile and emission power.

Due to THz photon energy is quite close to longitudinal optical phonon energy of GaAs most widely used material for QCL growth, the THz QCL is still operated in low temperature environment in which longitudinal optical phonon can be supressed. The highest reported operating temperatures of a THz-QCL are approximately and 200 K [76] 117 K [75] in pulsed and CW operation, respectively. The highest powers obtained from a THz-QCL are 1 W [67] at 3.5 THz and 138 mW at 4.4 THz [68] for pulsed and CW mode, respectively.

THz QCLs have a very narrow intrinsic spectral linewidth, which can be stabilized to the order of Hz [68-70]. Additionally, QCLs are compact, which is a significant advantage for satellite-based LO development. However, there are still significant challenges, such as the requirement for low temperature operation, which will be discussed in more detail in Section 1.5.

1.4 THz detectors and mixers

Detection methods at terahertz frequencies can typically be divided into two categories: coherent (i.e., measurement of both the amplitude and phase of the THz signal) and incoherent (i.e., amplitude only) [71]. Devices that are sensitive to thermal changes are the most commonly used form of incoherent THz detection, examples of which include Golay cells [72-74], bolometers [75] and pyroelectric detectors [76].

For coherent detection, the THz radiation can be detected directly [e.g., in Fourier Transform Infrared (FTIR) spectroscopy] or through heterodyne mixing methods using nonlinear devices such as Schottky diode detectors, photoconductive antennas and photomixers [77]. In radiometry applications, nonlinear devices are required to downconvert the spectrum of the incident THz radiation to a more easily measureable intermediate frequency (IF); typically, in the 1–10 GHz range [78,79].

1.4.1 Superconducting Bolometers

The bolometer uses a material’s resistive and thermal properties to incoherently detect THz radiation. The general operation principles are shown in Figure 1-3. The temperature of the bolometer will increase when the bolometer receives THz radiation, causing a significant detectable change in the electrical resistance [80]. THz bolometers are commonly based on either semiconductor [81] or superconductor [82] materials.

If a bolometer is designed to be used as a THz mixer, the response time must be short enough to generate the IF. Conventional bolometers, like other thermal devices, for a long time had very slow responses compared with electronic devices, making them unsuitable for use as mixers. However, Hot Electron Bolometers (HEBs) have been developed in recent years, [83] which respond fast enough to be used for THz mixing [82].

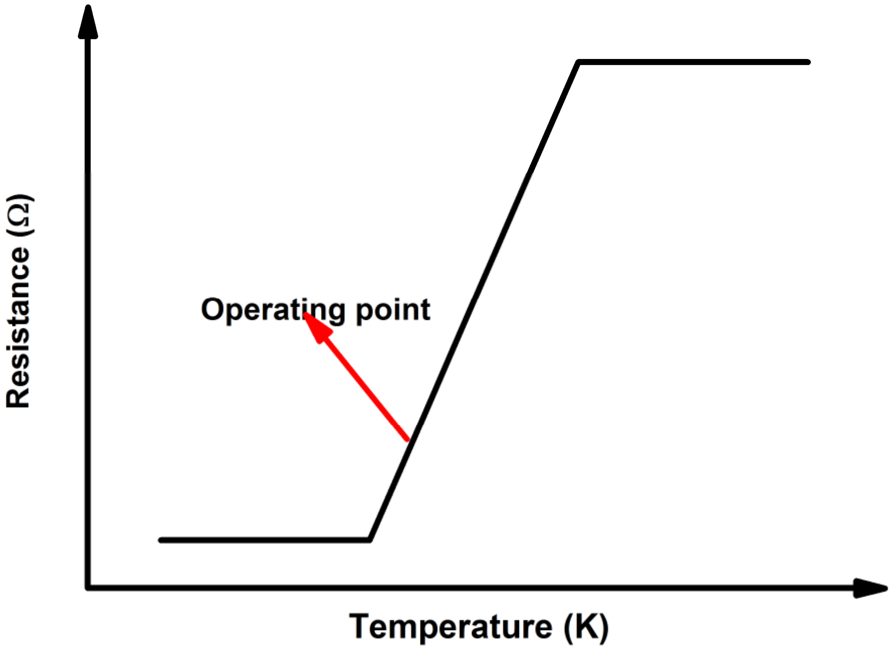

Figure 1-3 Operating principle of a superconducting bolometer

: The temperature of the bolometer increases as a function of the intensity of the incident THz radiation.

Hot electrons are non-equilibrium electrons in semiconductors, which follow the Fermi–Dirac distribution [83]. The number of electrons above the Fermi level of the semiconductor will significantly increase with temperature. Materials such as *n*-InSb and NbN are the most commonly used for HEBs, [75] although other materials, such as Ge [84], AlGaAs/GaAs [85], and Si [86] have also been proposed. HEB mixers are fast enough to allow GHz output IF bandwidths. However, bolometers must work at a low temperature, cooled by liquid helium, for increased sensitivity. Another drawback of bolometers is that energy accumulation in the detector can cause a DC drift of the detected signal and a reduction in the accuracy of detector are long time period [71]. To avoid this, an optical chopper is used to modulate the THz signal and to provide time for energy dispersion within the detector. All those factors add extra cost to LOCUS satellite if a superconducting bolometer is installed on it.

1.4.2 Golay cell detector

Golay Cells [74] work by heating a gas inside a cavity using incident THz radiation. The resulting expansion of the cavity (proportional to the incident power) distorts a flexible membrane at the rear, which can be measured using an optical read-out system. A diagram of the Golay cell is shown in Figure 1-4 [74].

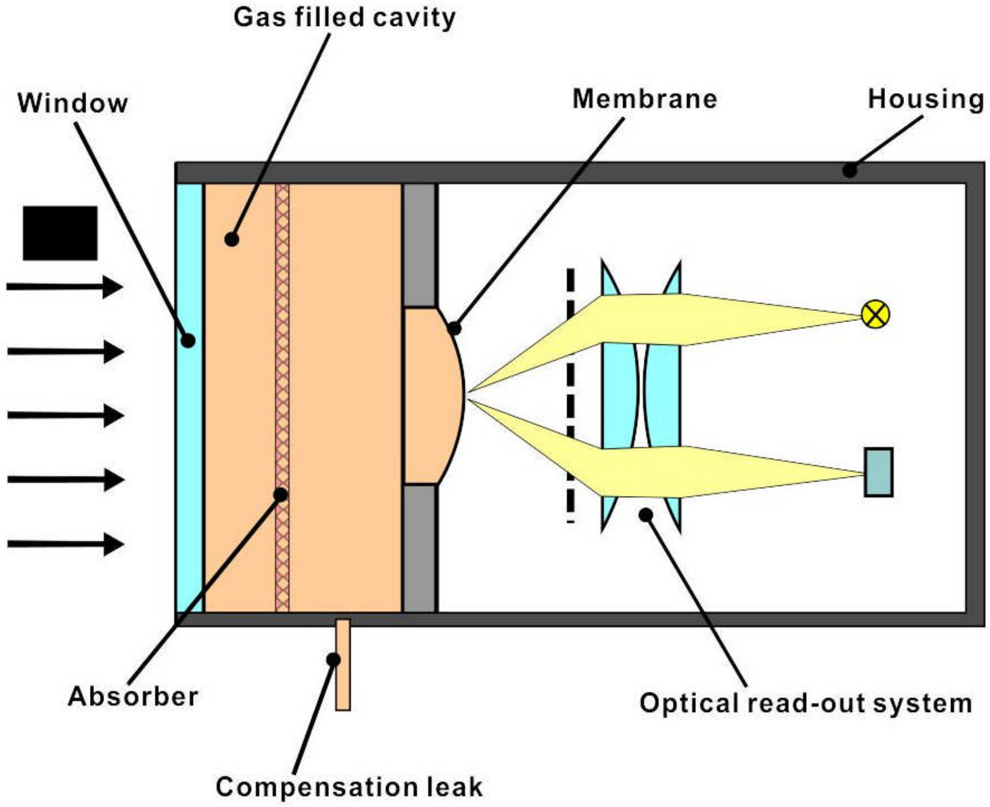

Figure 1-4 Golay cell detector operation principle [74].

One advantage of the Golay Cell detector over the bolometer is that they do not require cryogenic cooling. However additional noise is introduced by ambient infrared flux during the measurement, which requires the effective suppression of the incoming near infrared radiation. THz low pass filters [72], rough surface mirrors [87] and commercial membranes are applied to achieve this goal. The Golay cell detector is too slow to be used in LOCUS project as other thermal based detectors.

1.4.3 Pyroelectric detectors

The pyroelectric detector is another thermal THz detector, operating at room temperature. A schematic of the device is shown in Figure 1-5 [88]. Again, the detector is equipped with an IR filter to reduce background noise. After the radiation passes through the filter, the THz signal is used to heat a dielectric material [89]. The change of temperature can change the polarization of the dielectric material, which gives rise to a voltage across the material. If the temperature stays constant at its new value, the pyroelectric voltage gradually disappears due to leakage current [88, 89]. The filter material is one of the key elements for this detector, as is the case for Golay detectors. The other important part of the pyroelectric detector is the dielectric material. Lithium tantalate ($LiTaO_3$) has been successfully demonstrated for direct infrared radiation [90, 91] detection with a very good noise equivalent power performance [92] in the THz region.

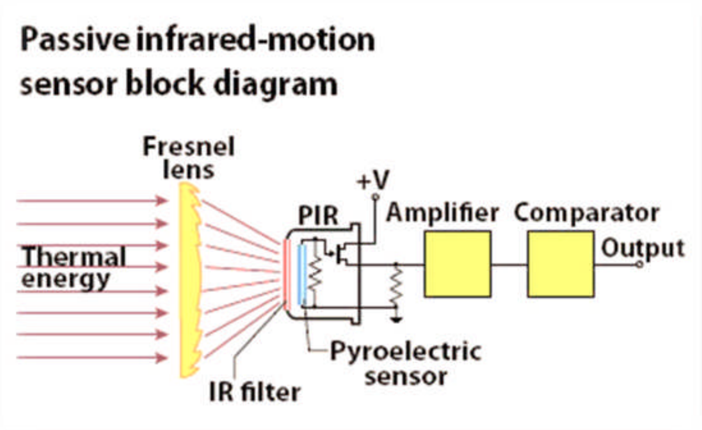

Figure 1-5 Schematic of a pyroelectric detector [88].

As with most other thermal detectors, pyroelectric detectors have a slow response and also the accuracy of the detector can be affected by accumulated heating if the detection time is too long [71].

1.4.4 Photoconductive broadband THz antenna sensors

Photoconductive detectors are based on similar antenna structures to those used for the pulsed broadband THz emitters, as discussed in Section 1.3.4 . These kind of detectors are typically used in time domain spectroscopy (TDS) experiments [93, 94] or imaging [95, 96].

The generation and detection of THz radiation by photoconductive antenna (PA) is discussed in detail in Chapter 6. The device consists of two metallic electrical contacts, deposited in a specific geometry onto a semiconducting material. As with photoconductive emitters, the antenna works by focusing a femtosecond laser beam between the electrodes, which introduces a transient bias voltage across the gap. A photocurrent is generated when the laser pulse coincides spatially and temporally with the THz electric field of the incoming THz radiation, and this allows THz detection by measuring the pulsed current. Low-temperature grown GaAs [50] and narrow-gap InGaAs [97] are commonly used materials for the antennas.

1.4.5 Schottky diode detectors

Schottky diode detectors make use of the electronic properties of Schottky diodes, under the influence of electromagnetic waves. A detailed description of the working principle of Schottky diode detectors can be found in chapter 4. Most diode detectors are GaAs-based Schottky barrier detectors. Since Young and Irvin [98] developed the first lithographically defined GaAs Schottky diodes for high frequency applications, more and more research has been conducted in THz detection using Schottky diode detectors [99-101].

The Schottky diode has previously been demonstrated for both heterodyne and direct detection of THz radiation, and has been shown to work at ambient or cryogenic temperatures below 300 K [102]. Furthermore, they have an extremely fast response time compared with other room temperature detectors, such as Golay cells and pyroelectric detectors [100, 101]. An ultrafast Schottky barrier detector with a response time of 20 ps has recently been reported [101]. However, a drawback of using Schottky diodes for THz detection is their poor sensitivity and the high LO power requirements of 3–5 mW, which is roughly 3–4 orders of magnitude higher than that of a cooled HEB receiver. But we develop a LO based on a THz QCL which can give the power required to pump the Schottky diode detector. In this thesis Schottky diode detector direct detection is characterised in chapter 4 and the heterodyne signal is studied in chapter 5.

1.5 The LOCUS satellite concept

This thesis focuses on the development of THz instrumentation and sensing techniques for a proposed satellite mission—'Linking Observations of Climate, the Upper-atmosphere and Space-weather' (LOCUS) [9, 103] whose payload includes a multi-THz channel radiometry system to perform a global mapping of key species in the MLT and hence to improve understanding of climate change processes. Table 1-1 lists the species of interest, and the frequencies of the principal spectral lines that will be studied.

Table 1-1 THz spectrum of targeted species [104]

Species	Transition Frequency (THz)
O	4.745
OH	3.544
HO_2	3.543 3.544
NO	1.153 1.153
CO	1.152
O_2	0.773

A high spectral resolution detection method is essential for detection of these species in the MLT because of the low pressure and temperature environment in this atmospheric region. As such, the planned resolution of LOCUS is 1 MHz.

LOCUS is a UK collaboration between RAL space, University of Leeds, SSTL and STAR Dundee, involving antenna design, novel engineering, THz, IR, digital electronics, and cryocooler technology. The LOCUS proposal has been submitted as a mission candidate for the European Space Agency (ESA)

Earth Explorer 9 (EE9) programme. The payload of this satellite mission contains a 45 cm used-diameter off-axis antenna, THz and IR receivers, and an aluminium optical bench used to feed the detectors. A schematic of the payload is shown in Figure 1-6 [103].

To target the lines in Table 1-1, four THz heterodyne radiometry channels are included (4.7 THz, 3.5 THz, 1.1 THz and 0.8 THz). The two higher frequency channels (4.7 THz and 3.5 THz) use QCL LOs, while the other two LOs are multiplied microwave oscillators. All four channels generate an intermediate frequency (IF) between the LO and the species emission. The IF is then read using a high-resolution digital fast Fourier transform (FFT) spectrometer.

Schottky diode detectors are used for heterodyne detection in all four THz channels. Compared with thermal detectors, Schottky diode detector are faster and avoid the requirement for 4 K cooling associated with HEBs. However, since THz QCLs require a low operating temperature, the system design includes a 100 K closed-cycle cooler system, which will be developed by Rutherford Appleton Laboratories Space Division (RAL Space). CW operation is also necessary for this high resolution spectroscopy.

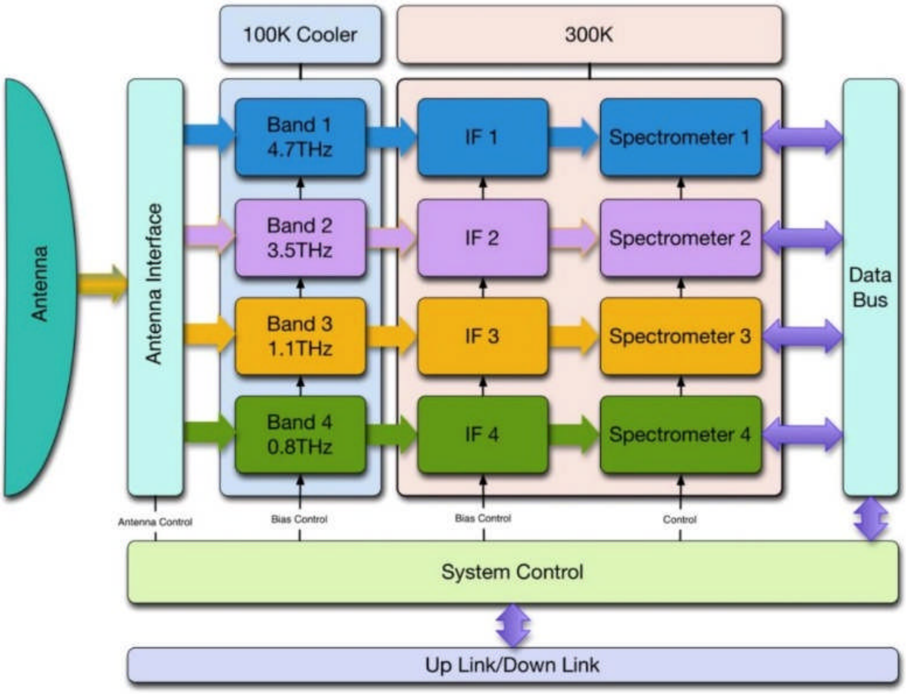

Figure 1-6 Payload schematic of LOCUS project [103].

THz QCLs with double-metal waveguides can operate at higher temperatures than single-plasmon devices, which is explained in Section 2.1.2 . However, the beam divergence from double-metal devices is much wider, which makes it difficult to couple power efficiently from the QCL into the Schottky diode detector using lenses or mirrors. As such, both devices are required to be integrated within a single waveguide structure. This integrated waveguide approach can both improve the coupling and reduce the volume of the system dramatically.

The linewidth of the LOs is required to be < 1 MHz to meet the frequency resolution specifications. In THz QCLs, the linewidth is broadened by fluctuations of the working environment, such as temperature, bias and mechanical stability. Typical temperature and current tuning coefficients of −200 MHz/K and −45 MHz/mA have been measured for THz QCLs [105], and therefore good stability of the cooling system and bias control system are required.

1.6 Thesis structure

The work presented in this thesis aims to develop and characterise key components and techniques for the THz radiometry channels in LOCUS. This includes design and fabrication of tuneable single-mode THz QCLs for use as LOs, characterisation of Schottky diodes and waveguide-integrated QCLs, and the demonstration of gas analysis using THz systems. The structure of the thesis is illustrated schematically in figure 1-7,

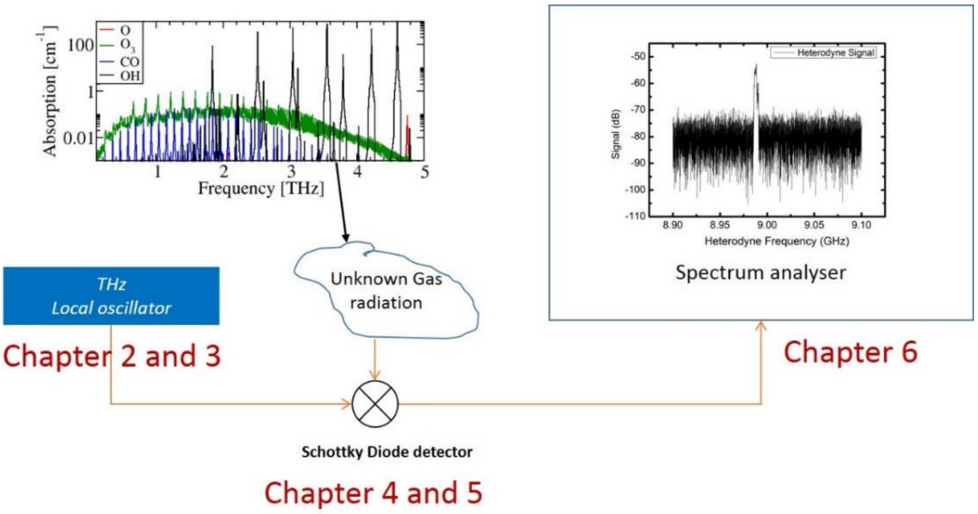

Figure 1-7 Schematic illustration of the LOCUS radiometry concept, and associated work presented in the thesis.

The next two chapters focus on fabrication and characterization of THz QCL LOs. Chapter 2 describes the standard methods used to fabricate and characterize Fabry–Pérot (FP) THz QCLs, while Chapter 3 presents describes the development of single mode THz QCLs, based on photonic lattices.

The following two chapters focus on system development and integration. 0 describes the characterisation of optically-mounted Schottky diodes as THz detectors using QCLs as a source. Chapter 5 describes the characterisation of waveguide-integrated QCLs and a commercially-sourced waveguide-integrated Schottky mixer.

Chapter 6 demonstrates the use of a single-mode QCL to target molecular absorption lines in a gas spectroscopy application. For comparison, THz spectroscopy is also performed using a photomixer. Chapter 7 presents a conclusion of the investigations, and potential directions for future work.

Chapter 2Fabrication and characterisation of terahertz quantum cascade lasers

2.1 Introduction

As discussed in Chapter 1, one of the LOCUS mission objectives is the realisation of a high power, compact THz local oscillator emitting a stable single frequency, with the quantum cascade laser selected as the optimum solution. In order to achieve this a number THz QCLs were fabricate and characterised. This chapter describes the cleanroom processing techniques used to fabricate THz QCLs and the experimental techniques used to evaluate the laser characteristics.

2.1.1 Active region

Figure 2-1 shows the working schema of a quantum cascade laser, (a) illustrate an interband semiconductor device whose emission is from recombination of electrons in the conduction band with holes in valence band. (b), (c) and (d) show how a quantum cascade laser works. A single quantum well has quantized energy levels and electrons distributed across those energy levels [106] illustrate in figure 2-1 (b). Several single quantum wells can be combined together to form a superlattice [107] structure, with electrons confined to subbands as figure 2-1 (c). When those superlattices are under a current bias, electrons in one subband can drop to a lower energy level [65] leading to radiation, as shown in figure 2-1 (d).

In semiconductor laser diodes, electrons and holes recombine to emit a photon. In a QCL, however, the electrons tunnel to the next period of superlattice after dropping to a lower energy level subband and generating radiation. This gives a greater quantum efficiency than a semiconductor laser.

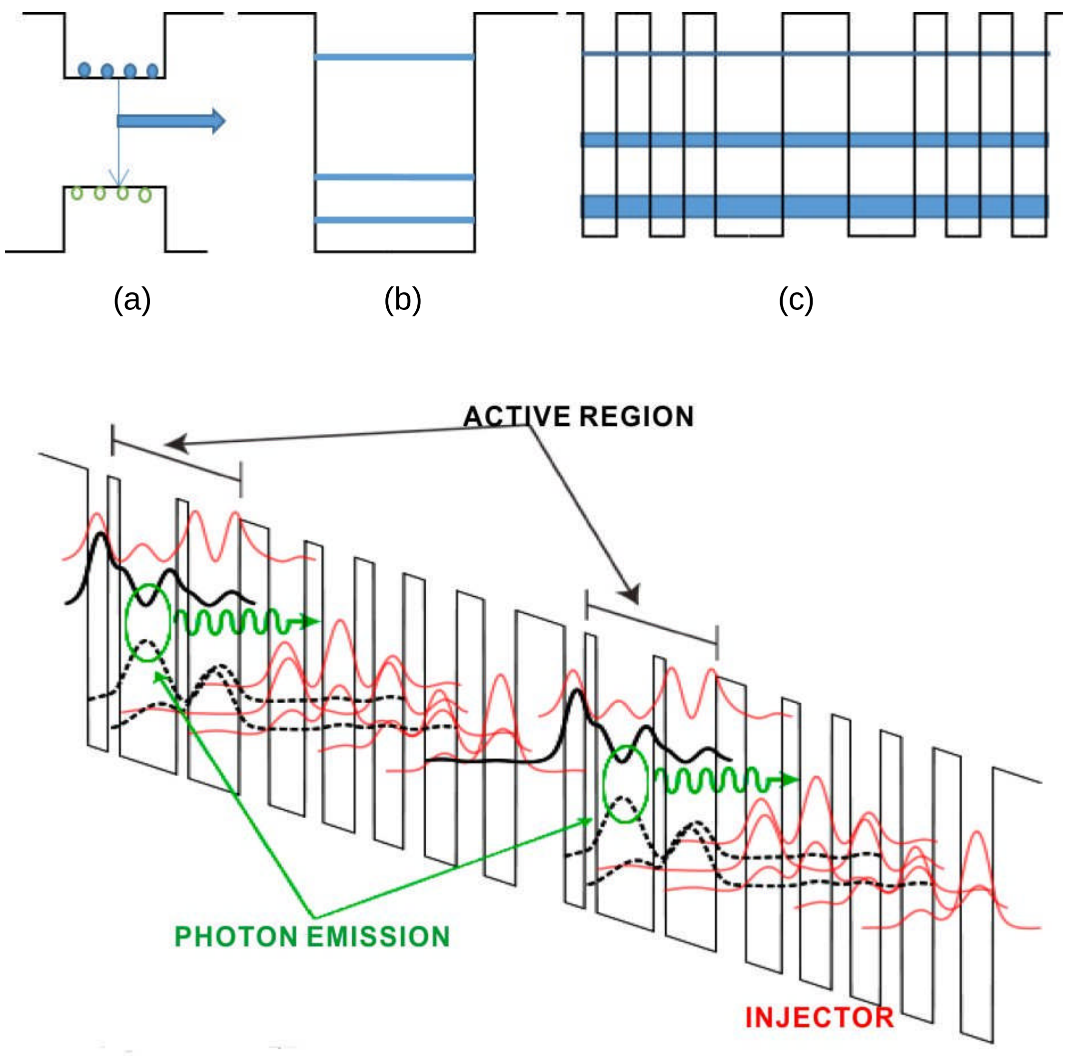

(a) (b) (c)

(d) [108]

Figure 2-1 QCL active region conduction band structure. (a) is a normal semiconductor laser where lasing arises from recombination of electrons in the conduction band with holes in valence band. (b) is a single quantum well in which electrons are distributed in quantized energy levels. (c) is the combination of many quantum wells, with electrons distributed in subbands. (d) is a biased superlattice, lasing occur from electron transition between different subbands.

Subband structure can be engineered by using different layer thickness. Different emission frequencies can then be obtained by changing the molecular beam epitaxy (MBE) [61] growth. The emitted frequency is determined by the energy difference between upper-level subband and lower-level subband, given as the green circle marked area in figure 2-1. The radiation emitted by a QCL has a very narrow intrinsic linewidth due to the quantized subbands.

The QCL working environment, such as the temperature and bias, can affect the subbands. The increase of bias across the device will increase the voltage difference between each period of quantum wells, which will increase the energy difference between subbands. This will cause the frequency of the emitted radiation to undergo a blue shift. At the same time, an increase of applied bias will cause an increase in the operating temperature caused by the QCL's electrical resistance. This causes the material's refractive index to increase [109] resulting in a redshift in the radiation. The temperature and current tuning of a THz QCL were measured to be −202.2±1.4 MHz/K and −45.2±0.4 MHz/mA respectively, by A. L. Betz [105].

The highest reported operating temperature of a THz-QCL in continuous wave (CW) is approximately 117K [75] and in pulsed mode 200K [76]. The cryogenic temperatures required for operation of the THz QCL currently limit its applications. There is a decrease in the gain of the laser when the working temperature increases. There are two main reasons for the gain decrease. Firstly, the electron concentration in the higher level subbands will increase according to Boltzmann distribution. The increased population of electrons in the higher energy level subband causes backfilling from lower energy level subband, which will decrease the gain [65]. Secondly, the lifetime of upper level subband electrons decrease because of longitudinal optical (LO) phonons, which increases with temperature.

Although there are proposals to use other materials with high phonon energy to overcome those two limitations, GaAs/AlGaAs quantum wells are still most widely used THz QCL material system because the mature growth technology for this material system gives higher wafer quality than other III-V materials.

2.1.2 THz QCL waveguide

Due to the large free carrier loss for radiation with a longer wavelength compared with the traditional MIR laser, a dielectric index waveguide has high losses at terahertz frequencies. The longer wavelength of THz QCLs require a thick dielectric index waveguide sandwiching the active region, which has proved to be difficult using MBE growth. In order to decrease the overlap of modes with the QCL active region, surface-plasmon (SI-SP) and double metal (MM) waveguide are most widely used waveguide for THz QCLs.

A SI-SP waveguide is formed by two thin (<0.8 μm) layers of heavily doped layers sandwiching the active region layer. Those two thin layers confine the THz modes. MM waveguide is achieved by directly fabricating a metal layer above and below the active region layer. In this instance, THz modes are almost completely confined to the active region [62]. Due to this strong confinement, THz modes can be confined in all directions, which minimize the dimension of the device and reduces the generated heat and also provides a better thermal dissipation. Consequently, the MM waveguide gives a higher working temperature for THz QCLs, especially in CW operation mode. The MM waveguide has a poor beam pattern and lower output power compared with SI-SP waveguide device. The low power of the MM waveguide is caused by the small mirror loss, so most photons generated are reflected back into cavity instead of radiating out [68]. The low power performance of the MM waveguide is made worse by the poor beam profile which is caused by the long free space wavelength of THz radiation, around 100-200 μm, which is much larger than the MM device's facet (around 10 μm). The divergent angle of the beam is therefore larger than 120°.

In order to obtain a better performance at higher temperatures and an output power as large as possible, MM device can be integrated into an external waveguide. This integrated device will be introduced in Chapter 5. The LOCUS project requires the LO working at a high temperature (100K) [103], in CW operation and with enough output power to pump a Schottky diode detector (several mW [103]). The external waveguide together with a feed-horn can help the MM device to have a higher output power and a significantly better beam profile (20°).

2.2 Material used for fabrication

THz QCLs used in this project were grown using InAs/AlGaAs by molecular beam epitaxy (MBE) [61], due to the mature growth technology of this material systems. A 250 nm GaAs buffer layer is first deposited on a 500 μm commercial GaAs wafer which is used as a substrate. The active region is grown between two highly doped electrical contact layers forming the anode and cathode respectively. The two heavily doped n^+ layers are usually only <0.8 µm thick and are used to confine the THz modes and minimize the influence of free carrier loss.

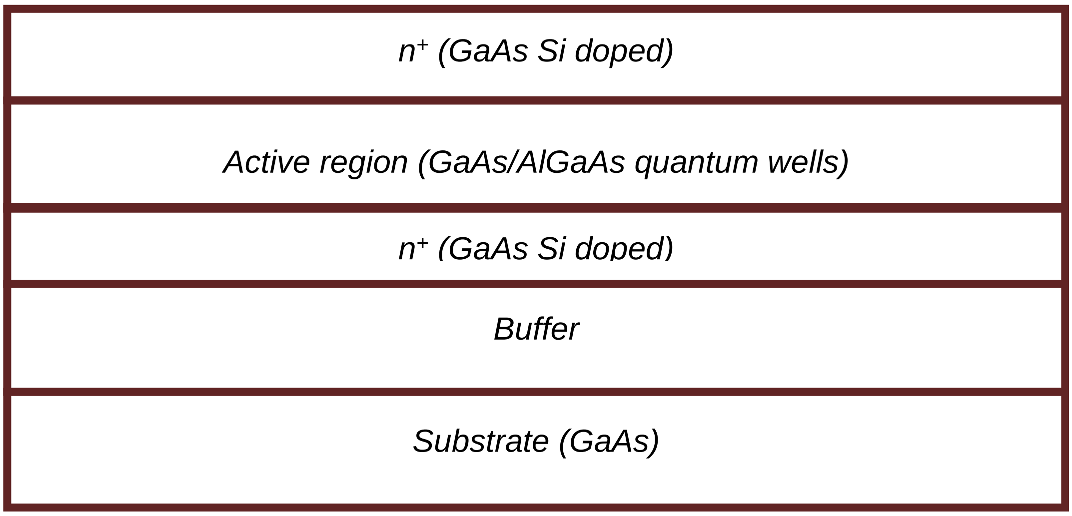

Figure 2-2 Structure of the cross-section of a THz QCL wafer

A 600-700nm-thick GaAs layer doped with Si (typical concentration of 3.5×10^{18} cm^{-3}) was grown to form a buried electrical contacting layer on top of the GaAs buffer. The THz QCL active region material comprising of GaAs/$Al_{0.15}Ga_{0.85}As$ hetero-structures were grown next. The thickness of each of the barriers (AlGaAs) and wells (GaAs) depends on the QCL active region design. Growth concluded with a 50-80nm-thick GaAs layer doped with Si (typical concentration of 5×10^{18} cm^{-3}) to form another electrical contacting layer. The maximum doping level of the n+ layers is limited by the MBE growth [110]. The higher the doping, the smaller the electrical resist, which can reduce the threshold Voltage and increase CW operation temperature. A schematic of the cross-section of a typical MBE grown THz QCL wafer is given in figure 2-2.

After growth, the THz QCL wafer is diced into 8mm x 6mm chips, which are processed in the cleanroom to fabricate laser ridges. The cleanroom processing of THz QCLs involve multiple iterations of photolithography, subtractive etching, and thin film metal deposition. Once the THz QCL chip is fully processed individual lasers are diced to form high quality mirror facets and are packaged on a copper block. The following sections briefly describe the major cleanroom processing techniques used to fabricate THz QCLs.

2.3 Methods used in the cleanroom

2.3.1 Photolithography

Photolithography [111] is used in the fabrication procedure to pattern micron and nanometre scale features on to parts of the QCL chip coated with a thin film of ultraviolet (UV) sensitive photoresist. Typically, photolithography comprises three major steps: photoresist preparation, UV exposure, and pattern development.

A photoresist [112] is a chemical which can react with certain energy of photon. The underlying principle of photolithography relies on the way photoresists respond to exposure by UV light. There are two types of photoresist - positive and negative photoresists. In a positive photoresist, areas that have been exposed to UV will exhibit selective solubility in a developing solution, which results in an exact copy of the pattern on the chrome mask being transferred onto the photoresist coated sample. Whilst, a negative resist will result in the inverse of the pattern being transferred onto the photoresist coated sample.

The photoresist Microposit S1813 and the developer Microposit MF-319 (an aqueous solution of tetramethylammonium hydroxide) were used for all photolithography based processing of THz QCLs chips. A homogenous and 1.2-1.3-µm-thick layer of S1813 is spin coated at 5000 rpm (for 1 minute) on the surface of the chip. The photoresist coated chip was then baked at 115°C on a hot plate for 1 minute to remove the solvents from the resist and to harden the resist for further processing stages.

The photoresist coated chip is then exposed to UV light through a photo mask [113]. The photo mask consists of chrome patterns on the glass substrate and is the master pattern which is replicated onto the photoresist. The photomask allows UV light to pass through its transparent area and block the light by its metal area. So after UV light exposure behind the mask, the device achieves a copied pattern from the mask.

Development is a method that dissolves the exposed part and keeps all the other areas of the photoresist. After development of the pattern in a developer [114] (MF319), the exposed part of the photoresist is removed. During the exposure, it is the exposure time and UV source power that determines development time. Enough development time can remove exposed part of the covered photoresist while the pattern copied from mask was clear. After that, the device is rinsed in DI-water and dried by a nitrogen jet. The pattern is then checked under microscope before the next step.

Important parameters for photolithography are the spin speed for photoresist, time of exposure, and time of development. A higher the spin speed will give a thinner covered photoresist. The exposure time and development time cannot be too long, because the pattern may be etched away or too short to obtain a clear pattern. After experiments, the spin speed was chosen to be 5000r/min and development selected to be 75 s when exposed under 3mW/cm^2 for 90 s.

2.3.2 Metallisation

Metallization is the method used to deposit a homogenous thin film layer of metal on a chip. In this thesis, metallization is used for Ohmic contact formation, waveguide formation and improving thermal conductance. The principle of metal deposition in a vacuum [114] is shown in figure 2-3. A patterned wafer is placed in a vacuum chamber at the bottom of which is a heater. Metal ingots are then placed in a ‘boat’ heater and the temperature of the heater is gradually increased to the boiling point of the metal, at which evaporating will occur.

The deposition quality is determined by the background pressure in the chamber, and the purity of the metal material used. In order to achieve a high quality deposition, the mean free path [115] of the metal gas in the chamber should be bigger than the distance between solid metal source and the place of the sample.

The mean free path length of a metal atom in the vacuum is given by [115]:

$$\boldsymbol{\lambda = \frac{1}{\sqrt{2}\pi d^2 N_V}} \qquad (2.1)$$

Here, λ is the mean free path, *d* is the diameter of the gas molecules and N_V is the number of molecules per unit volume.

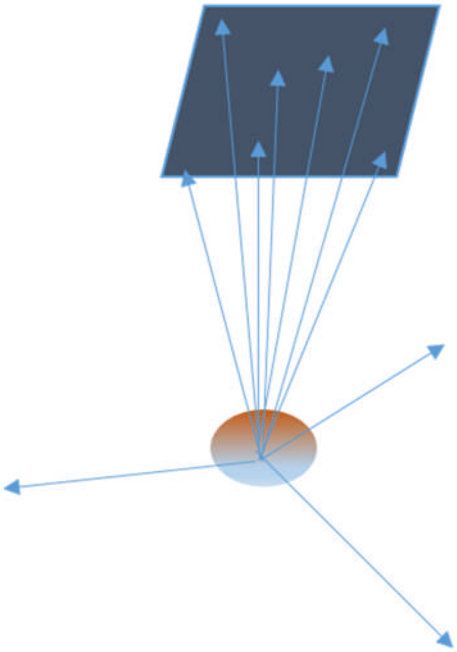

Figure 2-3 The principle of metal deposition in a vacuum chamber

Typically, the pressure in the chamber is below 2×10^{-6} mbar which will give a molecular mean free path of more than 100m [114] which is much larger than the size of chamber. There is therefore is no molecular collision inside the chamber during the evaporation, which will make the molecule travel homogenously in every direction. Deposition occurs when the hot molecular vapour meets the cold sample at the top of the chamber or the chamber walls.

After the deposition, the sample should be kept in the vacuum for 15 mins to allow it cool and prevent contamination by water from the atmosphere. Then the deposited sample is put into acetone to cause the photoresist on the sample to dissolve and remove the metal deposited on the photoresist. As such, the areas exposed to the UV light and dissolved by developer will keep the metal deposited on them and the pattern is obtained.

There are two types of contact between semiconductor and metal: Ohmic contact and Schottky contacts. Schottky contacts are described in detail in Chapter 4. In the THz QCL fabrication, bottom and top Ohmic contacts are needed for the mesa whilst Schottky contacts are required for over-layer and back side metallization. The type of contact is determined by the semiconductor Fermi level [116] and metal work function [116] and the interface between the semiconductor and metal. The contact resistance of a THz QCL is a very important parameter because a high contact resistance can result in high heat generation, which prevents the QCL operating at high temperature. In order to increase the working temperature of a THz QCL and the power efficiency, the contact resistance should be as low as possible, which is realised by annealing the contacts. At the same time, a Schottky contact is used for waveguide because it leads to a more abrupt interface and a less interaction with optical field [117].

For the Ohmic contact, a fast annealing in a vacuum was carried out. The heating process makes the deposited metal atoms penetrate into the GaAs lattice forming an Ohmic contact [118]. The vacuum applied during the annealing creates an inert environment which will prevent any chemical reaction between the device and atmosphere. Dry N_2 was used during the cooling to conduct the heat much more efficient.

2.3.3 Etching

Etching is used to selectively remove material from a sample. The etching must be very precise and the etching speed must be controllable. The most important factor is having a solution that can etch away the wafer material, without effecting the photoresist. The etching should occur at a reasonable rate, typically completing the process in 10 minutes for 10 μm thick active region layer. As QCLs in the project are all GaAs/AlGaAs based semiconductor, the solution chosen is a mixture of H_2SO_4, H_2O_2 and H_2O. This is a widely used solution for GaAs wet etching [119].

The etching speed can be controlled by the concentration of H_2SO_4, the higher the concentration, the higher the etching speed will be. The reactions in the solution are as follows [120, 121].

$$\mathrm{2GaAs{+}9H_2O_2 \longrightarrow Ga_2O_3As_2O_6 + 9H_2O}$$

$$\mathrm{Ga_2O_3As_2O_6 + 2H^+ \longrightarrow 2Ga^{3+} + 2AsO_4^{2-} + H_2O}$$

For a volume ratio of H_2SO_4:H_2O_2:H_2O at 1:8:40, the etching speed is 1.5 μm/min at the beginning of etching and decreasing to 0.8 μm/min due to a reduction of chemical concentration and the formation of a layer of oxides on the substrate surface. Sulfuric acid is exothermic when dissolved in water and the etching speed is strongly influenced by solution temperature. To allow the solution to cool, a delay of 30 minutes is needed between preparation the solution and starting etching.

The Alpha step profile is used to measure the etched depth before, during and after the etching. The sample is removed from the etching solution, rinsed with DI-water and measured. This process is repeated until the bottom contact can reach the lower n+ layer.

During the entire THz QCL fabrication process, wet etching is completed three times: for ridge etching, backside thinning and PL patterning. Different etch concentration were used. Ridge etching and PL pattern etching should be slow because precision is more important than the etching speed for those two steps. However, the backside thinning process requires a quick etch, about 450 µm GaAs needs to be removed. The concentrations of the mixed solution are thus different. Details of the individual solution will be presented in the QCL process section of this chapter and single mode QCL development in Chapter 3.

2.4 Processing

The QCLs used in this thesis were fabricated in the Wolfson Nanotechnology Cleanroom at the University of Leeds. The processing procedure includes cleaning the wafer, ridge etching, bottom contact metallisation, top contact metallisation, over-layer metallisation, backside thinning, backside metallisation, annealing, sintering, cleaving and bonding. All processing steps should be performed in the cleanroom that has stringent dust control measures, as any dust may contaminate the chemicals or solutions. This is important as the size of dust particles is similar to that of patterns on the wafer. The flow chart of QCL processing is shown in figure 2-4, The whole detailed processing recipe is attached in appendix I.

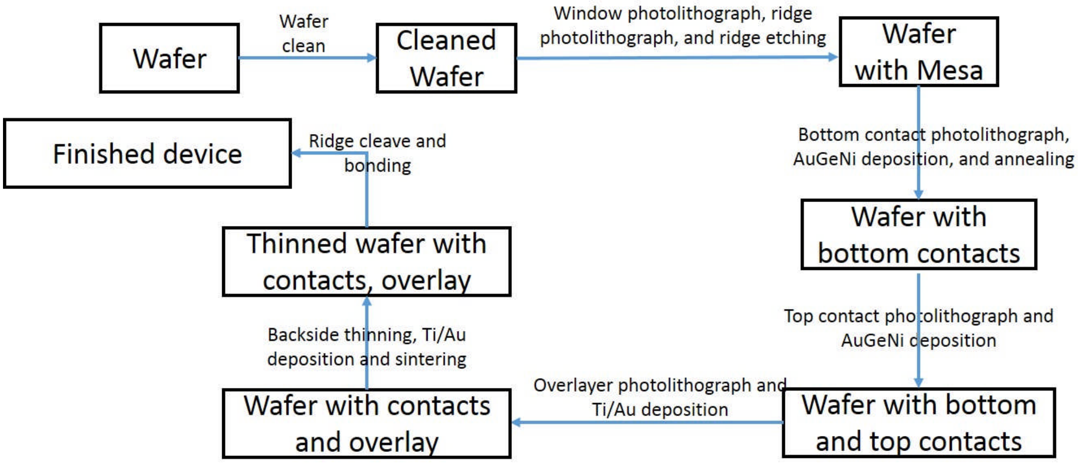

Figure 2-4 Flowchart of QCL processing

2.4.1 Cleaning wafer

After a QCL is grown via MBE, it is then cleaved into parts, typically 8×8 mm. This can introduce dust and contaminations. Contamination can remain on the wafer and become programmatic during the photolithography and etching steps. This can result in defects on the device and decrease the yield of QCLs manufactured.

Before processing begins, the wafer is placed in acetone for 2 minutes then in room temperature IPA for another 2 minutes. A repeat of this step is necessary to make sure all the small organic contaminants are removed. The wafers are then put into an oxygen plasma asher which can clean the organic waste shown in figure 2-5. This is a fully automated, table top oxygen plasma asher, used primarily for sample cleaning and etching graphene. The substrate was put in the plasma asher for 5 minutes, under 50 W of power. After these steps all organic waste and dust should be removed, as shown in figure 2-6 (a). However, there may still be something left as figure 2-6 (b) shows. They are probably defects of the wafer.

Figure 2-5 Oxygen plasma asher

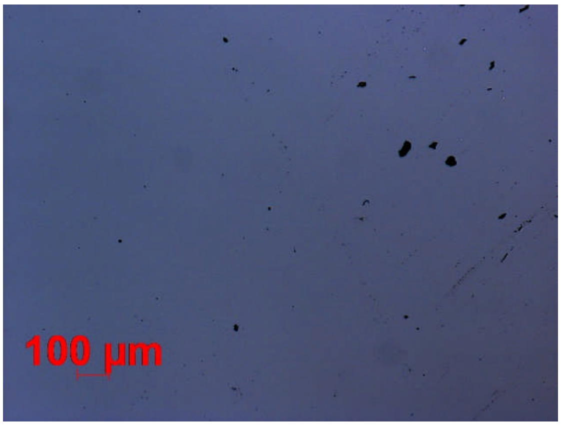

(a)

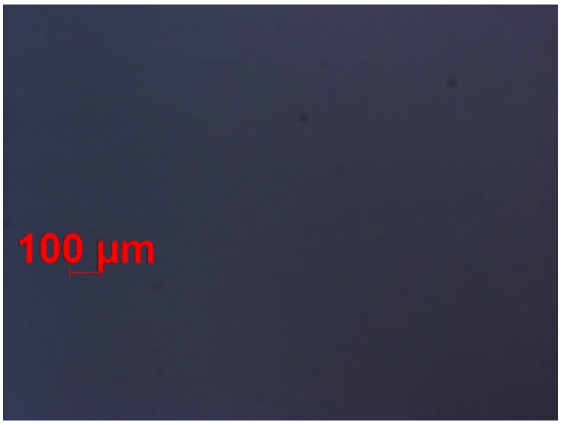

(b)

Figure 2-6 The wafer used for QCL fabrication. (a) is the wafer surface before cleaning and (b) is the same region of wafer surface after cleaning.

2.4.2 Ridge etching

Having cleaned the chips to be processed, the laser ridge is etched. Figure 2-7 shows the device after ridge photolithography. The dark area is covered by photoresist S1813, whilst the pink area is GaAs.

The patterned sample was then etched in H_2SO_4:H_2O_2:H_2O (1:8:40). The photoresist S1813 is acid resistant as well. After the etching, the pattern is checked under a microscope and recorded, (figure 2-8 (a) and (b)). The etched wafer with photoresist is given in figure 2-8 (a) which shows the shape of the ridge.

After etching, the device is cleaned with acetone and IPA as shown in figure 2-8 (b). The dimensions of the ridge are slightly different from the pattern put onto the wafer. It is around 10 μm narrower than the 150 μm wide pattern and the shape of the ridge is trapezoid instead of rectangular, which is caused by anisotropic wet etching [122, 123] of GaAs by the acid solution used in the processing.

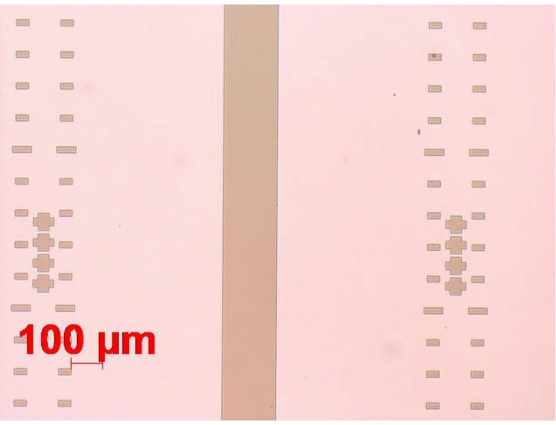

Figure 2-7 The device after ridge photolithography

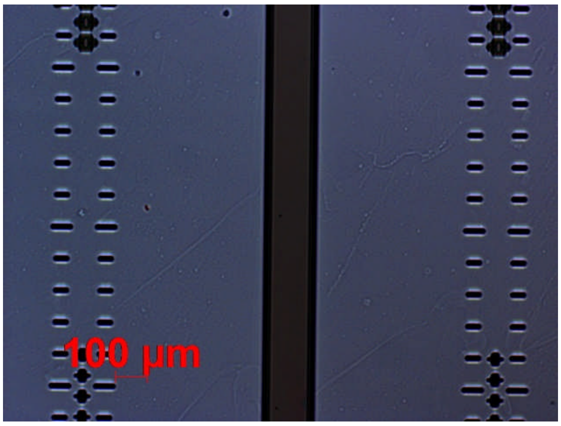

(a)

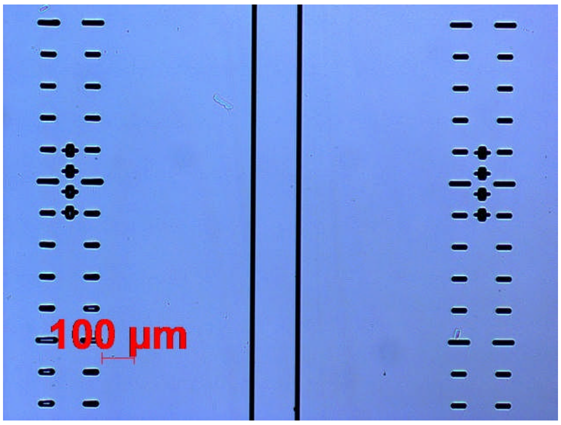

(b)

Figure 2-8 Process of ridge etching. (a) is the device after etching and (b) is the etched device after cleaning

2.4.3 Bottom contact metallization and Ohmic contact annealing

A bottom Ohmic contact is formed to the n+ layer which is exposed when the top n^+ layer and active region are etched away. The doping level of this n+ layer is Si doped and the doping level is around $1.0\times10^{18}cm^{-3}$. There are four steps needed: photolithography, metal evaporation, lift off and annealing. Pictures taken under the microscope after each processing steps are shown in figure 2-9 (a), (b) and (c).

Figure 2-9 (a) is the device after bottom contact photolithography. The dark area is covered by photoresist S1813 and the white area is exposed to UV light and dissolved in the developer MF319. In order to avoid direct contact between bottom n^+ layer and the top n^+ layer, the pattern used to cover the ridge should be wider than the size of ridge, as seeing in figure 2-9 (a).

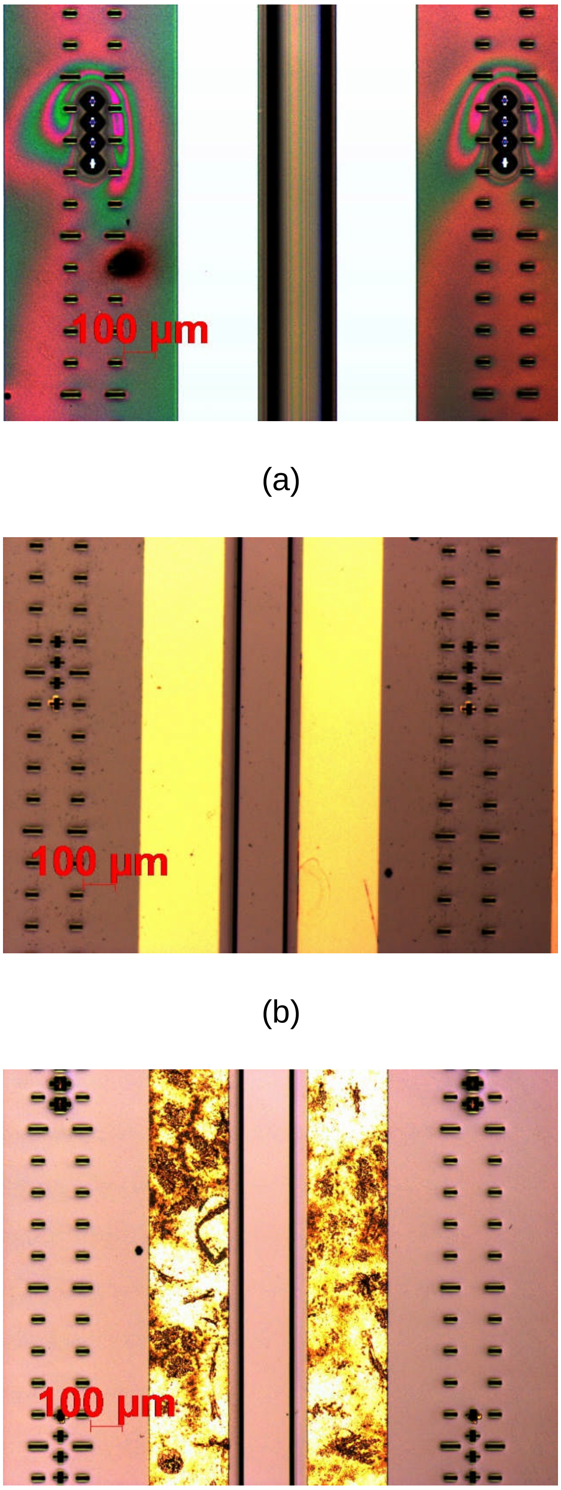

(a)

(b)

(c)

Figure 2-9 Process of bottom contact metallization. (a) is the picture after photolithography, (b) is the picture after metal deposition and lift off and (c) is the picture after bottom contact annealing.

After obtaining the pattern, 0.5-0.6g of AuGeNi alloy was deposited with an evaporator to achieve a 240 nm thick bottom contact layer, which is shown in figure 2-9 (b).

Following the deposition of a thin film of metal on the surface, an annealing process is required to make the GaAs and AuGeNi intermix. The annealing is carried out for 1 min while temperature is maintained at 430℃, which will make metal atoms penetrate deeper than 30 nm into GaAs [121]. After annealing, the n-GaAs and AuGeNi contact resistance is around 0.1Ω [116]. The resist between the two bottom contacts is then measured to make sure the whole bottom contact processing is correct. Normally, the resistance should be less than 10 Ω at room temperature. If the resistance is much higher than this value, the sample has been over-etched and the bottom n+ layer is partially or completely etched away. The device can no longer be used.

2.4.4 Top Ohmic contact metallization

Top contact processing forms a metal-semiconductor contact to the top n^+ layer which is Si doped GaAs with a doping level 5×10^{18} cm^{-3}. There are two differences between the bottom and top contact formation. Firstly, the size of the top contact is much smaller than the bottom contact. The reason for this is that the Ohmic contact will introduce free carrier loss and affect the laser performance, such as threshold current, maximum working temperature and the radiated power. The other difference is the annealing temperature after contact metallization, as it is important that the metal doesn't penetrate the active region.

For the top contact, sintering is used to make the AuGeNi and GaAs intermix. The sintering is carried out for 4 minutes while the temperature is kept at 270℃. A higher temperature would make metal atoms penetrate into the active region, which would damage the active region structure and affect the performance of the laser. Top Ohmic metallisation is illustrated in figure 2-10 (a) and (b). The sintering process for top contacts is performed after the metallisation has taken place.

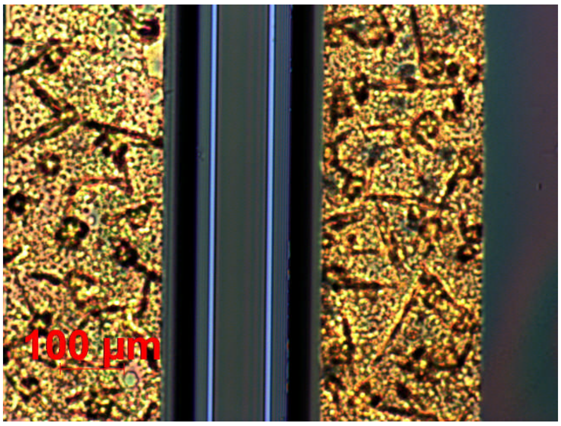

(a)

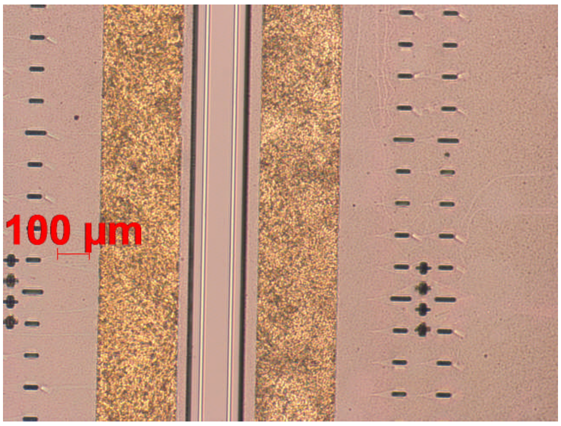

(b)

Figure 2-10 Process of top contact formation

(a) is the picture taken after photolithography and (b) is the picture taken after metal deposition and lift off.

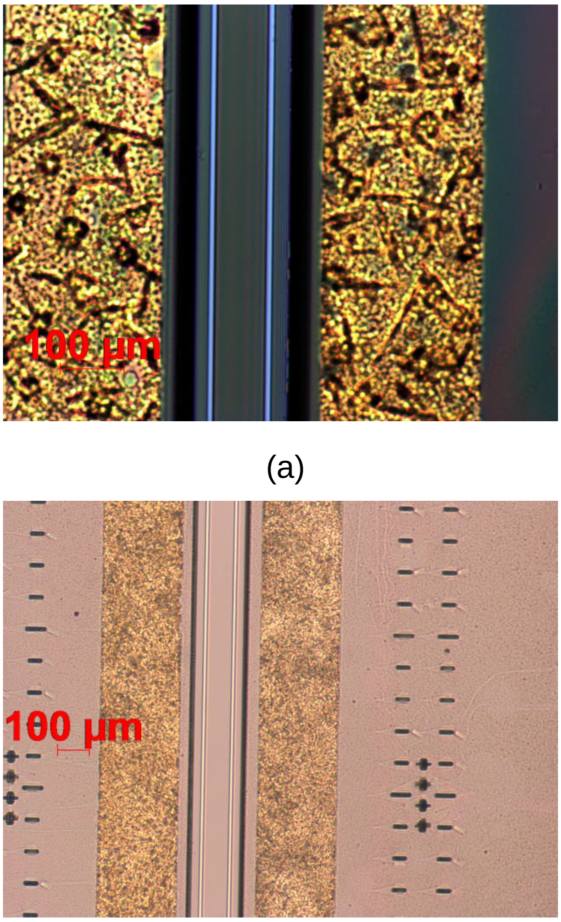

(a)

(b)

Figure 2-11 Process of top contact formation. (a) is the picture taken after photolithography and (b) is the picture taken after metal deposition and lift off.

2.4.5 Over-layer metallization

The over-layer metallisation is a thin film of metal covering the ridge and bottom contact. The over-layer metal has two functions: 1, it forms a Schottky barrier with the top layer of GaAs and this layer of metal will form the plasmonic waveguide cladding; 2, the bottom contact layer is actually very rough after annealing and a layer of metal (Ti/Au) deposited on top makes it smooth and easy to bond.

Photolithography, metal deposition and lift off are all used to achieve an over-layer metallization. The over-layer metal is 150±10nm Au deposited on the top of 20 nm of Ti. The following figure 2-11 shows a picture of the device taken under microscope after over-layer metallization processing.

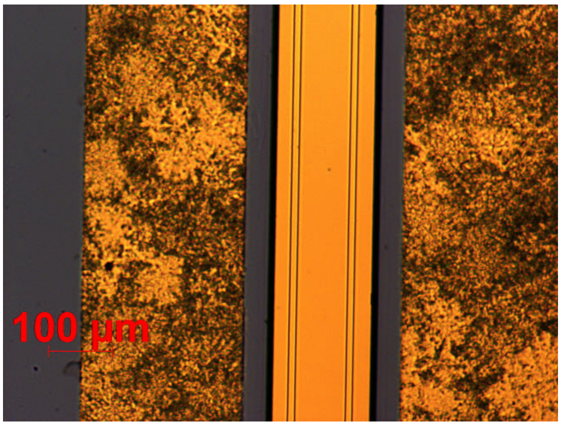

Figure 2-12 Device picture after over layer metallization

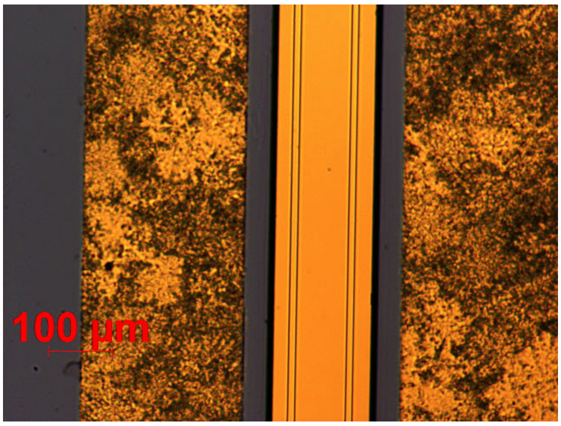

Figure 2-13 Device picture after over layer metallization

2.4.6 Back side thinning

The thickness of the wafer used is around 500µm. This prevents efficient heat extraction when bias is applied to the contacts. The thickness of the wafer should be as thin as possible but it becomes very difficult to process if it is below 150µm. After several tests, a substrate thickness of 180 µm was chosen.

The etching solution used was $H_2SO_4:H_2O_2:H_2O$ (1:8:1), given an etching speed of 8-15 µm/min. The width of the wafer before backside thinning is around 602 µm which is shown in figure 2-12 (a) which is 440 µm thicker than the substrate width after the backside thinning processing shown in figure 2-12 (b).

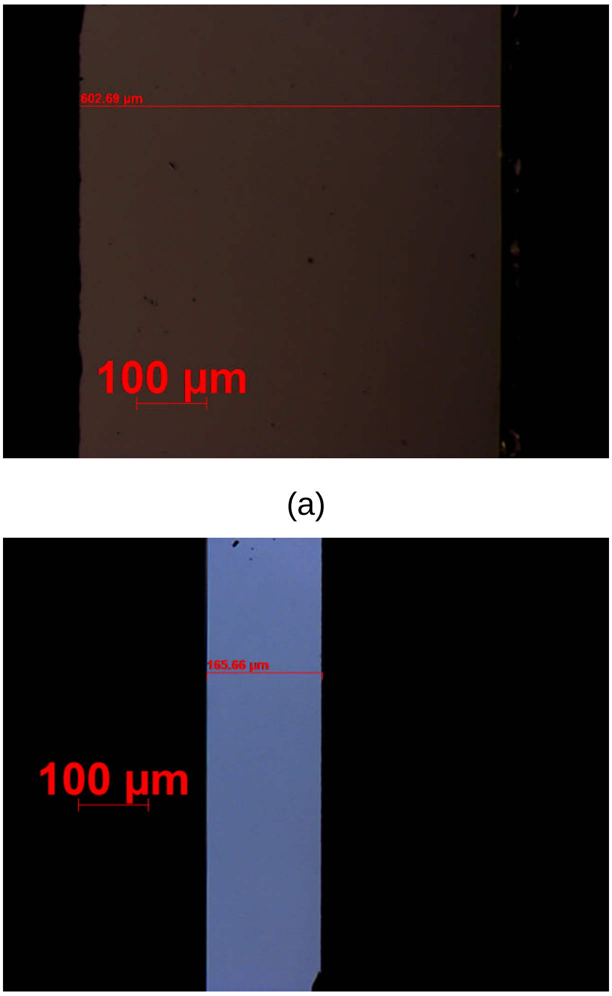

(a)

(b)

Figure 2-14 The substrate thickness of the fabricated QCL wafer. (a) is the cross section of the device which is around 600 µm before backside etching and (b) is the cross section of the device which is around 165 µm after backside etching.

2.4.7 Back side metallization and sintering

In order to improve the thermal conduction, a 20 nm/150 nm Ti/Au is deposited on the backside after wafer thinning. After the metallization is finished, the device is sintered for 4 min at 270℃. The sintering makes the top contact, over-layer and back side metallization penetrate into the GaAs.

2.4.8 Cleaving

The length of a THz QCL can affect the device power and temperature performance. Longer devices have larger gain and generate more heat than the shorter devices. On the other hand, the heat emitted will increase the electron gas temperature making the gain smaller.

A scriber is used for cleaving which has a precision of 0.1 µm. The scriber gives a high probability (up to 85%) of good facet. A high quality facet partially reflects the radiation back into the cavity and partially radiates. A well-cleaved facet is presented in figure 2-13 (a), and (b) presents a poor facet.

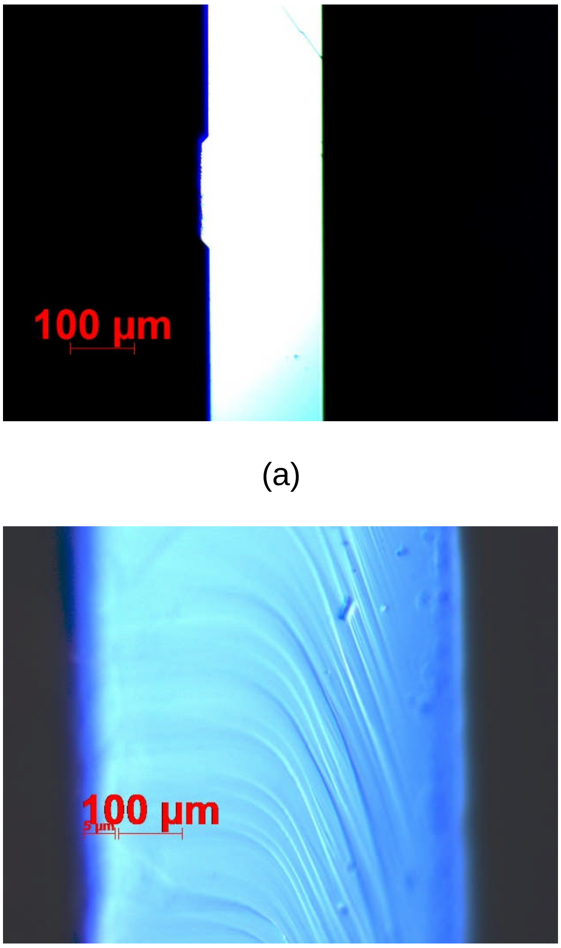

(a)

(b)

Figure 2-15 The cleaved facet of the fabricated QCL. (a) is a good facet which can give a mirror like reflection while (b) shows a poor facet which will give too much loss.

2.4.9 Wire bonding

The cleaved device is then placed on a copper block, which acts as a convenient mount for the cryostat and a good thermal conduction. In order to stick the cleaved device to a copper block, an indium ingot is put on the surface of copper block and heated to a molten state and spread into a thin and smooth layer. The cleaved sample is put on this thin layer of molten indium which is then cooled. The QCL and copper block are then bonded by a thin and homogenous layer of indium.

After the device is bonded to the copper block, the bottom and top contacts are bonded with gold wires to two different ceramic pads. The bias applied to the ceramic pads will be transferred to the QCL contacts by the gold wires. The bonded QCL is shown as figure 2-14.

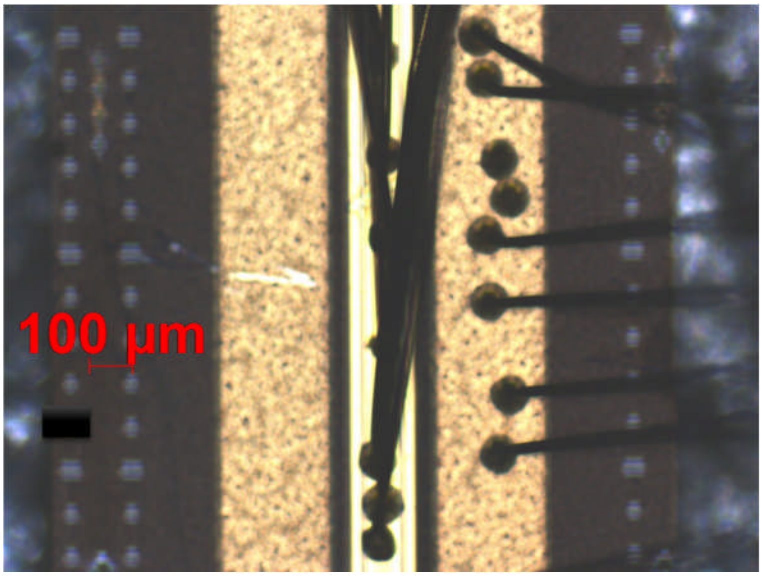

Figure 2-16 Gold wire bonded QCL. The black wires are gold wire connecting the contacts of QCL and the ceramic pads.

2.4.10 Summary of processing

The performance of a QCL is dependent on the active region design and waveguide. However, the processing also has a big influence on the performance. During the project, many devices were fabricated to give feedback on MBE growth and fabrication.

The most important processing step is ridge etching. It creates an area for the bottom contact and also defines the waveguide. Both over and under etched will give bad device performance. Usually, the ridge etching stops at 0.5 µm above the bottom n^+ layer. There will be a large electrical resistance if the bottom n+ layer is etched away due to the lack of carriers. The normal resistance between the two bottom contacts on both sides of the QCL is around 10 Ω. The resistance will be several orders larger than that value if the device is over etched. On the contrary, the device will be shorted if the etched depth isn't enough because the metal contacts will contact the active region directly. So the etching speed is controlled at around 1 µm/min.

The etching depth of the backside substrate is also important. A thinner substrate will improve heat dissipation of the device but it will make processing difficult when the substrate is too thin. The substrate thickness presented in the thesis is 180 µm which proved to be a good compromise.

The length of device is also critical. A longer device can emit more power but gives more heat, leading to a compromise between power and maximum working temperature.

2.5 Characterization of a THz QCL

2.5.1 Parameters need to be characterized

THz QCLs offer the advantages of high power, easy integration with other semiconductor devices, good beam profiles and low cost compared to other THz sources. However, there is also a critical disadvantage, which is the need to operate at cryogenic temperatures. The current-voltage relationship (I-V curve) is another important characterization parameter, both from the view of application and also understanding designs and wafer growth. The other two parameters are emission power and emission frequency as a function of bias.

Much information can be obtained from the L-I-V curves of a QCL including the QCL operating resistance, power efficiency, dynamic range and highest operation temperature. The I-V curve also allows better understanding of the active region design, with the threshold current density being closely related to the n^+ doping level.

Another important parameter for a THz QCL is the emitted frequency, which is dependent on active region structure. The active region structure of a QCL is determined by the MBE growth procedure. The emitted frequency can provide feedback to active region designer and MBE growth for adjustment. The frequency of a QCL is also important to the application of spectroscopy and imaging.

The output power of the QCL is also an important parameter. The highest recorded output power to date from a THz QCL is 1.02W [63]. A higher power from the QCL indicates higher wafer quality, which is very important to MBE growth.

Some other parameters such as beam profile can also be measured according to the need of application.

2.5.2 Operation modes of characterization

There are two operating modes in which the QCLs are characterized: pulsed mode and continuous-wave (CW) mode. In pulsed mode the QCL is electrical pumped for a short period of time at a high repetition rate, whereas in cw mode electrical power is used to bias the QCL without turning it off at any point.

Under a pulse bias, the heat generated by resistance of the QCL in the ‘on’ period of the pulse can dissipate when the QCL is temporarily turned off during the ‘off’ period of the pulse. During most of my characterization, a pulse duty cycle of 2% (10 kHz repeat frequency) is applied to obtain a sufficient cooling effect. At the same time, the THz detector used in the characterization is thermal based and therefore can only operate at a slow detection speed (167Hz). In order to obtain a lock-in detection, which is used to improve the signal to noise ratio (SNR) of the measurement, a modulation frequency (167 Hz) is applied to gate the 10 kHz pulse train. A figure showing the bias pulse train applied in the measurement is provided in figure 2-15.

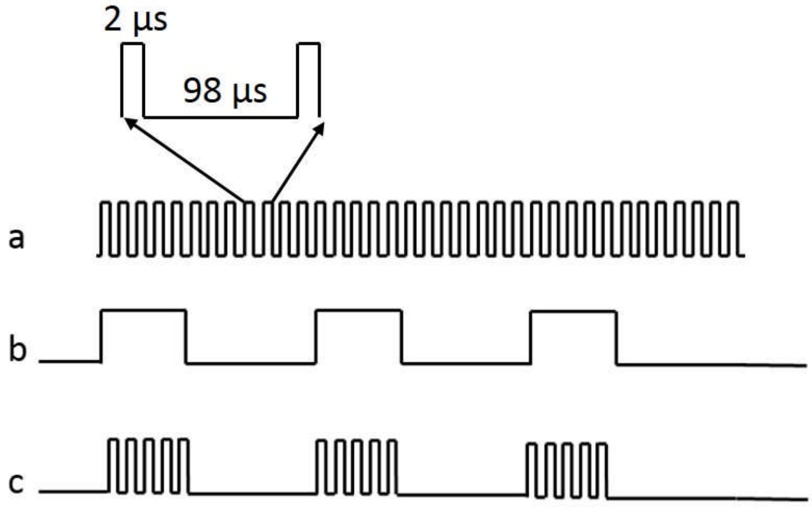

Figure 2-17 The pulse used to drive a QCL. (a) is the period of the pulse is 100 µs (10kHz) which contains 2-µs-wide ON state (2% duty cycle). (b) is detector modulation frequency (167Hz). And (c) is the gated pulse (between the detection pulse and the drive pulse trains) bias applied to the QCL during the measurement.

2.5.3 LIV characterization

A cryostat contained the QCL is cooled using liquid helium to temperatures as low as 4K. Due to heavy absorption of THz radiation in the atmosphere, the cryostat is placed into a dry-nitrogen purged box and the emission is coupled to a liquid helium-cooled bolometer using a pair of parabolic mirrors, in order to minimize the loss of THz power during the measurement. The bias voltage applied to QCLs is from a current source, where the output pulses has been modulated. When the measurement begins, the QCL bias device is steadily increased. At a certain point, the current exceeds the laser's threshold and the outputted THz radiation is detected using a helium cooled bolometer. The detected radiation has the same period as modulated current source so do the reference of phase locker which is used to lock the radiation generated at a given point of current. This point represents the current source. Therefore, the power given by phase locker can represent the power generated by a constant continuous current source.

The oscilloscope, lock-in amplifier and power-meter are directly connected to the computer. Using this equipment, integrated with specially designed LabVIEW software, values for the bias applied bias (voltage and current) and the corresponding output power are retrieved and can be plotted to form LIV curves. These are then performed at different temperatures. The absolute power from the device are different bias conditions can also be determined.

As mentioned before, T_{max} is one of the most important parameters in QCLs measurements. As such, a temperature controller connected to the cryostat is used to set the working temperature of the device.

As the heat sink temperature increases, the THz power emitted from the QCL will decrease. T_{max} is the temperature at which the THz radiation outputted from the QCL can no longer be detected by the bolometer, therefore it is the highest operation temperature of device. The setup for pulse mode measurement is given as figure 2-16.

As well as characteristic LIV curves, the TK power meter can also be used to measure the absolute power from QCL. The TK power meter is also sensitive to changes in temperature and thus has a response time that is too long for use in QCL dynamic power measurement sweeps. Therefore, usually a single measurement of absolute power is taken at a single bias condition, which acts as a scaling factor for the data taken using the bolometer. An example of a set of LIV curves in pulsed mode is provided in figure 2-17.

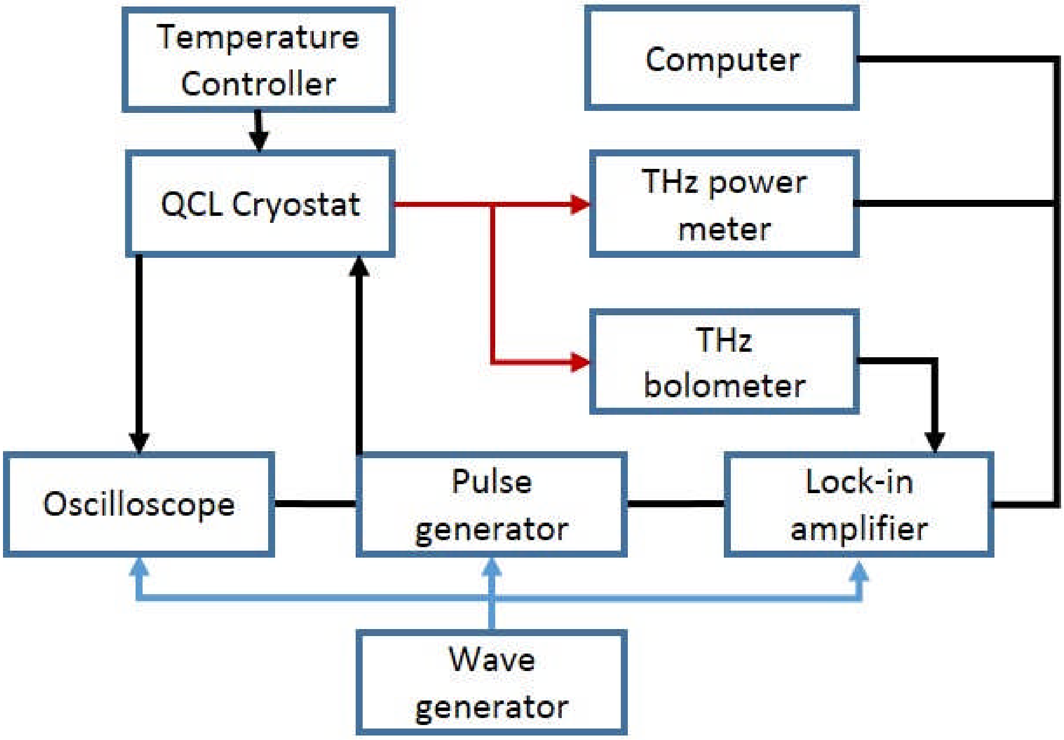

Figure 2-18 QCL LIV characterization setup (pulse). The trigger is the gate modulation frequency generator which modulates lock-in amplifier (LIA), oscilloscope, and pulse generator at 167 Hz given as blue arrows. LabVIEW code running on a computer is used to collect the signal from the lock-in amplifier and the I-V signal from the oscilloscope. The LabVIEW code is also used to control pulse generator given as black lines. The red arrow is THz radiation and black arrows are electrical signals.

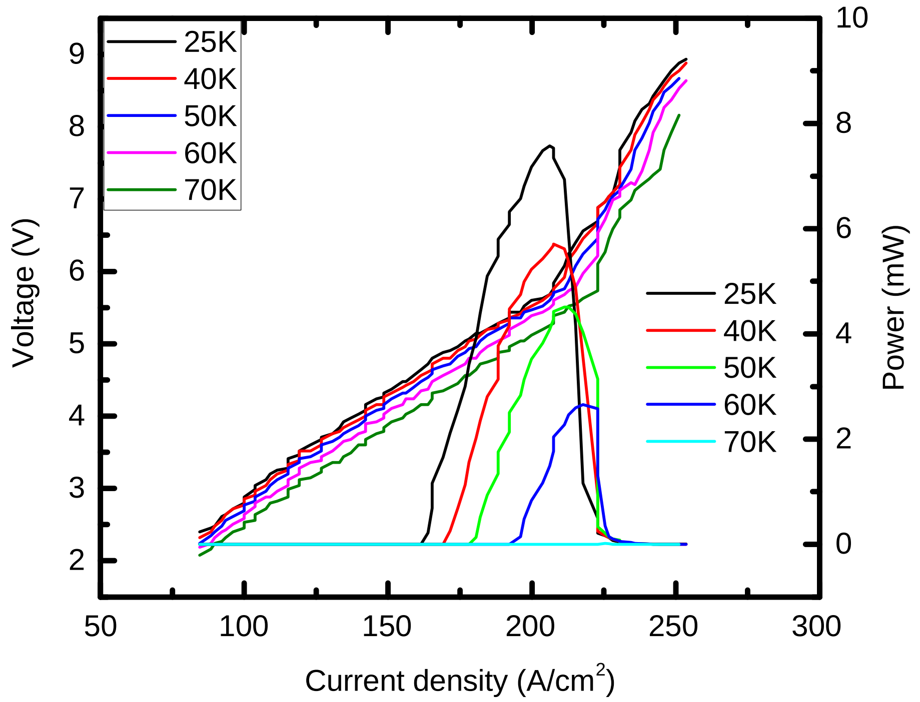

Figure 2-19 Measured LIV of a 180 µm-thick-BTC device**.** The device dimensions are 3.5mm×150 µm operating at 2.2 THz for various heat sink temperatures. The measurement was performed under pulsed operation using 2% duty cycle at a repetition rate of 10 kHz, gated at 167 Hz.

The LIV curve contains LI and IV curves. All the IV curves remain a similar shape as heat sink temperature increases, while the magnitude of the LI curves decreases as heat sink temperature increases. This decrease in power is caused by a drop in QCL gain at high working temperatures. An explanation for this is presented in the introduction section. There is also a slightly decrease in voltage at the same current density, which is due to increased carriers at high temperature. As the current density scans from zero to the threshold current density, there is no lasing at all. Once the bias reaches the devices threshold current density, lower lever subbands begin to align with the higher level subband of next lasing period and the QCL begins lasing. The peak power occurs when the two subbands align. As the current density continues to increase, parts of the subband begin to misalign which will decrease the gain of laser. The power therefore decreases with an increase in bias.

If the bias continues to increase after the two subbands have completely misaligned, there is no longer gain and the power decreases to zero. The device conductance decreases dramatically when misalignment occurs as the electron carriers are bound to separate quantum wells again.

For some QCL applications such as imaging and spectroscopy, CW operation is a more common choice than pulse mode. To fully characterise a device CW mode operation is also required. Running a QCL in CW mode will generate much more heat than pulse operation during a certain period of time (longer than the pulse duty cycle). The heat will increase the QCL real working temperature, which will make the phonon energy big enough to stop the lasing of QCL. Thus before any CW characterization, the QCL is characterized by a high duty cycle (95%) pulse mode.

The setup for CW operation is similar to that of pulsed except for the power supply and lock-in detection shown as figure 2-18. A DC current source is used to electrically drive the QCL. An optical chopper at a frequency of 167 Hz is used as a reference for the Lock-in amplifier. The measured CW mode LIV curves are given in figure 2-19.

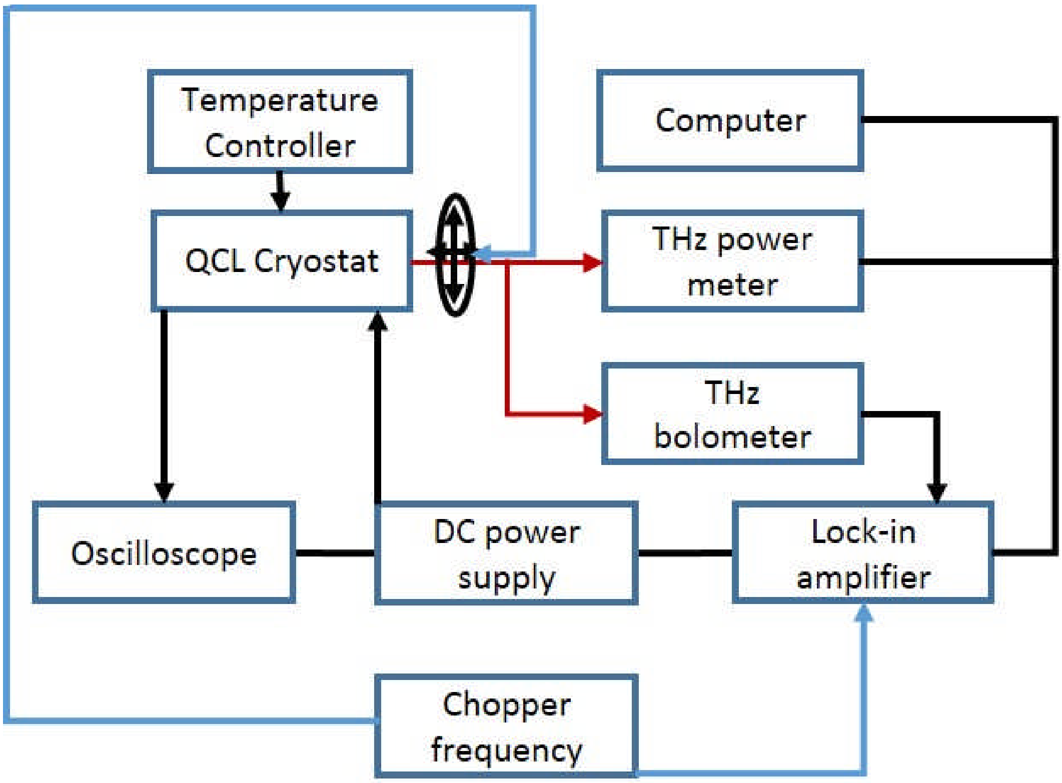

Figure 2-20 QCL LIV characterization setup (CW). Compared with pulse operation, A DC power supply is used instead of the pulse generator. The LIA is modulated by the chopper frequency which also modulate the THz radiation receiver mechanically given as the blue arrows.

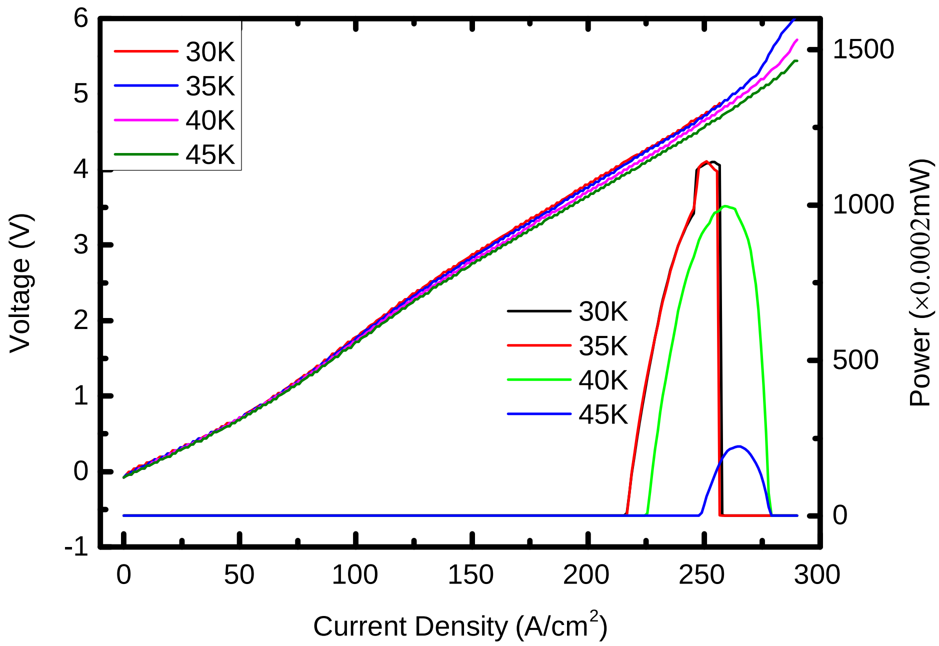

Figure 2-21 Measured LIV of a 180 μm-thick-BTC device (CW). The device has dimensions 2.4mm×150 μm operating at 2.2 THz for various heat sink temperatures. The measurement was performed under CW operation mode.

The CW LIV curves is the same shape as in pulse mode. However, CW operation will generate more heat than in pulse mode, which will decrease the maximum working temperature. This device can only lase up to 45K in CW mode, when in pulse mode can output radiation as high as 65 K. Due to heat accumulation resulting a decrease in gain, CW mode also provides lower power for the same heat sink temperature, when compared to pulse mode operation. The threshold current density in CW mode is also higher than that in pulsed mode. This is again due to the accumulation of heat resulting in a decrease in the gain.

After the LIV curve is obtained, the lasing dynamic range of the QCL is also determined. The emission spectrum of the QCL can be measured. This is achieved using a Fourier transform infrared spectroscopy (FTIR) [9] system. The spectrum obtained is given in figure 2-20 and 2-21 for pulse and CW QCL radiation spectrum respectively. In pulsed mode, spectra at bias currents ranging from 0.78 A to 0.98 A have been measured. Spectrum in CW mode at different bias current from 0.74 A to 1.04 A are measured.

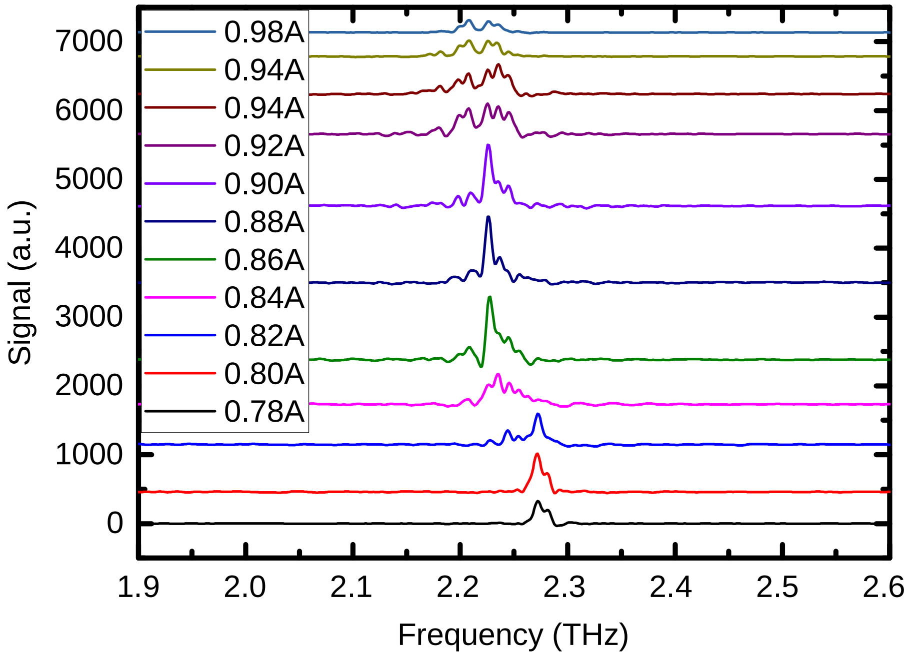

Figure 2-22 Measured spectrum of a 180 µm-thick-BTC device of dimensions 2.4mm×150 µm operating at 2.2 THz for various bias at 30 K. The measurement is taken under pulsed operation using 2% duty cycle at a repetition rate of 10 kHz, gated at 167 Hz.

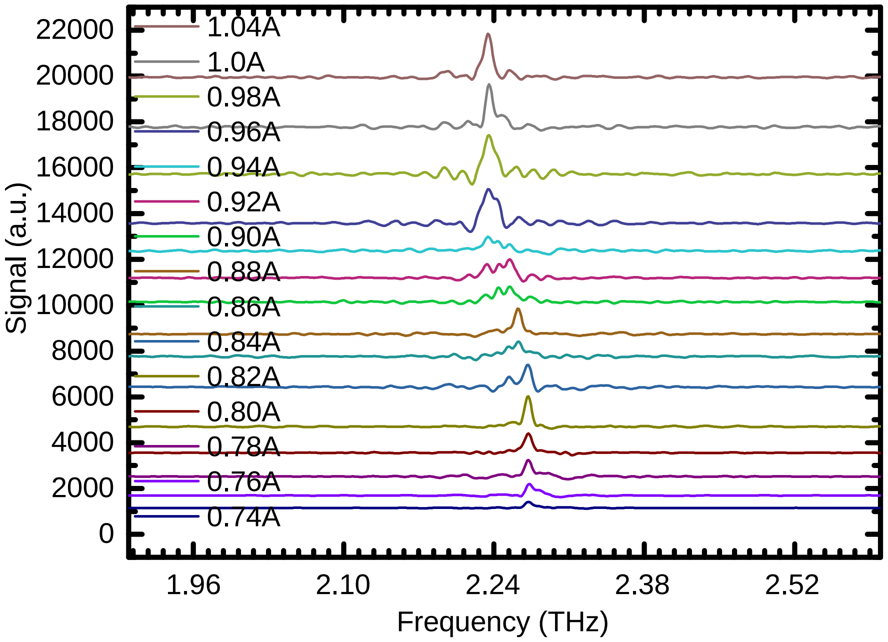

Figure 2-23 Measured spectrum of a 180 µm-thick-BTC device of dimensions 2.4 mm×150 µm operating at 2.2 THz for various bias at 30 K (CW)

2.6 Conclusion

In this chapter, the fabrication of a single plasmon waveguide THz QCL is presented including the cleanroom fabrication method. All the fabrication parameters and the reasons for the choice of these parameters is introduced.

After introducing the fabrication procedures, the characterization of this QCL is presented. The basic theory of the QCL is also introduced to explain how the QCL works under forward bias and why the parameters chosen are measured during the characterization. Two operation methods are applied for the characterization, pulse mode and CW mode. For both operation modes, the experimental setup is presented and the parameters used in the measurement are also given. Two types of measurement, LIV curves and spectrum for both operation modes are presented. The results of this characterization of a single metal THz QCL are given as figure 3-5, figure 3-7, figure 3-8 and figure 3-9 for LIV and spectrum characterization result for pulse and CW operation mode respectively.

Chapter 3Development of single mode THz QCL

3.1 Introduction

In Chapter 2, a typical spectrum of an as-cleaved Fabry-Pérot laser was presented. This displays multiple modes over the gain spectra of the laser. As mentioned in Chapter 1, however, the LOCUS [9, 103] project aims to address high definition spectroscopy in MLT region. This is achieved by heterodyne detection between the Local oscillator (LO) radiation and the detected emission. This requires development of a highly stable LO, operating on a single mode.

The THz LO proposed in the project uses a single mode THz quantum cascade laser (QCL). The development of this single mode THz QCL is presented in this chapter.

3.1.1 Fabry-Pérot laser

In a semiconductor laser with cleaved facets, a resonator is formed between two partially reflecting mirrors. The radiation is partially absorbed by electrons in upper level subband to undergo stimulate emission and partially reflected by the facet, with the other part of the radiation being emitted into air. The basic principle of such a FP laser is shown in figure 3-1.

Figure 3-1 The generated electromagnetic wave in FP lasers

Electromagnetic wave superposition happens when the constituent waves have the same phase. When an electromagnetic generated by a gain medium travels from one facet and returns to this facet by reflection, the total travel distance is 2L, where *L* is the length of resonator. The wave function,

$$\varphi(\mathrm{t}) = \mathrm{asin}(\omega\mathrm{t} + \theta) \qquad (3.1)$$

shows that ωt should equal to $2m\pi$ during this period if the waves are to interface, and the corresponding electromagnetic wave phase requirement is shown as Equation 3.1. So 2L equals to nλ as shown in Equation 3.3.

$$\omega t = 2m\pi \tag{3.2}$$

Here, ω is the angular velocity and m is an integer. So the frequency of the selected mode can be calculated from Equation 3.3.

$$\omega\frac{2L}{v} = 2m\pi$$

$$v = \frac{c}{n}$$

$$\omega = \frac{m\pi c}{nL}$$

$$f = \frac{\omega}{2\pi} = \frac{mc}{2nL} \tag{3.3}$$

In which, n is the refractive index of the laser and c is the light speed in vacuum.

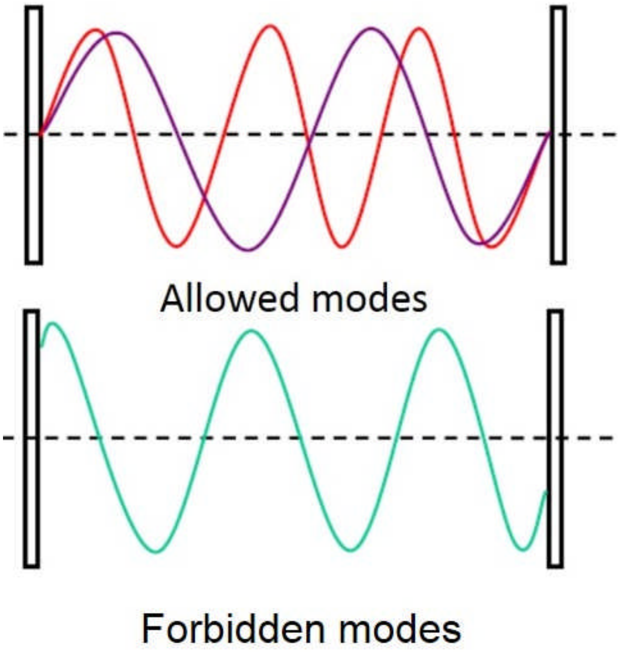

Figure 3-2 The modes allowed and not allowed in FP lasers

As figure 3-3 (a) shows, any modes which satisfy the requirement f=mc/2nL can resonant within the cavity. These modes are known as Fabry-Perot modes. However, it is the gain of the laser which limits the observable modes that emitted from the cavity. The gain function of a semiconductor laser is complicated and a simplified schematic is presented in figure 3-3 (a). The superposition of the laser's gain spectrum with the FP modes permitted within the cavity, provides the radiated laser modes shown in figure 3-3 (b).

Experimental results typically show multiple modes as seen in figure 2-21 and figure 2-22, presented in Chapter 2.

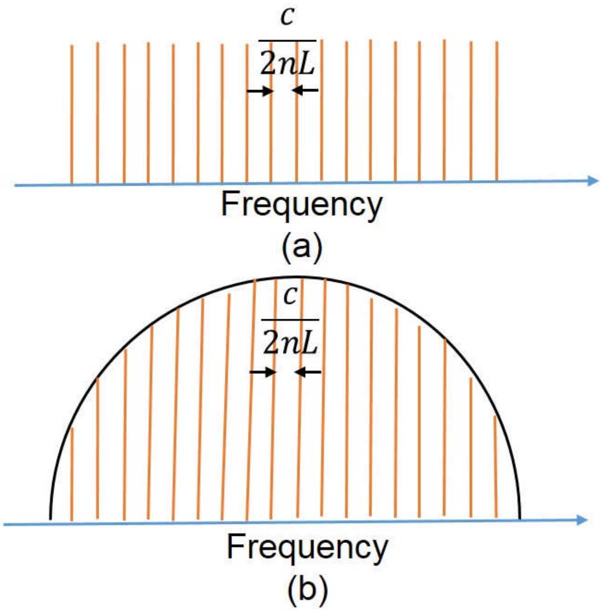

Figure 3-3 The modes selected by combining laser gain with FP resonances. (a) Schematic of FP laser modes unrestricted by laser gain. (b) FP laser modes with laser gain included.

3.1.2 Single mode quantum cascade laser design

Many laser applications require stable, repeatable single mode emission at a precise frequency. One of the most reliable way to generate single mode operation is the introduction of an artificial mode modulation into a FP laser by fabricating a periodical interrupted waveguide. This results in periodic modulation of waveguide loss and refractive index. A desired single frequency can be selected from the laser's gain spectrum by specifically tailoring the periodicity of the waveguide.

Distributed feedback (DFB), distributed Bragg reflector (DBR) and photonic lattice structure (PL) are widely applied to achieve this modulation. These devices all employ refractive index and waveguide loss modulation, due to periodic interruption of the FP waveguide structure. As mentioned in Chapter 2, the vertical waveguide of a FP THz QCL can be formed by two n^+ thin GaAs layer sandwiching the active region. Periodic disruption of the waveguide is then achieved by etching away the top n^+ GaAs. Typical gratings for DFB, PL and DBR structures are given in figure 3-4 (b), (c) and (d), respectively. Λ_{m},

Λ_e and Λ are the width of the non-etched section, etched section and a whole period respectively. Those three parameters must be optimised for the design.

Figure 3-4, (a) shows a normal FP THz QCL resonator with a single metal plasmon waveguide, which is formed at the interface of the active region and metal. Artificial modulation of the QCL modes is obtained by simply etching away the plasmon cladding waveguide.

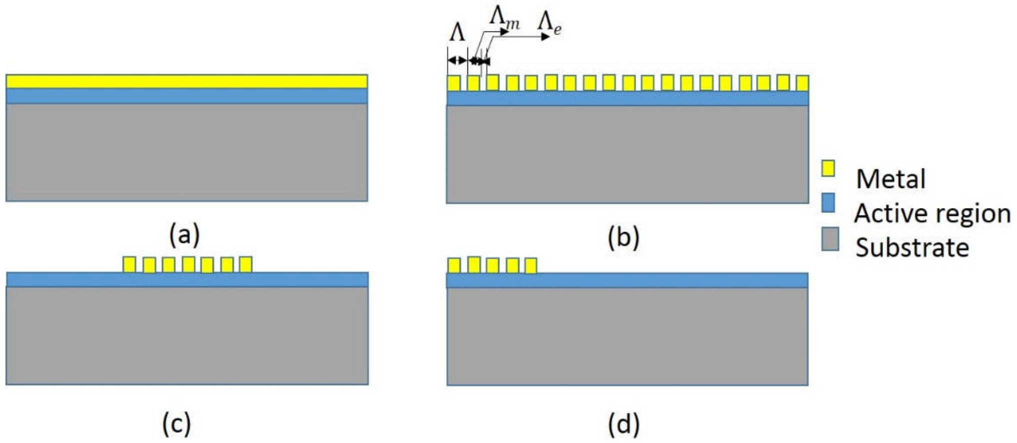

Figure 3-4 Different patterning schemes to achieve single mode lasing. (a) is a normal FP THz QCL resonator, (b) is a DFB THz QCL resonator, (c) is a photonic lattice THz QCL resonator and (d) is a distributed Bragg reflector for THz QCL

A photonic lattice (PL) resonator forms a ‘bandgap’ for photons. The bandgap, like the electron bandgap in semiconductors, forbids generation of photons with certain energies. Thus, radiation frequencies with only selected photon energies can be obtained. This bandgap is formed by materials with different dielectric constant. There are one dimensional, two dimensional and three dimensional PL designs depending on the structure of the optical nanostructure.

A DFB resonator builds on the one dimensional PL structure concept and also provides optical feedback for the laser. So the selected modes in a DFB laser are amplified by these gratings and not the end mirrors. In contrast, a DBR structure as given in figure 3-4 (d), only acts as a mode selector. So DFB structures use the gratings to both select modes and reflect radiation, while DBR and one dimensional PL use the grating to simply select modes.

The emission frequency is determined by the design of the grating rather than the laser gain spectrum. The grating is designed to reflect only a narrow band of wavelengths, and thus produce a single longitudinal lasing mode. In this chapter, single mode emitting devices are presented at a wavelength of 2.22 THz.

This chapter discusses the modelling, design, fabrication and measurement of THz QCLs with PLs. PL design parameters, such as the grating pitch, are calculated from analytical expressions. Photonic bandgap in PLs are calculated from the variation of detuning factor and propagation constant of the PL. THz QCLs with PL are fabricated by different methods and their spectra are measured.

3.2 Photonic-lattice pattern design

In this work, a PL is used to achieve a low-cost and reliable single mode frequency THz radiation source based a QCL. The frequency selected by those gratings corresponds to the Bragg frequency [124].

3.2.1 Grating design parameters of photonic-lattice design

The Bragg frequency is determined by ʌ as the equations [125] below.

$$\lambda_B = 2n_{eff}\Lambda = \frac{c}{f_B} \tag{3.4}$$

$$\Lambda = \Lambda_m + \Lambda_e \tag{3.5}$$

$$\Lambda {n_{eff}}^2 = \Lambda_m {n_m}^2 + \Lambda_e {n_e}^2 \tag{3.6}$$

Here λ_B is the targeted Bragg wavelength, f_B is the Bragg frequency, Λ_m Λ_e and Λ are the grating pattern width of the metal, gap and the whole pitch respectively. n_{eff} is the effective refractive index at the Bragg frequency, n_m is the refractive index of the mode with a metal cladding on the laser cross-section and n_e is the refractive index of the etched part of the PL laser.

Another important parameter for PL grating design is the duty cycle of the pitch γ. This is defined by Equation 3.7, and for all designs shown in this thesis, the value was chosen to be 0.5. A small duty cycle tends to increase the loss of the waveguide, as well as making it more difficult it fabricate, especially when using low resolution optical photolithography.

$$\gamma = \frac{n_m \Lambda_\mathrm{m}}{n_\mathrm{eff}\Lambda} \tag{3.7}$$

For those equations, Λ_m and Λ_e are the parameters used in fabrication for a certain desired emission frequency. To determine these two parameters, $\mathrm{n_m}$ and $\mathrm{n_e}$ are also required and these are acquired from experimental results.

3.2.2 Measurement of the QCL refractive index

As was discussed in Section 3.1.1 , the mode spacing emitted from a normal FP THz QCL is $\frac{mc}{2nL}$ where n is the refractive index of the laser, and the beating mode of two neighbouring FP modes is $\frac{c}{2nL}$. n_m has the same value of n because the waveguide of a normal FP laser is the same as the part covered by metal in a PL laser. So the refractive index of the metal section of a PL laser is given as:

$$f_{beat} = \frac{c}{2n_m L}; \qquad n_m = \frac{c}{2f_{beat}L} \tag{3.8}$$

The value of n_m can be obtained by measuring the gap (f_{beat}) between two neighbouring FP modes. The beating mode was measured by a Schottky diode detector, which gives a heterodyne signal. The detailed measurement of this beating frequency is given in Section 5.3.5 , and a value of 3.77 is obtained for the device.

The refractive index of the etched part of the PL is also obtained by measurement, after obtaining the value of n_m. The etched part is treated as pure GaAs and an estimated value for $\mathrm{n_e}$ is given as 3.5 [126]. Λ_m, Λ_e and Λ can be calculated from Equation 3.4, 3.5, 3.6 and 3.7 for a targeted f_B. The first PL patterned QCL can then be fabricated and characterized. The actual frequency emitted by the laser is then used to calculate the actual value for refractive index $\mathrm{n_e}$, since $\mathrm{n_{eff}}$ can be calculated by equation 3.4, 3.5, 3.6 and 3.7. Finally, the pattern can then be optimised. The design process is given in figure 3-5. The designed parameters of PL pattern for a 2.22 THz QCL (L1007) and a 2.62 THz QCL (L1014) are given in table 3-1, both devices contain a bound-to-continuum active region.

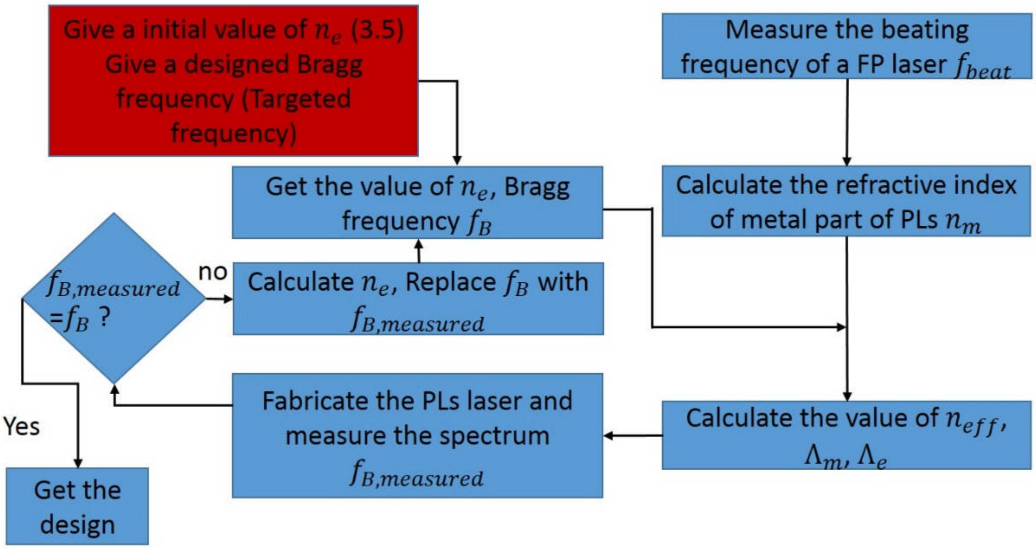

Figure 3-5 Schematic of PL pattern design

Table 3-1 Designed PL patterns for 2.22 THz and 2.62 THz QCL

	f_B(THz)	n_{eff}	n_e	n_m	Λ_m (µm)	Λ_e (µm)
L1007	2.22	3.61	3.46	3.77	8.96	9.76
L1014	2.62	3.36	3.15	3.60	7.95	9.09

3.3 Fabrication of a 2.2 and a 2.6 THz single mode QCL

From table 3-1, the width of the PL pitches is around 20 µm, which means only a 2 µm variation to the design can result in a 10% error. The fabrication precision, therefore, much be <1µm. Three methods can be applied for this fabrication: optical photolithography using a mask aligner, electron beam lithography and focused Ion beam lithography. Fabrication is presented in the following section.

3.3.1 Optical photolithography

Optical photolithography is the simplest way to pattern the QCLs. However, there must be a mask allocated for each possible design, which makes the optimising process for the desired emission frequency quite difficult. However it is a very convenient and fast method when the frequency is already close to the desired frequency and only small adjustment is needed for the design.

The fabrication is based on the processing of single metal FP lasers presented in Chapter 2: ridge etching, bottom contact realisation, top contact realisation, over-layer waveguide metallisation, backside etching, backside metallisation and packaging. The differences are the top contact and upper waveguide pattern. There are no defects in an FP laser upper waveguide in contrast to a PL laser. As such the top contact and over-layer mask must be different. After top contact and over-layer photolithography and metallisation, as shown in figure 3-6, the designed pattern can be obtained.

To obtain the pattern shown in figure 3-6(a, b), the following processing was applied after ridge etching and bottom contact metallisation, which are the same as the single metal FP laser processing presented in Chapter 2.

1. **top contact realisation:**
   The top contact is slightly different to a FP laser. There is no top contact and n+ layer in the PL region, this is to reduce waveguide losses from n+ layer. S1813 is put on the surface and spun at 5000rpm for 70s. This is followed by a 3.5 s exposure to UV under the designed mask. MF319 is then used for development, which takes 75s. The pattern after development is shown in figure 3-6 (a). Figure 3-6 (b) is the pattern after metallisation of a layer of around 120 nm AuGeNi.

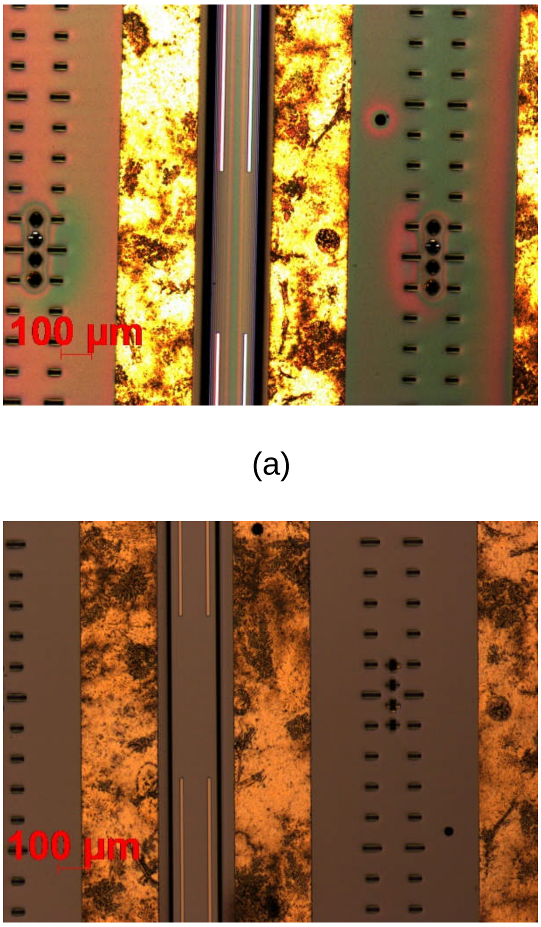

(a)

(b)

Figure 3-6 Optical microscopy of a THz QCL chip with a PL. (a) is the pattern after top contact development and (b) is the pattern after metallization of the top contact

2. **Over-layer waveguide metallisation**

   The over-layer metallisation also needs to avoid the PL window region, which is $150\mu m \times 0.53mm$. The PL pattern will be placed on the left window area as shown in figures 3-7 (a) and (b). The over-layer is a layer of Ti/Au(20/150nm).

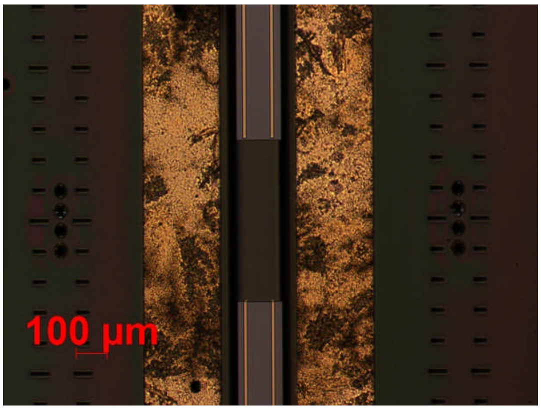

(a)

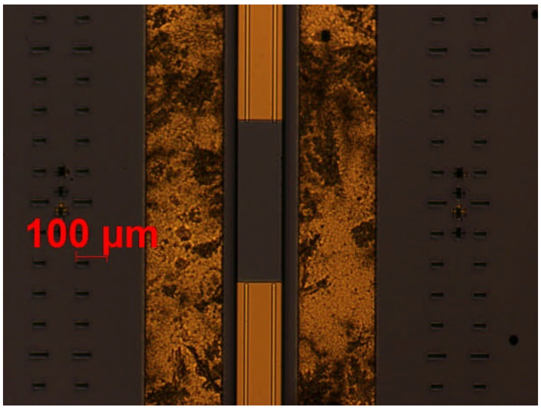

(b)

Figure 3-7 Process of over-layer deposition for PLs lasers. (a) is the pattern after PL over layer development and (b) is the pattern after PL over-layer metallisation.

3. **n+ layer etching in the PL region**

   In order to increase the waveguide loss contrast between the metal and non-metal area, the top n+ layer is etched away. Before etching, photolithography is used to create a pattern to protect areas excluding the PL window. The n+ layer is a Si doped 50nm thick GaAs layer and this is removed. Selected etching solution is H_2SO_4:H_2O_2:H_2O (1:8:400) with an etching speed of 30 nm/min.

4. **PL pattern photolithography and metallisation**

   The designed pattern is placed on the PL window by a further photolithography step. Ti/Au(20/150nm) is then deposited on the etched window surface. The patterns can be seen in figures 3-8.

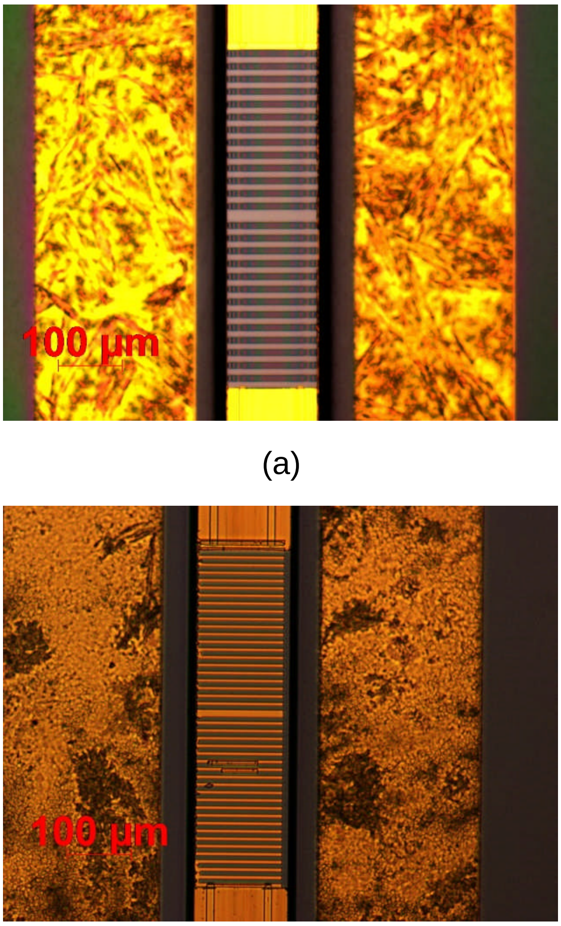

(a)

(b)

Figure 3-8 Fabricated PL device with patterning of the PL region. (a) is the pattern formed by photolithography and development, and (b) is the pattern obtained after metallisation. The double size metal in the middle of the device gives bigger stopband for PL, which make the chance of single mode emission bigger [127].

5. **Backside thinning, backside waveguide metallisation, annealing, sample cleaving and bonding**.

   In order to have a better thermal dissipation, the substrate is wet etched to 180 μm as was done for FP laser fabrication presented in Chapter 2. This is a compromise between good thermal dissipation and convenience of fabrication. All other packaging processes are the same as for a single metal FP laser, except for the cleaving processing. Because the position of the PL patterns is critical to the emission frequency. The cleaving should make sure the PL patterns is in the centre of the whole laser cavity, as designed.

3.3.2 Focused Ion beam lithography

A focused ion beam (FIB) system is an important tool for imaging, analysis and sample modification of materials at the nanoscale. It can be used for material etching, in situ characterization of materials, and imaging of nanoscale structures including 3D structures. Here we use an FIB for milling the PL as an alternative to photolithography.

It has a higher precision than optical photolithography and does not require the photoresist used in electron beam lithography. At low primary beam currents, very little material is sputtered and modern FIB systems can easily achieve a 5 nm imaging resolution (imaging resolution with Ga ions is limited to ~5 nm by sputtering [128, 129] and detector efficiency). At higher primary currents, a great deal of material can be removed by sputtering, allowing precision milling of a specimen down to a sub micrometre or even a nanometre-scale. Instead of a new mask design and new device fabrication, FIB can mill and put a pattern directly on the device. Photonic lattices defined with FIB achieved here with the guidance of Dr Iman Kundu and Dr Li Chen at the University of Leeds. The FIB fabricated PL patterns are given in figure 3-9. The devices were achieved on an already tested device, which could not be done using photolithography and EBL.

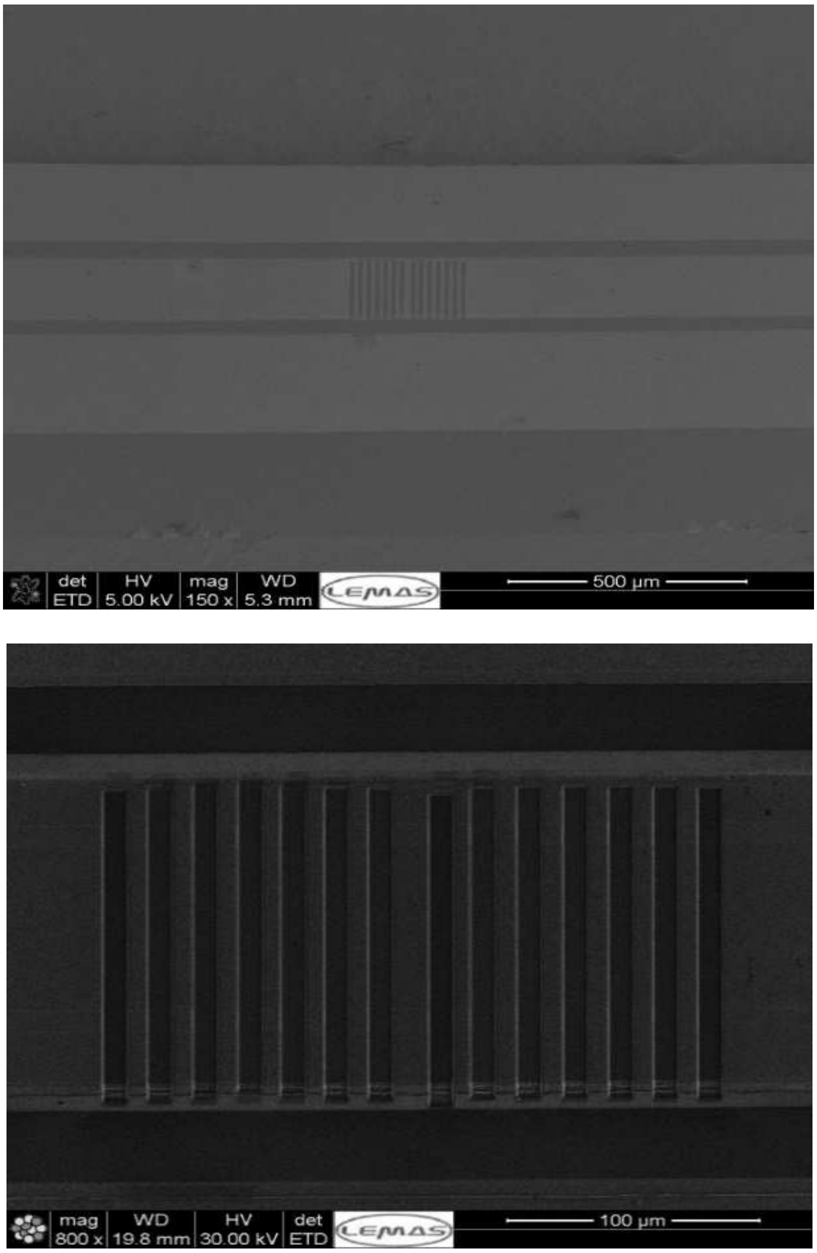

Figure 3-9 SEM imaging of an FIB fabricated PL pattern

3.3.3 Electron beam lithography

The wavelength of an electron beam can be much smaller than that of an optical source, and so has a better resolution than optical lithography. Another advantage of electron beam lithography (EBL) is the convenience of the mask design. Optical photolithography needs one physical mask for every pattern, whilst EBL only needs to redefine the mask based on a computer.

EBL and optical lithography use different photoresists. During a EBL processing, two layers of photoresists were put on the sample. The EBL resist PMMA® 495 A8 was spun at 3000 rpm for 40 seconds. Then it was baked on a hot plate at 170°C for 5-10 mins. Then a second layer of EBL resist PMMA® 950 A4 was spun subsequently in two stages – initially at 2000 rpm for 15 seconds, followed by 5000 rpm for 40 seconds. After that the resist covered device was kept in a 170°C oven for 8 hours. The two stages make photoresist thick enough for fabrication.

A Leo-Raith 50 EBL workstation was used to do pattern exposure. The position and movement of the electron beam is monitored and controlled by a computer connected to the work station. During the exposure, the movement of electron beam is guided by a digital mask designed and opened on the computer. There are two types of area in the digital pattern, manifested by two different colours (green and blue). The areas covered by green will be exposed by the electron beam whist the blue areas will remain. So the photoresist covered by green areas will be removed after development. The sample is put in a solution of MIBK and IPA in a volume ration of 1:3 for development. Optical microscopy of samples after EBL resist development are shown in Figure 3-10 a.

A 20-nm thick layer of Ti and a 100-nm thick layer of Au were deposited after EBL patterning. Optical microscopy of a sample after metal lift off is shown in Figure 3-10 (b).

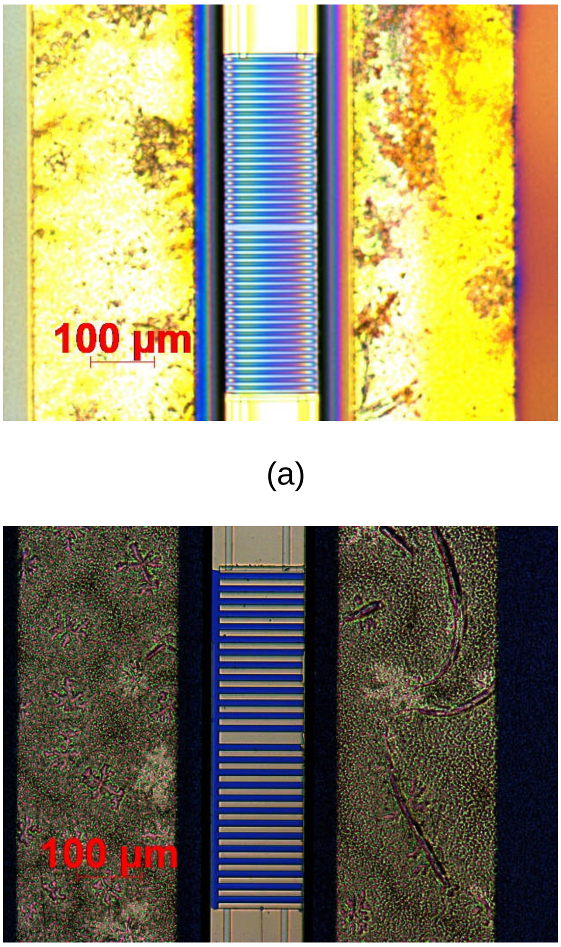

(a)

(b)

Figure 3-10 Fabricated PL device using EBL. (a) is after development, (b) is the pattern after pattern metallisation

The actual pattern put on the device is a few tens of nanometres shifted compared with the designed pattern caused by the shift of the electron beam during the exposure and a mismatch of the digital mask compared to the real position of the sample. A typical wire-bonded PL device is shown in figure 3-11.

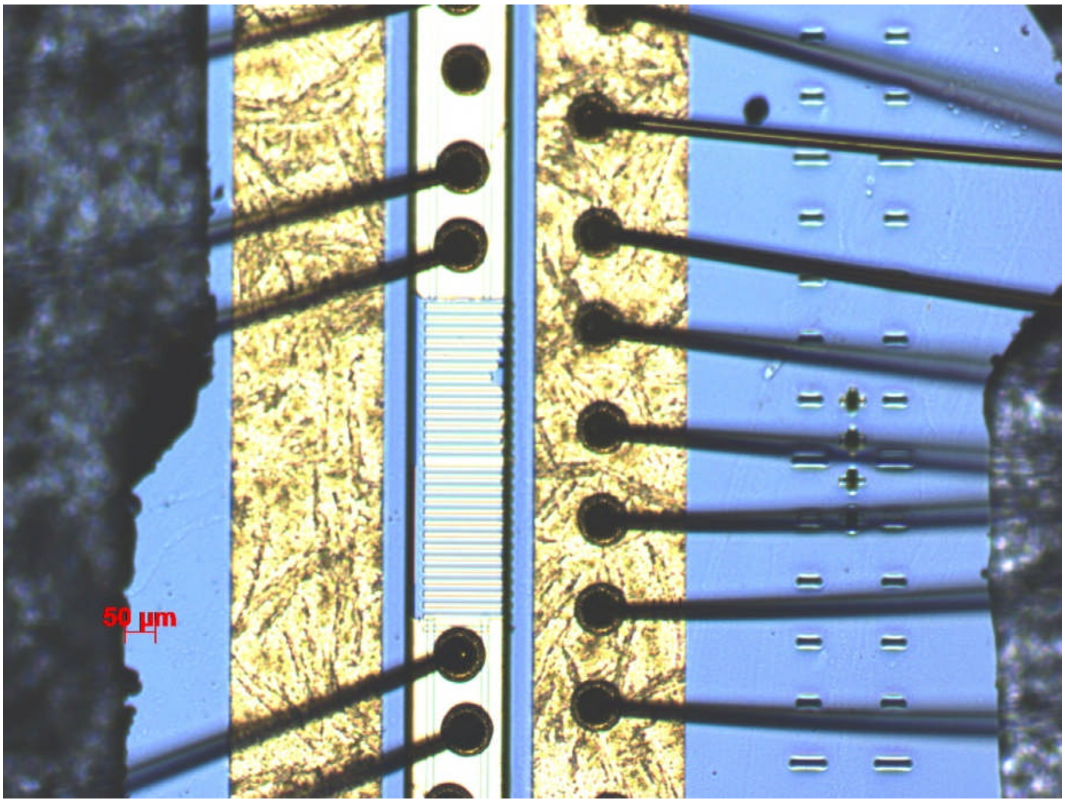

Figure 3-11 Wire bonded PL device

3.3.4 Comparison of the three fabrication methods

Compared with electron beam lithography and FIB, optical lithography is much faster. The whole optical lithography takes only round 15 mins when EBL and FIB needs several hours. However, the mask for optical lithography can’t be changed once the design is finished, whist the patters of EBL and FIB can be edited directly on a computer. Another disadvantage of optical lithography is that the resolution is worse than the other two methods. The resolution of EBL and FIB can be controlled under 100 nm, when the wavelength of UV source limits optical lithography resolution.

EBL is typically used when a new design is required. It will be an economic way to test new designs and give feedback. Once the new device is fully characterized, FIB can be used for modification of the pattern directly by ion beams if only small a modification is needed. Compared with EBL, FIB is faster because it doesn’t need preparation of photoresist.

3.4 Measured result

The QCL LIV and spectra before and after defining a photonic lattice pattern are presented and compared in this section.

3.4.1 Spectra measurements of fabricated QCL

Two wafers were fabricated into PL lasers: L1007 (2.22THz) and L1014 (2.56THz). The spectrum and LIV of L1014 will be presented in Chapter 6 where the PLs are applied for gas spectroscopy. So the following section will focus on the PL LIV and spectra of L1007 (2.22THz).

The PL device is 4mm long with a 0.53 mm long PL pattern on the top of QCL ridge. Figure 3-12 and figure 3-13 are pulsed mode and CW spectra of a normal single metal device respectively. The spectra are measured under different bias currents which covers the dynamic range of the QCL. Figure 3-14 and figure 3-15 are pulsed mode and CW spectra respectively, of the PL single metal device fabricated from the same wafer.

All the measurement conditions remain the same including the setup, heat sink temperature and the wafer. The FTIR used for spectral measurement has a resolution of 7.5 GHz. The heat sink temperature is 20K during all the measurement, and spectra at different biases in the dynamic range of the QCL are measured. The values of the biases are given in the legend of the figures.

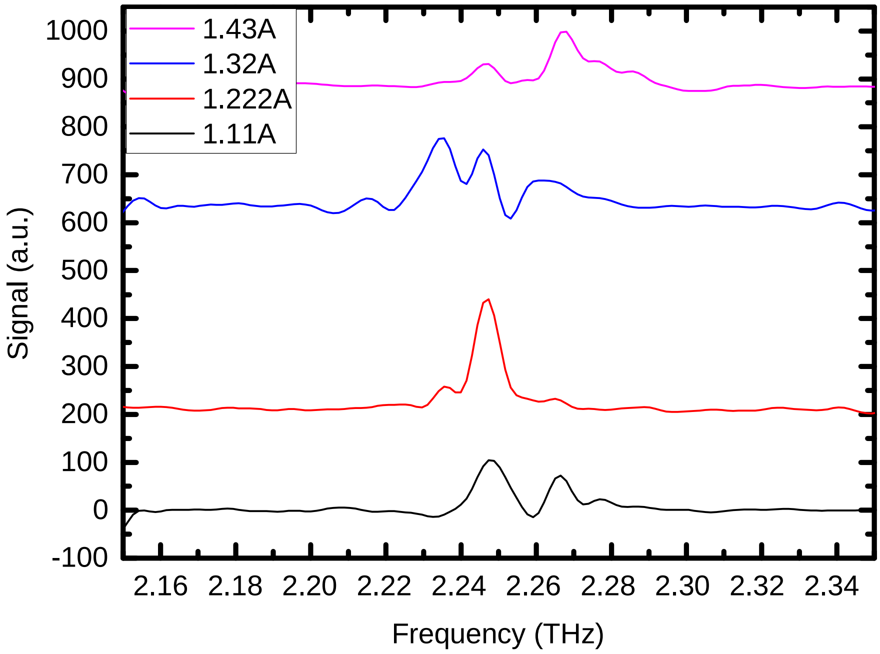

Figure 3-12 Spectrum of normal single metal L1007 (pulsed). The device is 4 mm*150 µm. The duty cycle of the pulse is 2%.

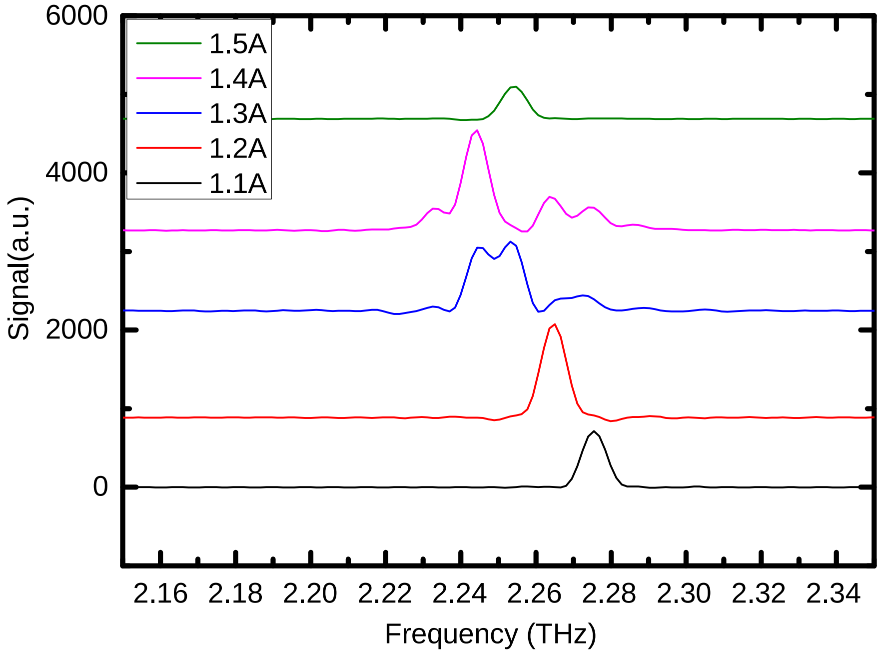

Figure 3-13 Spectrum of normal single metal L1007 (CW). The device is 4 mm*150 µm.

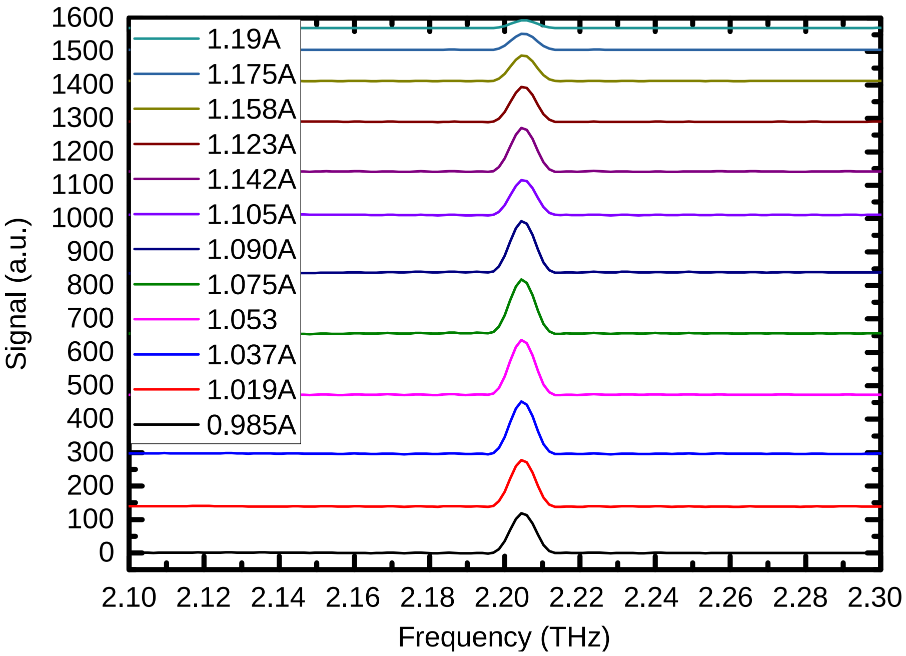

Figure 3-14 Spectrum of PLs single metal L1007 (pulsed). The device is 4 mm*150 µm. The duty cycle of the pulse is 2%.

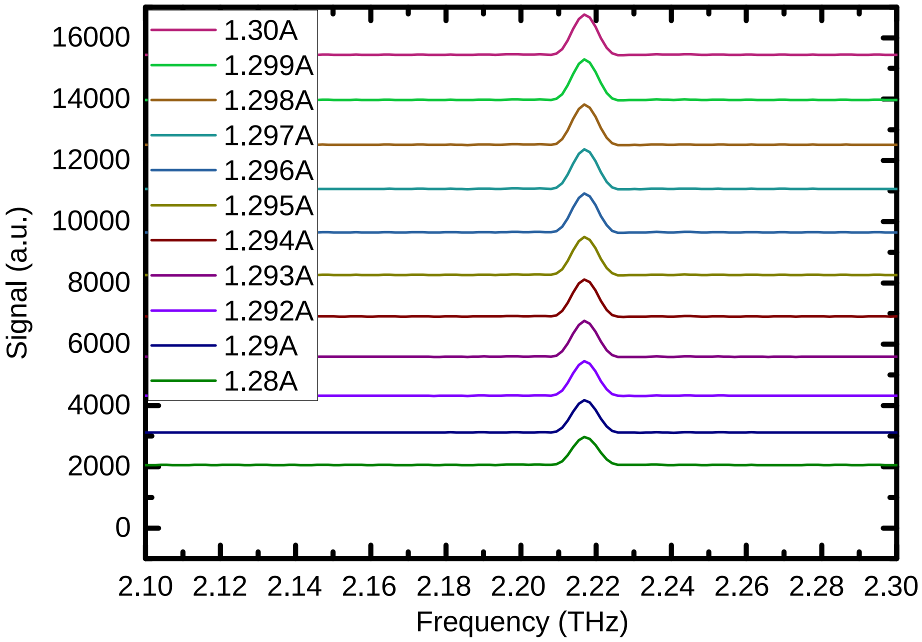

Figure 3-15 Spectrum of PLs single metal L1007 (CW). The device is 4 mm*150 µm.

In figure 3-12 and figure 3-13, multi-mode spectra seen under both pulsed and CW bias for single metal FP devices. Single mode spectra are, however, seen for both pulsed and CW biased PL single metal device, and the designed 2.2 THz is achieved. A slightly different frequency is seen for pulsed and CW modes. The reason for this is the real working temperature for pulsed and CW modes, these differ from the heat sink temperature. The QCL should have a slightly higher real working temperature under CW mode, owing to power dissipated in the active region during the ‘switch off’ in pulsed mode. Current tuning is seen for both devices and bias modes.

3.4.2 LIV measurement of fabricated QCLs

LIV curves were also measured for a FP single metal device and PL QCLs. Both pulsed and CW modes are considered. Figure 3-16 and figure 3-17 show the pulsed mode LIV for the FP single metal device and the PL QCL respectively, whist figure 3-18 and figure 3-19 show CW mode LIV.

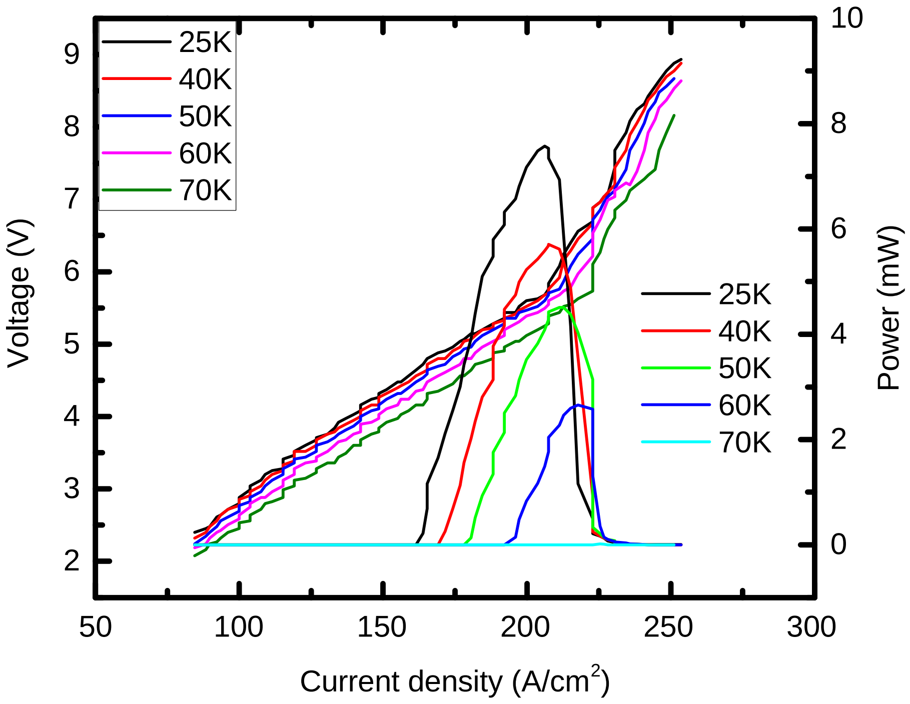

Figure 3-16 LIV curve of an FP single metal L1007 (pulsed). The duty cycle of the pulse is 2%. The dimension of the device is 4mm*150µm.

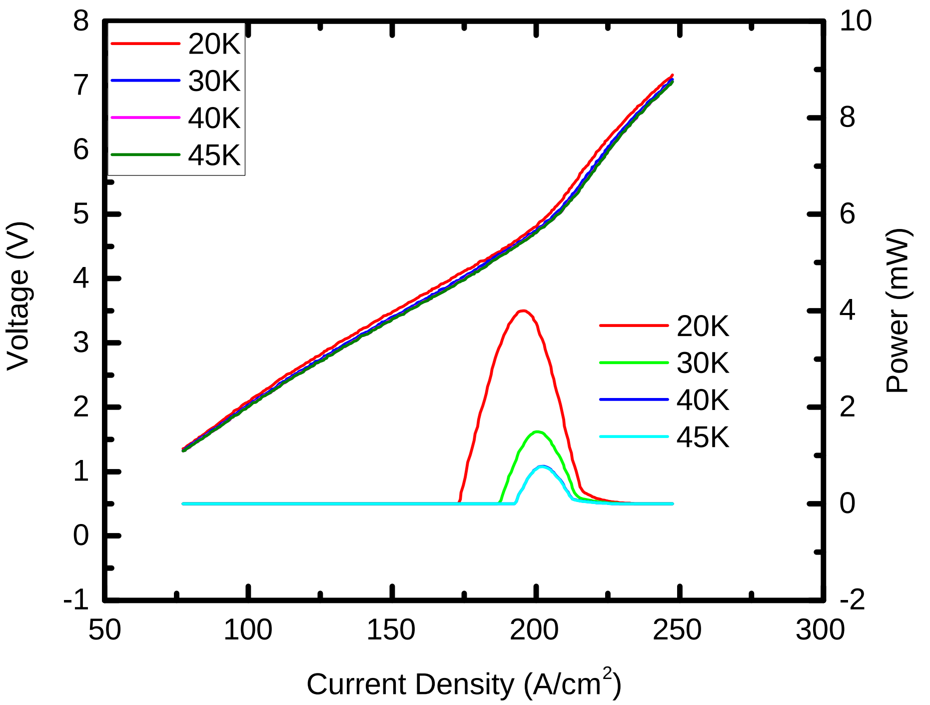

Figure 3-17 LIV curve of PL single metal L1007 (pulsed). The duty cycle of the pulse is 2%. The dimension of the device is 4mm*150µm.

As figure 3-16 shows, the FP single metal device has a maximum working temperature of 70K, a threshold current density of 155A/cm^2 at 25K and a maximum power around 8.0 mW at 25K. Compared with this, the PL QCL shown as figure 3-17, has the following characteristics. 1, PL QCL have a slightly higher threshold current density at the same heat sink temperature, 173 A/cm^2 compared with 155 A/cm^2 at 25K of a FP single metal device. 2, PL QCL have a lower maximum working temperature, 45K compared with 70 K for FP laser. And 3, PL QCL have a smaller maximum emission power at the same heat sink temperature, 4 mW compared with 9mW at 25K. The dynamic range is also smaller for a PL QCL compared with a FP device.

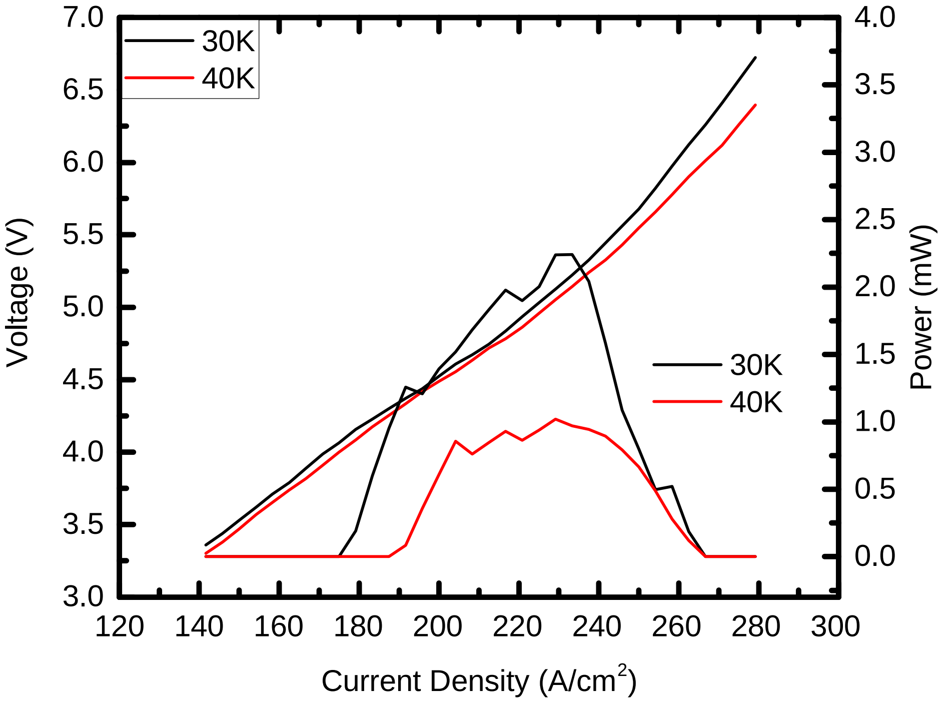

Figure 3-18 LIV curve of FP single metal L1007 in CW.

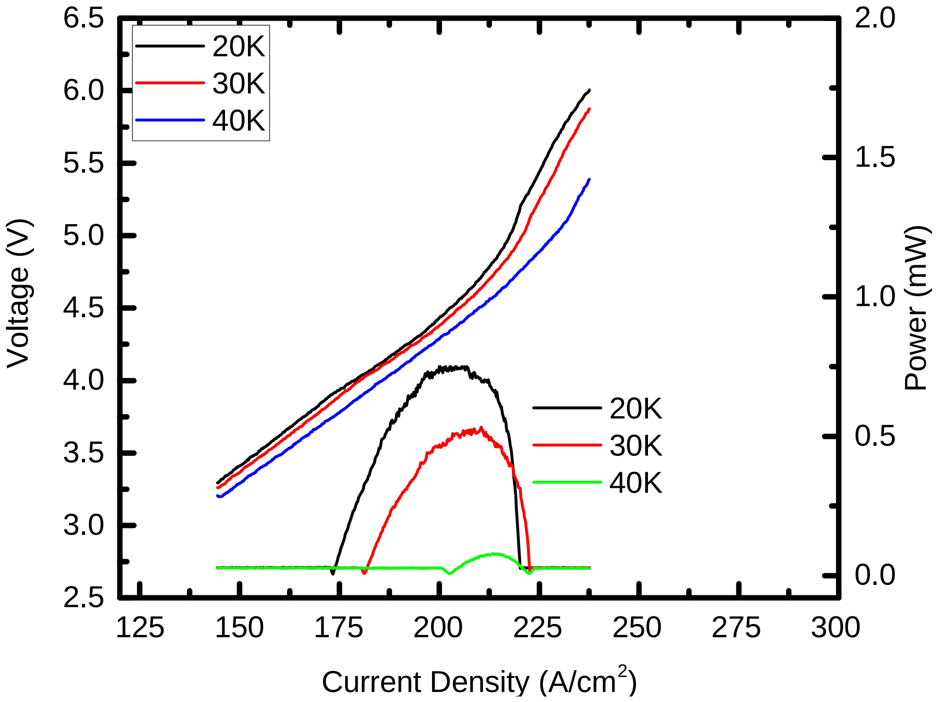

Figure 3-19 LIV curve of PL single metal L1007 in CW.

The PL QCL has three different characteristics compared with a FP single metal QCL. Firstly, the top Ti/Au waveguide of PL QCLs are partially etched to form index and waveguide loss modulation. The total waveguide loss is increased after etching part of the waveguide. So the PL laser gain should be bigger than a FP device in order to have a net gain above zero. This is the reason why the threshold current density of a PL QCL is larger than a normal device.

Secondly, the PL lasers have a lower maximum power under a same heat sink temperature compared with a FP laser. This is caused by a bigger waveguide loss as well. The maximum operation temperature of the PL is also lower that of the FP laser which is caused by the bigger loss.

The dynamic range of the PL lasers is also much smaller than the normal FP laser, 50 A/cm^2 for PL and 90 A/cm^2 for FP laser. As given in figure 3-3 (b), a PL laser only selects limited number of modes over the whole range of the FP laser gain. The limited gain and waveguide loss together make the dynamic range of a PL laser much smaller than a FP laser.

Another single mode device was developed in the project from L1014 whose central frequency is 2.56 THz. The fabrication methods are same as here. The spectrum of this device will be presented in Chapter 6.

3.5 Conclusion

In this chapter, the principles of refractive index and waveguide loss modulation of a FP laser were introduced. Three methods to achieve modulation were discussed: DFB, DBR and PL. The PL pattern was chosen to obtain single mode emission in this thesis.

Design of the pattern parameters was presented. A Schottky diode mixing signal is used to measure the refractive index of the PLs covered with metal. And a measurement method to determine the refractive index of the PLs without metal are given. The measured and calculated parameters of the PL patterns for 2.22 THz and 2.62 THz are given as table 3-1.

After presentation of single mode waveguide design, three different fabrication methods: optical lithography, electron beam lithography (EBL) and focused ion beam (FIB) were introduced. Fabricated photonic lattice structure waveguide devices were shown in each case.

Finally, the measured LIV and spectral performance were compared between the FP single metal device and a PL QCL fabricated from the same wafer. The characteristics of the PL device were studied and their parameters were explained.

Chapter 4Schottky diode detector characterization with THz QCLs

4.1 Introduction to the Schottky diode

Heterodyne detection with a Schottky diode detector was proposed for high resolution spectroscopy in LOCUS project. In this chapter, Schottky diode detectors are introduced, characterised and studied.

4.1.1 History and basic theory

The first observation of the rectifying effects of Schottky diodes dates back to 1894, when Ferdinand Braum performed experiments on metal-sulphides [130]. The Schottky diode was, however, named after Walter Schottky for his pioneering work during the 1930's and 1940's in the field of metal-semiconductor interfaces [131]. The Schottky rectifier characteristics [132] can be explained by the Schottky-barrier model first proposed by Cowley and Sze [133, 144], which also novice understanding the effects of surface states at a metal-semiconductor junction [132].

Compared with p-n junctions, only electrons are involved in current conduction in Schottky diodes, rather than electron-hole recombination after travel through the depletion region. Owing to the high mobility of electrons, Schottky diodes are thus preferred for high frequency devices.

4.1.2 The Schottky barrier

There are two types of contacts that characterise the possible interfaces between a semiconductor and a metal: an Ohmic contact and a Schottky contact. The I-V curves of the two are illustrated by figure 4-1. As the voltage across the contacts increases, they demonstrate very different responses. The Ohmic contact has a linear I-V relationship, whereas the Schottky contact has a highly non-linear response. The current increase is minimal until a voltage threshold is reached, at which point the current increases exponentially. The reason for the different I-V performance lies in the conduction band structure of the semiconductor where it meets the metal. Due to the differing Fermi levels of the materials, the conduction band "bends" where the materials meet, as figures 4-2 and 4-3 show.

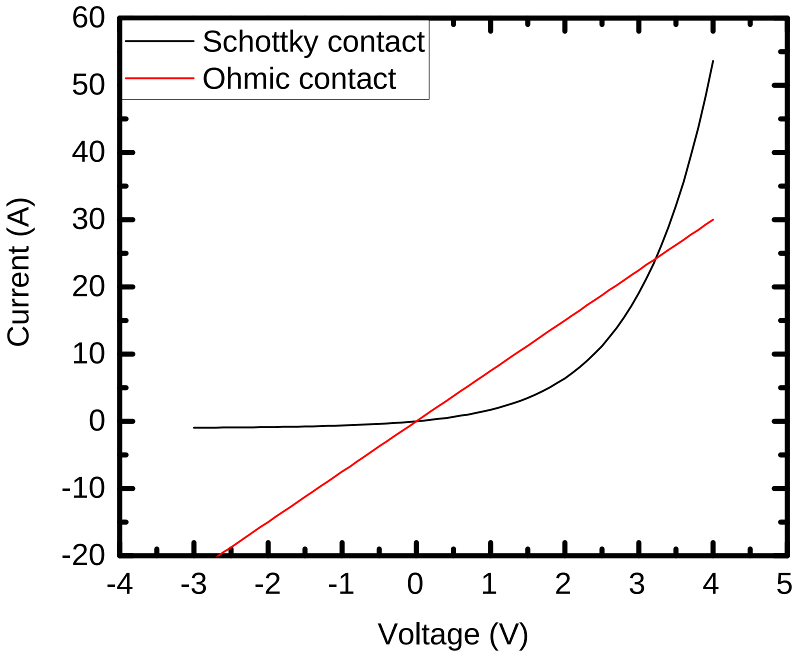

Figure 4-1 Typical I-V curves of Ohmic and Schottky contacts

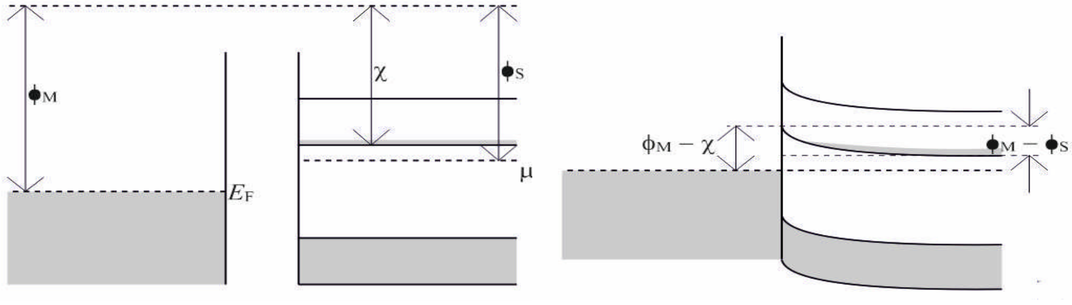

(a) (b)

Figure 4-2 Conduction band structure of a Schottky contact [135]

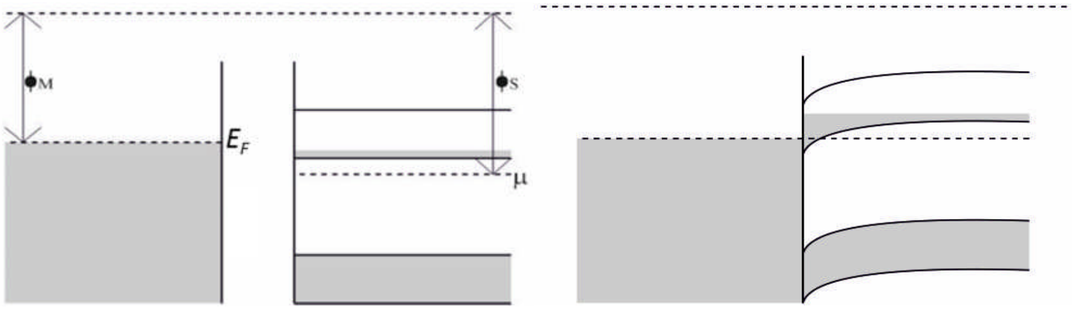

(a) (b)

Figure 4-3 Conduction band structure of an Ohmic contact [135]

In figure 4-2 and figure 4-3, Φ_M is the work function of the metal, Φ_S is the work function of semiconductor, E_F is the fermi level of the metal, μ is the chemical potential of semiconductor, and χ is the electron affinity. The work function of a material is the energy required to remove an electron from the chemical potential and provide enough just energy for it to escape to infinity.

If the Fermi level of the metal, E_F, is lower than the chemical potential, μ, electrons from the semiconductor move to the metal when they join, lowering the chemical potential of the semiconductor to the same level as the Fermi energy of the metal. As a result, the conduction band will bend and a potential barrier will be formed arising from electrons flowing from the semiconductor to the metal. This is shown in figure 4-2 [135]. Below threshold and under reverse bias, electrons don't receive enough energy to overcome this barrier so the current across the contact remains near zero. In the forward bias the barrier decreases both before and after the threshold and, beyond a threshold, the current will increase exponentially.

On the other hand, if E_F is higher than μ, electrons from the metal move to the semiconductor when they join and μ will rise to the same level as E_F, as figure 4-3 [135] shows. Although the conduction band also bends, there is no barrier formed when electrons flow from the semiconductor to the metal. This kind of contact is known as an Ohmic contact and the I-V curve is linear.

In a Schottky diode, quantum effects allow tunnelling of electrons through the barrier, which is a process independent of temperature [136]. The tunnelling current increases with decreasing barrier thickness and is not so pronounced at forward bias [137].

For resistive mixers it is the non-linear resistance-voltage (R-V) relationship in the forward direction that is used for mixing. This is the basis of Schottky diode heterodyne mixing and is explained below.

4.1.3 The principle of detection using a Schottky diode

4.1.3.1 Schottky diode direct detection

Some of the most common uses of Schottky diodes are in multiplier and mixer applications, where the devices are well suited for high-speed operation with reported cutoff frequencies reaching several THz. In particular Au-GaAs (n doped) Schottky barriers are widely used in microwave and submillimetre wave detection.

To understand the principle of detection, the IV performance of a Schottky- diode should be studied first. The exponential characteristic with respect to electron energy distribution in the semiconductor gives rise to a highly non-linear relationship between the forward current and applied voltage over the barrier [138] as given in Equation 4.1. The working principle of a Schottky diode detector is then given in figure 4-4,

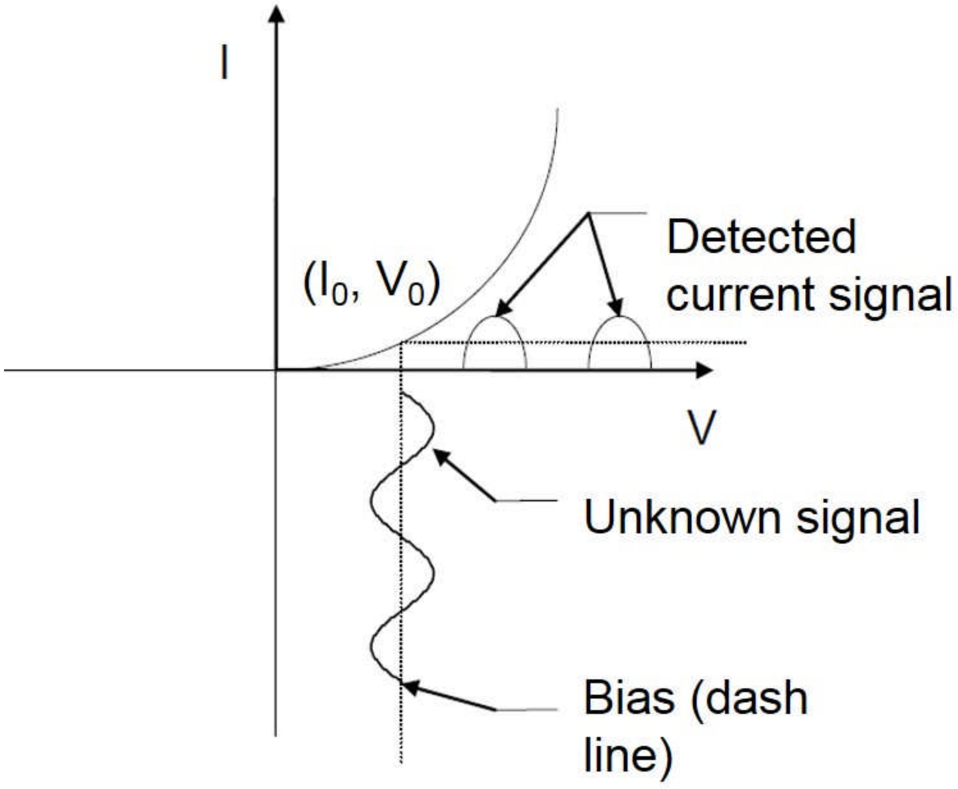

Figure 4-4 The working principle of Schottky Diode detection. When the diode is biased at the operating point (DC bias), there will be a measurable current change (detected I) after the unknown signal is detected by the Schottky Diode.

The *I–V* characteristic of a semiconductor based Schottky diode is given by [168].

$$I(V) = I_S\left(e^{\frac{qV}{\eta k_B T}} - 1\right) \tag{4.1}$$

$$I_S = AA^*T^2e^{-\frac{q\phi_b}{k_B T}} \tag{4.2}$$

where I_S is the reverse saturation current, *A* is the contact area of the metal with the semiconductor, A^* is the effective Richardson constant (varies with material and dopant), R_S is the series resistance, η is the diode ideality factor (determined by the metal-semiconductor interface), k_B is Boltzmann's constant (1.37×10^{-23}J/K), q is the charge on an electron (1.6×10^{-19} C), ϕ_B is the barrier height in volts and T is the absolute junction temperature in Kelvin.

Detection of an electromagnetic wave is realized by measuring the current change of the Schottky contact. Due to the exponential relationship between current and voltage given in Equation 4.1, a small change in voltage incident on the Schottky diode leads to a large change in current. When the diode is biased at an operating point (I_0, V_0), the voltage will change to V_0+V_{signal} when an electromagnetic wave is incident on the Schottky diode illustrated as figure 4-4. The total output current from the Schottky diode then changes to $I_S\left(e^{\frac{q(V_0+V_{signal})}{\eta k_B T}}-1\right)$ and the detected signal is $I_{\mathrm{signal}}=(I_0+I_s)(e^{\frac{qV_{\mathrm{signal}}}{\eta k_B T}}-1)$.

4.1.3.2 Schottky diode mixer

Mixing is also based on the non-linear I-V characteristic of the Schottky diode. The mixer is pumped by a local oscillator (LO) and the signal to be detected with the LO is mixed with the radiation of LO in the Schottky diode detector. Two frequencies are thus present in the mixer, V_{LO} from the LO radiation, and V_D from signal. ω_1, ω_2, θ_1 and θ_2 are the LO frequency, detected signal frequency, initial phase of the LO and initial phase of detected signal. I_S and b are the reverse saturation current and $\frac{\eta k_B T}{q}$ in Equation 4.1, respectively.

$$V_{LO}=A_{LO}\cos(\omega_1\mathrm{t}+\theta_1) \quad (4.3)$$

$$V_D=A_D\cos(\omega_2\mathrm{t}+\theta_2) \quad (4.4)$$

Substitution into Equation 4.1 and applying a Maclaurin series expansion, the total current generated by the LO and detected signal can be expressed as,

$$(I(V)+\ I_S)=I_s\cdot(\exp\left(\frac{V}{b}\right)-1)+I_s$$

$$=I_s\cdot\exp\left(\frac{V}{b}\right)=a_0+a_1\left(\frac{V}{b}\right)+a_2\left(\frac{V}{b}\right)^2+a_3\left(\frac{V}{b}\right)^3+a_4\left(\frac{V}{b}\right)^4+\cdots \quad (4.5)$$

$$=a_0+a_1\left(\frac{V}{b}\right)+a_2\left(\frac{V}{b}\right)^2+a_3\left(\frac{V}{b}\right)^3+a_4\left(\frac{V}{b}\right)^4+\cdots\#(4.6)$$

$$
\begin{aligned}
(I_{LO+D}+I_S) &= \mathrm{a}\cdot\exp((V_{LO}+V_D)/b) \\
&= a_0 + a_1((V_{LO}+V_D)/b) + a_2((V_{LO}+V_D)/b)^2 \\
&+ a_3((V_{LO}+V_D)/b)^3 + a_4((V_{LO}+V_D)/b)^4 + \cdots \\
&= a_0 + a_1(A_{LO}/b)\cos(\omega_1\mathrm{t}+\theta_1) + a_1(A_D/b)\cos(\omega_2\mathrm{t}+\theta_2) \\
&+ a_2((A_{LO}\cos(\omega_1\mathrm{t}+\theta_1) + A_D\cos(\omega_2\mathrm{t}+\theta_2))/b)^2 + \cdots \qquad (4.7)
\end{aligned}
$$

$$
\begin{aligned}
&((A_{LO}\cos(\omega_1\mathrm{t}+\theta_1) + A_D\cos(\omega_2\mathrm{t}+\theta_2))/b)^2 \\
&= \frac{A_{LO}^2}{b^2}cos^2(\omega_1\mathrm{t}+\theta_1) + \frac{A_D^2}{b^2}cos^2(\omega_2\mathrm{t}+\theta_2) \\
&+ \frac{2A_{LO}A_D}{b^2}\cos(\omega_1\mathrm{t}+\theta_1)cos(\omega_2\mathrm{t}+\theta_2) + \cdots \\
&= \frac{A_{LO}^2}{2b^2}(\cos(2\omega_1\mathrm{t}+2\theta_1)+1) + \frac{A_D^2}{2b^2}(\cos(2\omega_2\mathrm{t}+2\theta_2)+1) \\
&+ \frac{A_{LO}A_D}{b^2}\cos((\omega_1-\omega_2)\mathrm{t}+(\theta_1-\theta_2)) \\
&+ \frac{A_{LO}A_D}{b^2}\cos((\omega_1+\omega_2)\mathrm{t}+(\theta_1+\theta_2)) + \cdots \qquad (4.8)
\end{aligned}
$$

So I_{LO+D} is composed of several terms: DC components: $a_0 + \frac{a_2 A_{LO}^2}{2b^2} + \frac{a_2 A_D^2}{2b^2}$, the signal of the LO $a_1(A_{LO}/b)\cos(\omega_1\mathrm{t}+\theta_1)$, the signal to be detected $a_1(A_D/b)\cos(\omega_2\mathrm{t}+\theta_2)$, the heterodyne signal $\frac{A_{LO}A_D}{b^2}\cos((\omega_1-\omega_2)\mathrm{t}+(\theta_1-\theta_2))$ from down conversion and $\frac{A_{LO}A_D}{b^2}\cos((\omega_1+\omega_2)\mathrm{t}+(\theta_1+\theta_2))$ from upward conversion, and higher order harmonics. Using a low pass filter, the heterodyne signal can then be isolated and detected.

4.1.4 Figure of merit for detector and mixer

GaAs is commonly used as the semiconductor material in Schottky diode due to its high electron mobility which is essential for high frequency operation.

From the principles of direct detection and mixing introduced in 4.1.3, the output signals are $(I_0+I_s)(e^{\frac{qV_{signal}}{\eta k_B T}}-1)$ and $\frac{A_{LO}A_D}{b^2}\cos((\omega_1-\omega_2)\mathrm{t}+(\theta_1-\theta_2))$ for direct detection and heterodyne detection, respectively. Both output signals should be described to be as large as possible. The exponentially amplified current signal is dependent on the I-V curve of the diode. The bigger the slope the bigger the output. The heterodyne component from the mixer is though determined by both the power of LO and the parasitic losses. A higher LO power can decrease the conversion loss.

The maximum frequency that can be directly detected by a Schottky barrier detector is determined by the cut-off frequency f_c[139]. The diode intrinsic cut-off frequency f_c is defined as the frequency at which the magnitude of the reactance $\frac{1}{\omega C_j}$ equals the diode series resistance R_S and is given by the equations [139]:

$$f_c = \frac{1}{2\pi R_S C_j} \tag{4.9}$$

where the voltage dependent junction capacitance C_j is given by [139]:

$$C_j(0) = A\sqrt{\frac{qN_d\epsilon_S}{2\left(\phi_b - \frac{kT}{q} - V_j\right)}} \tag{4.10}$$

$$C_j(V) = \frac{C_j(0)}{\sqrt{1 - \frac{V}{\phi_B - \frac{kT}{q}}}} \tag{4.11}$$

where ϵ_S is the relative permittivity of the semiconductor, N_d is the n-doping level in the semiconductor, V is the applied voltage, V_j is the voltage across the capacitor, and $C_j(0)$ is the junction capacitance with no applied bias.

The conversion loss is composed of two parts: a mismatch loss which is determined by the frequency mismatch of the input signals, and a parasitic loss, which is determined by the parasitic elements of the diode such as its junction capacitance (C_j) and series resistance (R_S).

The noise of the detected current is strongly affected by the shape of the IV curve. A larger series resistance R_S can make the forward current $I(V)$ smaller at a given bias, which will lead to a smaller current change when the same input signal is incident on the Schottky diode. The noise current will be comparably larger. The noise will also be worse at higher frequencies, as are approach the cut-off frequency [140].

Both direct detection of high frequency radiation and effective heterodyne detection require low junction capacitance (C_j) and series resistance (R_S).

Reducing of junction capacitance can be achieved by choosing a lower doping concentration for the epitaxial layer, N_d, or by decreasing the contact area, A, but this will lead to a higher series resistance.

Many designs of Schottky diode structures currently exist. Whisker contacted and planar air bridged devices are the most commonly used structures. Whisker contacted devices [141, 142, 143, 136] are illustrated in figure 4-5 (a) and have a very small contact area which gives a low junction capacitance (C_j). So in principle, whisker-contacted Schottky diode detectors have a high cut-off frequency, and a smaller parasitic loss, which is favourable for THz detection. But when it comes to the practical realization of modern Schottky diodes for THz detectors, planar air bridged devices [144] given as shown in figure 4-5 (b), are typically used, owing to their ability to withstand stress, their ease manufacture, their reproducibility and their ease of assembly.

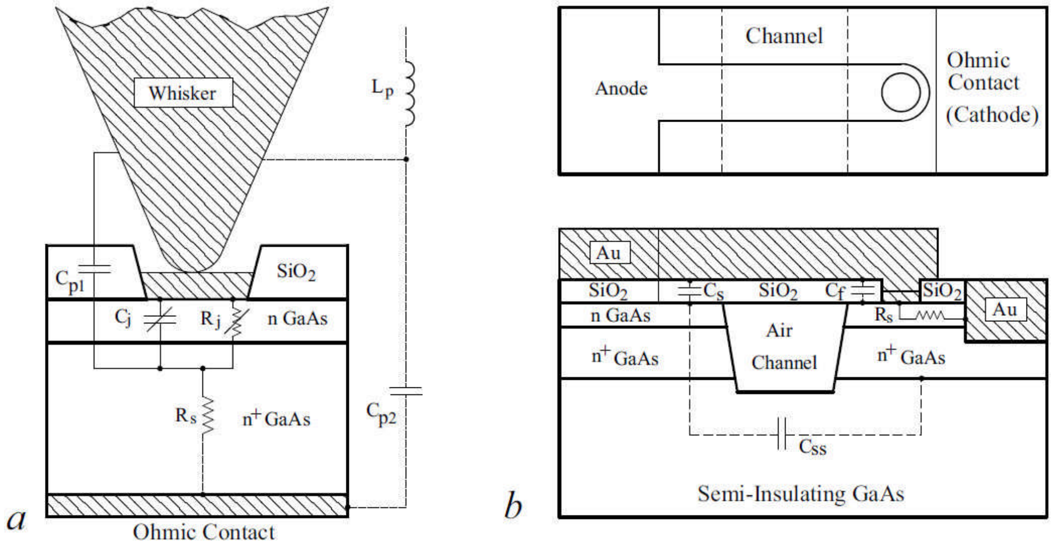

Figure 4-5 Two different structures of Schottky diode detector. (a) is a whisker-contacted Schottky diode [145] and (b) is a planar air bridged Schottky diode [146].

Moreover, planar technology enables simple realisation of complex diode structures such as anti-parallel, anti-series and in-series diode configurations used for subharmonic mixing [147]. To minimize parasitic capacitance, the GaAs substrate between the contact pad and anode is etched away, forming an air-channel. The noise of a GaAs Schottky diode detector at 400GHz is to be reported around 1700K [148]. The corresponding conversion loss is around 10 dB which requires a 2-4mW LO power to pump the mixer.

4.2 Setup of the characterization measurement

In the following sections, two planar air bridged Schottky diode detectors are characterized from 2.2 THz GHz to 3.5 THz. Five different THz quantum cascade lasers are used as THz sources. THz QCLs lasing at 2.22 THz, 2.56 THz, 2.75 THz, 3.05 THz and 3.50 THz.

The measurement setup is presented in figure 4-6. The THz power from the source is focused on to the Schottky diode detector with two parabolic mirrors. The output signal was monitored by an oscilloscope in real time and by a lock-in amplifier, see figure 4-6.

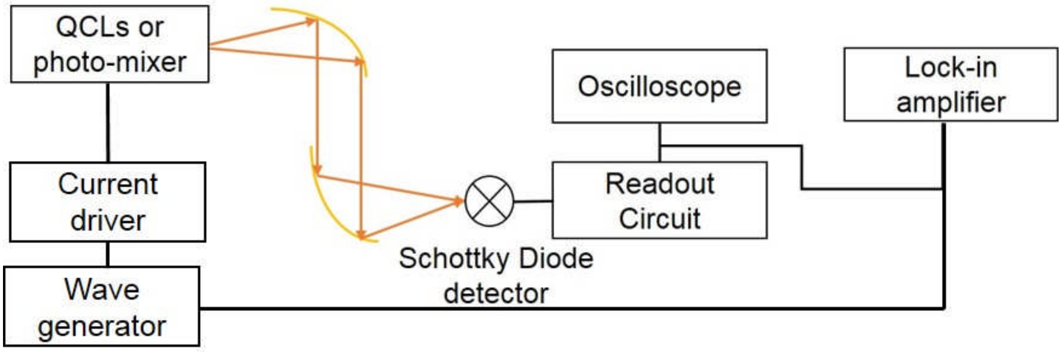

Figure 4-6 Schottky diode detector calibration setup

The QCL LIV curve, signal/noise ratio and detectivity are measured and analysed. The QCL LIV characterization is the similar to that with a bolometer in Chapter 2, but using a Schottky diode detector. The measured voltage will be the combination of the received THz radiation and system noise. In order to determine the noise response of the detector, the THz radiation was blocked by a metal sheet. The Signal/noise ratio (SNR) can be calculated by:

$$\mathrm{SNR} = \frac{V_{\mathrm{Total}}}{V_{\mathrm{Block}}} \qquad (4.12)$$

in which V_{Total} is the recorded voltage from the lock-in amplifier without metal sheet and V_{Block} is the recorded voltage when metal sheet is in place block the THz source. Detectivity is used to describe the relationship between the output voltage and the incident radiation on the detector. A larger detectivity means the detector has better performance. The responsivity (R*) of a detector is calculated using:

$$R^* = \frac{V_{Total}}{P_{source}} \qquad (4.13)$$

in which P_{source} is the real power of the THz source and is determined by a TK power meter, [149] as presented in Chapter 3.

4.3 Schottky Diode detector characterization with THz QCLs

One of the advantages of a Schottky diode detector compared to other (typically thermal) THz detectors is the fast response rate [101] (~ps compared to ~seconds). Five THz QCLs were used to characterize Schottky diode detectors based on a planar air-bridged structure. In order to demonstrate their performance, LIV curves, measured by a bolometer, were used to calibrate the Schottky diodes. The responsivity of two Schottky diode detectors was measured: a high gain detector with an integrated and a medium gain detector without an integrated amplifier. The setup of the QCL LIV characterization with the Schottky diode detectors is the same as was presented in Chapter 2 for LIV characterization with a bolometer.

4.3.1 LIV curves measured with Schottky diode detectors

Radiation from devices lasing at 2.22 THz, 2.56 THz, 2.75 THz, 3.05 THz and 3.5 THz was focused onto the Schottky diodes sequentially to measure the LIV response of the devices. These QCLs were previously characterized using a bolometer in order to allow a comparison, with the lasing spectra measured using an FTIR [2]. The spectra of the device are given as figure 4-7 and figure 4-8 for radiation at 2.75 THz and 3.05 THz, respectively. The spectrum for radiation at 2.22 THz, 2.56 THz and 3.50 THz are given as figure 2-22, figure 6-11 (a) and figure 5-4 (a) respectively. The heat sink temperature was monitored and maintained at 10K. The devices were driven in pulsed-bias mode, using a 15% duty cycle that is modulated at 10 kHz with the same frequency being used on the reference for the lock-in amplifier.

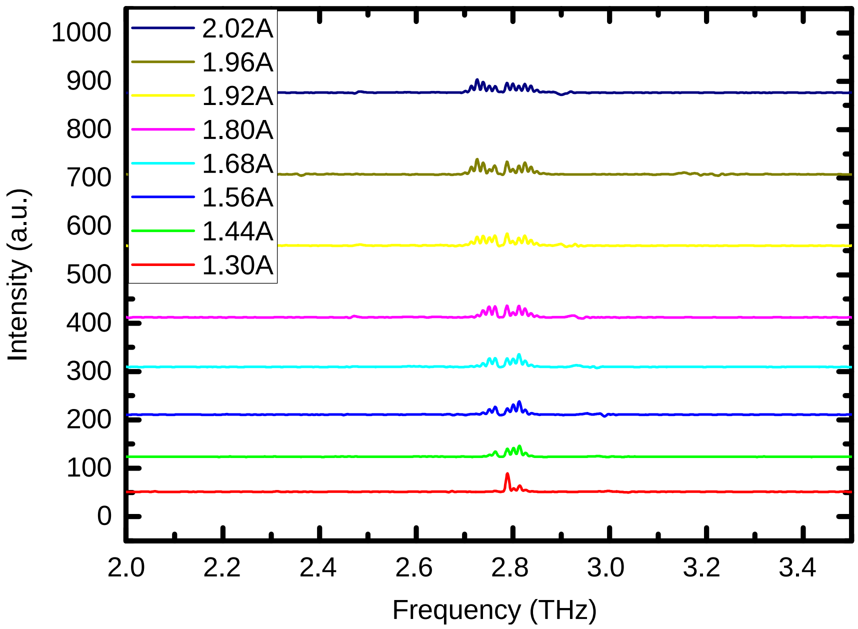

Figure 4-7 Spectra of the QCL (L701) lasing at 2.75 THz, provided by Dr Iman Kundu, University of Leeds

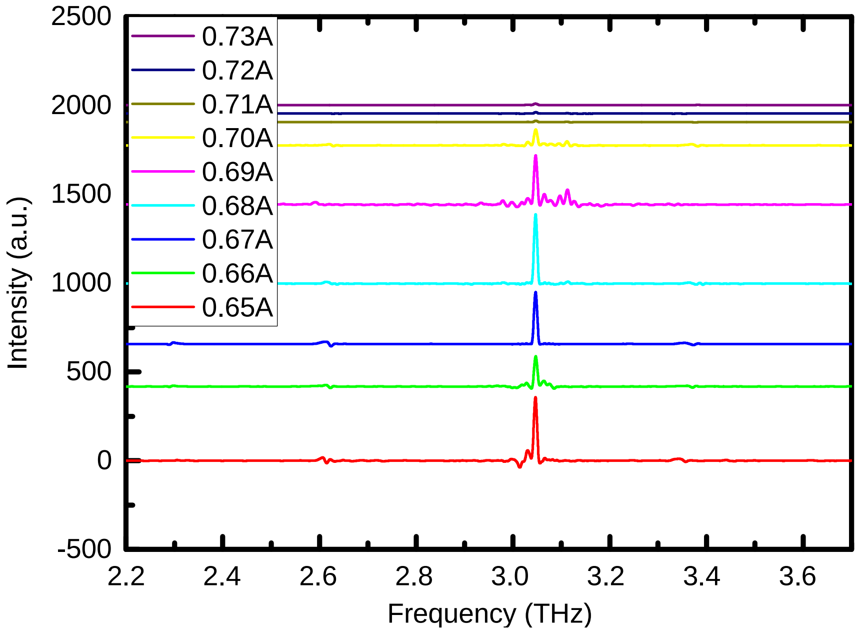

Figure 4-8 Spectra of QCL (L981) lasing at 3.05 THz, provided by Dr Iman Kundu, University of Leeds

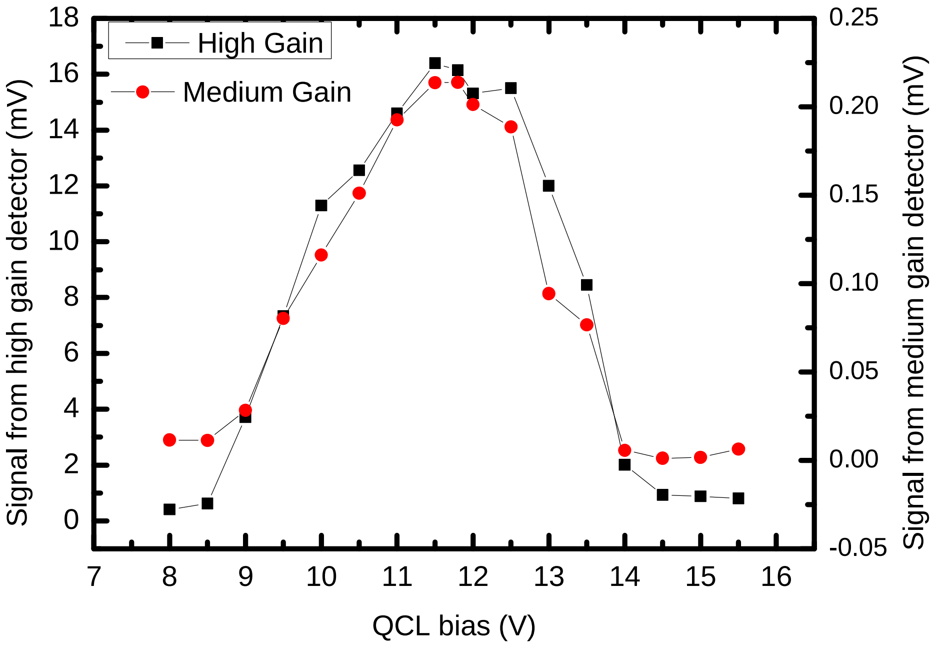

Figure 4-9 Measured LIV of L1007, lasing at 2.22 THz, with the Schottky diode detectors

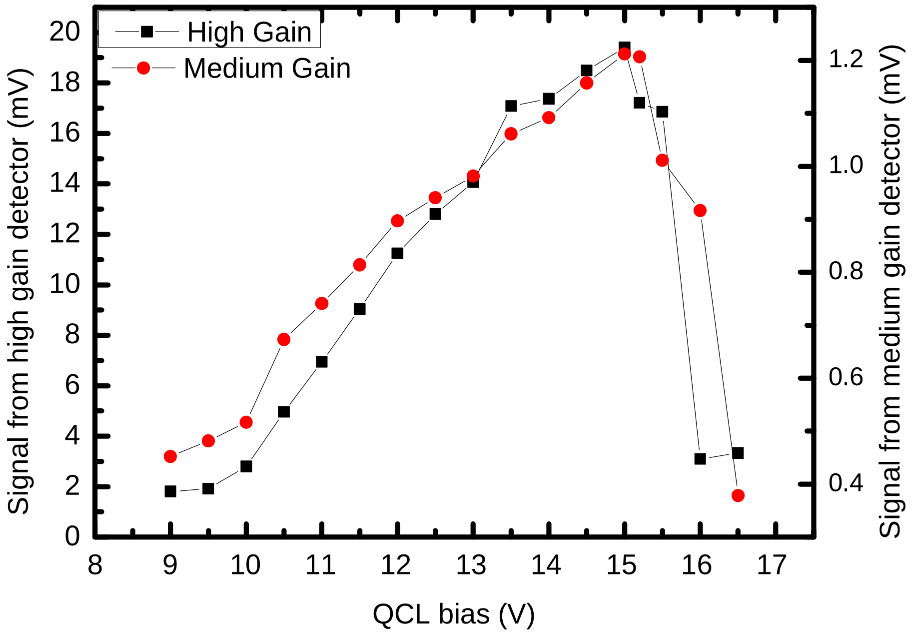

Figure 4-10 Measured LIV of L1014, lasing at 2.56 THz, with the Schottky diode detectors

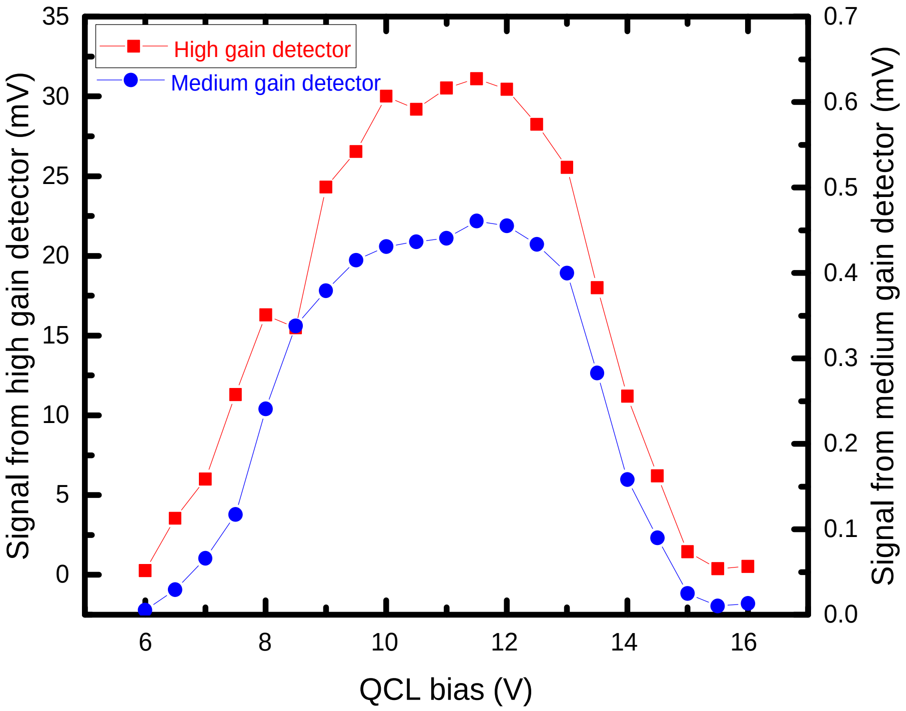

Figure 4-11 Measured LIV of L701, lasing at 2.75 THz, with the Schottky diode detectors

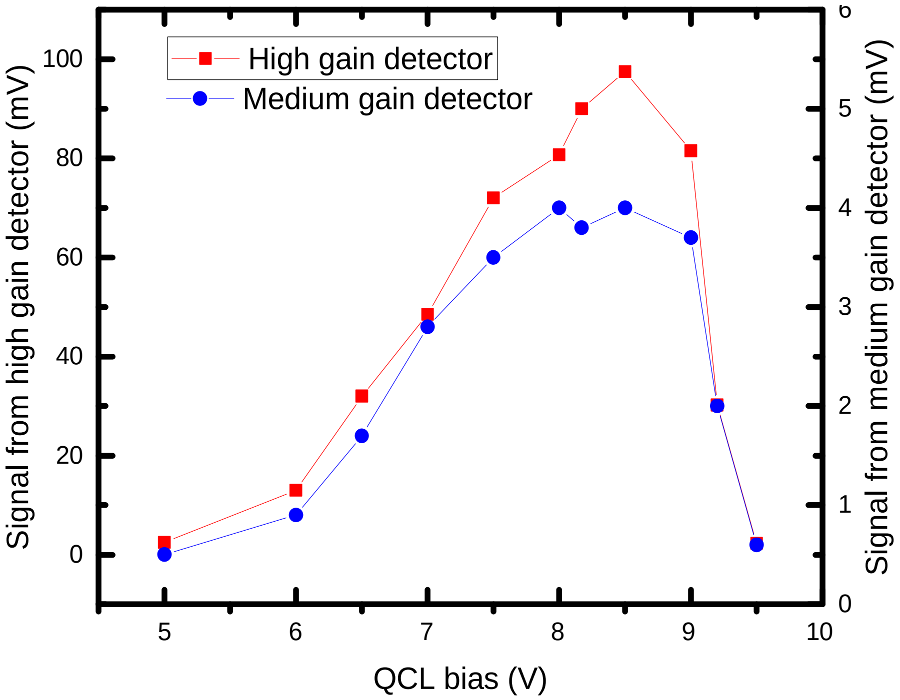

Figure 4-12 Measured LIV of L1156, lasing at 3.50 THz, with the Schottky diode detectors

The LIV responses of these devices are shown in figures 4-9 to figure 4-12. A study of the effect of different lock-in time constants is presented in figure 4-13 and figure 4-14 for the high gain and medium gain detector, respectively. Figure 4-13 and figure 4-14 show that the same LIV is measured independent of time constant, down to 50 ms, demonstrating that the Schottky response time is below this lower time constant. These results will be further analysed in the following section.

In order to compare the LIV measured with the bolometer to those measured with the Schottky diode detectors, the LIV curve measured by a bolometer for the QCL lasing at 3.05 THz is presented as figure 4-15. For each device, the LIV characteristic was measured by the medium gain detector and the high gain detector, respectively. In the measured LIV curves, both the lasing threshold and cut-off of the THz QCLs are clearly seen. This means that the detectors can detect the radiation at each frequency.

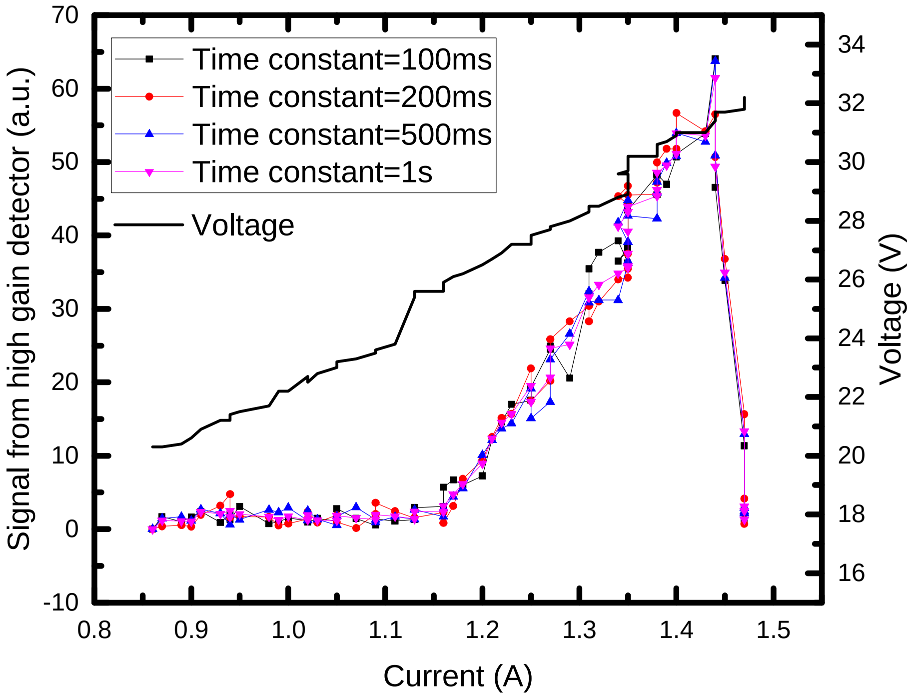

Figure 4-13 LIV curve of L981, lasing at 3.05 THz, taken with a high gain Schottky diode detector for various time constants.

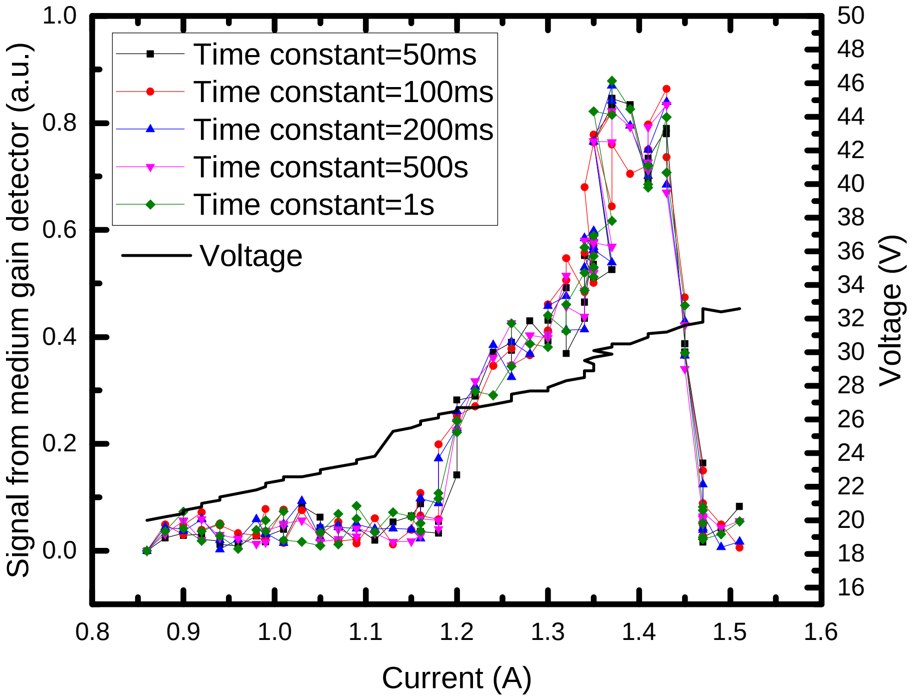

Figure 4-14 LIV curve of L981, lasing at 3.05 THz taken with a medium gain Schottky diode detector for various time constants

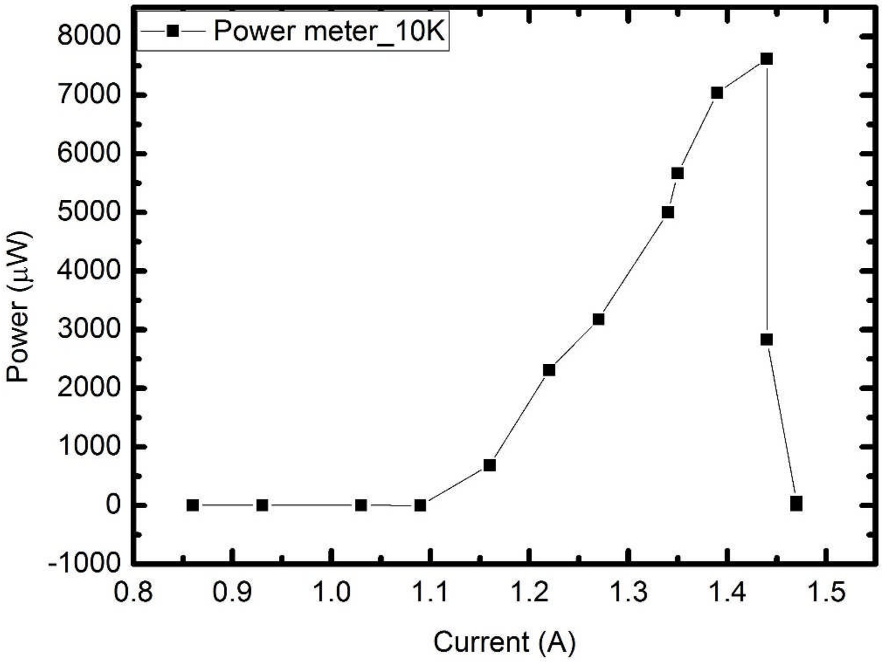

Figure 4-15 LIV curve of L981, lasing at 3.05 THz, taken with a power meter

From Figures 4-13 to 4-15, it can be seen that the Schottky diode detectors give the same threshold current (1.15 A), dynamic range (0.3 A) and peak power position (1.43 A) as the bolometer, thus proving their accuracy as a method of detecting THz radiation.

4.3.2 Schottky Diode detector responsivity measurement and analysis

Responsivity (see equation 4.12) is one of the most crucial parameters for choosing a detector. Detectors require a responsivity operating range large enough to measure the full range of the expected detected power. In order to find the working range of the Schottky diode detectors. The QCLs were driven at a range of current values and the corresponding output signal from the Schottky diode detectors was recorded. After measurement with the Schottky diode detectors, in order to quantify the absolute measured power, the detector was replaced with a TK power meter. All other measurement conditions, such as the QCL heat sink temperature, pulse duty-cycle, modulation frequency and measurement equipment are the same. The responsivity of the Schottky diode detector at different frequencies is given in figures 4-16 to 4-20 at 2.22, 2.56, 2.75, 3.05 and 3.50 THz.

At a certain frequency, the Schottky diode detectors has a constant responsivity to express how much output single the detector can give when a unit power of radiation is detected. Since the responsivity at a certain frequency is a constant, the output single from the detectors should increase linearly with the increase of radiation power. So a linear fitting is applied to fit measured output values against THz power coupled into the detector.

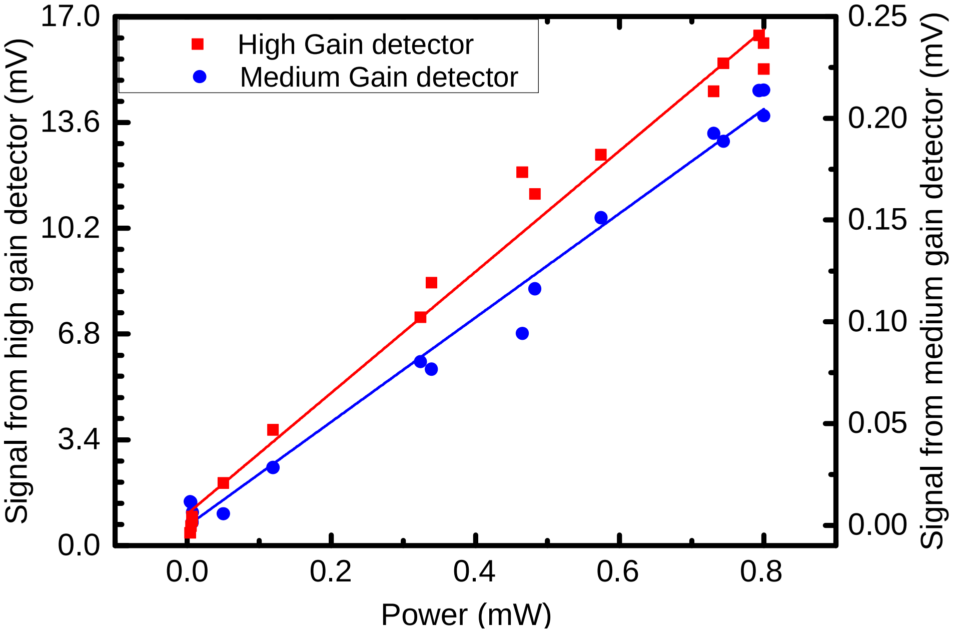

Figure 4-16 Responsivity of the Schottky diodes at 2.22 THz

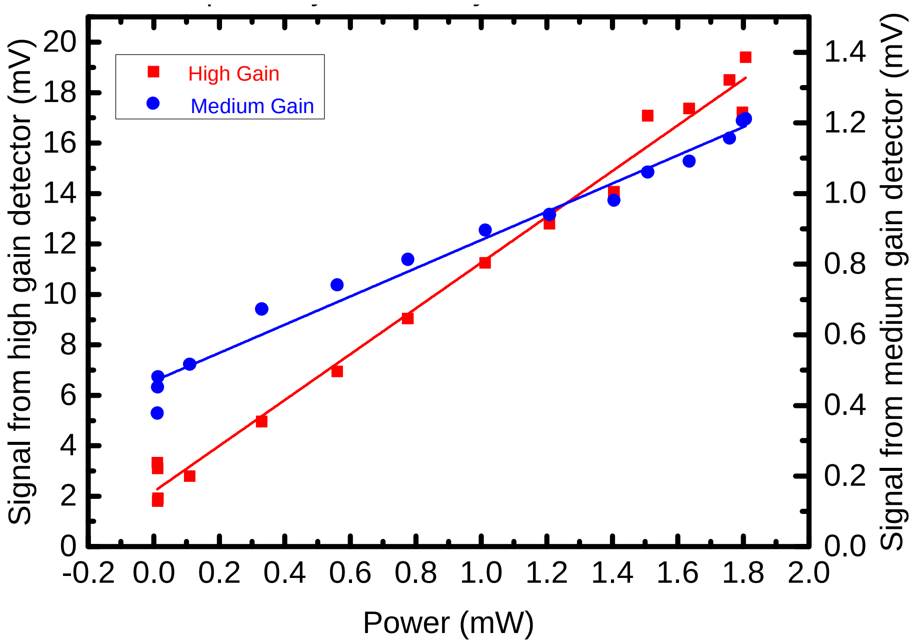

Figure 4-17 Responsivity of the Schottky diodes at 2.56 THz

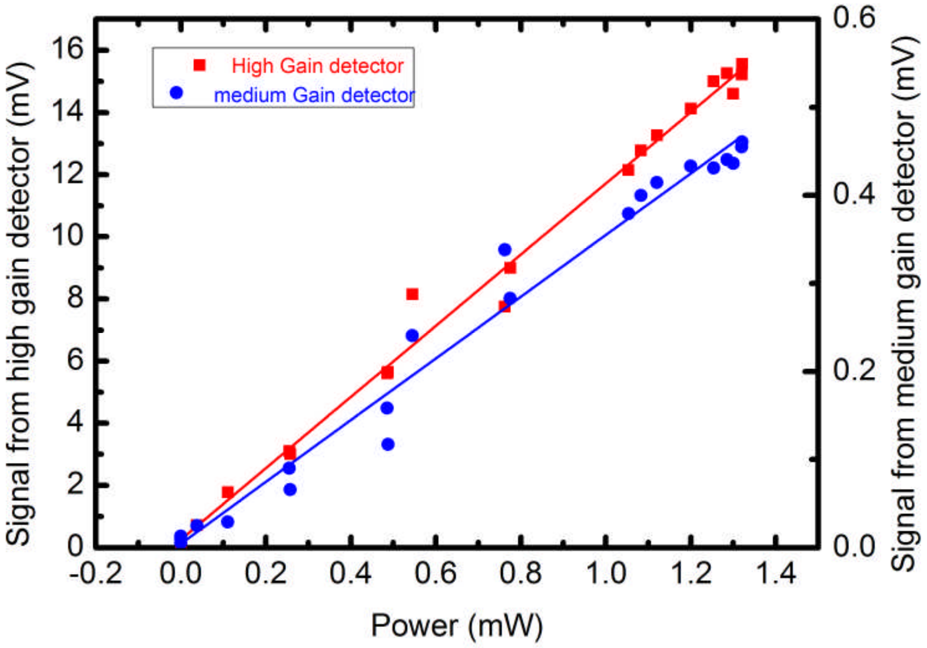

Figure 4-18 Responsivity of the Schottky diodes at 2.75 THz

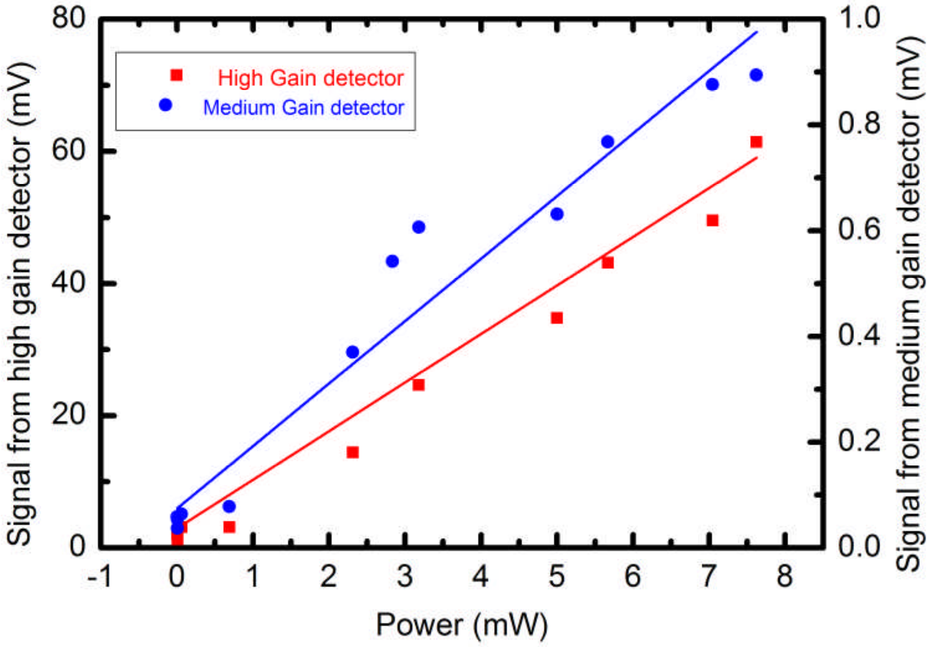

Figure 4-19 Responsivity of the Schottky diodes at 3.05 THz

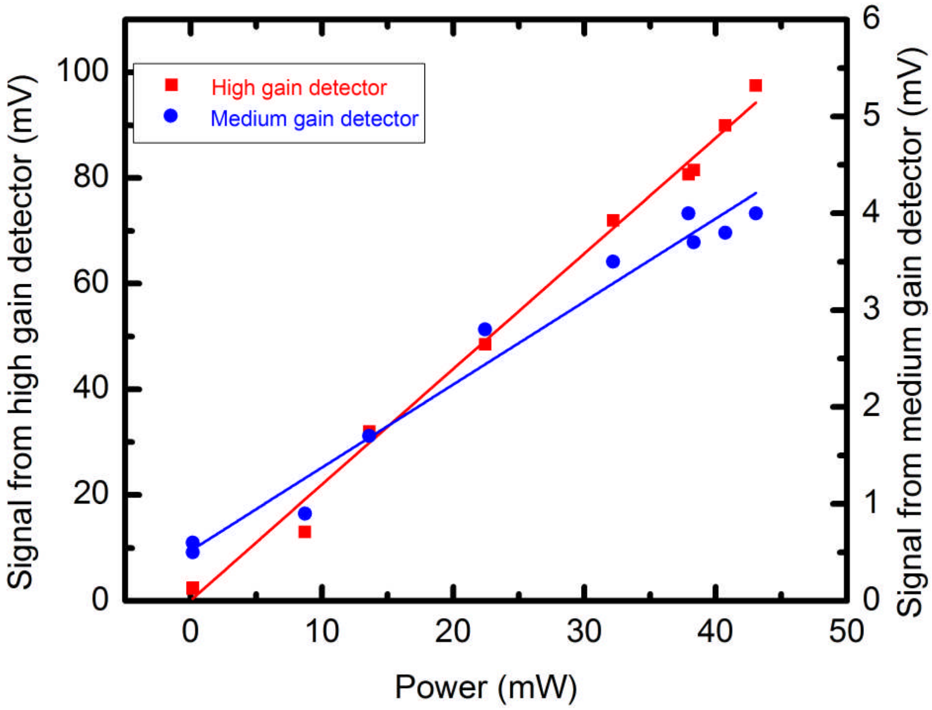

Figure 4-20 Responsivity of the Schottky diodes at 3.50 THz

As figures 4-16 to 4-20 show, the output of the Schottky diode linearly increases with the THz power at each frequency. The slope of the fitted line is responsivity of that frequency. The standard error of fitted the slope is collected and plotted together with the fitted slope in figure 4-21. The responsivity measurement at 2.56 THz presents a big noise signal, the signals shown in figure 4-17 are noise from measurement.

The high gain detector has a larger responsivity for all the frequencies tested, because it has a higher gain amplifier. But measured noise is also amplified, which will affect the detectors' sensitivity.

The responsivity is plotted for the various tested frequencies in figure 421 to study the cut-off frequency for the two detectors. Normally, the responsivity of a detector goes down sharply beyond a certain frequency range. This is found in the measurement of those two Schottky diode detectors.

The medium gain detector shows an increase in responsivity up to 2.56 THz, at which point the responsivity rolls off. The high-gain detector on the other hand shows a linear decrease in responsivity with an increase in detected frequency. The low responsivity of the medium-gain detector at 2.22 THz may be caused by several reasons. During the measurement, the detectors are aligned manually to the focus of the focusing parabolic mirror leading to the potential for human error in alignment, especially when the emitted power of the laser is low. Either lateral or longitudinal misalignment can cause a reduction in the measured THz power. The QCLs are also sensitive to alignment; where each device requires manual alignment to the focus of the mirror and the detector. Those factors combined can lead to variations in the measured power, even for repeating measurement of the same detector.

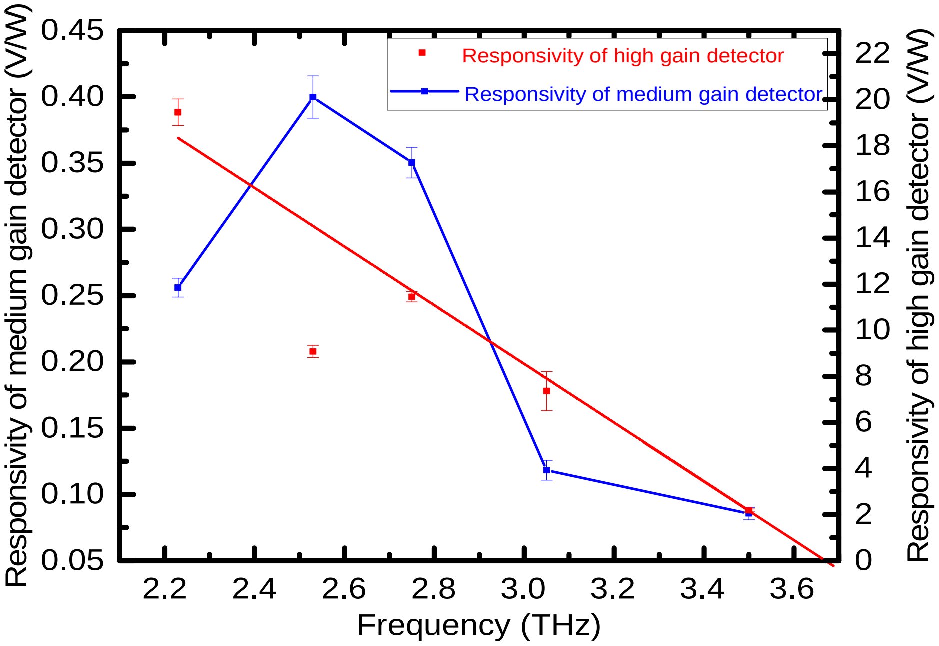

Figure 4-21 Responsivity of the Schottky diode detectors

The cut-off frequency of the high gain detector can be established from the intercept with the x-axis at 0 V/W of the line fitted to its measured responsivity. The relationship between frequency (f) and responsivity (R*) shown as the red fitted line in figure 4-21 is given by:

$$R^* = -12.73 \times f + 46.71 \qquad (4.14)$$

This value is calculated to be 3.67 THz.

The errors plotted in this figure are standard errors of fitted slope. This error only gives information on how good the fittings are to the measured data. For each frequency, a new QCL is installed in the cryostat to provide the THz power due to the limited frequency tuning of an individual QCL. So system alignment is needed after each new QCL is installed. Due to the different quality of alignment, different proportion of QCL power can be coupled into the detector. But due to the large detection area, the TK power meter isn't as sensitive to the alignment as the Schottky diode detector. It is possible the alignment was bad for 2.22 THz measurement with the medium gain detector and the 2.56 THz measurement with the high gain detector. In order to study the errors in more detail, repeat measurement with different alignments need to be undertaken.

4.3.3 Noise level characterization and analysis

The signal/noise ratio is also called the sensitivity, another important parameter for applications. Noise can come from multiple sources:

- From the detector
- From the amplifier
- From the electrical connections and equipment
- From thermal fluctuations in the QCL
- From voltage fluctuations in the QCL

Even when the Schottky diode detector is blocked from the THz source, a background signal is still measured; this signal can be treated as background noise as it doesn’t originate from the THz source. In order to detect the noise measured by the detector with no radiation source present, a similar measurement is performed as was used to measure the responsivity, but the THz signal is blocked using a metal isolator. This is not perfect as reflection can lead to portion of the radiation entering the detector; this can increase the noise level of the detector. In the two experiments, the total and background signals are measured, respectively.

The mean noise level of the medium gain detector is 6.06 µV and the standard deviation is 3.22 µV. For the high gain detector, the mean is 2.09 mV with a standard deviation of 1.40 mV. The noise level is given as figure 4-22.

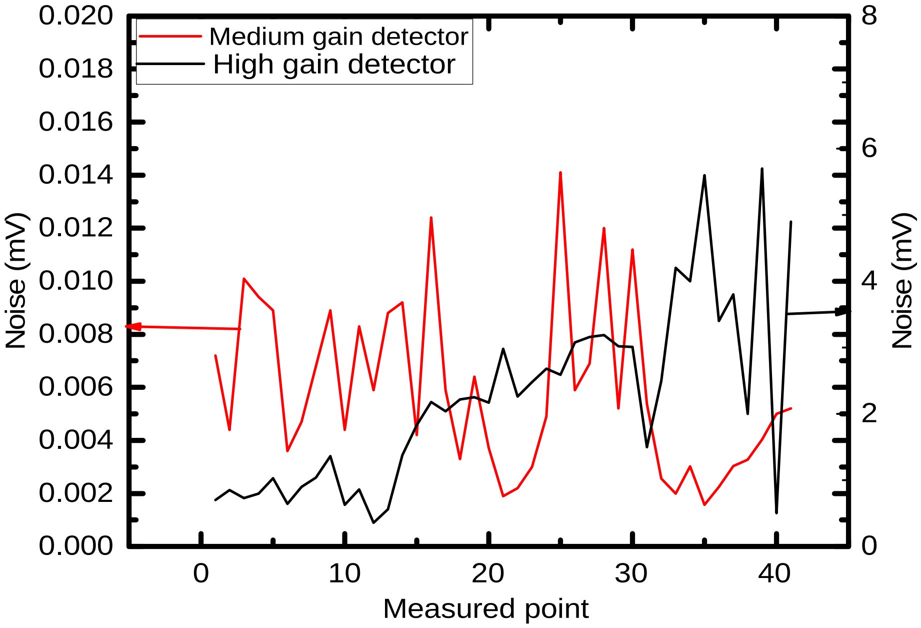

Figure 4-22 Noise level of the two detectors (The time constant was 200 ms). 43 signals recorded when the QCL is lasing and a metal sheet is used to block the THz radiation from reaching the Schottky diode detector.

Using Equation 4.11, the SNR is calculated and presented in figure 4-23. In figure 4-23, the SNR of the medium gain detector is shown to be much larger than that of the high gain detector; even though high gain detector has a larger signal. The added noise is from the amplifier circuit itself, but due to the enhanced detector performance, especially at high frequencies response, the trade-off in SNR can be tolerated. The responsivity measurement shown in previous figures shows that system noise at 2.56 THz are biggest, illustrated in figure 4-17 and figure 4-21. In order to study it, SNR at 2.56 THz is given in figure 4-23.

For application purposes, a detectable signal level of three times the background noise is required. With this is mind, the medium and high gain detectors require radiation levels corresponding to greater than 28 µV and 10.5 mV, respectively.

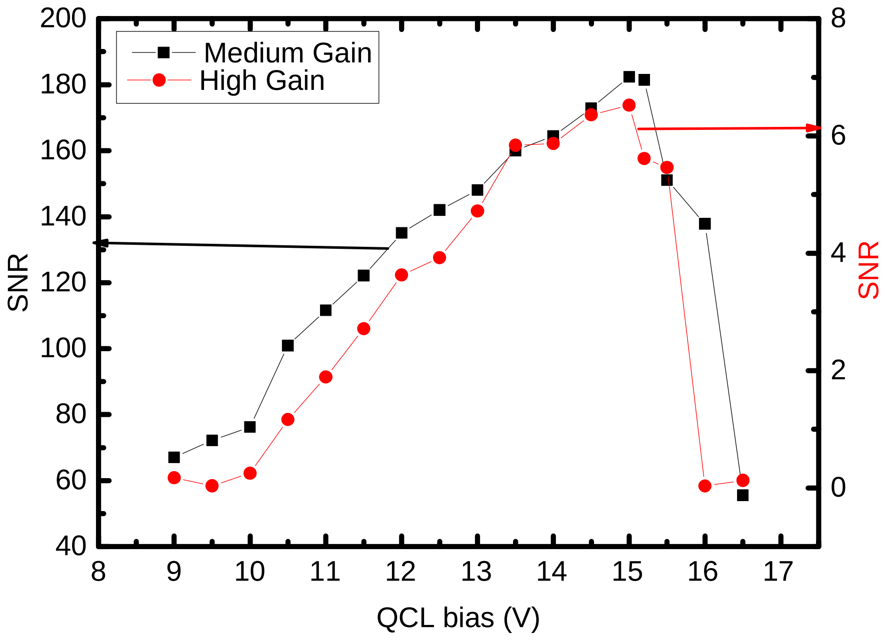

Figure 4-23 SNR of the Schottky diode detectors at 2.56THz

The SNR of medium gain detector (black one) is much larger than high gain detector (red line) due to noise introduced by integrated amplifier in high gain detector.

4.3.4 Response speed measurement

A very fast response rate is one of the main advantages of Schottky diode detectors compared with other THz detectors. Due to the electronic nature of the sensor, its response rate is limited only by electron transport time (~ps). Typically, the limiting component of using a Schottky diode as a sensor is the response rate of the accompanying measurement circuitry or equipment.

In order to test the response speed of a Schottky detector, the THz source was switched on and off at a high speed (1 kHz), and the measured signal compared to the driving signal. For this measurement, a THz QCL was driven with a current driver using a small duty cycle (2%) in order to minimise device heating. At this rate, each pulse is only 20 μs wide. The measurement system is based on that given in figure 4-7, but in order to acquire the signal at a high enough resolution to measure the response rate, the lockin amplifier was replaced with a fast reading oscilloscope.

In order to measure the power from the THz QCL source, the background radiation was measured separately by blocking off the THz beam, using the technique explained in Section 4.3.3 , and subtracted from the measured signal in analysis. This is shown in figure 4-24 and figure 4-25, for the high gain detector and medium gain detector, respectively.

The actual signal from QCL measured with high gain and medium gain Schottky diode detectors are given as figure 4-26 and figure 4-27, respectively. Here, the detector is able to measure the QCL switching at 1 kHz, even with pulses of only 20 µs. A smaller time scale should thus be studied in order to calculate the response time of the Schottky diode detector.

To analyse the detected signal, the data was magnified and fitted with an exponential decay, which is given in figure 4-28 and figure 4-29 for the high gain and medium gain detectors, respectively. A 4 µs time scale was used. The fitted equation is shown as:

$$y = y_0 + A_1 \times e^{-\frac{(x-x_0)}{t_1}} \qquad (4.15)$$

where x_0 is the time when the signal becomes stable and t_1 is the time to reach a stable state.

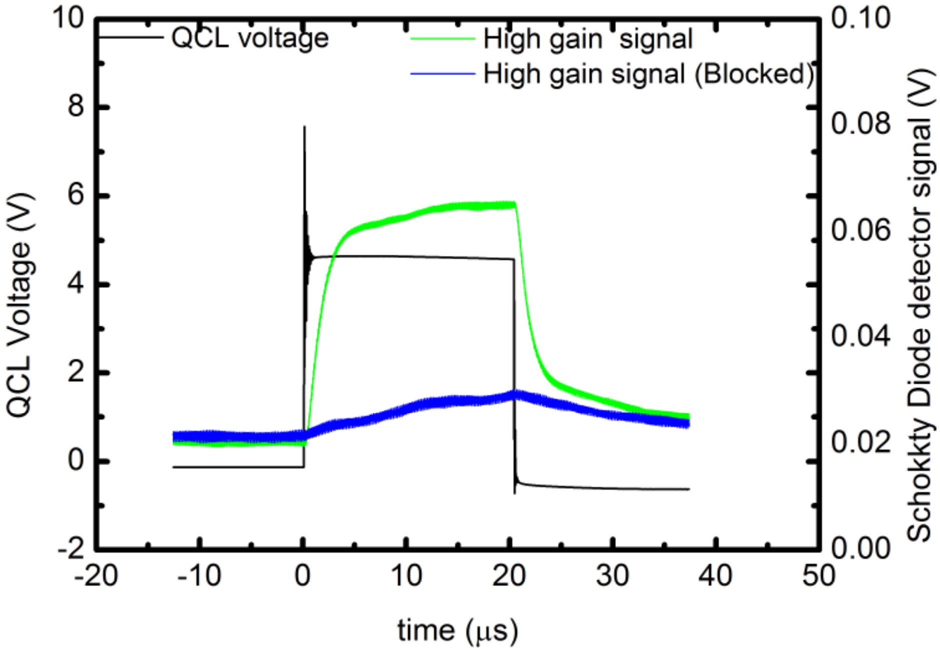

Figure 4-24 Recorded signals from the oscilloscope with the high gain detector. The blue and green line are total measured and background signals, respectively.

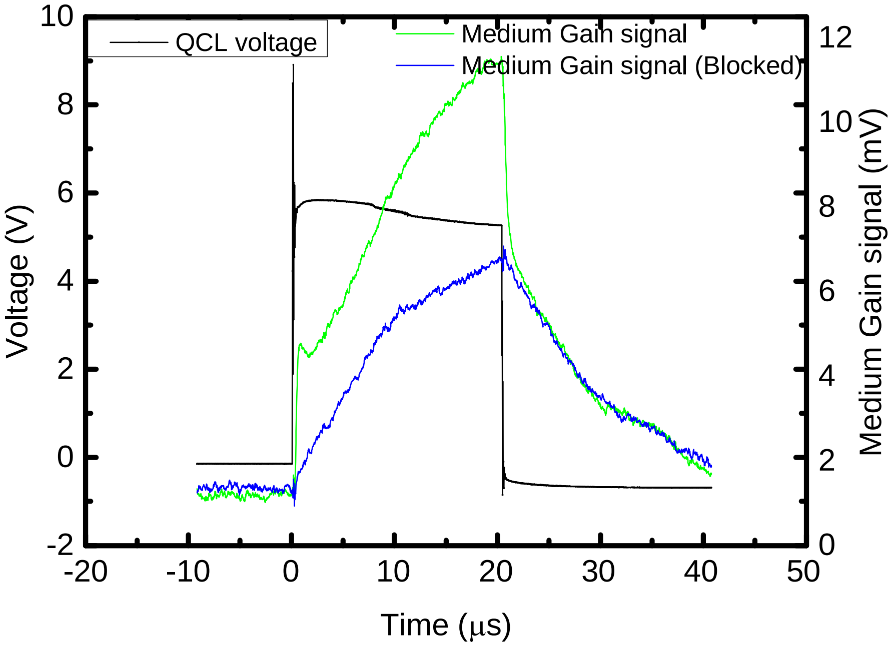

Figure 4-25 Recorded signals from the oscilloscope with the medium gain detector. The blue and green line are total measured and background signals, respectively

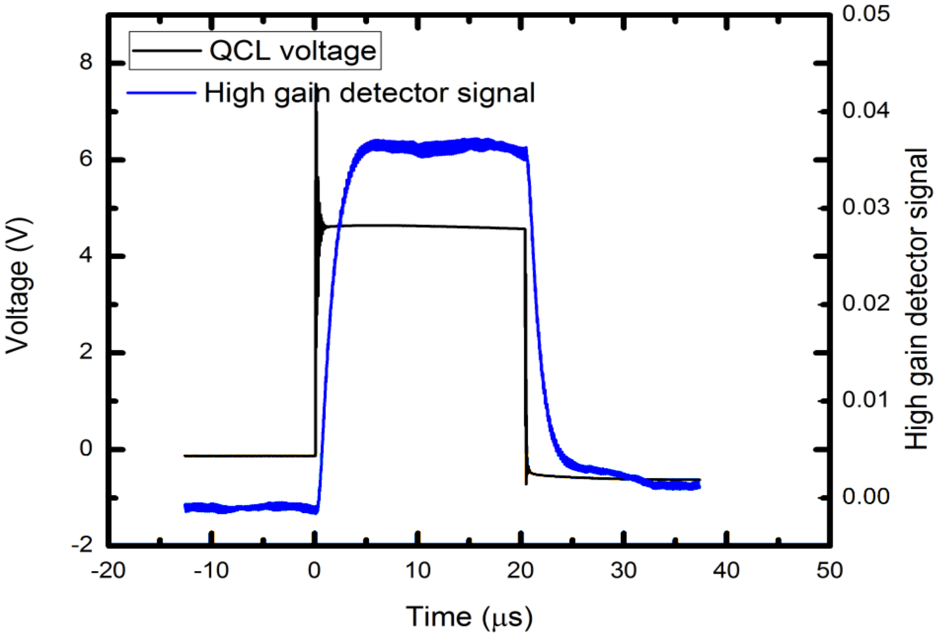

Figure 4-26 QCL signal measured with high gain detector

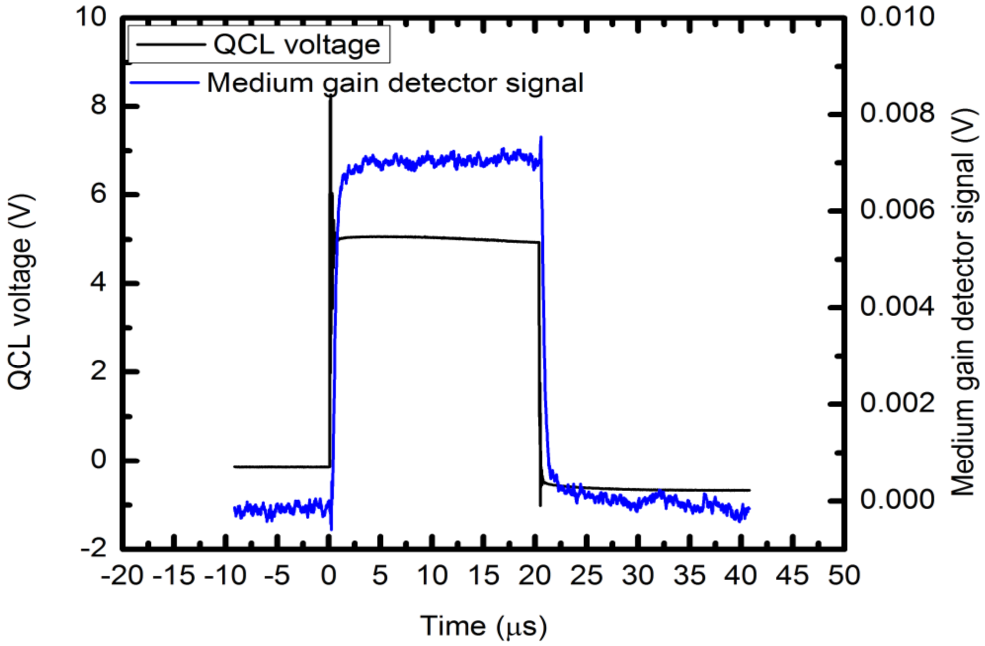

Figure 4-27 QCL signal measured with the medium gain detector

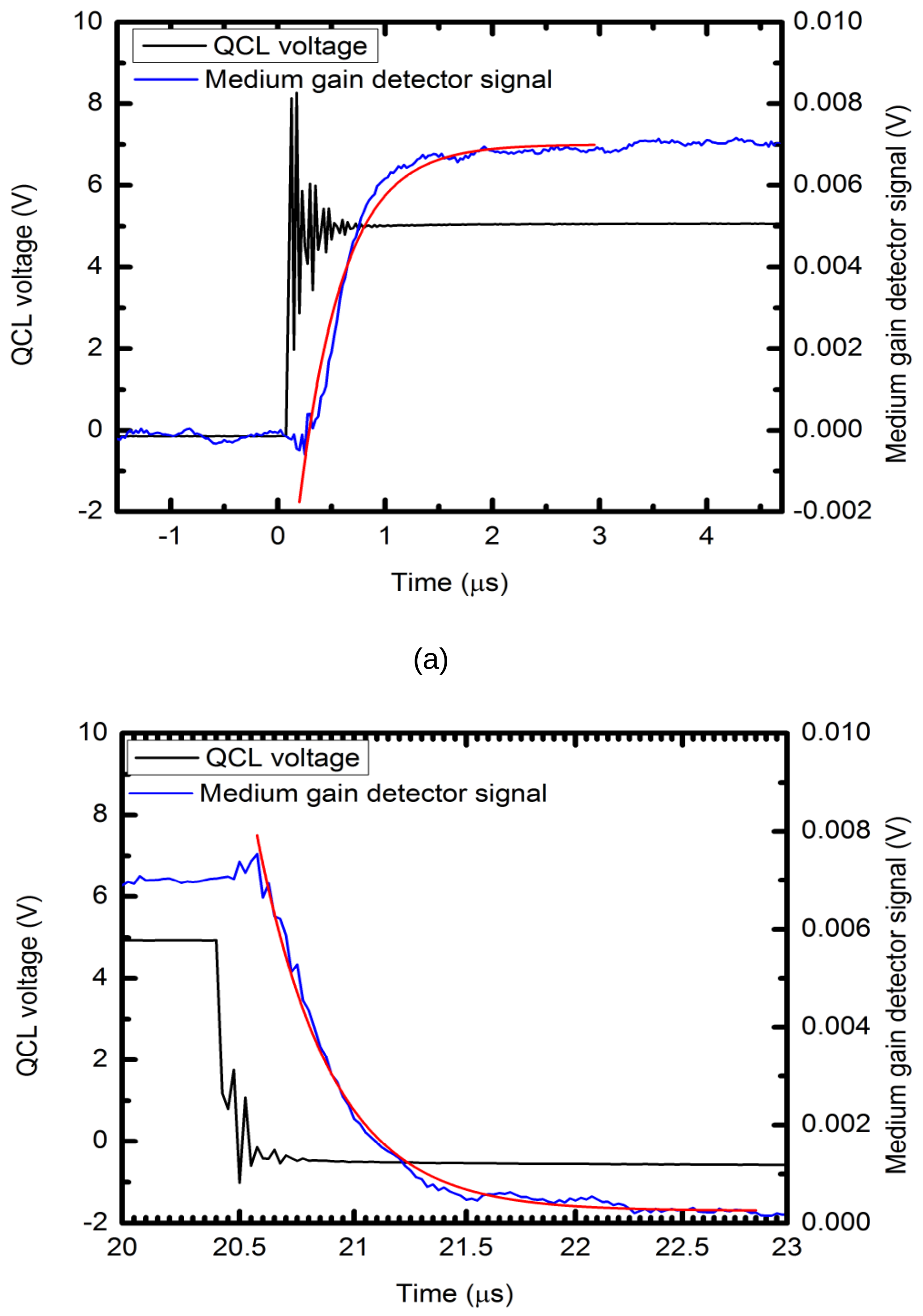

(a)

(b)

Figure 4-28 High gain detector response time when the QCL is (a) switched on and (b) switched off.

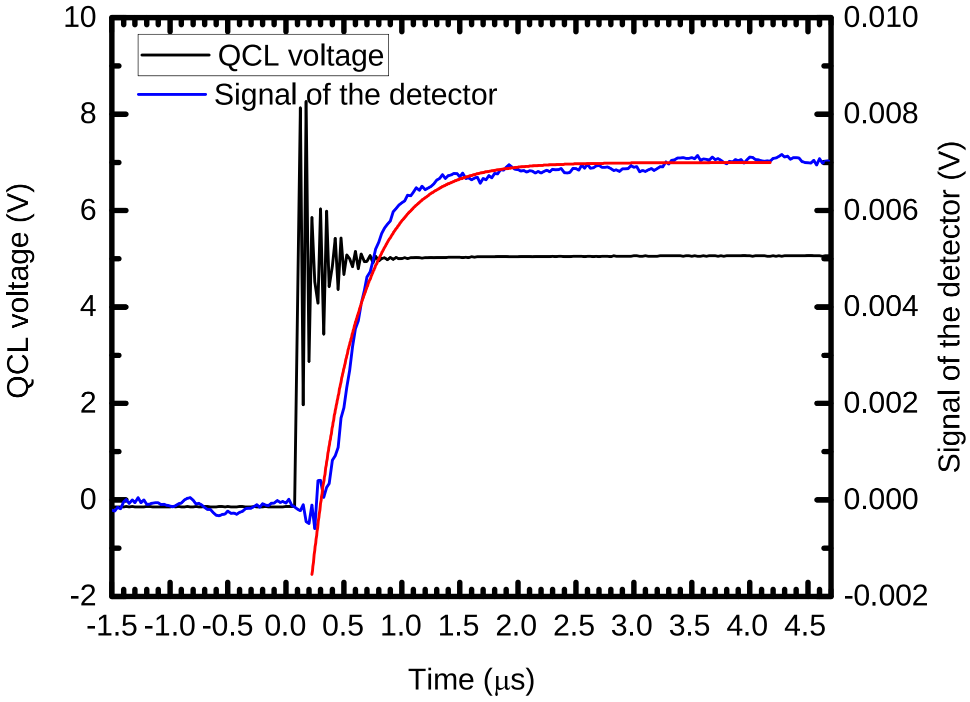

(a)

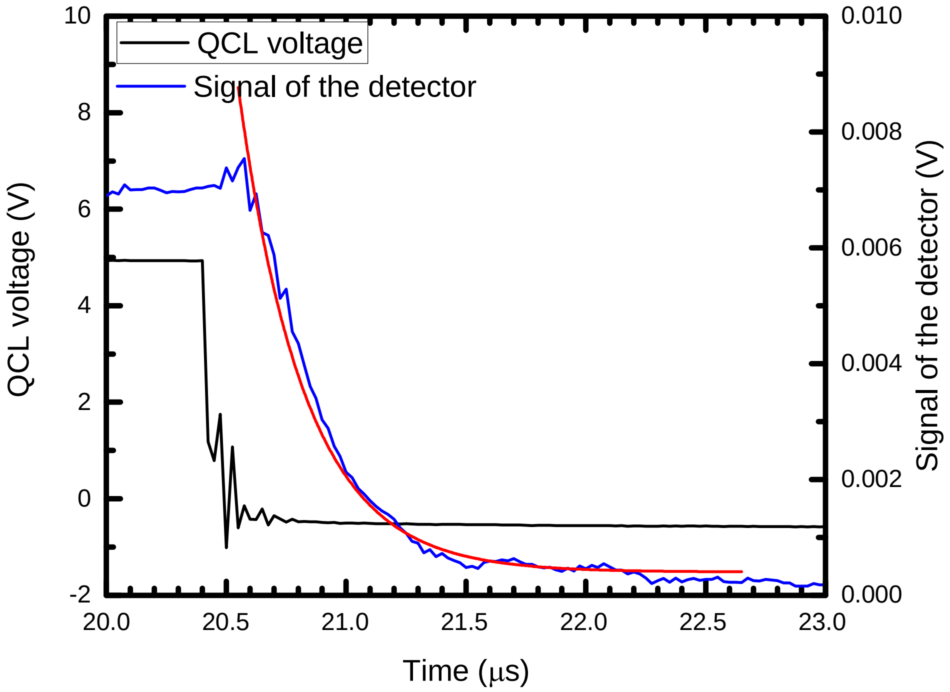

(b)

Figure 4-29 Medium gain detector response time when the QCL is (a) switched on and (b) switched off.

Table 4-1 Fitted parameters of Equation 4.

	y_0 (mV)	A_1	x_0	t_1 (μs)
Switch on-high gain detector	0.037	-0.093	7.1E-7	1.33
Switch off-high gain detector	0.0024	-0.035	2.1E-5	1.25
Switch on-medium gain detector	0.0070	-0.014	2.3E-7	0.41
Switch off-medium gain detector	0.0024	0.0076	2.1E-5	0.33

The fitted parameters for the high gain and medium gain detector response times are given in table 4-1. From the fitted result shown in figure 4-32, the medium gain detector response times are 410 ns and 330 ns, for switch on and turn off respectively. The time-resolution was limited by the readout electronics and was estimated to be 1.1 ns [150], which is far below the response times measured.

QCL switch on and off is limited by electron transport rates (~ps), so this isn't a limiting factor either. At switch on and off, the QCL temperature changes, and as this is a thermal effect it takes longer, so this could potentially be a factor that is measured by the Schottky diode. As such, it can be deduced that it takes ~410 ns for the QCL temperature to stabilise.

Figure 4-30 show the response time of the high gain detector under the same measurement conditions as above, using a 20 μs driving pulse. Compared with the medium gain detector, the high gain detector results in a larger output signal (~5×) and also a larger degree of noise, shown as the ripples in figure 4-30.

The exponential decay fitting gives a response time of 1.33 μs and 1.25 μs for switch on and off respectively. In this case, the QCL thermal equilibrium is not the limiting factor, but the amplifier read-in and out speed. The time taken by the amplifier is ~3.6× longer than the QCL takes to reach thermal equilibrium.

As this is still on the order of ~µs, it is much faster than typical thermal THz detectors such as bolometers, Golay cells or pyroelectric detectors, whose response times are on the order of ~s.

4.4 Conclusion

In this chapter, two Schottky diode detectors were calibrated and studied, which is necessary for developing compact local oscillators. The detection principle and detector structures were introduced. The detectors' LIV were referenced to a bolometer in order to understand their operation.

The responsivity of the detectors was tested using a range of THz sources lasing between 2 THz and 4 THz. A 3.65 THz cut-off frequency is obtained for the high gain detector. In addition to this, the response speed of the detectors was measured and it was shown to be much faster than most other typical THz detectors.

Chapter 5Waveguide-integrated THz QCLs, and Schottky diode detectors

5.1 Introduction

The previous chapters have described the development and characterisation of THz QCLs and Schottky diode detectors. For practical satellite-based systems, however, these devices must be integrated into waveguide structures, to provide compact, mechanical robustness systems, and to eliminate the need for separate optical components. This chapter describes preliminary work in integration of the system: Section 5.2 describes the integration of QCLs with metallic waveguides, and antennas. The work in this section is based on the publication in Ref. [151], in which the present author undertook device fabrication and characterization of the device and system. Section 5.3 describes the characterisation of QCL radiation using a commercially-sourced waveguide-integrated Schottky diode mixer.

5.2 Waveguide integrated THz QCLs

5.2.1 Introduction

Working temperature is one of the key factor that limits the application of THz QCLs, however the LOCUS LO system is required to work at temperatures above 50 K. Double-metal THz QCLs operate at higher working temperatures than single-metal THz QCLs, making them a much better choice for this LO source. However, double metal QCLs have poorer far-field beam profiles, making it challenging to couple power efficiently into a system [152]. The LOCUS radiometry channels require several mW of LO power to be coupled into the mixer, which will be very difficult to satisfy using a normal double-metal THz QCL. However, the near-field mode profile of the double metal QCL is potentially a close match to that of an external rectangular metallic waveguide; making them well-suited to system integration.

Many of the proposals for improving double-metal QCL beam profiles are either based on complex semiconductor processing technology [153] or using assemblies of antennas or lenses [154, 155]. However, these methods are relatively complex and their reproducibility and mechanical robustness is poor. Here, we have integrated a QCL into an external waveguide, using a reproducible method that has been successfully used for millimetre-wave devices in space applications [156].

5.2.2 Device structure

The QCL used in this work is a double-metal FP laser, which was fabricated and characterized in University of Leeds. The integration work was done by RAL Space. The QCL has a 3.4-THz bound-to-continuum active region [157], which contains 120 periods of GaAs/$Al_{0.5}Ga_{0.5}As$ layers and the total thickness of the active region is 14 µm (Leeds wafer L1152). A 10/500 nm Ti/Au layer was deposited onto the QCL wafer, and onto a separate carrier wafer, and the two wafers were thermal compression bonded at the metallic interface. The bonded wafers were processed into a double-metal QCL array with a separation of 100 µm between neighbouring devices.

The QCL was integrated within a copper heat-sink enclosure containing a rectangular cross-section metallic waveguide, as shown in Figure 5-1 (a). The integration work was performed at RAL Space and the waveguide-integrated device was returned to Leeds for characterization. A rectangular channel with $300\times75\mu m^2$ cross-sectional dimensions was precision-micro-machined directly into a copper block, along with a rectangular recess to house the QCL. A small gold-plated strip of AlN and a gold-plated quartz substrate is glued to the copper block using high conductivity silver loaded epoxy. These two pads are used as intermediate bonding pads between the QCL and a dc bias connector. The QCL array was placed into the cavity, as shown in Figure 5-1 (a), upon a 20-µm-thick layer of indium foil to ensure a good thermal contact. The facet of the central QCL in the array was aligned with the waveguide, and connected to the electrical contact as shown in Figure 5-2 (a) using a $125\times12.5\ \mu m^2$ Au ribbon bond to the top contact of the QCL. Three additional ribbon bonds are connected from the top of the unused QCL ridges and the copper block to provide mechanical compression when the complete waveguide unit is assembled, and to ensure a good thermal interface between the QCL and the surface of copper block. The open-ended waveguide structure of the complete waveguide is illustrated in Figure 5-2 (b).

A second copper block was also precision machined to the same size as the first one. In this copper block, there is an identical waveguide channel, which is co-registered with the equivalent part of the lower first block to form a rectangular channel of 300×150 μm^2 cross-section.

A sub-miniature (SMA) connector was used to provide an external electrical bias connection, as shown in Figure 5-1(b).

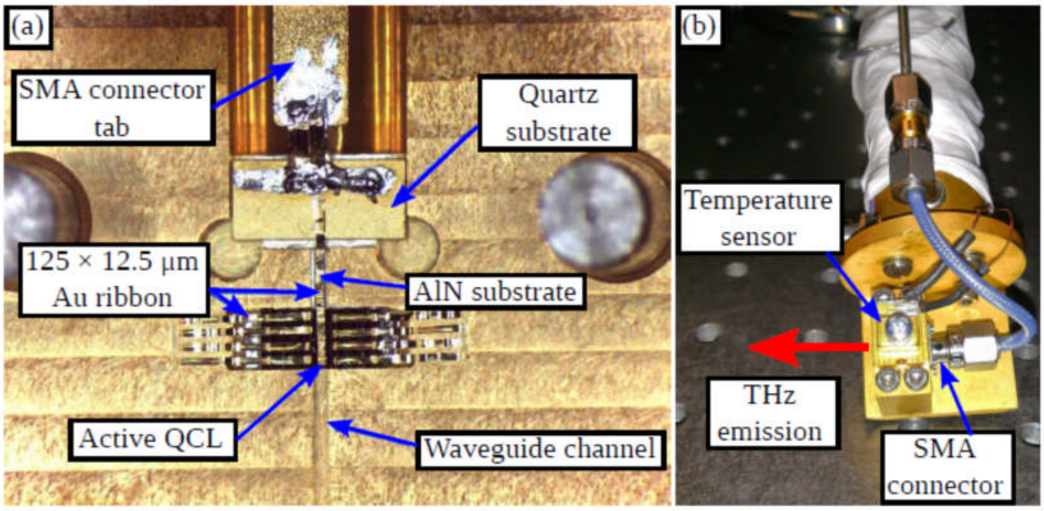

Figure 5-1 Waveguide integrated QCL [182]. (a) The inner structure of half of the opened waveguide integrated device. (b) The whole waveguide integrated device mounted in the cryostat.

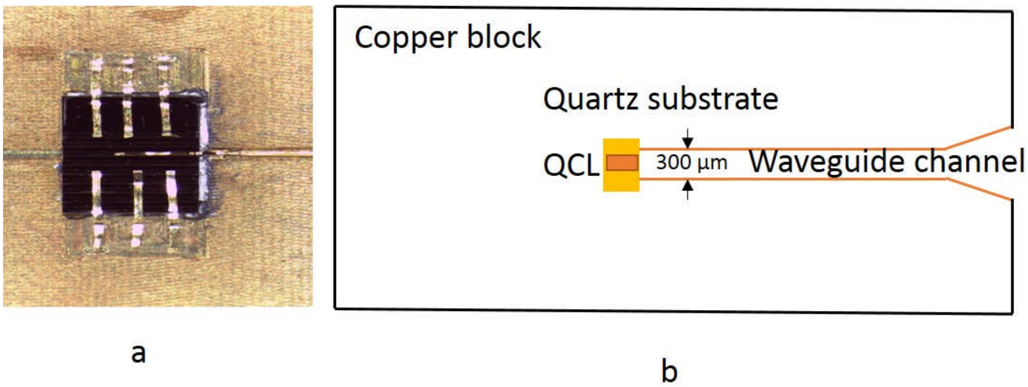

Figure 5-2 Ribbon-bonded QCL. (a) A microscopy image of the device and waveguide channel. (b) A schematic illustration of the waveguide channel.

5.2.3 Measurement setup

The waveguide-integrated QCL was mounted onto the cold-finger of a Janis ST-100 liquid-helium cryostat as shown in Figure 5-1 (b). and a LakeShore

DT-470 silicon diode was attached to the top of the block to monitor the heat-sink temperature during operation.

LIV curves at different working temperatures, emission power and device beam profile were all measured. The LIV curve measurement setup was the same as a normal QCL characterization described in Chapter 2. Power and spectral mapping was performed in both pulsed and CW modes.

For pulsed characterisation, a 10-kHz, 2% duty-cycle current pulse train, which was modulated by a 167-Hz square-wave to match the peak responsivity of a helium-cooled Ge:Ga photoconductive detector. An optical chopper, which is modulated at 185 Hz was used for continuous wave (CW) mode measurements. The CW bias was generated using a dc power supply. An FTIR spectrometer was used to measure the spectrum of the waveguide integrated QCL and the unmounted QCL.

A Golay detector with an entrance aperture of 1-mm diameter was employed for far field beam profile characterization. In order to ensure that the true far field beam profile was measured, the Golay detector was placed at 32.4-mm longitudinal distance from the laser facet, which is much larger than the 5.8-mm, Fraunhofer distance for these emitters. During the beam profile measurement, the device, which was working at 30-K heat-sink temperature was driven using a continuous 30-Hz square wave. The detector was scanned through the THz beam linearly in two dimensions over a 30×30mm^2 area. For each direction, the scan speed was the same and the step size was 0.5 mm. The beam intensity was read using lock-in amplifier and recorded at each position of the 30×30mm^2 area. The position of the beam intensity was translated into rotational coordinates along the epitaxial growth axis (θ), and in parallel with the substrate (ϕ).

5.2.4 Measurement result

5.2.4.1LIV curve and power measurement

The LIV of an equivalent (unmounted) device, and the integrated QCL were measured both before and after integration are measured, as shown in Figure 5-3. The performance in terms of threshold current, maximum heat sink temperature of the waveguide integrated and normal ‘unmounted’ QCL were measured. A comparison is given in Table 5-1 and Table 5-2 for pulsed mode and continuous wave (CW) mode respectively.

Table 5-1 Performance comparison between waveguide integrated and unmounted QCL (pulse mode)

	Maximum heat sink temperature (K)	Threshold current at 10K (mA)	Power (µW)
Waveguide integrated QCL	90	130	340
Unmounted QCL	97	100	1500

Table 5-2 Performance comparison between waveguide integrated and normal QCL (CW mode)

	Maximum heat sink temperature (K)	Threshold current at 20K (mA)	Power (µW)
Waveguide integrated QCL	77	130	30
Unmounted QCL	80	100	120

The power was measured using an absolute THz power meter. For pulsed measurements, the QCL current was modulated using a 30Hz square wave, and a mechanical chopper was used to modulate the beam at 30-Hz for CW measurements. The LI curve of the unmounted device at 60 K gives a bump when bias is between 200 mA to 220 mA. The origin of the bump is unclear, but could be the result of mechanical vibrations during measurements. The integration scheme does not significantly affect the threshold current density or maximum operation temperature. Although the integration introduces a significant power loss (80%).

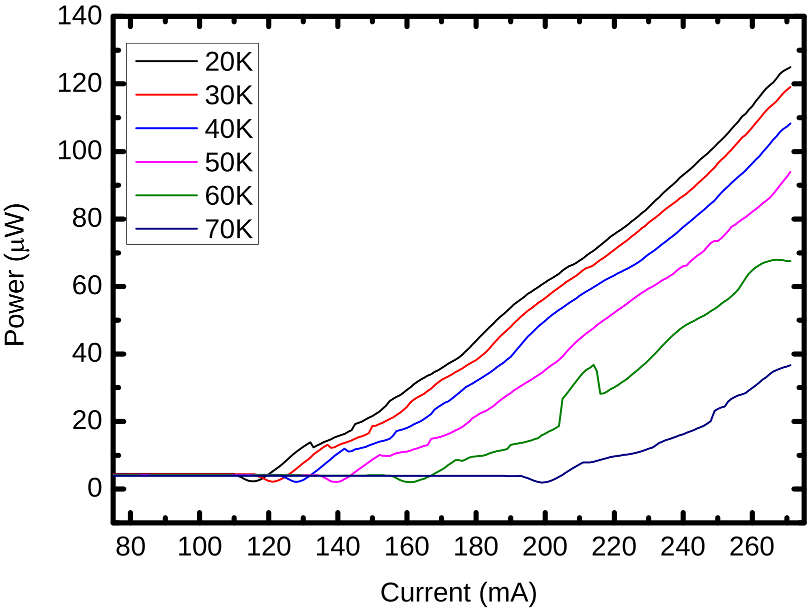

(a)

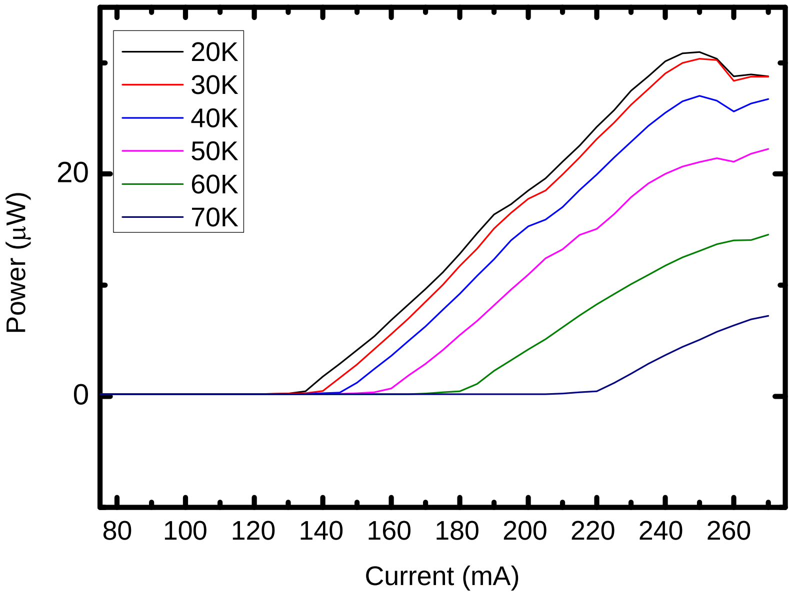

(b)

Figure 5-3 LIV curve of 3.4-THz QCLs.

(a) shows results for an unmounted QCL and (b) is for the waveguide integrated device.

Since the loss in THz power is not accompanied by any other significant change in device performance, this implies that the QCL itself has not been perturbed by the integration process. The power reduction is most likely to result from a mismatch between the transverse mode profile of the laser cavity and that of the relatively-wide rectangular waveguide, and between the waveguide aperture and free space.

5.2.4.2Spectral measurement

The FTIR emission spectra for the unmounted and integrated QCLs are shown in Figure 5-4. In each case, a similar spectral bandwidth (120 GHz) was observed and both devices are centred at 3.4 THz. This observation supports the conclusion that the mounting scheme does not introduce any significant perturbation to the performance of the QCLs.

5.2.4.3Beam profile measurement

The far-field beam profile was acquired by raster-scanning a Golay detector, as described in Section 5.2.3 . The polarization of the device was not filtered at this stage, so the measured far-field beam profile contains all the polarisation components of QCL. The measured far-field beam profile is shown in Figure 5-5.

Then the beam divergence angles were calculated in terms of x direction (θ) and y direction (φ). As stated previously, the distance between the detector plane and the QCL facet was 32.4 mm. The beam divergence was, therefore calculated from beam profile using: $\theta = \arctan(\frac{x}{32.4})$ and $\phi = \arctan(\frac{y}{32.4})$. Figure 5-6 (a) and (b) show the horizontal and vertical beam divergence respectively, showing that an approximately Gaussian beam pattern is obtained from both directions, with a full-width at half-maximum < 20°. This is a significant improvement compared with standard double-metal QCLs, which yield widely divergent emission [193, 194]. Furthermore, the spatial “ringing” and anisotropy that are commonly associated with double-metal QCLs have also been removed.

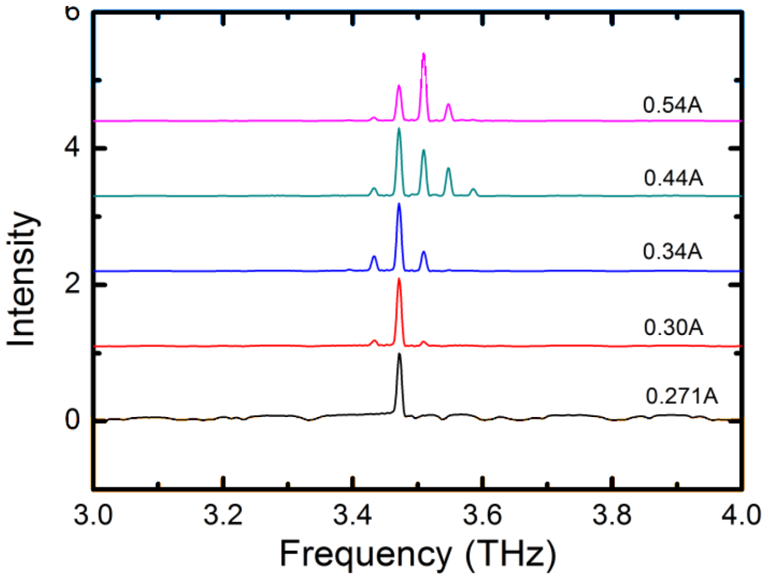

(a)

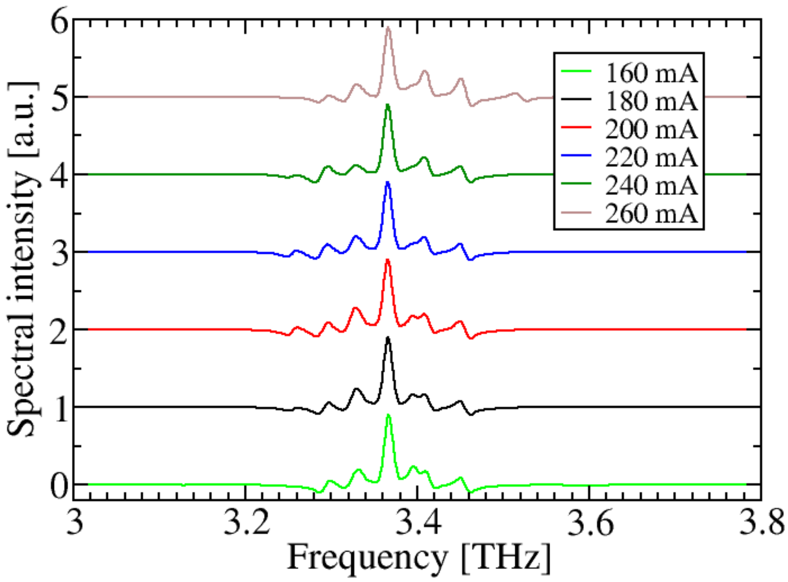

(b)

Figure 5-4 Emission spectra of 3.4-THz QCLs. (a) shows results for the unmounted QCL, (b) is for the waveguide integrated QCL.

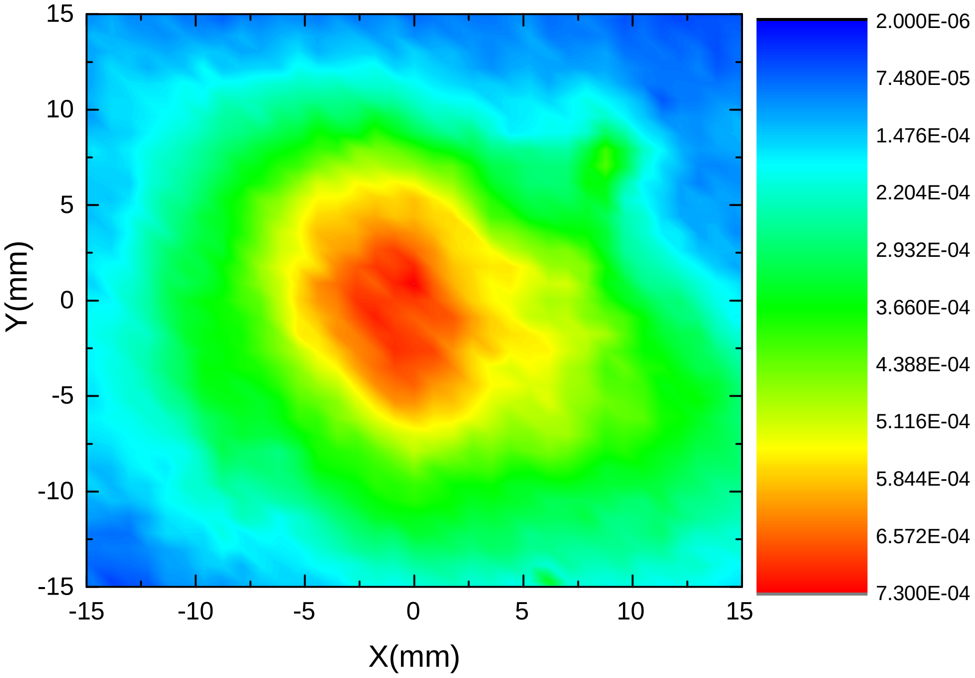

Figure 5-5 Golay detector measurement of waveguide integrated QCL far-field beam profile

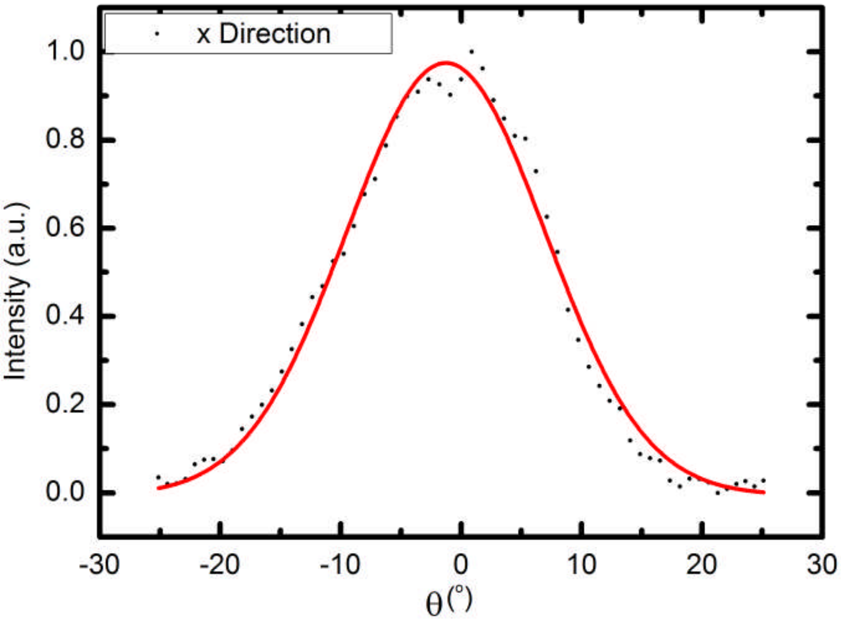

(a)

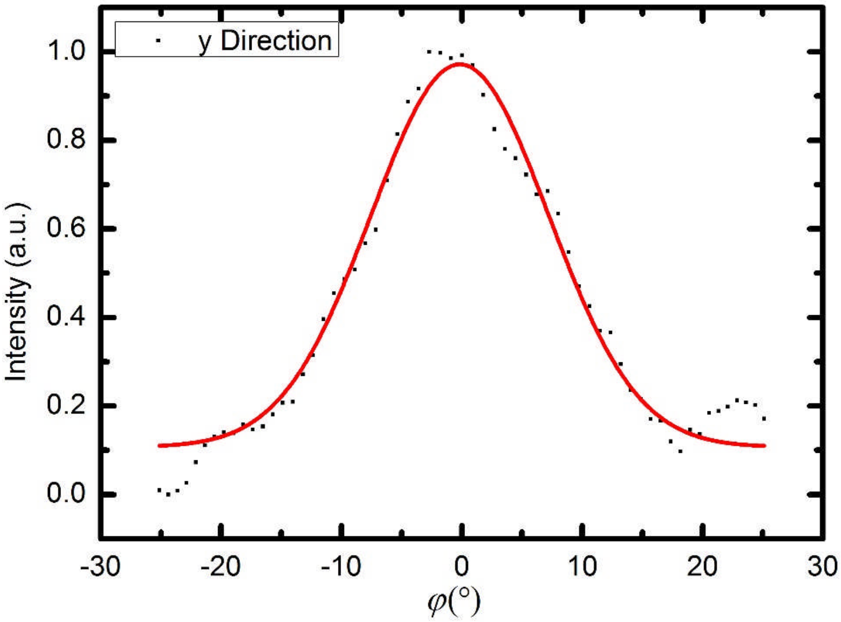

(b)

Figure 5-6 Gaussian fitted beam divergence of waveguide integrated QCL far field beam profile

5.3 THz QCL study using a waveguide-integrated Schottky mixer

5.3.1 Introduction

A narrow linewidth LO is the key component for a high resolution spectrometer based on heterodyne mixing. The linewidth of the LO is critical for Earth observation because of the narrow linewidth spectral of the researched atoms, molecules and gases under low pressure and low temperature conditions.

As a LO source, THz QCLs have a very narrow intrinsic spectral linewidth that can be reduced to the Hz level through phase locking [68-70], or to <20 kHz (FWHM) through frequency locking to a methanol gas cell [158]. However, external fluctuations of the QCL working conditions, such as temperature, bias and mechanical vibrations can increase the linewidth of the QCL.

In this section, the IF output from a Schottky diode detector is used to study the linewidth of a bound-to-continuum QCL and to demonstrate THz frequency detection using a waveguide-integrated detector. The result of the measurements presented in this section show that the free running QCL has a linewidth of around 3 MHz, in agreement with previously published values [105, 158].

By mixing the signal from a THz LO and a detected unknown THz signal in the Schottky diode detector, the detected radiation can be down converted to a GHz signal which is much more convenient to study. If the emission of the QCL itself is considered, then neighbouring FP modes can be mixed in the detector and the heterodyne signal provides information on the emission of the QCL.

The waveguide-integrated Schottky diode detector used in this work is commercially sourced (Virginia Diodes inc.) and has an RF detection range of 1.8−2.8 THz. The IF is limited to <12 GHz, by the bias-Tee and pre-amplifier. The QCL studied is a multimode, single metal FP laser whose lasing frequency is centred at 2.2 THz. The resonant cavity length of the laser is 4.2 mm. The FTIR spectra and LIV characteristics of the device are shown in Figure 5-7 and Figure 5-8 respectively. The resolution of modes in Figure 5-7 is limited by the ~7.5-GHz resolution of the FTIR spectrometer. However, the mode spacing can be seen to be approximately 9 GHz.

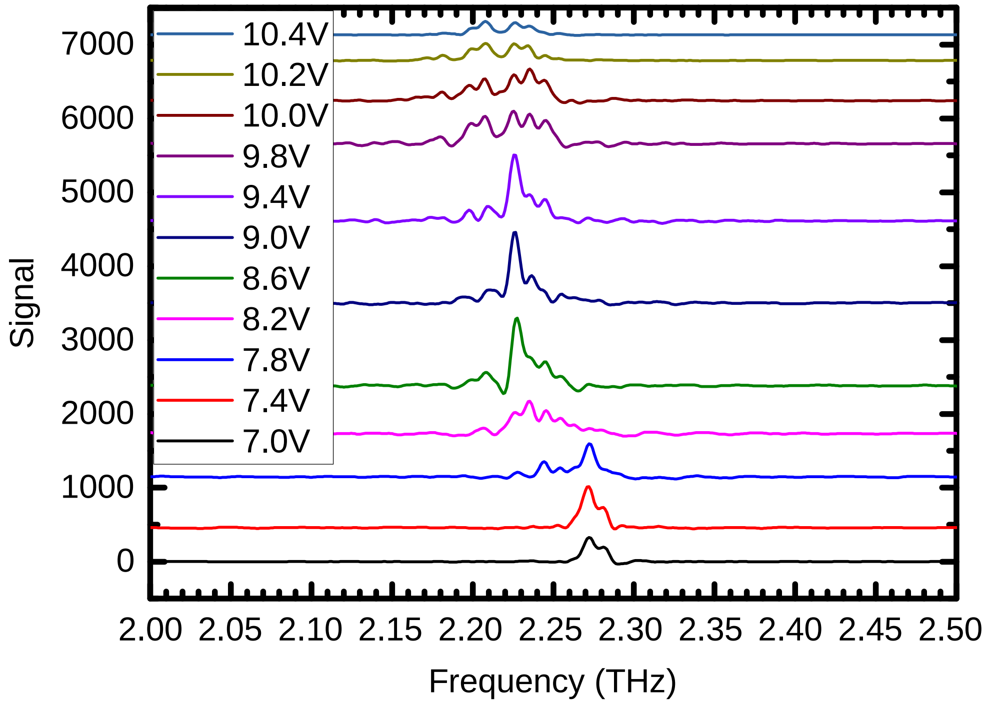

Figure 5-7 FTIR spectrum of the studied QCL

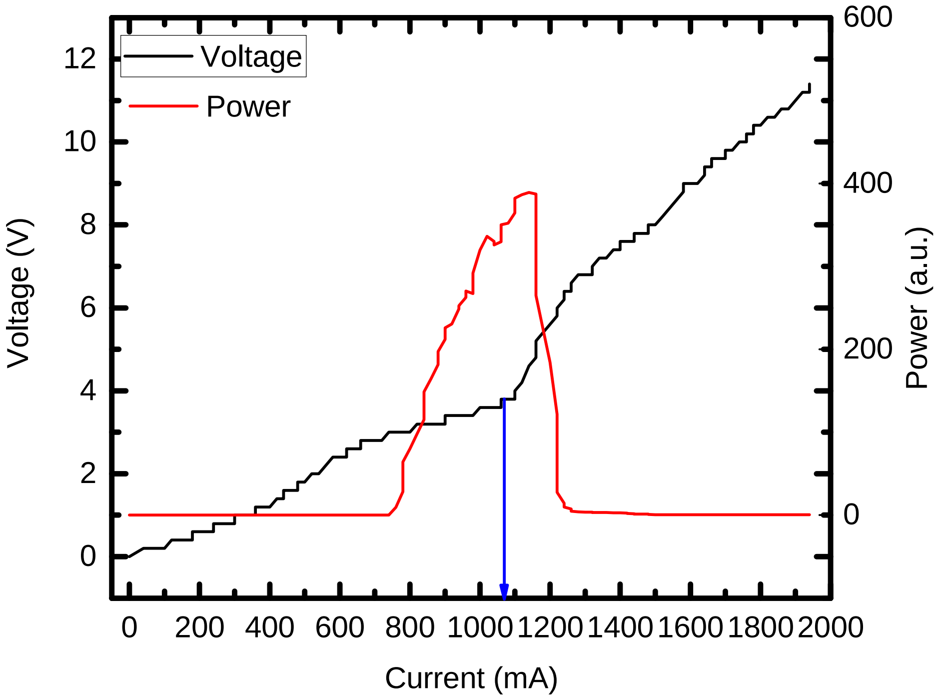

Figure 5-8 LIV curve of the studied THz QCL.

The QCL was powered by a 10-kHz, 2% duty cycle pulse train, which was modulated by a 167-Hz square wave.

5.3.2 Setup system and measurement method

The radiation emitted by the QCL was coupled into the Schottky diode detector using a pair of off-axis parabolic mirrors. DC bias was supplied to the diode, and was separated from the IF output using a bias-Tee. The IF signal was amplified using a low noise pre-amplifier and was connected to a spectrum analyser. The dc side of the bias-tee was also connected to a lock-in amplifier to monitor the video response of the diode. The setup of the measurement is shown in Figure 5-9.

The signals obtained from the spectrum analyser and lock-in amplifier were used to study the free-running QCL spectrum linewidth, thermal equilibration speed, and refractive index.

5.3.3 Spectral linewidth

The intrinsic linewidth of a laser can be calculated from the Schawlow–Townes law:

$$\Delta\nu_{Laser} = \frac{4\pi h\nu(\nu_c)^2}{P_{out}} \qquad (5.1)$$

In which, $\Delta\nu_{Laser}$ is the half width at half-maximum amplitude linewidth of the laser, ν_c is the half width of the resonances of the laser resonator, P_{out} is the laser output power and ν is the laser centre frequency. For a THz QCL, the intrinsic linewidth can be 1–10 kHz [68-70]. In this chapter, the linewidth is measured using a Schottky diode detector and a spectrum analyser and we find the free running QCL linewidth of a THz QCL is around 3 MHz. In 2003, A. Barkan *et al.* reported that the linewidth of a free running QCL can be around 30 kHz in a real time measurement and 21 MHz in a long-term averaged measurement [105]. They also used the beat signal output from a THz mixer, but used a pair of gas lasers to generate the local oscillator reference. They attributed the 21-MHz long-term linewidth to a 0.2 K variation in the QCL temperature [105].

In this section, the long-term average linewidth of a free running THz QCL was tested using a much simpler system as shown in Figure 5-9. The beatnote was recorded at a range of temperatures and currents. A typical spectral measurement is shown in Figure 5-10. During the measurement, the QCL was powered by a 10-kHz, 2% duty-cycle pulse train.

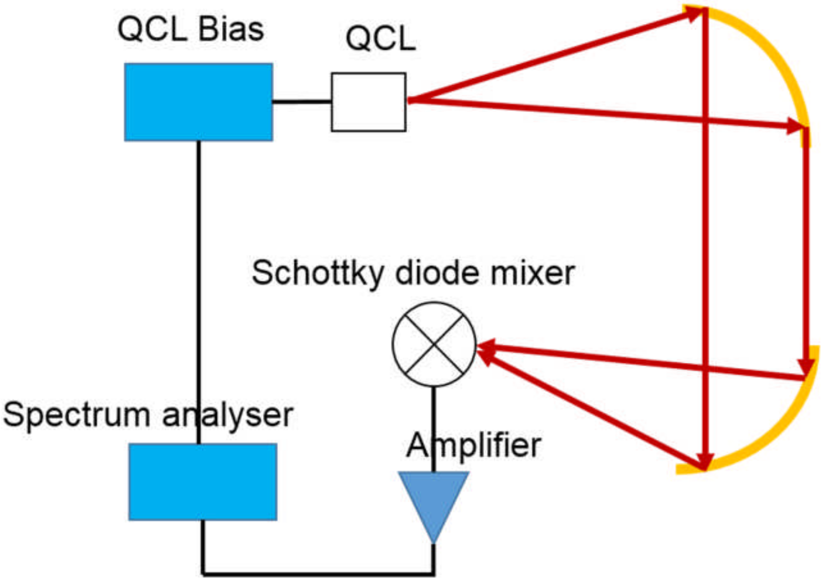

Figure 5-9 Setup of Schottky diode mixing apparatus

The beatnote between neighbouring FP modes of the multimode QCL was found to be 8.9875 GHz, as shown in Figure 5-10. The recorded beatnote was found to change slightly when the temperature or bias were changed. The instantaneous linewidth of the beatnote is shown to be at the kHz level.

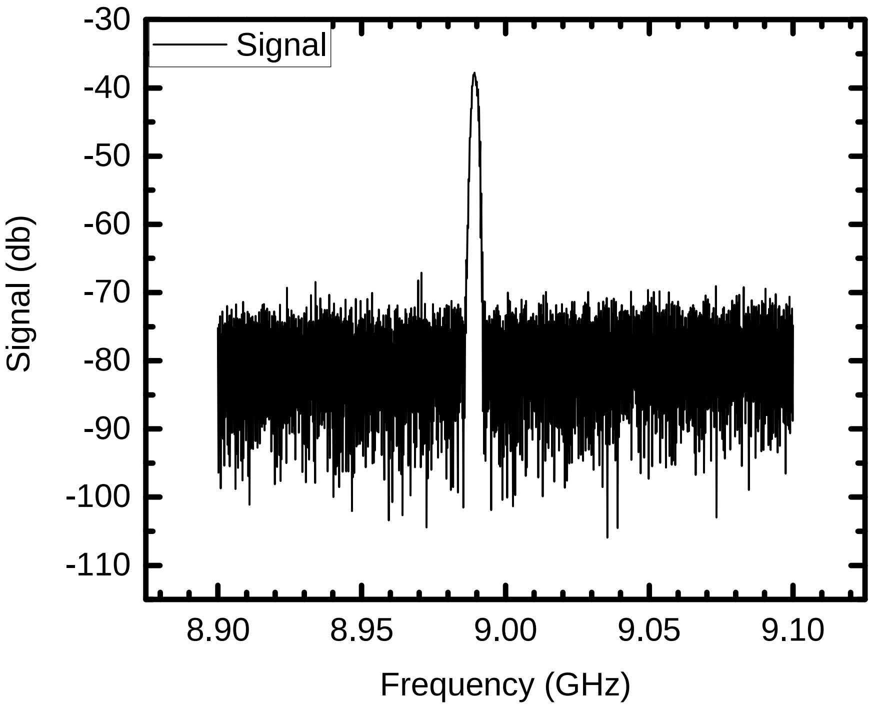

Figure 5-10 The beatnote recorded at 20 K when the QCL is driven by a CW 920-mA current

In order to study the time variation of the beatnote, the IF spectrum was recorded every 1 μs for 100 μs using a time-gated spectrum analyser. A spectrogram showing the variation in spectral intensity over time is shown in Figure 5-11. For each spectral measurement, a span of 8.9–9.1 GHz was used, with a resolution bandwidth of 0.2 MHz.

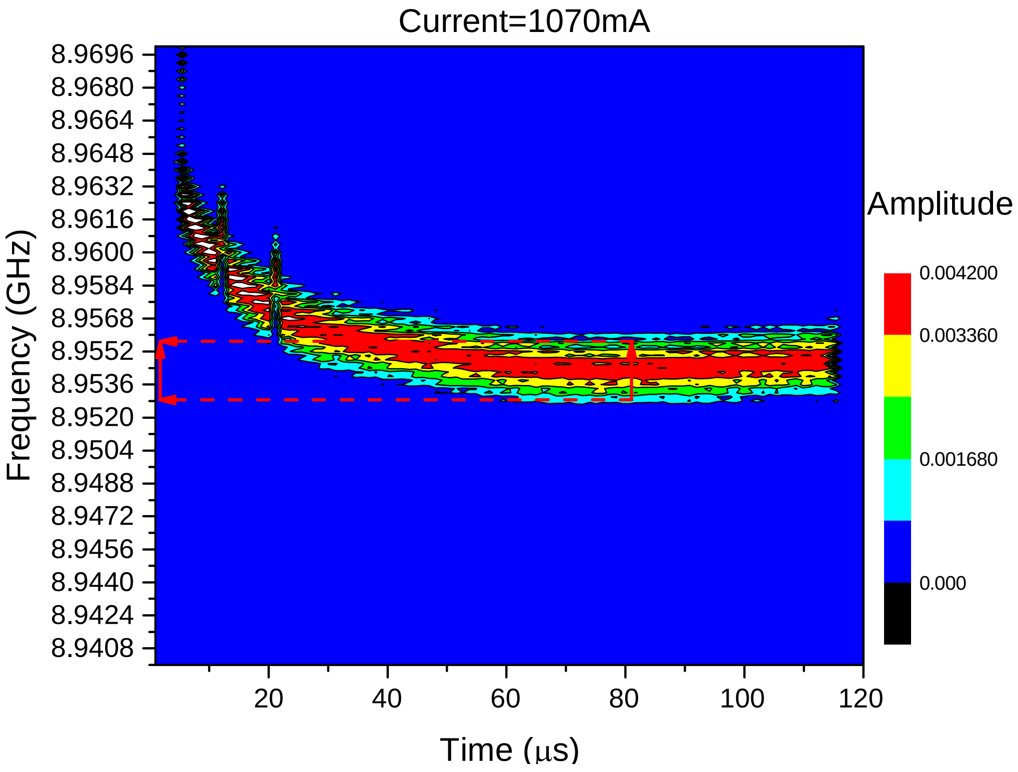

Figure 5-11 Spectrogram showing variation in QCL beatnote over time. This measurement is taken under 20K

The peak of the IF signal is shown in red in Figure 5-11, and the IF linewidth can be measured as the distance between the two cyan layers, as indicated by the red arrow. The length of the arrow is 3 MHz, which can be used to represent the linewidth of the IF signal.

Since the IF signal is the difference frequency between two neighbouring FP modes (as shown in the FTIR spectra in Figure 5-7), the linewidth of the IF signal corresponds to the THz QCL emission linewidth. Therefore, the linewidth broadening of the THz QCL by electrical, thermal, and mechanical noise is found to be around 3 MHz, in agreement with previous experimental results [105]. The linewidth of the free running QCL is broader than LOCUS' requirement (<1MHz). This can be improved by applying more stable current source containing a feedback loop or a better cooler which provides more stable temperature and better mechanical stability.

5.3.4 Thermal equilibration time

When the QCL is switched on, it takes a while to reach thermal equilibrium. As shown in Figure 5-10, the IF output initially covers a broad bandwidth over the first few microseconds, and settles to a steady-state value of 8.95 GHz after 20 µs. In this section, the thermal equilibration time is studied.

For each bias condition, the IF output was recorded at 1 µs intervals and a Gaussian fitting was used to find the peak IF frequency at each time step. The peak IF frequency was plotted as a function of time in Figure 5-13, Figure 5-14 and Figure 5-15 for the QCL biased at a range of currents within its 750–1200 mA dynamic range (see LIV curve in Figure 5-8). The peak emitted power occurs at 1080mA, as indicated by the blue arrow in Figure 5-8.

Figure 5-12 shows that at the QCL threshold current (750 mA), the peak in the time-averaged IF signal is broad and poorly-defined, while Figure 5-13 shows that the peak frequency varies randomly over time. When the QCL is biased by threshold, the emission is affected very heavily by working temperature, causing a broad IF signal.

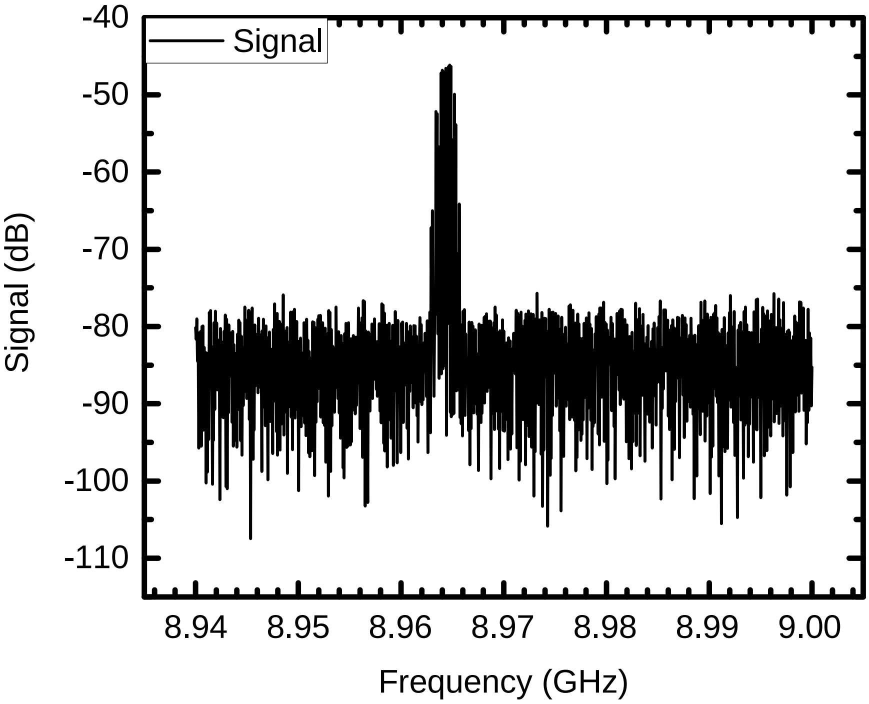

Figure 5-12 Recorded IF signal when QCL is biased by 750-mA current

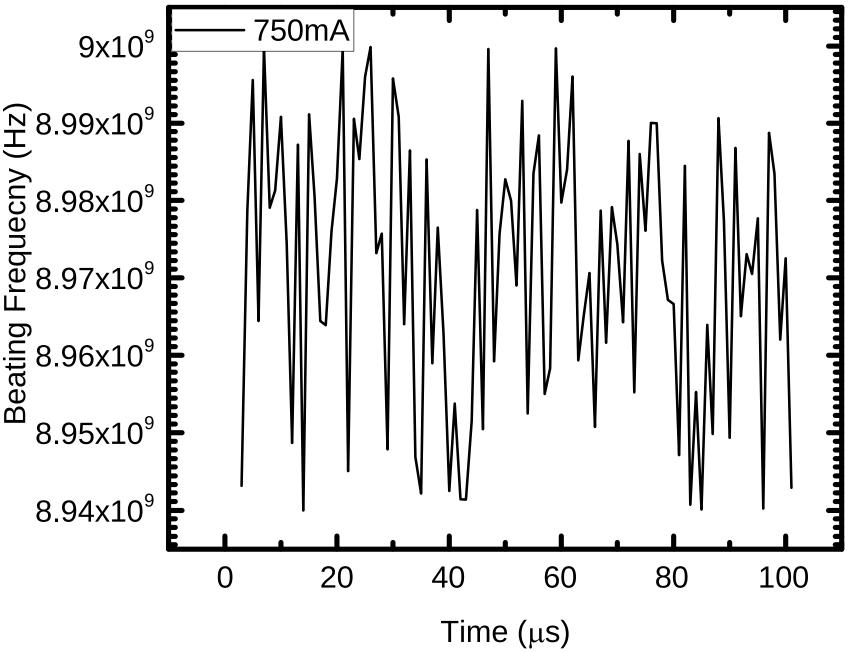

Figure 5-13 Time variation in QCL beatnote over time at 750-mA bias . The heat-sink temperature is the same as that in the LIV curve (20 K). 750 mA is the threshold current of this laser.

At higher currents, however, the IF peaks are clearer and an exponential decay is found to fit the time variation closely. Figure 5-14 and Figure 5-15 show that in each case, the IF peak is random when the QCL is initially switched on, owing to current fluctuations, but stabilises at a certain frequency after a stabilisation time. The reason for the unstable period is the non-equilibrium working temperature of the QCL. Heat accumulates inside the QCL when the bias is switched on and the device finally achieves thermal equilibrium. The refractive index of the QCL is highly dependent on the working temperature, which in turn affects the IF. As such, the variation in IF can be related to the thermal equilibration of the device.

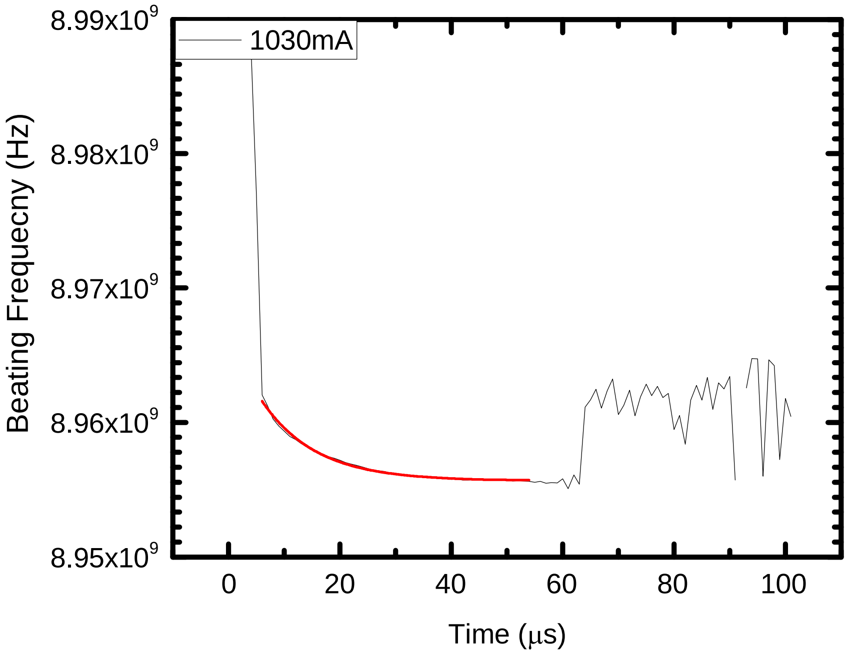

Figure 5-14 Time variation of QCL beatnote at 1030 mA bias . The heat sink temperature is 20 K.

Based on this assumption, an exponentially decaying curve described by Equation 5. is applied to fit the IF frequency–time relationships in Figure 5-14 and Figure 5-15. This curve is commonly used to fit heat diffusion processes. The fitted value of τ is the time taken by the process to achieve an equilibrium.

$$f = f_0 + A \times \exp\left(-\frac{t - t_0}{\tau}\right) \qquad (5.2)$$

Where f is the IF frequency, f_0 is a constant depending on the final stabilized IF frequency, A is another constant giving the size of the fluctuation, t is the time elapsed, t_0 is the time at which the decay starts and τ is the equilibration time.

The fitted exponential decay function for Figure 5-14 is $f = 8.956 \times 10^9 + 6.179 \times 10^6 \exp(-(\mathrm{t} - 5.607)/9.688)$. The thermal equilibration time is, therefore, 9.688 µs. The decay curves for each frequency were fitted using the same decay function, and the extracted parameters are presented in .

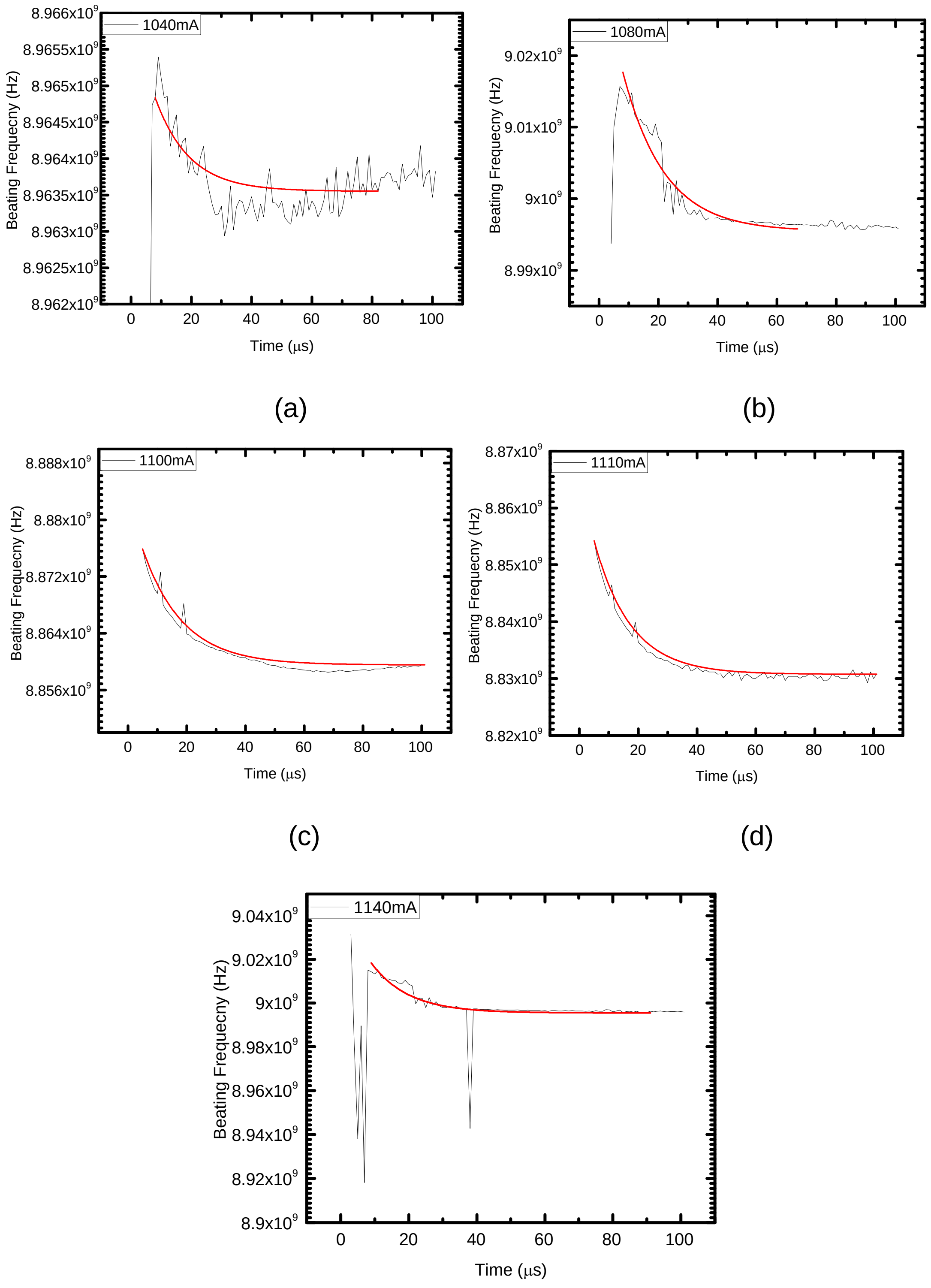

(a) (b)

(c) (d)

(e)

Figure 5-15 Time variation of QCL beatnote at a heat-sink temperature of 20 K . The QCL was biased at (a) 1040 mA, (b) 1080 mA (c) 1100 mA, (d) 1110 mA and (e) 1140 mA.

From the fitted f_0 values, we can conclude that the IF is around 8.95 GHz in each case, and equilibrium time is around 10 µs. The equilibration time varies slightly with respect to bias and is plotted in Figure 5-16.

Table 5-3 Fitted parameters for different biases

I (mA)	f_0 (GHz)	A (MHz)	t_0 (µs)	τ (µs)
1030	8.956	6.179	5.607	9.688
1040	8.964	1.286	8	11.277
1080	8.995	20.58	9.106	14.006
1100	8.960	16.35	5	13.731
1110	8.831	23.48	5	12.456
1140	8.995	37.57	3.653	10.808

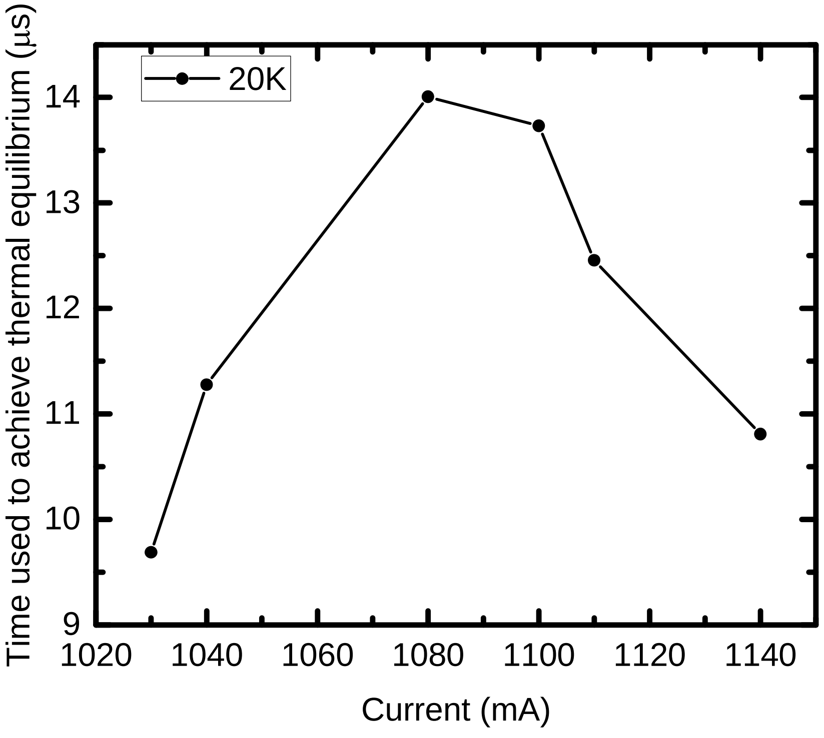

Figure 5-16 Time taken for QCL to achieve thermal equilibrium

Figure 5-16 shows that the peak equilibration time occurs at 1080 mA, which is also the bias that gives peak power in Figure 5-8.

The equilibrium time depends on the temperature difference (∇T) between the QCL active region and the heat-sink temperature (20K). The relationship of the rate of heat increase, υ and temperature difference (∇T) is given by [159]:

$$\upsilon = \frac{\partial T}{\partial t} = \alpha \frac{\partial^2 T}{\partial x^2} \qquad (5.3)$$

In which, α is a constant depending on the thermal conductor, x is the thickness of QCL. The LIV curve of the studied QCL is given by figure 5-8. A possible explanation could be the sharp increase of LO phonons that may occur within a QCL when the subbands come into alignment, as shown Figure 5-17 [160]. This effect is likely to cause a sharp increase in thermal resistance (R), and hence a longer equilibration time, owing to the increased phonon–phonon scattering in the active region.

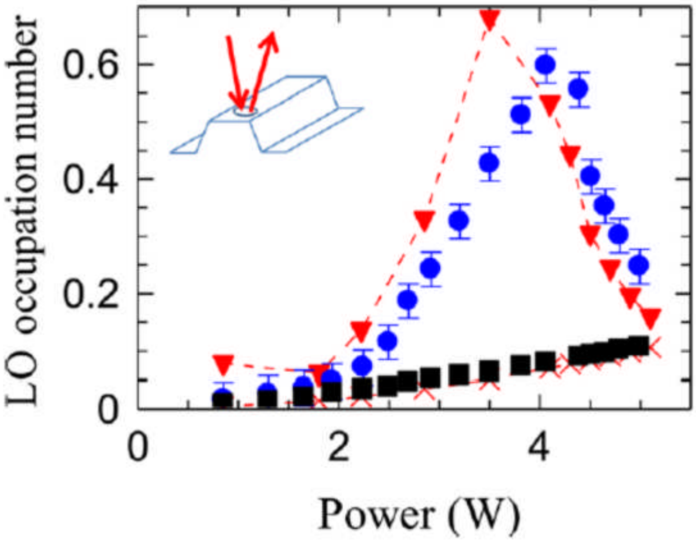

Figure 5-17 Longitudinal optic phonon occupation numbers in a QCL [160]. The occupation number is shown as red triangles and measured as blue round points at different input electrical powers.

The QCL study with Schottky diode detector provides a method to probe the equilibrium speed of THz QCLs, which could help to improve the thermal performance of future devices.

5.3.5 Refractive index

The refractive index of a THz QCL based on GaAs is around 3.5 in the THz range. But the exact value depends on the waveguide geometry and alloy composition in the device, the doping level of the material, the lasing frequency of the QCL, and the QCL working temperature. At the same time, it is a very important parameter to design waveguides, such as those based on refractive index modulation in photonic lattice structures. In the previous two sections, the QCL beatnote has been analysed. In this section, the refractive index is obtained from the IF signal recorded from the spectrum analyser. The refractive index of an FP cavity may be obtained from the beatnote using Equation 3.3 as:

$$f_{\text{beat note}} = \frac{c}{2nL}; \qquad n = \frac{c}{2f_{\text{beat note}}L} \tag{5.4}$$

in which, *c* is the speed of light in vacuum, *n* is the refractive index of QCL, *L* is the length of the QCL and $f_{\text{beat note}}$ is the beatnote frequency. The length of the studied QCL was 4.429 mm.

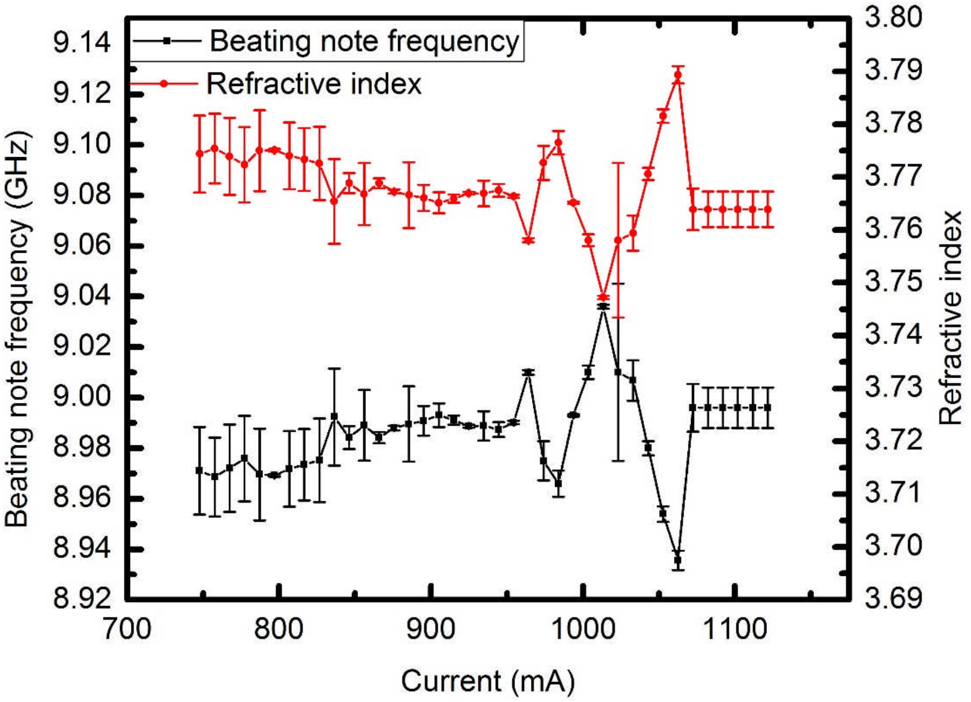

Figure 5-18 The measured beatnote frequency at each bias (black line and symbols) and the calculated refractive index (red line and symbols).

The beatnote frequency for each bias varies as shown in Figure 5-18 along with the calculated refractive index. In each case, the refractive index is around 3.77, which is slightly higher than the simulated value given as Figure 5-20. The calculated refractive index shows a fluctuation with respect to bias. This may be caused by the change of QCL temperature or intersubband alignment effects [163]. At low current bias (750–970 mA), the refractive index changes slightly through heating. We then observe two peaks which are caused by mode hopping, as shown in Figure 5-7. For example, the spectrum of the QCL is centred at 2.263 THz when the bias is 950 mA and hops to 2.231 THz when the bias is changed to 950 mA. The frequency change is much larger than that caused by current tuning.

The variation in refractive index with respect to temperature was also studied with the same method. An increase in refractive index with respect to temperature can be observed in Figure 5-19. This agrees with previously reported experimental results given as figure 5-20 [161, 162].

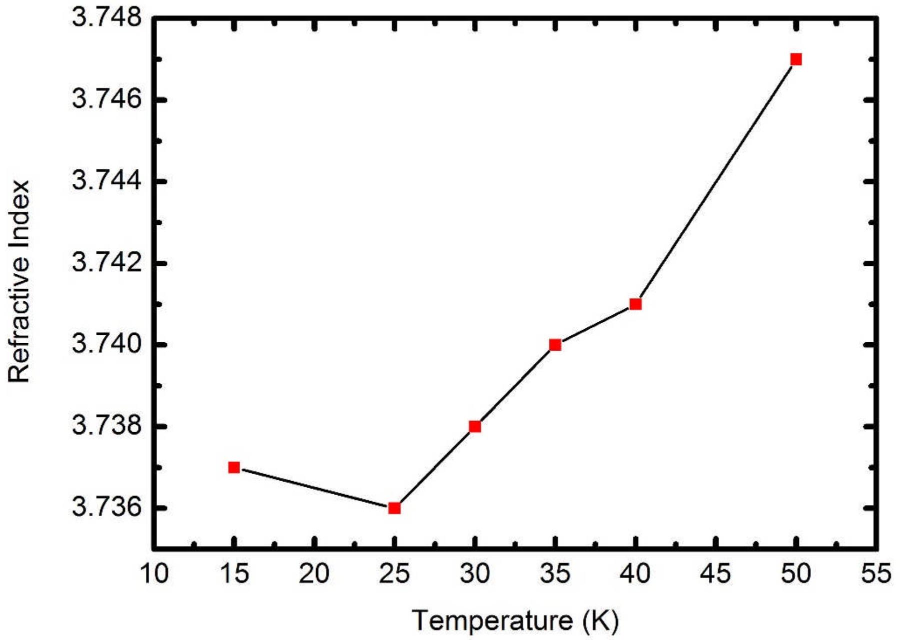

Figure 5-19 Calculated refractive index for different temperatures

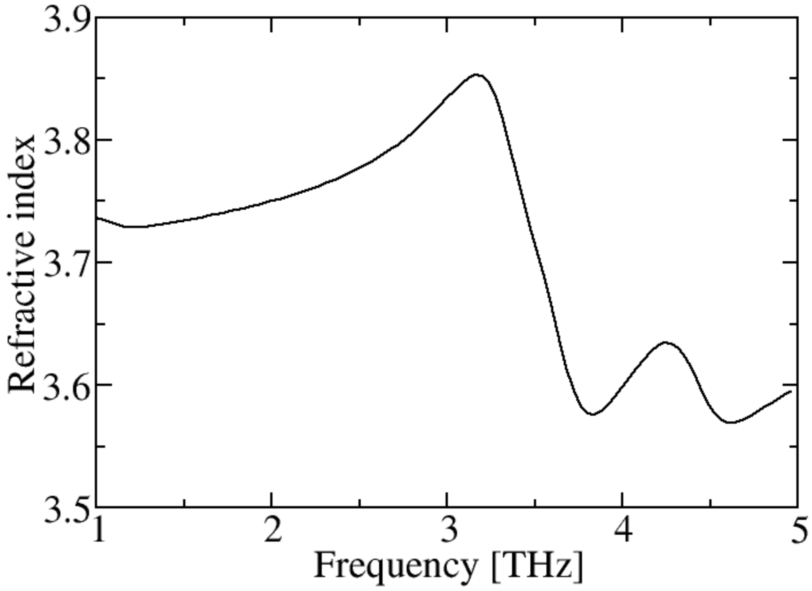

Figure 5-20 Simulated refractive index for GaAs in the THz range . This figure is provided by Alex Valavanis, University of Leeds.

5.4 Conclusion

In this chapter, two components of the LO: waveguide integrated THz QCL and a heterodyne Schottky diode detector have been investigated. The waveguide integrated THz QCL was characterized in terms of its LIV, power performance and far field beam profile. The measured result was compared with the corresponding QCL without an integrated waveguide. The conclusion from the comparison is that the integrated waveguide will not affect the QCLs performance, such as the highest working temperature, and LIV. At the same time, it can significantly improve the far field beam profile of the embedded double metal THz QCL. The far field beam profile divergence is reduced from 120° to 20° by the integrated waveguide. This work provides an effective method to handle the poor far field beam profile performance of double metal THz QCL.

A Schottky mixer for heterodyne detection was used to study a THz QCL in order to further understand the possible information that can be obtained from the signal given by the detector. The mixed signal of two neighbouring modes from the studied QCL were investigated. The linewidth of a free running THz QCL emission was studied and was shown to be allow measurement of the linewidth of THz emission by comparing the measured result with previously published results. The heterodyne signal from the Schottky diode mixer was also used to study the IF, and the thermal equilibration time for the QCL was obtained.

Finally, this study also provides a method to measure the refractive index of THz QCL. The measured refractive index of the studied QCL was around 3.77, which agrees with the values measured by other groups. The high definition of the measurement also gives a possibility to observe frequency change of THz QCL at a very high resolution, which is possibly a powerful complementary method to THz radiation frequency measurement using FTIR spectrometry.

Chapter 6THz gas spectroscopy with a photomixer and QCLs

6.1 Introduction

Previous chapters have described the fabrication and characterisation of THz QCLs for use as LOs. In this chapter, the suitability of the QCLs developed in this work for gas spectroscopy is assessed. This includes demonstrating the ability to resolve individual absorption lines of gases clearly, and to assess the sensitivity and tuning bandwidth of the system.

THz spectral data for common gases is available in the NASA Jet Propulsion Laboratory (JPL) molecular spectroscopy catalogue [104] which is also based on measurement result, and a broadly tuneable CW THz photomixer system has been used for initial system validation. The simulated absorption spectrum is obtained from the JPL catalogue data using a MATLAB program developed by Dr Alexander Valavanis, which takes pressure and temperature broadening into account.

An important factor for consideration in observations of the MLT is the low pressure compared with measurements in the lower atmosphere. This results in narrow spectral linewidths and small absorption cross-sections. In order to study the detection limitation, THz absorption in a low-pressure gas cell is investigated. Methanol is a good choice of gas for this preliminary investigation because it has a rich set of absorption lines in THz range, allowing it to be used for a wide range of QCL devices. These measurements will underpin future study of the MLT species targeted by LOCUS.

For QCL measurements, direct detection of transmitted radiation, using a pyroelectric detector has been carried out at this stage. However, a heterodyne detection scheme will need to be implemented in future to further improve the quality of detection and demonstrate the techniques required for LOCUS.

6.2 THz gas spectroscopy theory

Absorption spectroscopy describes a set of methods in which the absorption of radiation in a sample is analysed, for a range of different frequencies. The frequencies at which photons are absorbed depends on the sample being studied, and therefore the absorption spectrum can provide information about the microscopic structure of the sample, such as molecular vibrational and rotational modes, electron energy level separations and so on. The intensity of the absorption depends on the strength of the interaction and the concentration of the sample. As such, absorption spectroscopy provides a means both to detect and measurement the concentration of samples.

The whole range of the electromagnetic spectrum can be applied to perform absorption spectroscopy. In THz gas spectroscopy, the molecular rotational modes (and possibly molecular vibrational modes) provide the strongest interactions.

When radiation passes through an absorbing medium, the absorbance, A ,can be calculated using the Beer–Lambert law [164, 165]:

$$A = \log\left(\frac{I_0}{I}\right) = 2\log\left(\frac{E_0}{E_{\mathrm{THz}}}\right) \tag{6.1}$$

in which E_0 is the measured field strength of a reference signal scan (i.e., without the sample) and E_{THz} is the strength of the field after passing through the sample. A spectrum can be obtained by plotting the absorbance as a function of frequency. The absorption coefficient, α (in units of cm^{-1}) is given by:

$$\alpha = \frac{A}{L} \tag{6.2}$$

in which, L is the length of gas cell.

6.2.1 Spectral lineshape

THz absorption occurs when gas in a lower energy state absorbs energy and transitions to a higher energy state. In principle, the absorption line should be infinitely sharp because the energy difference between two quantum energy level of the gas is well defined. However, the measured absorption spectrum has a far broader linewidth. There are three major types of broadening mechanisms:

- **Natural broadening:** this is caused by the quantum uncertainty in the two quantum energy states involved in the absorption.

- **Collisional broadening**: gas molecules collide with each other and with the walls of the gas cell. These collisions can distort electron energy levels.
- **Doppler broadening**: this is caused by thermal motion of gas molecules in the gas cell. The high speed of gas molecules makes the observed absorption frequency shift. Since all the molecules are moving in random directions, this gives redshift and blueshift at the same time, which contributes the linewidth broadening.

The broadened lines can take a range of shapes, which can each be characterised in terms of their 'Full width at half maximum' (FWHM), expressed in units of the horizontal axis or in percent of the peak position [207]. Figure 6-20 illustrates the FWHM of a single peak.

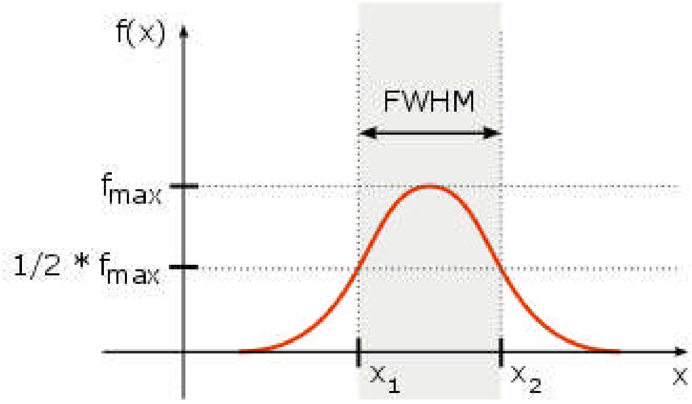

Figure 6-1 The definition of full width at half maximum (X_2-X_1) [13]

The shapes of spectral peaks depend on the type of broadening. Natural and collisional broadening can be described by a Lorentzian lineshape:

$$y = y_0 + \frac{2A}{\pi}\left(\frac{w}{4(x-x_0)^2 + w^2}\right) \qquad (6.3)$$

In which y is the absorption, y_0 is an offset, A is the peak absorption, x is the frequency, x_0 is frequency at the peak absorption and w is the FWHM of the fitted peak. Doppler broadening, however is described by a Gaussian shape [167]. In general, all three broadening effects occur at the same time, and a more general Voigt lineshape is needed.

The Doppler broadening linewidth can be calculated using [167]:

$$\Delta f(FWHM) = 2\sqrt{\frac{2kTln2}{m}}f_0 = 7.17 \times 10^{-7} f_0 \sqrt{\frac{T}{M}} \tag{6.4}$$

In which, *k* is Boltzmann constant, *T* is temperature and Δf is the broadening for frequency *f*. *M* is the molar mass (g/mol).

The pressure broadening effect is given by [167]:

$$w = w_0 \left(\frac{p}{p_0}\right) \left(\frac{T_0}{T}\right)^n \tag{6.5}$$

in which *w* is the value of FWHM, w_0 is the value of FWHM at a reference temperature T_0 and pressure p_0 and *n* is an empirical constant depending on different gas absorption peak. Therefore, the linewidth of an absorption peak should increase linearly with gas pressure at a given temperature.

6.3 Gas spectroscopy study using THz photomixers

6.3.1 CW THz radiation generation by photomixers

A THz photomixer is based on a heterodyne mixing method: two near-infrared laser diodes with different emission frequencies illuminate the surface of a nonlinear crystal, as shown in Figure 6-2 [168]. Carrier oscillations are generated in the crystal with a frequency equal to the difference between the two laser diodes. This heterodyne THz signal is radiated by an antenna structure on the device.

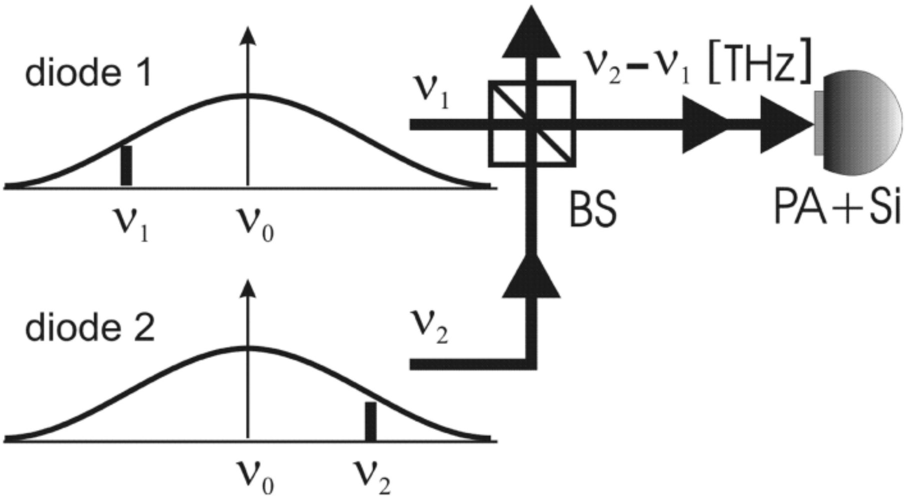

Figure 6-2 THz generation using a photomixer

. Two infrared diode lasers emit radiation at frequencies, $\boldsymbol{\nu_1}$ and $\boldsymbol{\nu_2}$, which are each near to the same central frequency $\boldsymbol{\nu_0}$. PA is the THz antenna and Si is a silicon lens [168].

6.3.2 Coherent detection of THz radiation

A second photomixer is used for coherent detection of the THz signal [169]. The same pair of laser diodes, is also focused onto the second antenna and a periodically modulated photocurrent can be detected in response. The intensity of the photocurrent I_{photo} is given by [168, 170, 171]:

$$I_{\text{photo}} \propto E_{\text{THz}} \cdot P_{\text{Infrared}} \cos\left(\frac{\omega_1 - \omega_2}{c}\right) \Delta d \tag{6.6}$$

In which P_{Infrared} is the incident infrared power, $\omega_1 - \omega_2$ is the angular frequency difference of the two laser diode sources, and Δd is the travel difference of the two-part heterodyne wave.

A schematic illustration of the detection principle, and of the system used in the present work is given in Figure 6-3(a) and (b) respectively. The first photomixer emits radiation with frequencies ranging from 500 GHz to 2.0 THz. The sample gas is contained within a 26 cm long gas cell with an outer diameter of 3.46 cm. On both sides of the gas cell are 4mm-thick polymethylpentene- (TPX) windows with a 3-cm clear diameter. The whole system is sealed within a plastic box, which is purged with dry N_2, to avoid water absorption.

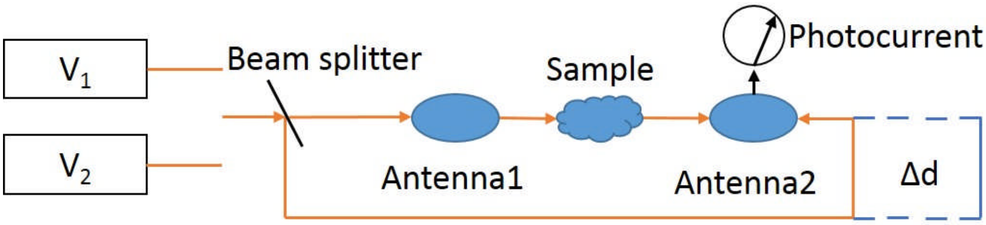

(a)

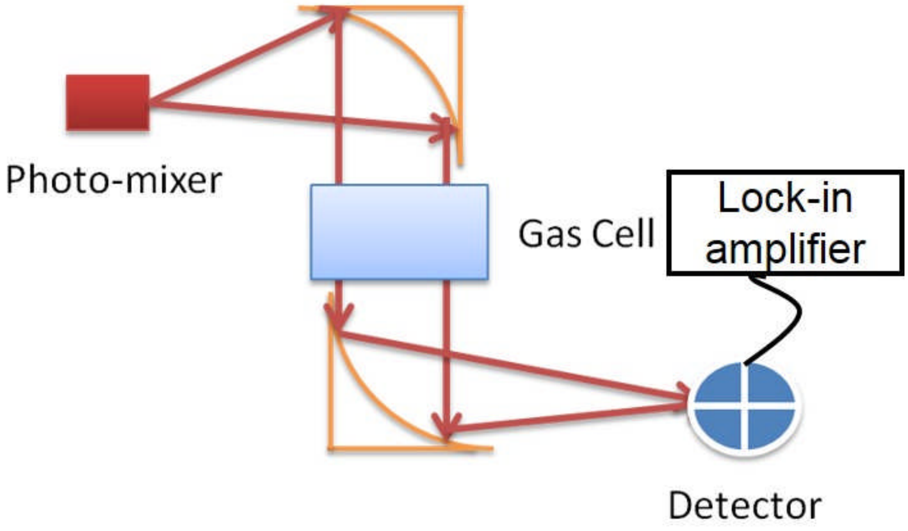

(b)

Figure 6-3 Schematic illustration of coherent detection using a photomixer

(a) illustrates the principle of coherent detection. Radiation from the incident laser diodes, with frequencies $\boldsymbol{\nu_1}$ and $\boldsymbol{\nu_2}$, is split into two paths using a beam splitter. One part of the radiation is focused onto antenna 1, for THz wave generation and the other part is focused onto antenna 2, which acts as a THz detector. The time delay of the radiation determined by the difference in path-length, which can be changed. (b) shows the apparatus used in the measurements in the present work. The detector is a second photomixer, from which a lock-in amplifier records the modulated photocurrent.

6.3.3 System calibration

When the measurement is taken, a LabVIEW code controls the bias (and hence emission frequency) of the diode lasers, resulting in heterodyne frequencies between 1400 and 2000 GHz being emitted by the photomixer. The heterodyne signal passes through the gas cell and is focused onto the second photomixer. This photomixer generates a photocurrent, which is proportional to the THz field strength. The time delay, *t*, between the THz generation and detection, is adjusted by increasing the difference in optical path-length Δd linearly. The photocurrent is measured 40 times with a 4 ps time delay, using a lock-in amplifier attached to the detector. A function of the form, cos(x), is fitted to the data and the amplitude of the fitted function, *A*, is taken to be proportional to E_{THz}.

Before any scan can be taken, calibration of the laser frequency must be performed first to account for the small variation between the set-point THz frequency and the frequency obtained from the photomixer measurements, as plotted in Figure 6-4. The fitted frequency is given by:

$$f_a = 0.9994 \times f_s + 2.3624 \text{ GHz} \tag{6.7}$$

in which, f_a is the fitted accurate heterodyne frequency and f_s is the frequency set by LabVIEW code.

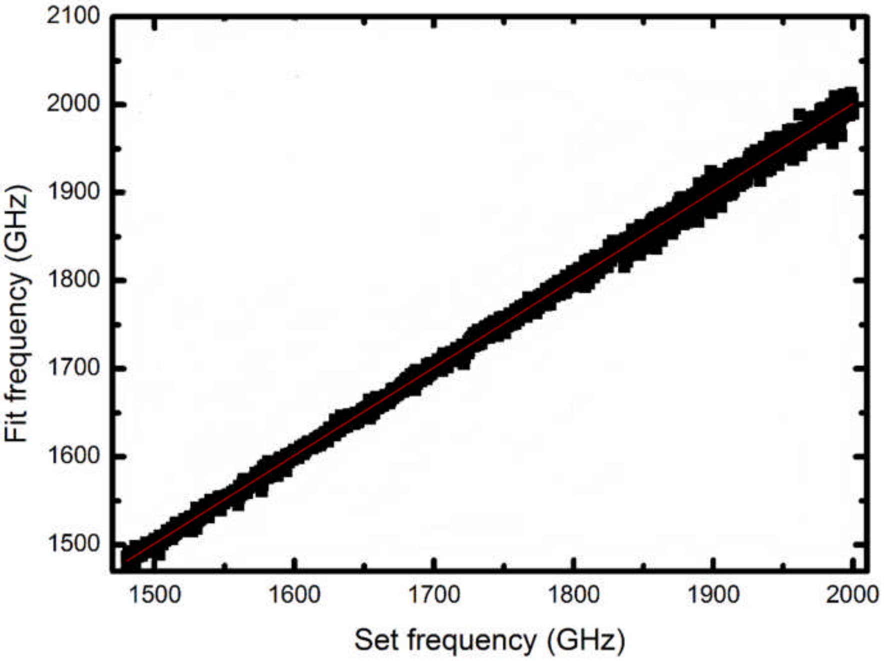

Figure 6-4 Calibration of the photomixer system

. The black data points are experimental measurements of the heterodyne frequency, and the red line is a linear regression to the data.

6.3.4 Spectroscopy of 95 Torr methanol

Since the gas absorption lines are narrow (~100 MHz) at low pressures, the step in laser frequency used in spectroscopy measurements must be small. For example, a 200 MHz resolution scan from 1–3 THz would require 4000 mins. This is not only time consuming but also introduces long-term stability issues, since environmental temperature and system alignment may drift significantly during the long scan time. As such, an initial scan was undertaken, using relatively high-pressure (95 Torr) methanol vapour. This gives broad, strong absorption lines which can be used to identify frequency ranges for further high-resolution study at lower pressures.

The radiative power of the transmitting photomixer varies significantly with respect to the heterodyne frequency of the two optical lasers. As such, before a real scan of the gas sample is taken, the reference power must be determined. The gas cell is evacuated using a molecular pump and then filled with dry N_2. The recorded reference signal is shown in Figure 6-5.

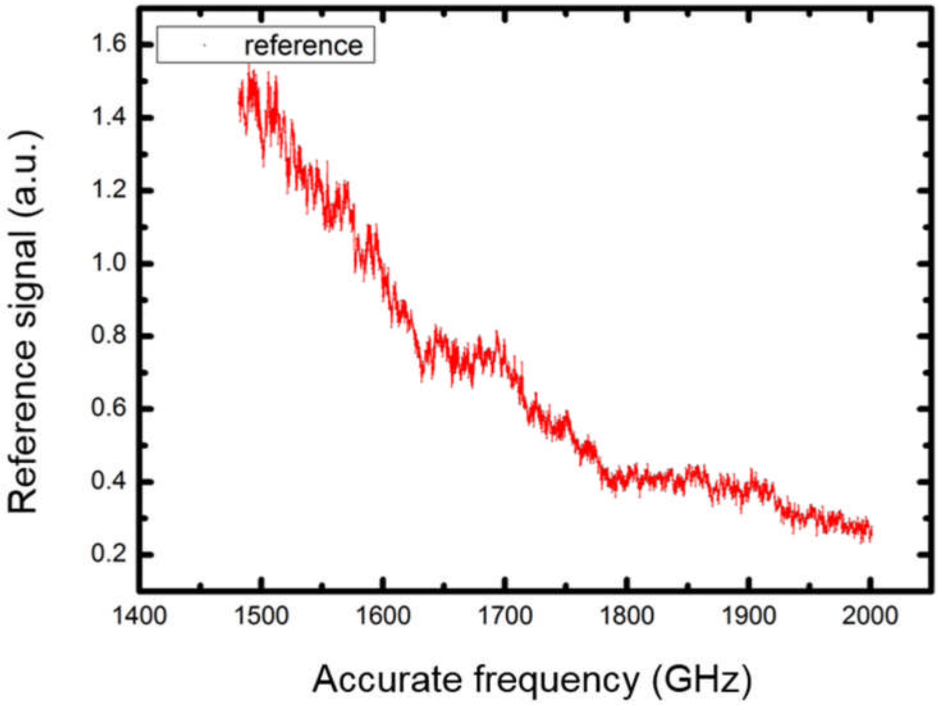

Figure 6-5 Reference scan for the photomixer system, obtained for a gas cell filled with N_2. The red line shows a low-pass filtered curve to the data.

The measurement was repeated, with the cell filled with methanol vapour at 95 Torr. During the two scans, all settings in the LabVIEW code remained the same. The recorded signal from LabVIEW code is given as figure 6-5. The red line in figure 6-5 is low pass filtered signal.

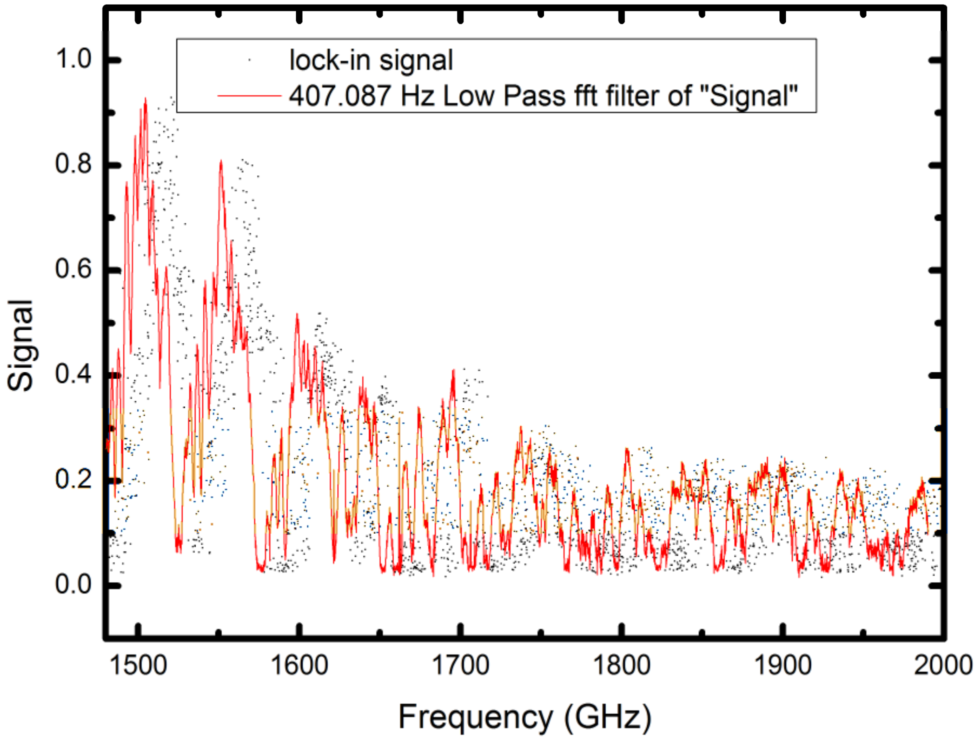

Figure 6-6 Transmitted signal for a 95 Torr methanol vapour cell

. The recorded black data points were low pass filtered to reduce noise from the detector and lock-in amplifier.

The absorbance spectrum was calculated using Equation 6.1, and is plotted as the red line in Figure 6-7. A simulated spectrum obtained from the JPL database [138] is included for comparison as the black line.

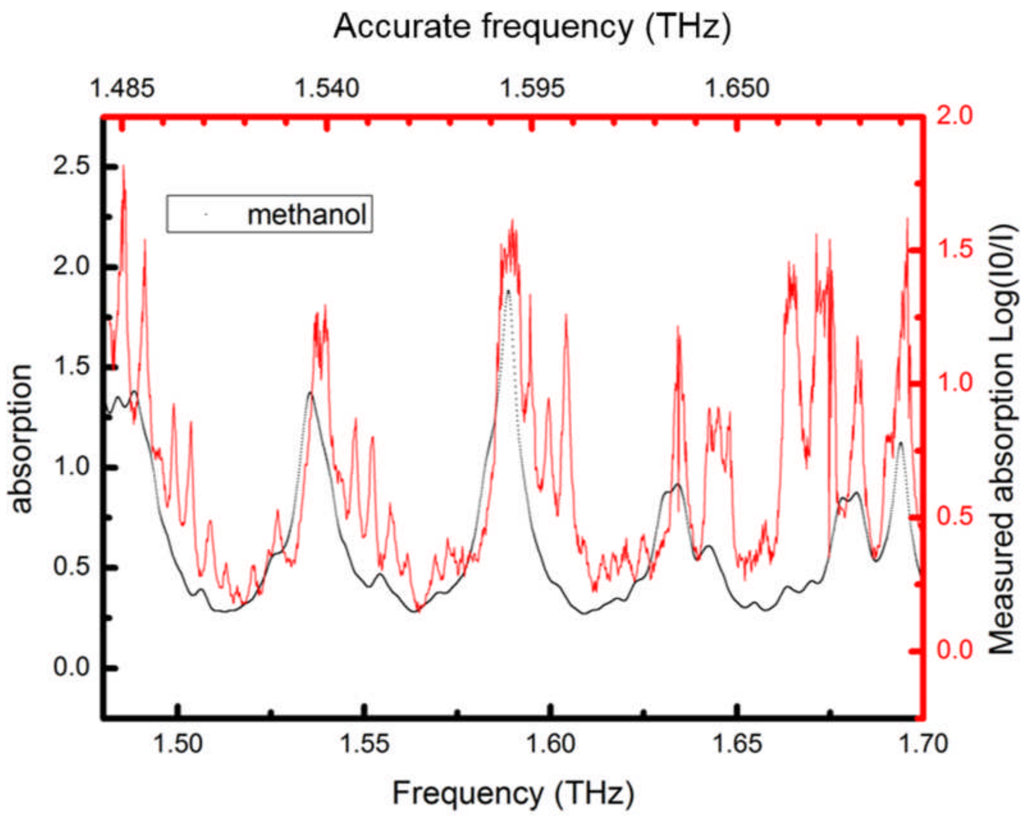

Figure 6-7 Absorption spectrum of 95 Torr methanol. The red line is calculated from the photomixer measurements and the black line shows the simulated spectrum from the JPL database [138].

The photomixer measurements show more spectral lines than the simulated absorption. These may be methanol absorption lines that have not been included in the JPL catalogue, or absorption lines of other species such as water vapour. Additionally, the periodic features in the spectrum may be caused by the periodic change in transmission from two gas cell windows. The Airy formula [172] is used to describe this phenomenon:

$$T = \frac{1}{1 + F\sin^2(2\pi Lnf)} \tag{6.8}$$

Where F is a constant, L is the width of the two gas cell windows, n is refractive index of gas cell window, and f is the radiation frequency. So the transmission periodically changes with the change of nf.

6.3.5 Spectroscopy of 20 Torr methanol and water vapour

In order to study the sensitivity limit of the technique, the measurement was repeated at lower pressures. The gas cell was initially filled with 5 Torr methanol. However, no obvious absorption features were observed, due to the much weaker absorption (i.e., fewer gas molecules being present) at low gas pressure, resulting in a low signal to noise ratio. To compensate for this, the methanol pressure was increased to 20 Torr and the measurement was repeated. The transmitted signal is shown in Figure 6-8 and the calculated absorption spectrum is shown in Figure 6-9. The results show sharper lines than in the previous section, as expected from the reduced pressure broadening. The results also show good agreement with the data from the JPL database.

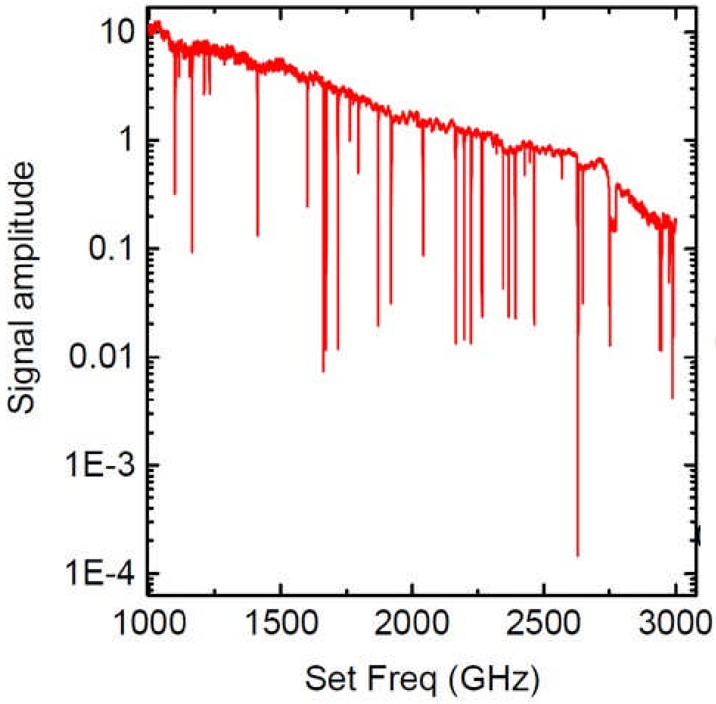

Figure 6-8 Transmitted signal from photomixer scan of 20 Torr methanol vapour from 1–3 THz.

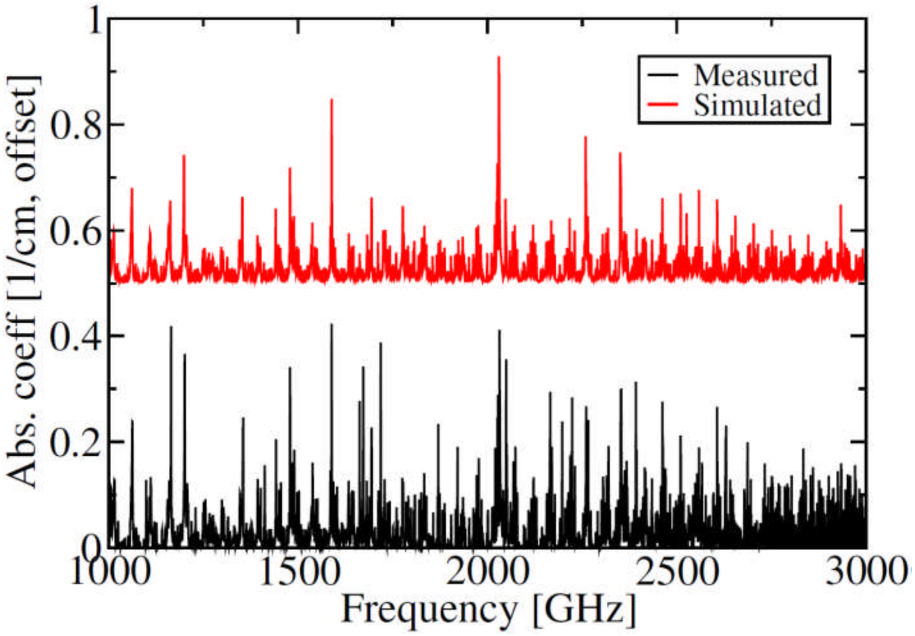

Figure 6-9 Absorption spectrum of 20 Torr methanol vapour. The black line is the calculated absorption coefficient from photomixer measurements and the red line is obtained from JPL database. The figure was provided by Dr Alexander Valavanis, University of Leeds.

A second measurement was performed, using water vapour instead of methanol. The gas cell was pumped to vacuum using a molecular pump first to ensure that there was no residual methanol in the chamber. Water vapour was then allowed into the gas cell through a needle valve. A Baratron pressure gauge was used to monitor the pressure, and the cell was sealed at of 20 Torr. The calculated absorption spectrum is shown in Figure 6-10.

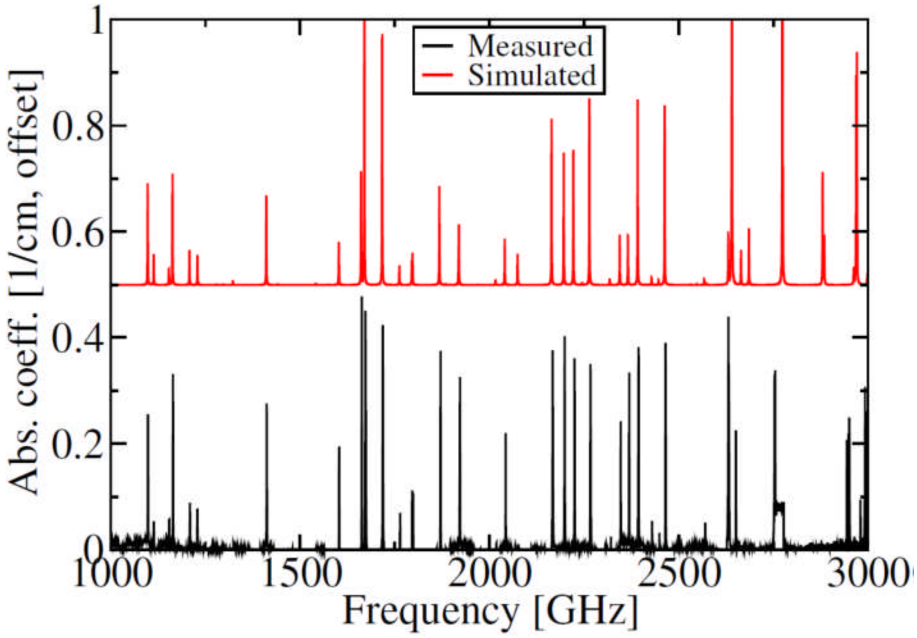

Figure 6-10 Absorption spectrum of 20 Torr water vapour. The black line is the calculated absorption coefficient from photomixer measurements and the red line is obtained from JPL database. The figure was provided by Dr Alexander Valavanis, University of Leeds.

There is a trade-off between frequency resolution of the measurement and scan speed. Here, a 2 THz span (1 THz to 3 THz) and a resolution of 200 MHz was used, which requires 4000-minute scan time. The results show that scans of both water and methanol vapour yield clear absorption lines with almost the same spectra as the JPL database. However, the reduction of photomixer power at frequencies higher than 2 THz is significant, and the bandwidth of this technique is effectively limited to 3 THz. Conversely, QCLs emit much greater power in this range. The following sections describe the use of QCLs for narrowband gas spectroscopy in this higher-frequency range.

6.4 Gas spectroscopy using a THz QCL

In this section, a free running QCL, lasing at 2.62 THz, is used to replace the photomixer source in Section 6.3 for gas spectroscopy. The noise level and also sensitivity limitation of this method are assessed.

6.4.1 Setup of the measurement

The system used for QCL spectroscopy is given in Figure 6-11. A single-mode THz QCL source is mounted within a continuous-flow liquid-helium cryostat. The THz radiation emitted by the QCL is focused on the detector using two off-axis parabolic (OAP) mirrors. The gas cell placed between two parabolic mirrors is 73 cm long, with the cross-section and windows as described in Section 6.3.2 . A pyroelectric detector is used as the receiver, which gives a voltage signal proportional to the THz power.

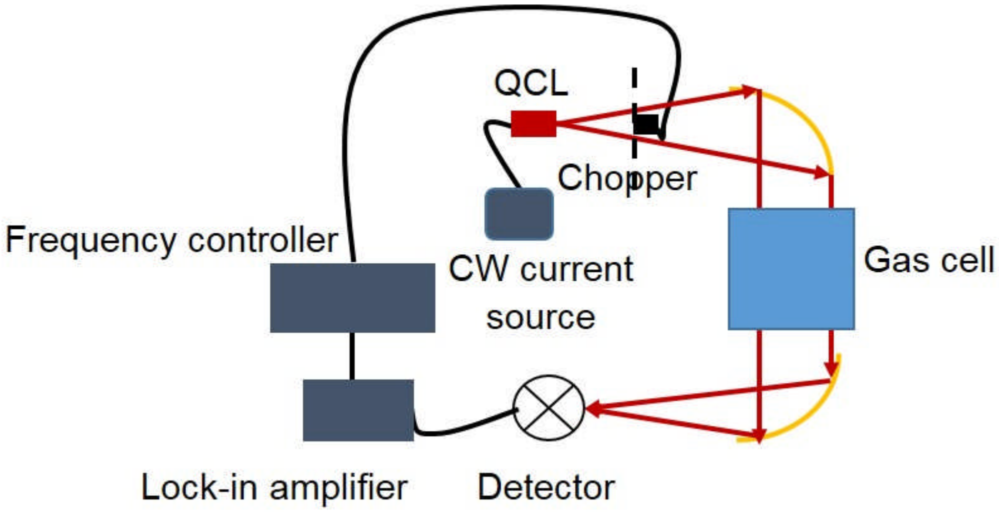

Figure 6-11 The setup of using a free running THz QCL to do methanol spectroscopy. The QCL is CW pumped and a chopper is applied to mechanically modulate the signal.

The THz QCL is biased by a continuous wave current source. The radiated THz wave is mechanically modulated at 20 Hz by a chopper, which is controlled by the frequency controller. This modulation frequency is also used for lock-in amplification of the detector signal.

During the measurement, a LabVIEW code is used to increment the QCL current by a fixed step size, and to record the bias on the QCL and the signal from the lock-in amplifier.

6.4.2 Development and characterization of the THz QCL used

A single mode 2.62THz PL-QCL, based on Leeds MBE wafer L1014, was used as the source in this system. This QCL was single mode, with continuous-wave operation and was continuously tuneable over the range of targeted absorption line frequencies. The device was initially processed into a single-metal Fabry–Pérot- (FP) ridge waveguide with a length of 1.85 mm and a width of 150 µm. The LIV characteristics and emission spectra of this FP device are shown in Figure 6-12 and Figure 6-13 respectively.

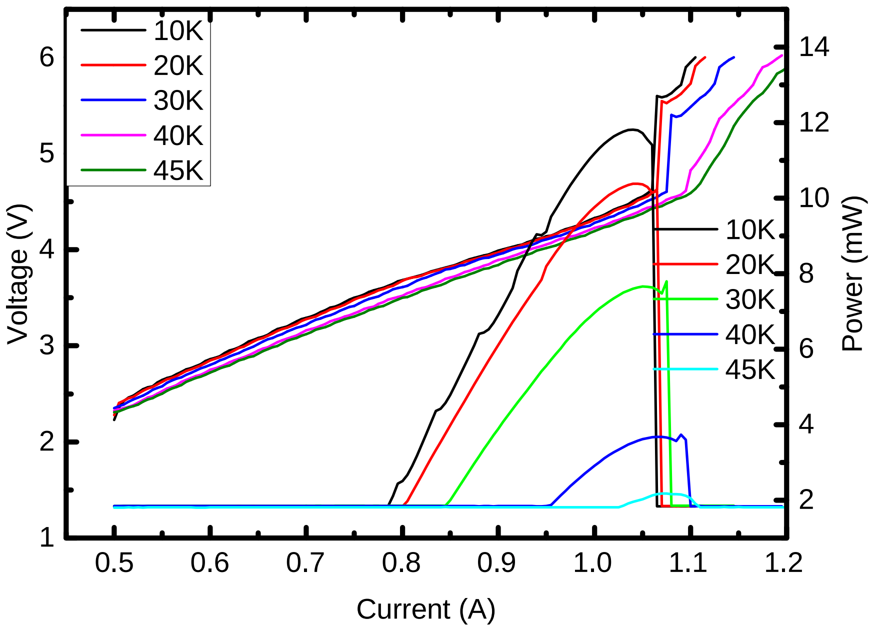

Figure 6-12 CW LIV curve of the FP QCL used to develop the PL device. The maximum working temperature for the FP laser was 45 K. The threshold current was 0.78 A at 10 K, and increased to 1.045 A at 45 K. The dynamic range of this device was 0.285 A at 10K and decreases to 0.085 A at 45 K. The FP laser was shown to lase across multiple modes, covering frequencies from 2.50–2.58 THz with a 2.55 THz central frequency.

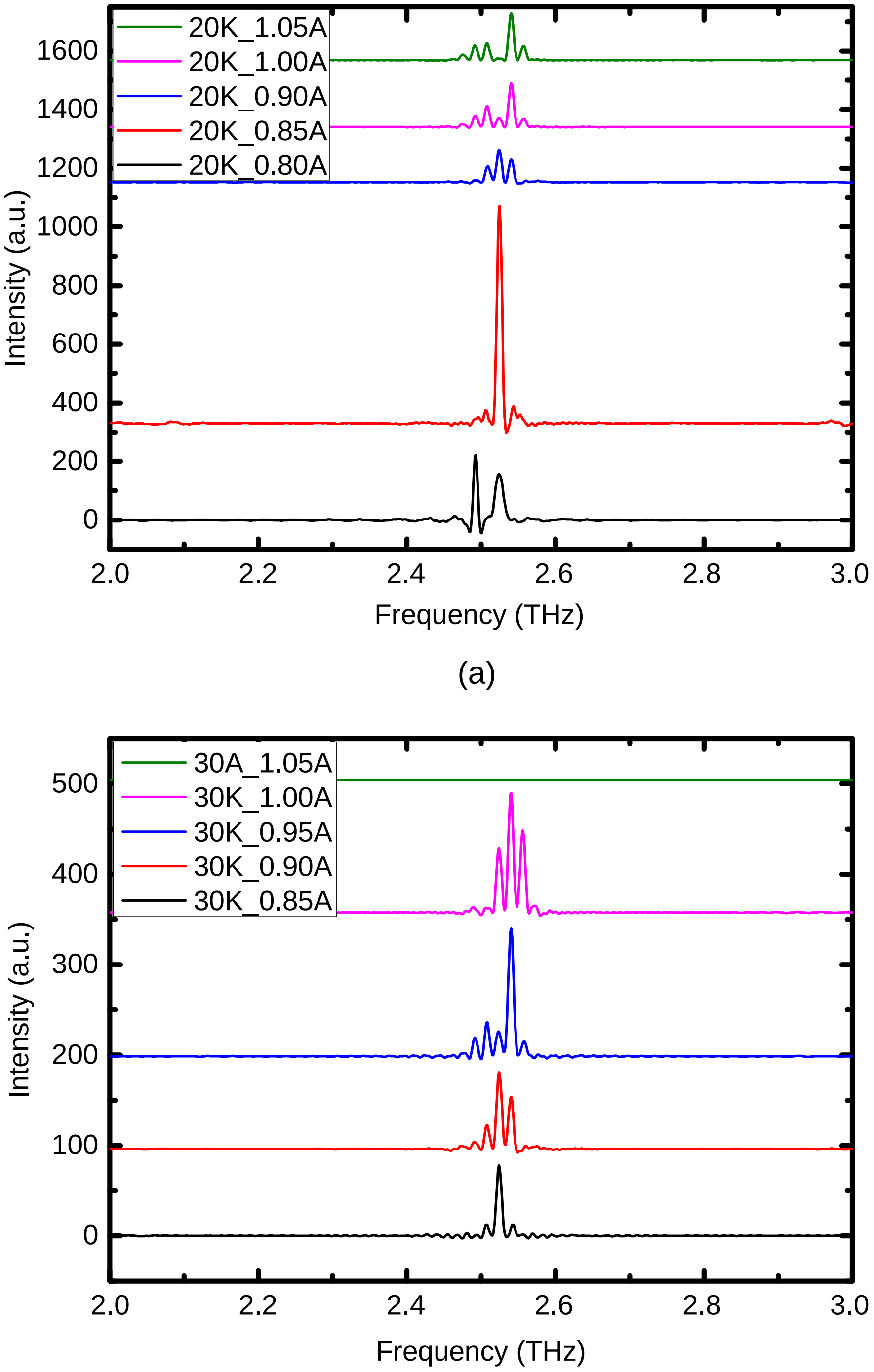

(a)

(b)

Figure 6-13 Spectrum of the initial FP laser used to fabricate the PL device. (a) and (b) show spectra at 20K and 30 K respectively.

After initial characterization, FIB milling was used to fabricate the PL device, as described in Chapter 3. The fabricated PL-QCL waveguide is shown in Figure 6-14. The fourteen etched slits were 5.31-µm wide and the corresponding width of the metal part is 12.39 µm. A central double-sized metal region width was used to introduce the π shift shown in Figure 3-9. A duty cycle of $\gamma = 0.8$ was chosen to obtain more power for the spectroscopy measurement.

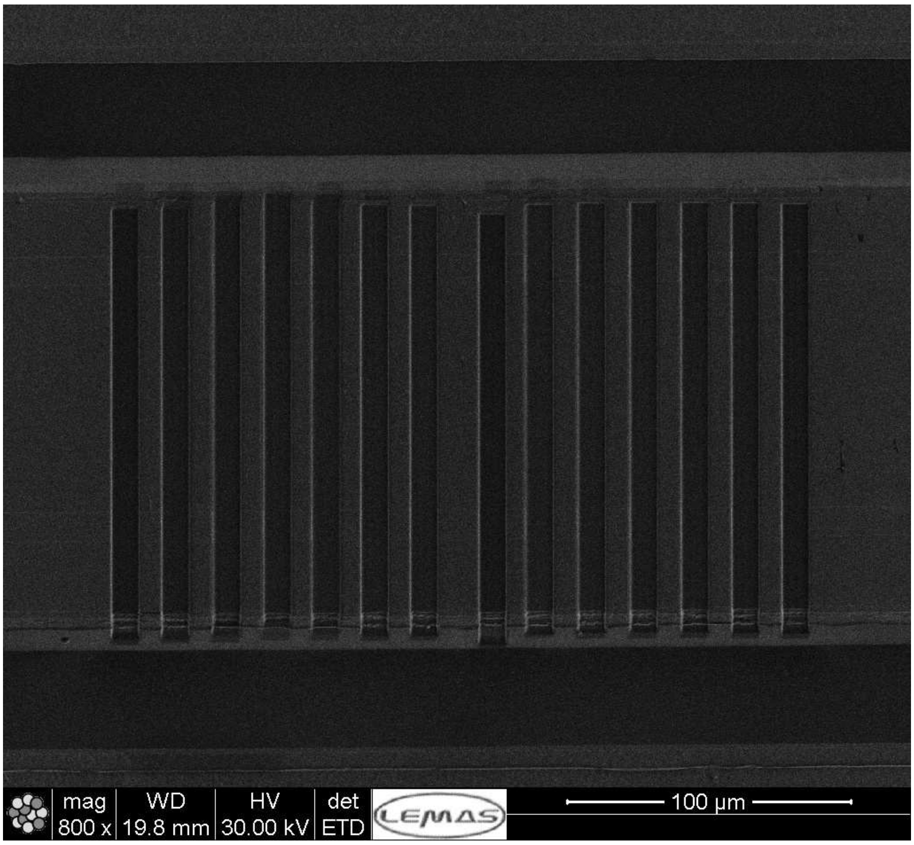

Figure 6-14 PL-QCL pattern fabricated with FIB

The LIV curve for the PL-QCL is shown in Figure 6-15. A pyroelectric detector was used for these measurements for consistency with the subsequent gas spectroscopy measurements. During both LIV and spectrum characterization, the optical path of the QCL radiation was purged by dry N_2, which is applied to make sure the LIV and spectrum are not affected by water vapour, a significant absorber of THz radiation.

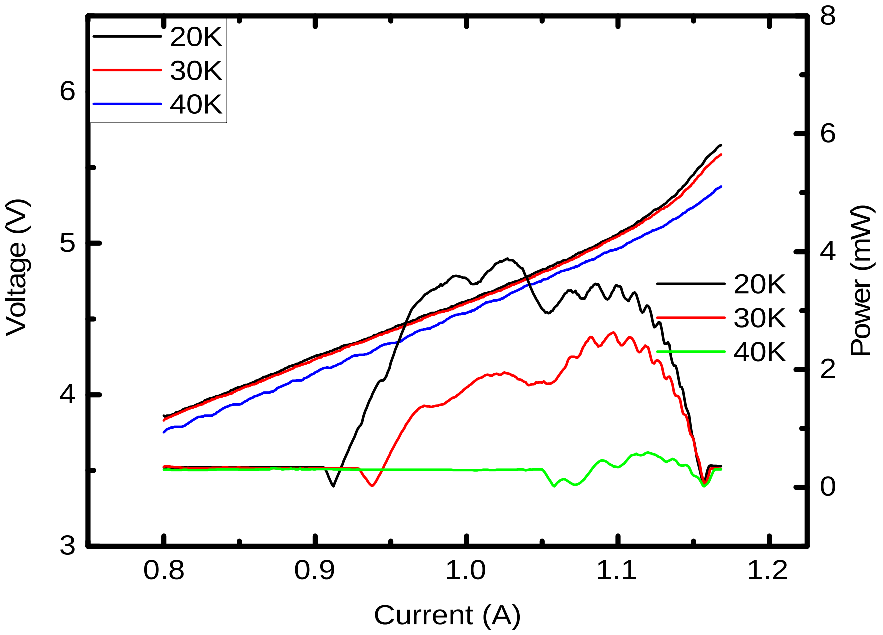

Figure 6-15 LIV curve of the PLs QCL used in the measurement, taken under CW bias.

Compared with the LIV curve of the FP laser in Figure 6-12, the LIV curve of the PL-QCL has a higher threshold current, a smaller dynamic range and lower operating temperature range than before. This is due to the increased waveguide loss caused by etching the metal cover of the FP-QCL. This leads to a higher threshold current being needed to provide a net gain in the laser. The smaller dynamic range occurs because the gain of the laser will decrease as the current surpasses the peak position and the bigger loss will stop the QCL lasing at an earlier stage.

The spectrum of the PL-QCL was characterized using a long-pass FTIR with a resolution of 125 MHz. The central frequency was found to be around 2.622 THz. The measured spectra are shown at a ranges of currents in Figure 6-16 at 20 K and 30 K heat-sink temperatures. The frequency of the emission is shown to tune, in each case, as the bias current is varied within the dynamic range of QCL.

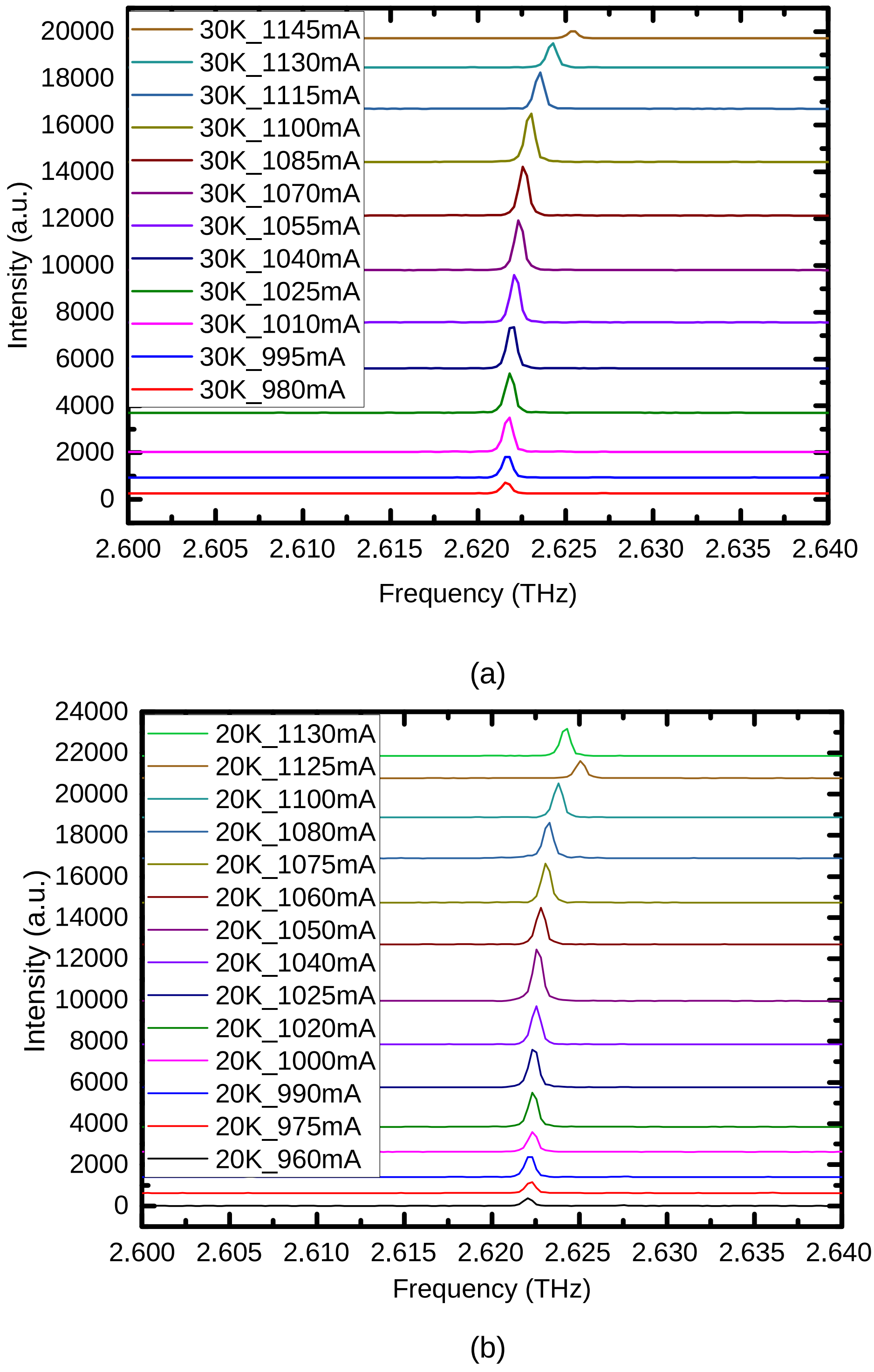

Figure 6-16 Spectrum of the PL-QCL used in the measurement, taken under CW bias at (a) 20 K and (b) 30 K.

A Gaussian fitting was used to extract the peak emission frequency from each spectrum, and the frequency is plotted against current in Figure 6-17. The data were found to follow an exponentially growing curve of the form:

$$f = f_0 + A \times \exp(BI) \tag{6.9}$$

As shown by the red lines in the figure. The current tuning relations are given by $f = 2.6224 + 1.4 \times 10^{-13} \times \exp(0.0214I)\,\mathrm{THz}$ and $f = 2.62134 + 4.303 \times 10^{-12} \times \exp(0.0180I)\,\mathrm{THz}$ for temperatures of 20 K and 30 K respectively. The current is in mA in the calculation.

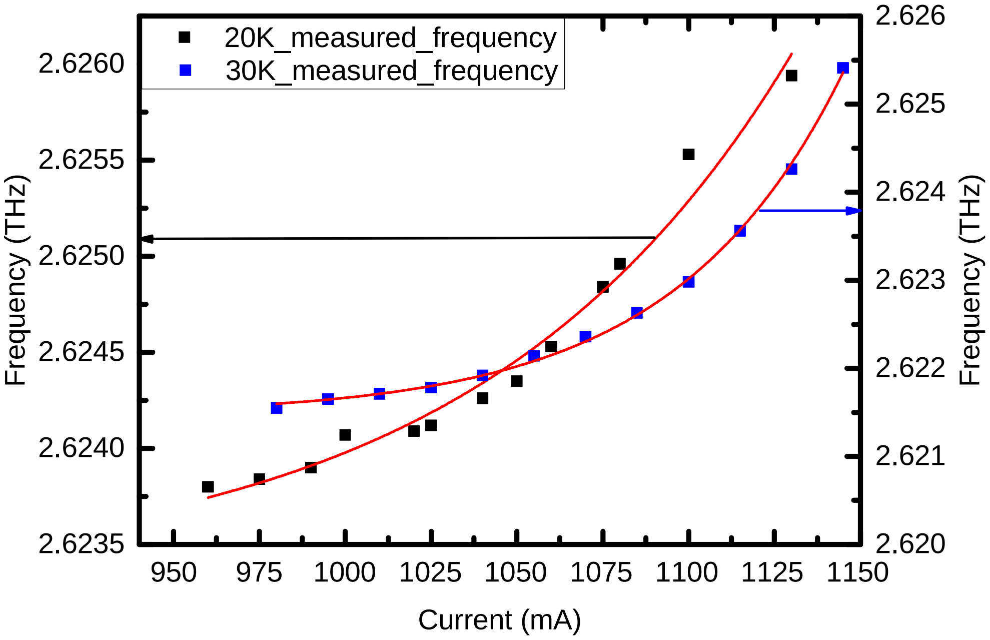

Figure 6-17 The central frequencies of QCL lasing spectrum. The black rectangular data points and blue round data points are central frequencies fitted from 20 K and 30 K QCL spectrum respectively. The two red lines are exponentially growing curves, given by Equation 6.9.

6.4.3 Methanol spectroscopy using a THz PL-QCL

6.4.3.1 Methanol vapour

As described above, the laser frequency was adjusted by sweeping the QCL drive current and the transmitted THz power was recorded both through the vapour, and through an evacuated gas cell. Initially, the cell was pumped to vacuum by a molecular pump, and subsequently filled with methanol at a range of pressures, from 1 to 5 Torr. Figure 6-17 shows the transmitted THz power as a function of the QCL drive current for each methanol pressure, and for the empty reference cell. The five different pressure applied is targeted at finding the detection limitation of this system.

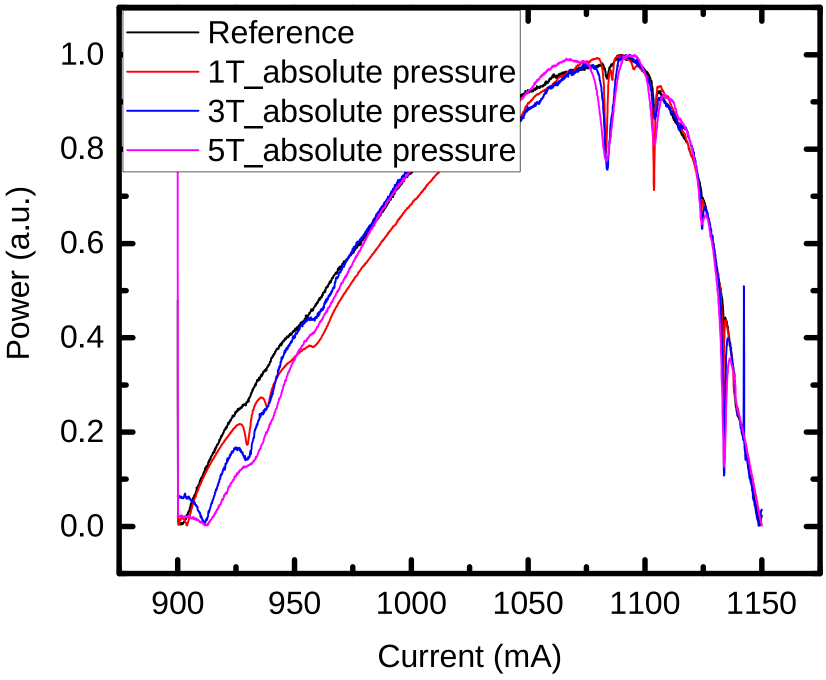

Figure 6-18 Transmitted THz power through methanol vapour at a range of pressures as a function of QCL current. The black line is an empty-cell reference. ‘1T_absolute pressure’ in the legend means the measurement was taken when the gas cell is filled with 1 Torr pure methanol. The other two measurements are similarly labelled.

A set of distinct spectral absorption features are observed in the range of drive currents from 1050 to 1150 mA, with their intensities increasing as a function of pressure. The weak absorption line in the reference curve is caused by residual methanol vapour in the cell.

The absorption coefficient was calculated using Equation 6.1, where I_0 is taken as being the transmitted power through the empty reference cell and I is the power transmitted through the methanol. The absorption, as a function of current is shown in Figure 6-19. After transferring the bias current to QCL lasing frequency, using the tuning relations above, a calculated methanol absorption spectrum is obtained from 2.622–2.628 THz, as presented in Figure 6-20, along with the simulated spectrum from the JPL database. There are two major absorption peaks (centred at 2.6240 and 2.6272 THz) in the JPL database, and they are also found in the measured absorption spectrum at the same frequency. Two additional absorption peaks were found at 2.625 and 2.6265 THz in the measured spectra, which do not appear in the JPL database. These are attributed to residual water vapour.

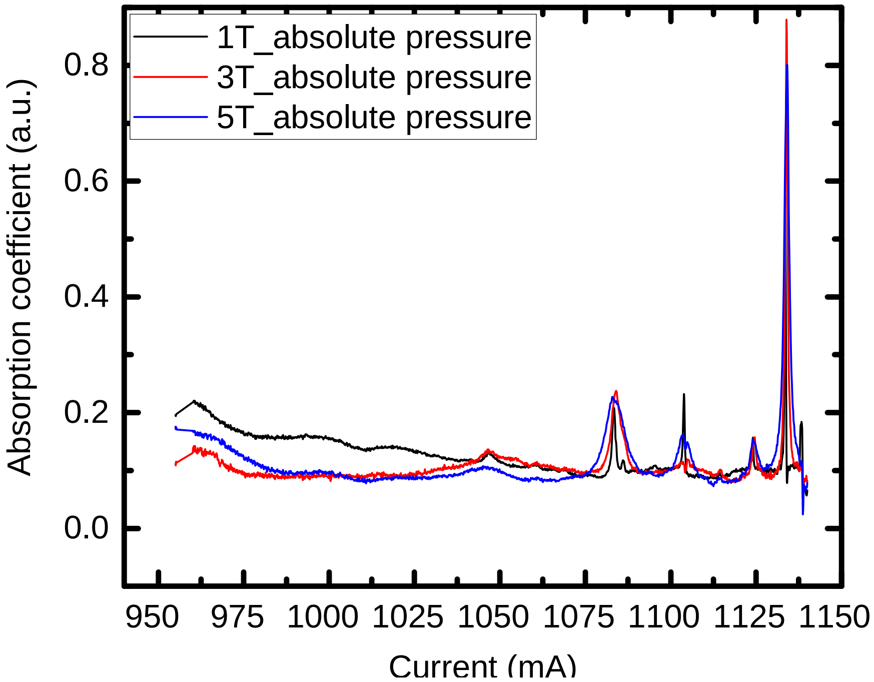

Figure 6-19 Calculated absorption coefficient of methanol at a range of absolute pressures as a function of QCL bias current. ‘1T_absolute pressure’ in the legend means the measurement was taken when the gas cell is filled with 1 Torr pure methanol. The other two measurements are similarly labelled.

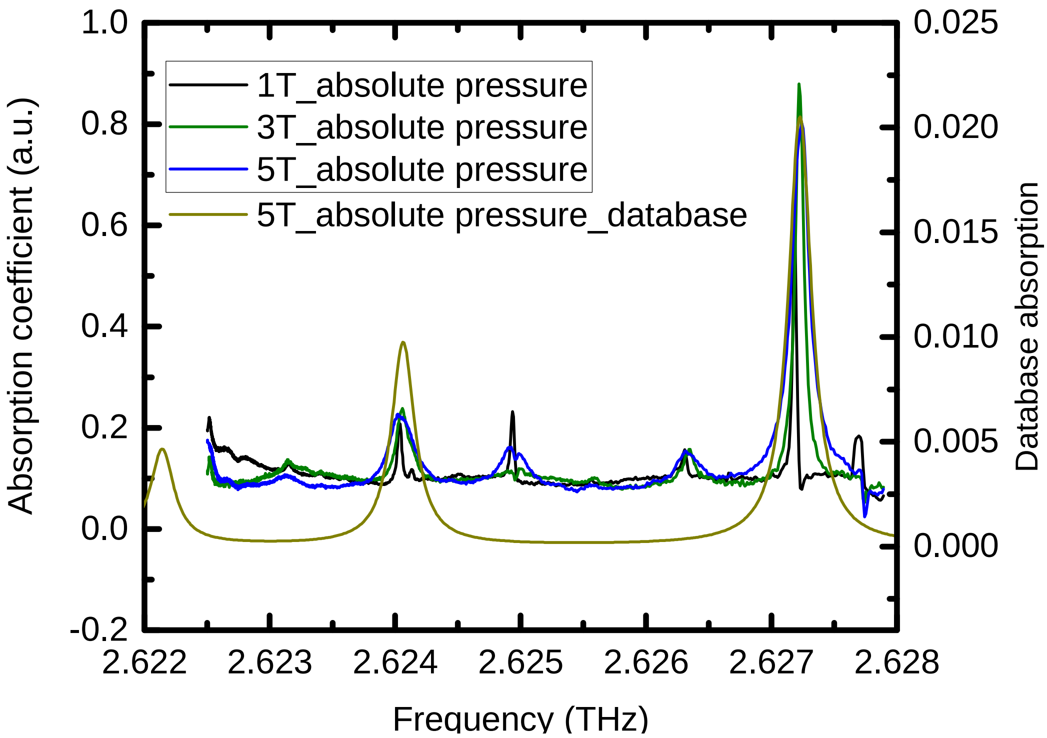

Figure 6-20 Calculated absorption coefficient of different absolute pressure methanol in the range of QCL lasing frequency. The black, green and blue lines are the measured absorption coefficient of 1Torr, 3Torr and 5Torr methanol in a gas cell. The dark yellow line is the absorption coefficient from the JPL database. '1T_absolute pressure' in the legend means the measurement was taken when the gas cell is filled with 1 Torr pure methanol. The other two measurements are similarly labelled.

The lineshapes of the absorption peaks were then studied. The Doppler broadening linewidth for methanol was calculated using Equation 6.4 at 292 K as 5.6×10^{-6} THz, which is negligible, compared with the measured values. As such, collisional broadening is the dominant effect, and a Lorentzian function was fitted to the two major peaks in the spectra.

Figure 6-21 shows fittings at 1, 3 and 5 Torr. The width of peaks increases with respect to the absolute methanol pressure and the FWHM for each pressure is given in Table 6-1. The table also shows the linewidths (in Torr) calculated using a pressure broadening coefficient of 339 kHz/Pa (4.52×10^{-5} THz/Torr), as reported previously for methanol vapour at similar frequencies [176]. The experimental linewidths are plotted in Figure 6-22.

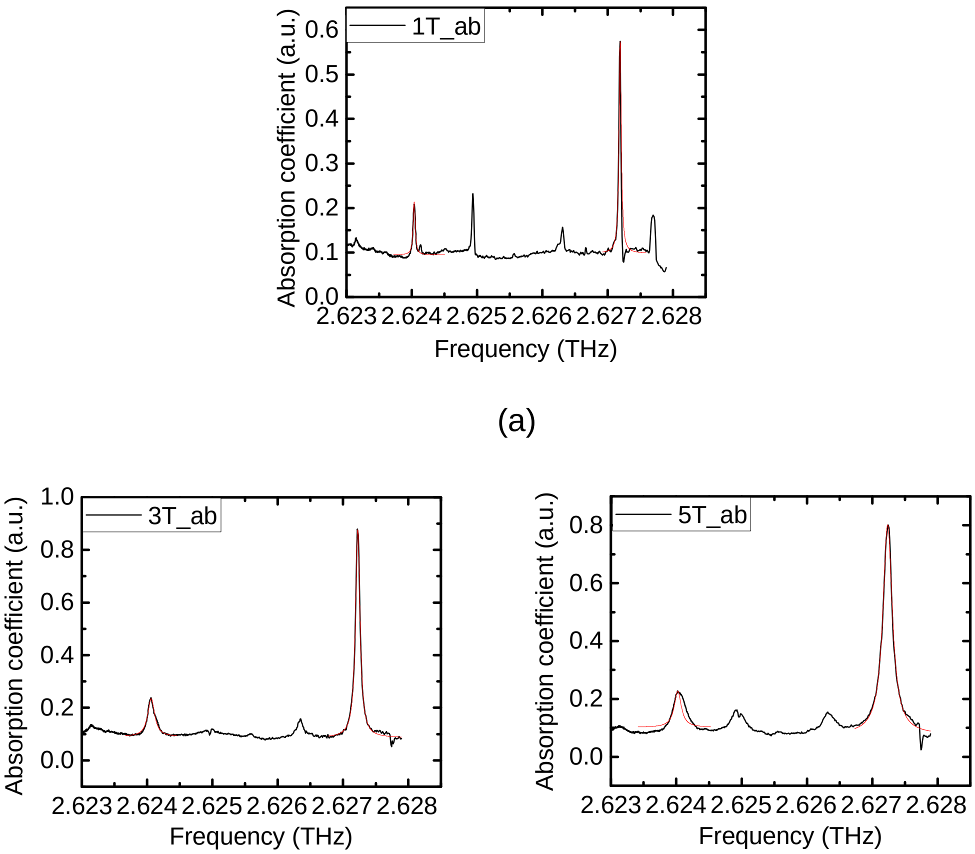

(a)

(b)

(c)

Figure 6-21 Lorentzian fittings to the calculated absorption spectra of pure methanol. (a), (b) and (c) show results for 1, 3 and 5 Torr respectively.

The broadening coefficient was obtained from a linear fitting to the experimental data as, 2.31×10^{-5} and 3.34×10^{-5} THz/Torr for the first and second peaks respectively. The measured values are lower than the expected values from the literature, and do not precisely follow a linear broadening.

Table 6-1 Measured and JPL database absorption peak position, f_0, and linewidth, w, for a gas cell filled with pure methanol vapour

Pressure (Torr)	f_0 (THz)		w (THz)	
	1st peak	*2nd peak*	*1st peak*	*2nd peak*
1 (measured)	2.6240	2.6272	3.66×10^{-5}	4.13×10^{-5}
1 (database)	*2.6241*	*2.6272*	4.52×10^{-5}	4.52×10^{-5}
3 (measured)	2.6241	2.6272	1.27×10^{-4}	8.2×10^{-5}
3 (database)	*2.6241*	*2.6272*	1.36×10^{-4}	1.36×10^{-4}
5 (measured)	2.6240	2.6272	1.29×10^{-4}	1.75×10^{-4}
5 (database)	*2.6241*	*2.6272*	2.25×10^{-4}	2.26×10^{-4}

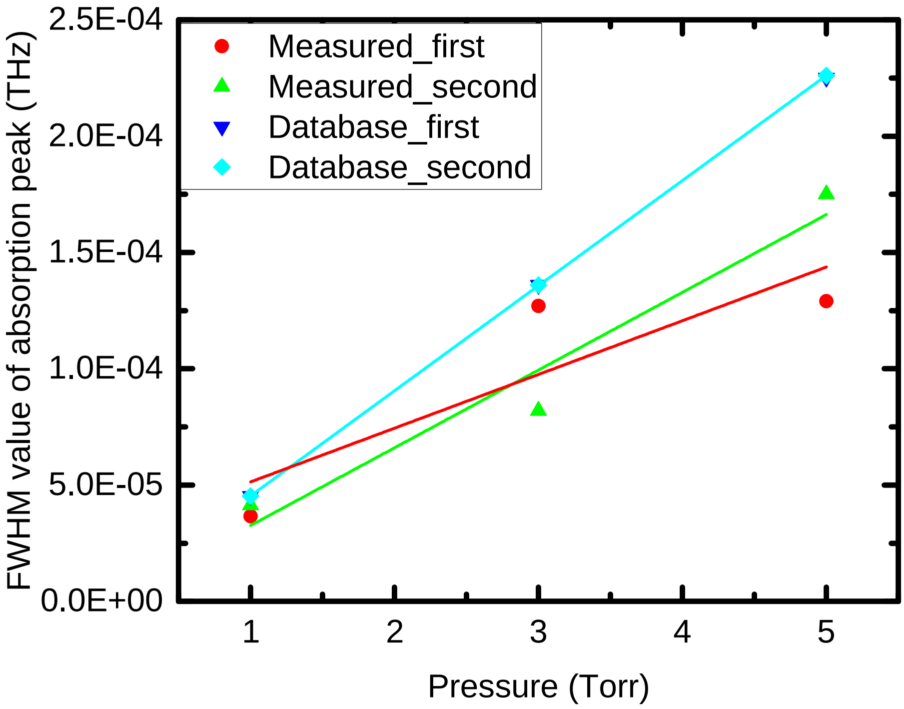

Figure 6-22 FWHM value of absorption peaks of methanol at different pressures. The red and green lines are for the measured absorption peaks; the blue lines show the literature value of 339 kHz/Pa for comparison. The straight lines show linear fittings to the data.

There are three possible reasons why the measured linewidth does not agree with broadening theory. Firstly, there is a linewidth broadening effect from QCL itself. The measurements in Chapter 4 indicated that the QCL linewidth is broadened by temperature and bias fluctuations to ~20 MHz. Mechanical vibrations can also cause linewidth broadening through external cavity effects. This can be reduced by adding a stabilization feedback loop to QCL, which will be the subject of future work. Secondly, the linewidth of the absorption peak can be affected by the measurement system. In the measurement, a pyroelectric detector was applied to record radiation power through gas cell. But the stability of pyro detectors is poor as it can be affected by heat accumulation during the measurement. Finally, the absorption coefficient is calculated indirectly from the current–absorption measurements and the frequency–current tuning curve. A component of the apparent linewidth broadening can be introduced through inaccuracies in the frequency–current tuning curve.

6.4.3.2Methanol and nitrogen mixtures

This section will discuss the spectroscopy of methanol mixed with nitrogen. The gas cell was first pumped to vacuum and then filled with 1 Torr methanol. Dry N_2 was then introduced to fill the gas cell to 5 Torr total pressure. The same steps were taken for 2, 3, 4 and 5 Torr partial pressures of methanol. A 5 Torr dry N_2 cell was taken as reference.

Figure 6-23 shows the transmitted THz power as a function of the QCL drive current for each partial pressure. As before, 4 absorption peaks are visible in each measurement, when the QCL was driven between 1050 mA and 1150 mA. The intensities of the peaks increase with respect to pressure. The absorption coefficient was also calculated using equation 6.1, as shown in Figure 6-24. The same absorption peak frequencies are visible as those in Figure 6-19. After transferring the bias current to QCL lasing frequency, methanol absorption spectra are obtained from 2.622–2.628 THz, as shown in Figure 6-25. As with the pure methanol scans, two major absorption peaks from the JPL database have been identified, while the additional two peaks are attributed to water absorption.

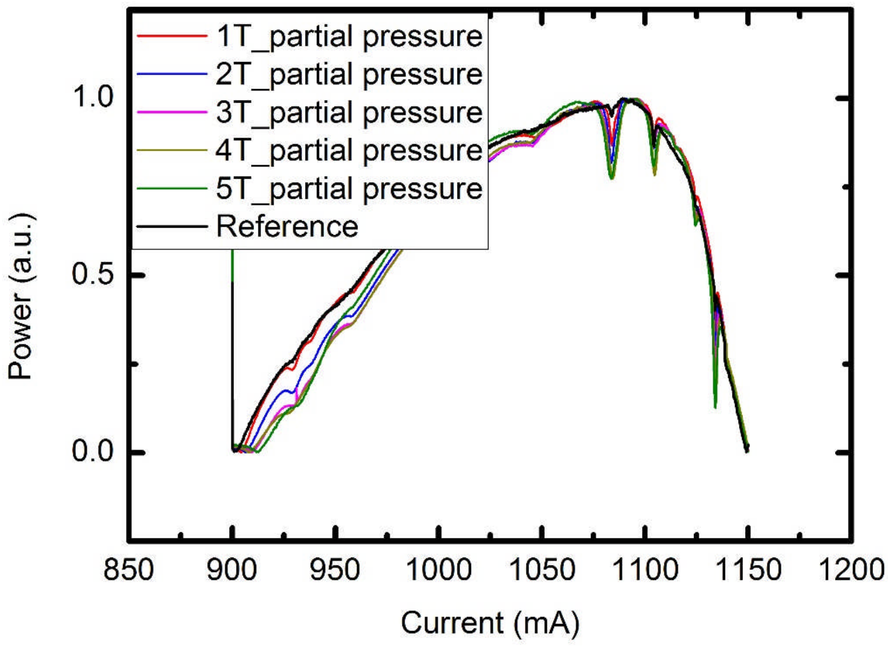

Figure 6-23 Scan of different partial pressure of methanol in the gas cell with methanol and N_2. The black line shows a reference scan for 5 Torr dry N_2 in the gas cell.

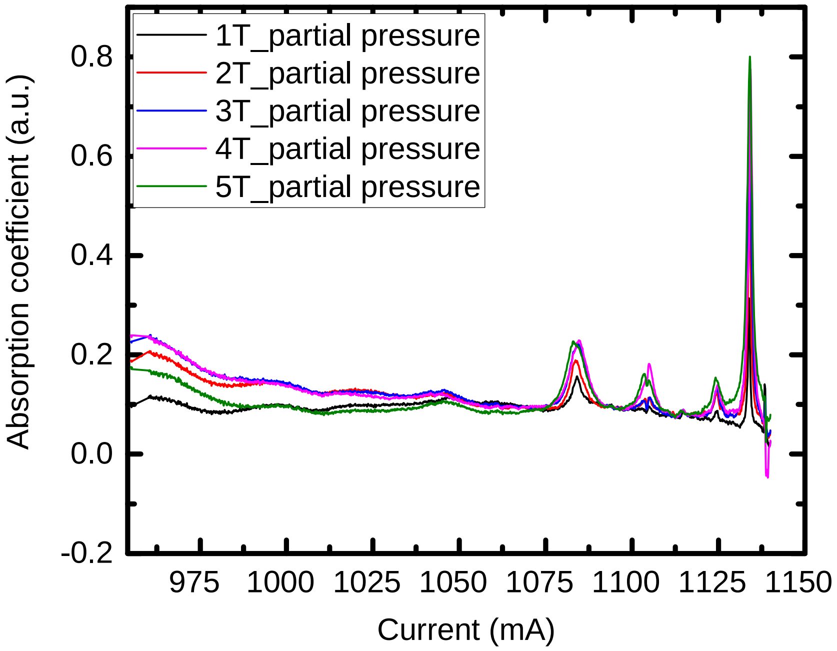

Figure 6-24 Calculated absorption coefficient of methanol as a function of QCL bias. Results are shown for 1–5 Torr methanol partial pressure, balanced with N_2 to a total pressure of 5 Torr.

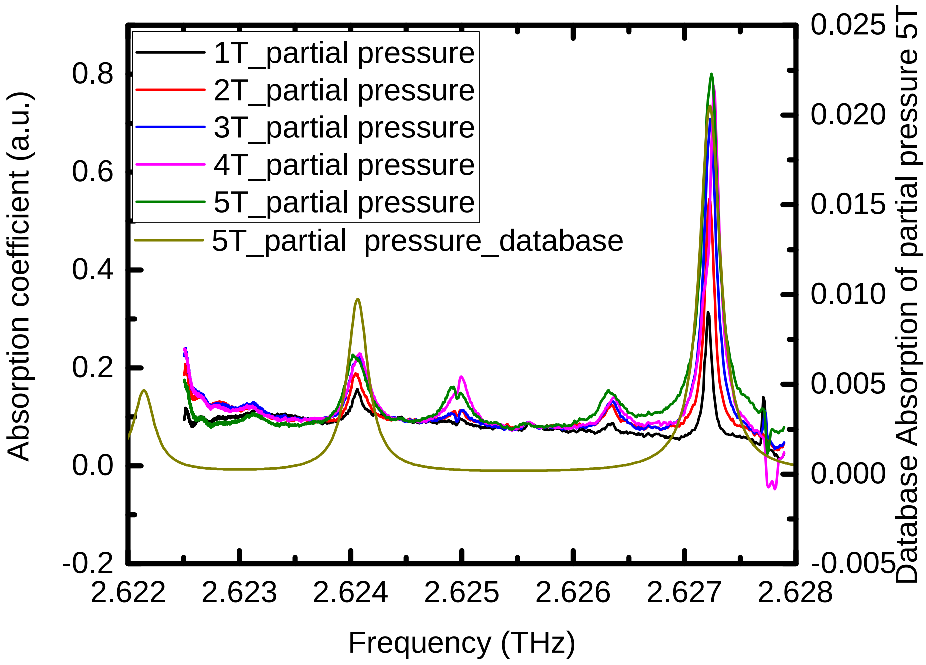

Figure 6-25 Calculated absorption spectra of methanol at a range of partial pressures. The black, red, blue, violet, and green lines show the experimentally measured results; the dark yellow line shows the absorption coefficient obtained from the JPL database over the same frequency range.

The FWHM was analysed for each of the partial pressure absorption scans, using the two major absorption features as before. Lorentzian fittings to the lineshapes are shown in Figure 6-26 for each partial pressure and the linewidths are tabulated in Table 6-2. The fitted features indicate, in all cases, that the absorption frequencies are 2.6241 THz and 2.6272 THz for biases of 1084 mA and 1130 mA respectively—the same as for pure methanol. The measured FWHM values are of similar magnitude to those in the literature, and remain almost the same as the partial methanol pressure changes from 1–5 Torr, as shown in Figure 6-27.

The lines tabulated in Table 6-1 and Table 6-2 have FWHM around 200 MHz, which is much broader than the linewidth of a free running QCL (20 MHz). As such, the free-running QCL can provide sufficient resolution for 1 Torr methanol. However, a better resolution is needed for Earth observation. Furthermore, sensitivity needs to be analysed to determine the noise limitation for this method.

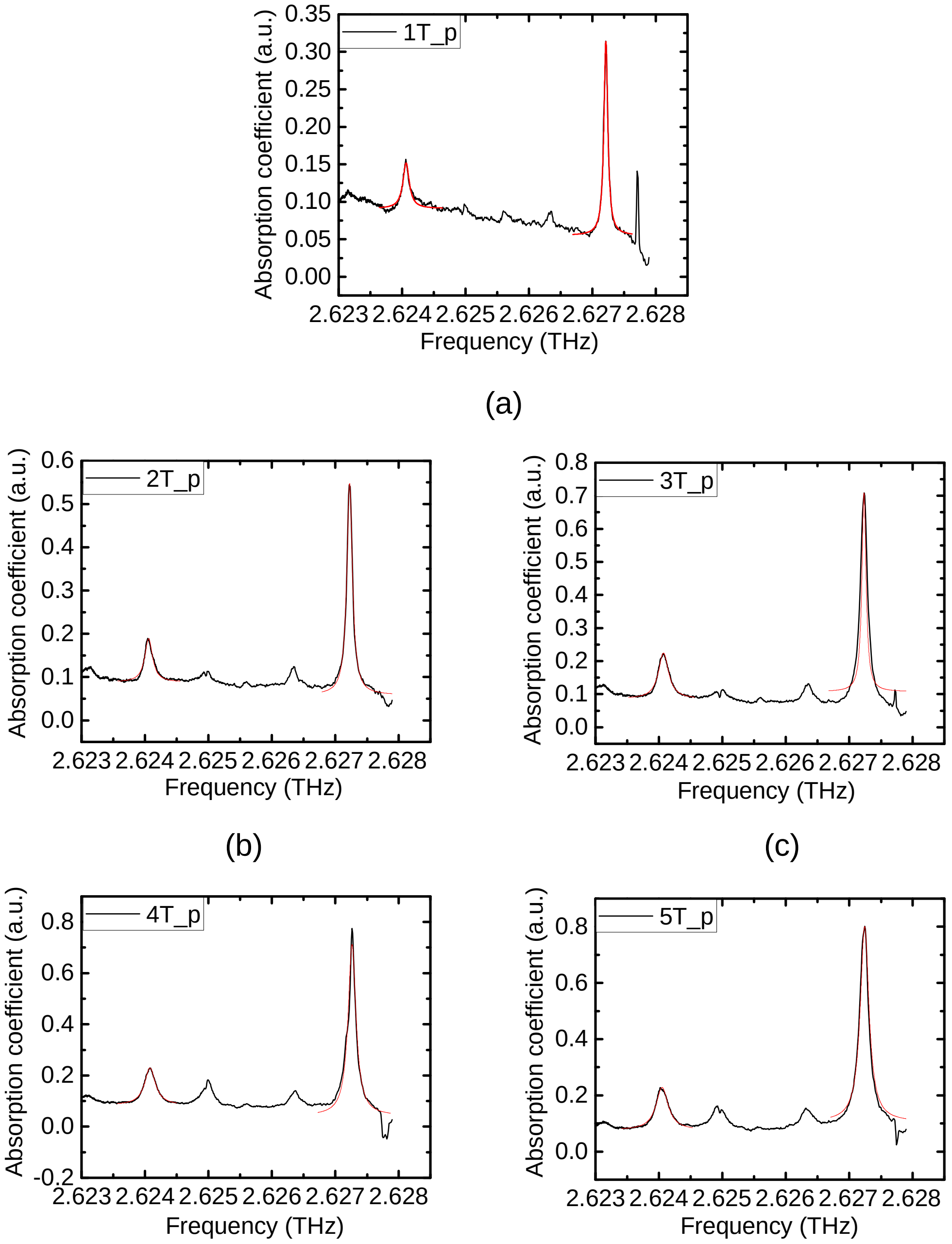

(a)

(b)

(c)

(d)

(e)

Figure 6-26 Measured absorption spectra of methanol at different partial pressures**.** Lorentzian fittings to the peaks are shown as red lines.

Table 6-2 Measured spectral parameters for peak frequencies and linewidth for gas cell containing methanol at a range of partial pressures in nitrogen. Values for 5-Torr methanol from the JPL database, and expected linewidth are shown for comparison.

Partial Pressure (Torr)	f_0 (THz)		w (THz)	
	1st peak	*2nd peak*	*1st peak*	*2nd peak*
1	2.6241	2.6272	1.207×10^{-4}	7.371×10^{-5}
2	2.6241	2.6272	1.478×10^{-4}	1.056×10^{-4}
3	2.6241	2.6272	1.430×10^{-4}	7.722×10^{-5}
4	2.6241	2.6273	1.310×10^{-4}	1.503×10^{-4}
5	2.6241	2.6272	1.287×10^{-4}	1.662×10^{-4}
5 (database)	*2.6241*	*2.6272*	2.252×10^{-4}	2.258×10^{-4}

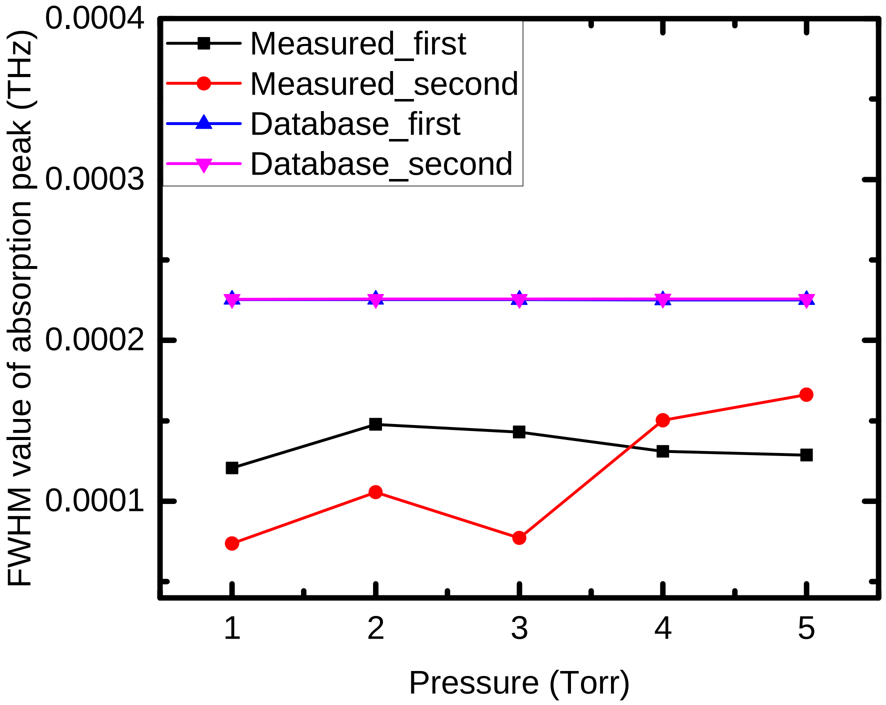

Figure 6-27 FWHM value of absorption peaks of methanol as a function of partial pressure**.** The red and black lines are for the measured first and second absorption peak in Figure 6-26; the pink and blue lines show literature values for comparison.

6.4.4 Sensitivity analysis

6.4.4.1 Noise analysis

The sensitivity of a trace gas detection system is defined as the lowest concentration (gas pressure or molecular concentration) of gas that can be detected. The sensitivity is limited by the system noise coming from QCL and measurement system. In order to analyse the noise level of the measurement, the QCL was biased at 1087 mA, at a heat-sink temperature of 20 K, and the transmitted power was recorded consecutively 102 times with the gas cell empty.

All the measurement conditions remain the same as the gas sensing measurement except for the bias being kept constant. The detector signal was recorded using a lock-in amplifier, and the results are shown in Figure 6-28. Lock-in time constant of 50 ms, 100ms, 200ms, 500ms and 1s were used. A statistical analysis of the measurements is shown in Table 6-3.

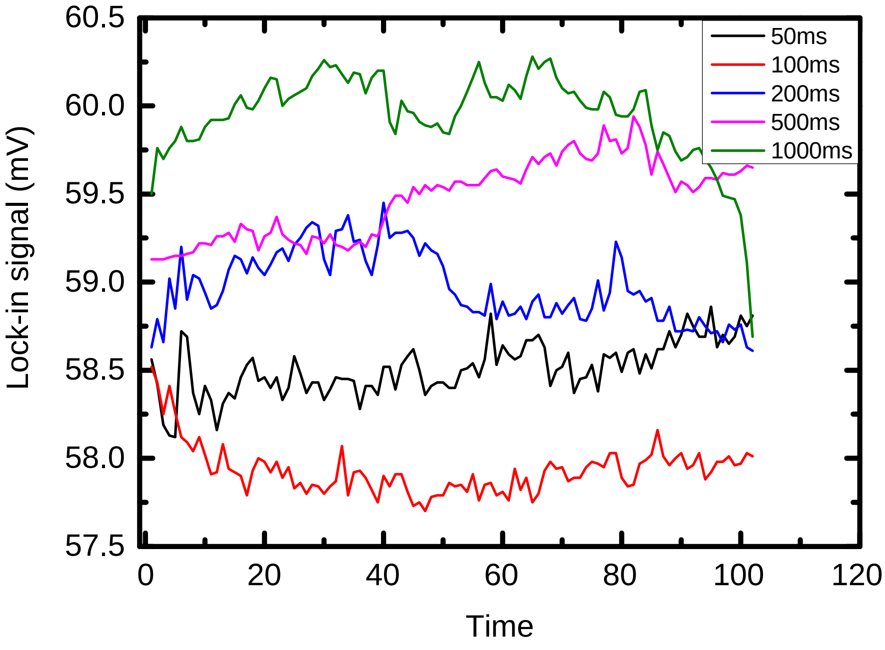

Figure 6-28 The recorded THz signal when QCL is biased at 1087mA for 102 sequential measurements. The legend shows the time constant of the lock-in amplifier for each plot.

Table 6-3 Mean and standard deviation of the detector signal through a purged gas cell, at a range of lock-in time constants

Time constant [ms]	Mean value [mV]	Std. dev. [mV]	$\frac{\sigma}{\sqrt{n}}$
50	58.51	0.1522	0.001492
100	57.93	0.1396	0.001369
200	58.98	0.2034	0.001994
500	59.47	0.2204	0.002161
1000	59.95	0.2472	0.002424

The standard error (i.e., the uncertainty in the mean value), caused by system noise, during the measurement can be calculated as:

$$\text{std. err.} = \frac{\sigma_\alpha}{\sqrt{n}} \tag{6.10}$$

in which, σ_α is the standard deviation of the signal, and *n* is the number of samples (102).

The noise is caused by fluctuations in the bias supplied by the current source, temperature fluctuations in the cryostat and also mechanical vibration given by chopper used for modulation.

6.4.4.2 Sensitivity analyse

As discussed in last section, there are 4 principal absorption peaks within the dynamic range of the QCL and the strongest occurs at a bias of 1134 mA (2.6272 THz emission). Figure 6-29 shows this peak at a range of methanol partial pressures, from 1–5Torr.

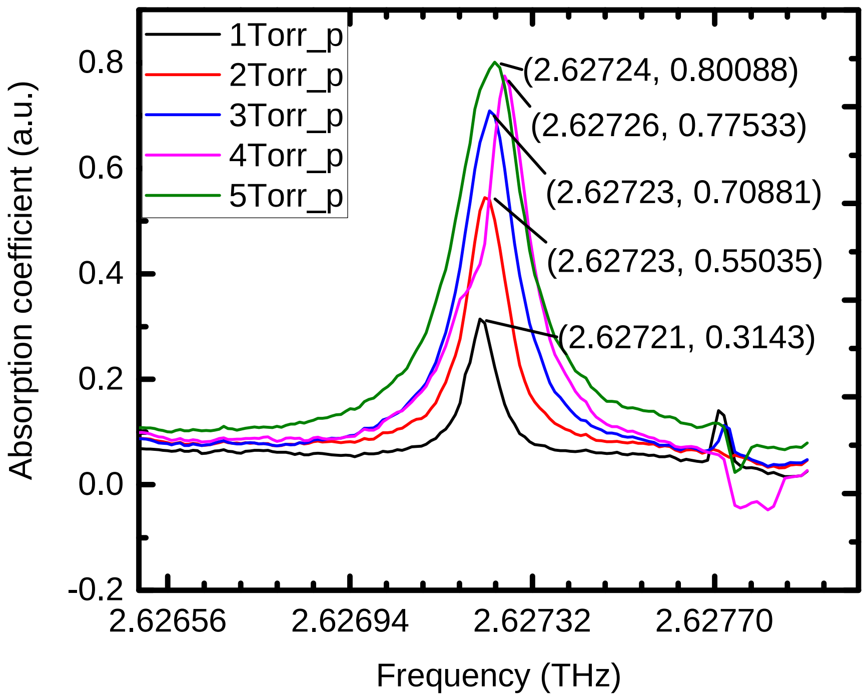

Figure 6-29 Measured absorption peak of methanol when QCL bias is 1134 mA. The frequency is calculated using the current tuning equation.

In theory, the absorption should linearly increase with respect to pressure according to [209]:

$$\alpha = \varepsilon l c \tag{6.11}$$

In which, ε is a constant, *l* is the length of gas cell here and *c* is the concentration of methanol. *c* increases linearly with respect to the methanol partial pressure. The measured absorption coefficient at different partial pressures is shown in Figure 6-30.

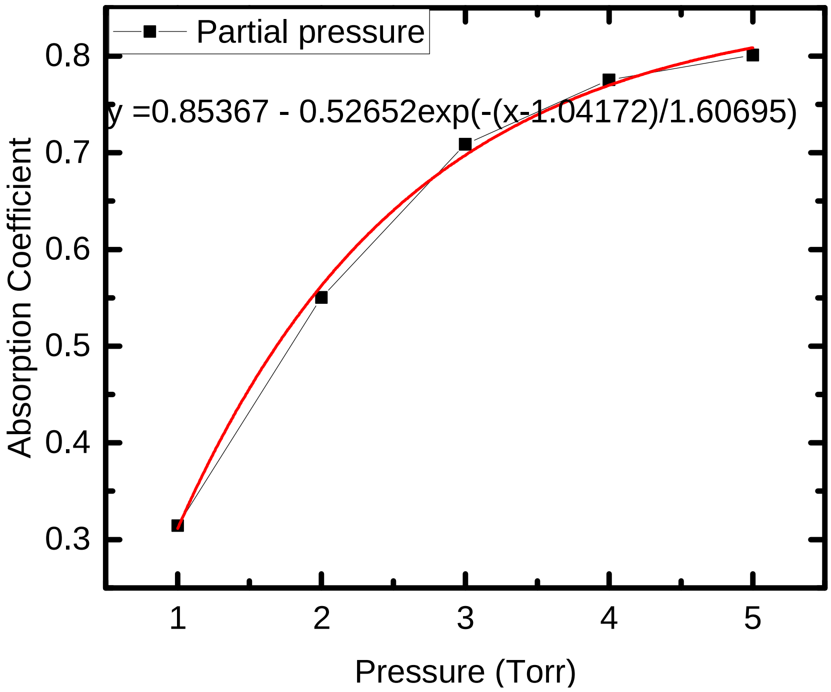

Figure 6-30 Measured absorption coefficients at different partial pressures of methanol. The black data points are the measured values and the red line is an exponentially fitted curve to the data.

An exponential fitting is applied to describe the relationship between measured absorption coefficient and gas pressure instead of linearly fitting. The fitted relationship between calculated absorption coefficient and the gas pressure can give the minimum and maximum pressure that this system can detect. The minimum pressure is determined by the noise of the system, while the maximum pressure is determined by the maximum absorption coefficient the fitted relationship can give.

The following equations can be obtained from Equations 6.1 and Equation 6.2,

$$\alpha = \frac{(\lg(I_0) - \lg(I))}{L}$$

$$\frac{\partial\alpha}{\partial I} = \frac{\frac{1}{I_0 In(10)}\frac{\partial I_0}{\partial I} - \frac{1}{IIn(10)}}{L} \tag{6.12}$$

$$\frac{\partial^2\alpha}{\partial I^2} = \frac{\frac{1}{In(10)}\left(-\frac{1}{{I_0}^2}\frac{\partial I_0}{\partial I} + \frac{1}{I_0}\frac{\partial^2 I_0}{\partial I^2} - \frac{-1}{I^2}\right)}{L} \tag{6.13}$$

In the measurement, absorption is small compared to QCL power. So $I_0 \approx I$ and $\frac{\partial I_0}{\partial I} \approx 1$. And then the following equation can be obtained:

$$\frac{\partial^2 \alpha}{\partial I^2} = \frac{\frac{1}{In(10)}\left(-\frac{1}{{I_0}^2}\frac{\partial I_0}{\partial I} + \frac{1}{I_0}\frac{\partial^2 I_0}{\partial I^2} - \frac{-1}{I^2}\right)}{L}$$
$$= \frac{\frac{1}{In(10)}\left(-\frac{1}{{I_0}^2}\left(\frac{\partial I_0}{\partial I} - 1\right) + \frac{1}{I_0}\frac{\partial^2 I_0}{\partial I^2}\right)}{L}$$
$$\approx \frac{1}{In(10) \times L \times I_0} \times \frac{\partial^2 I_0}{\partial I^2} \qquad (6.14)$$

So

$$\sigma_\alpha^2 = \frac{\sigma_I^2}{In(10) \times L \times I_0} \qquad (6.15)$$

The minimum σ_α^2 is obtained when lock-in amplifier time constant is 100, $\sigma_I^2 = 0.001369$ given as table 6-3. So $\sigma_{\alpha,minimum}^2 =$ 1.406 × 10^{-7} and $\frac{\sigma_{\alpha,minimum}}{\sqrt{n}}$=3.713×$10^{-5}$. So the minimum error of absorption coefficient caused by the measurement system is 3.713×10^{-5} cm^{-1}.

In the measurement, absorption coefficient increases with respect to partial pressure given as Figure 6-30 and the minimum detectable methanol partial pressure detected is given by the fitted equation:

$$y = 0.8537 - 0.5265\exp\left(\frac{-(x - 1.042)}{1.607}\right) \qquad (6.16)$$

In which *x* is the partial pressure detected and y is the corresponding absorption coefficient. If the minimum absorption coefficient is defined as 3 times of the coefficient error value, the minimum partial pressure, x that can be detected, is given by:

$$3 \times 3.713 \times 10^{-5} = 0.8537 - 0.5265\exp\left(\frac{-(x - 1.042)}{1.607}\right) \qquad (6.17)$$

The minimum detectable partial pressure detected is therefore 0.265 Torr or 35.40 Pa. The minimum number of molecules per unit volume can be obtained from the gas law as:

$$\left(\frac{n}{V}\right)_{min} = \frac{P_{min}}{RT} = \frac{35.40}{8.314 \times 10^6 \times 291} = 1.463 \times 10^{-8} mol \cdot cm^{-3} \qquad (6.18)$$

Finally, the minimum detectable molecular concentration is given by:

$$\rho_{min} = \left(\frac{n}{V}\right)_{min} \times N_A = 1.5 \times 10^{-8} \times 6.0 \times 10^{23} = 9.0 \times 10^{15}\ cm^{-3} \qquad (6.19)$$

This is very close to the 1× 10^{14} molecule/cm^{-3} level required for sensing radical species in the MLT region of the atmosphere.

Now, taking the volume of the cell, V = 686 cm^3 gives the minimum detectable number of molecules within the cell calculated as:

$$N_{min} = \rho_{min} * V = 6.0 \times 10^{18} \qquad (6.20)$$

6.5 Conclusion

In this chapter, two different methods have been used to detect methanol gas. Spectroscopy of 20 Torr and 95 Torr methanol with a photomixer was introduced. The results were shown to reproduce the expected spectral lines from the JPL database, although additional features were also seen.

A THz QCL was also used to perform spectroscopy: both absolute pressure and partial pressure of methanol were investigated. For both measurements, two major absorption peaks of methanol were analysed. The linewidth of the absorption peaks was calculated and compared with literature values. A similar trend of linewidth change with the change of pressure was found for both absolute pressure and partial pressure measurements. The noise level of spectroscopy with a THz QCL was determined and the detection limitation of this method was obtained based on the noise level analysis.

Chapter 7 Conclusion and future work

The mesosphere and lower thermosphere (MLT) regions of the Earth's atmosphere plays an important role in understanding climate change on Earth. This thesis focuses on the development of THz instrumentation and sensing techniques for a proposed satellite mission—'Linking Observations of Climate, the Upper-atmosphere and Space-weather' (LOCUS) whose payload includes a multi-THz channel radiometry system to perform a global mapping of key gaseous species in the MLT and hence to improve understanding of climate change processes. Two of the channels proposed in the LOCUS payload are based on THz QCLs operating at 3.5 THz and 4.7 THz for studying OH and O, respectively.

The work presented in this thesis address the engineering of THz QCLs, which are being developed for this satellite mission.

7.1 THz QCL fabrication and characterization

One of the LOCUS mission objectives is the realisation of a high power, compact THz local oscillator emitting a stable single frequency for use in heterodyne spectroscopy of gaseous species. The quantum cascade laser was selected as the optimum solution for this local oscillator owing to its high power and its ability to be engineered into compact and integrated device. In order to achieve this, a number of THz QCLs were fabricated, characterised and optimised. Both multimode Fabry-Perot (FP) THz QCLs and single mode photonic lattice (PL) THz QCLs were demonstrated and a double metal THz QCL was integrated with a robust waveguide which improves beam pattern of this device, and enables future waveguide coupling into a Schottky diode detector.

7.1.1 Fabrication and characterization of FP THz QCLs

In Chapter 2, the fabrication using photolithography of a single plasmon waveguide THz QCL was presented, with all fabrication parameters, and the reasons for the choice.

Two operation methods were used to the characterize the FP QCLs: pulsed and CW modes. For both, the experimental setup was presented and the parameters used in the measurements were given. The LIV curves and spectra were obtained in both cases.

7.1.2 Single mode THz QCL development

The heterodyne detection of THz emission from MLT species requires a highly stable THz local oscillator (LO), operating on an single mode. A refractive index modulation is introduced by photonic lattice (PL) structure patterned on the waveguide of the FP QCLs, which gives a single mode lasing to the lasers. The design, fabrication, optimisation and measurement of the PL patterned QCLs were presented. Fabrication of PL structure using there different methods: optical photolithography, electron beam lithography, and focused ion beam, were used to fabricate the PL patterns.

Two sets of PL QCLs operating at 2.22 THz and 2.62 THz, were characterised, and the measured LIV and spectral performance were compared with FP single plasmon device fabricated from the same wafer. Successful single mode operating was obtained.

7.1.3 Waveguide integrated device characterization

In satellite missions, power consumption should be as small as possible. Part of this power is needed to feed the cooler for the QCL. A higher operating temperature for the QCL will decrease the power consumption. Due to strong confinement of double metal (MM) waveguide QCLs, THz modes can be confined in all directions. The strong confinement gives a larger gain in MM devices, which increases the maximum operating temperature.

During detection, power from the THz LO must be coupled into Schottky diode detector, but there must be enough power (3-4 mW) to pump the detector unfortunately. MM device output lower power than single plasmon devices, which is made worse by the poor output beam profile. In order to solve this problem, MM THz QCLs were integrated into a robust waveguide. The integrated devices were characterised in terms of the LIV, maximum operating temperature, spectrum, and beam profile. The integrated device showed a significantly better beam profile (20°) than the MM device before integration.

7.1.4 Future work on QCL development

In this thesis, single plasmon waveguide photonic lattice QCLs were fabricated and characterized, with the QCLs emitting at 2.22 THz and 2.62 THz in single mode were achieved. The highest CW working temperature was 40 K and the peak power at 40 K was 0.125 mW for 2.22 THz QCLs. The highest operation CW temperature for the 2.62 THz QCL was 40 K and the peak power was 0.5 mW at 40K. Further refinement of QCL active region design can increase maximum operating temperature.

Multimode QCLs lasing at 3.5 THz and 4.7 THz were also demonstrated targeting at OH and O emission detection, respectively. But photonic lattice structure need to be designed and optimised to target the exact emission frequency for the two species. Improved maximum operating temperature was shown with double metal waveguide device, but the power performance needs improving for LO application. Firstly, the output power can be increased by fabricating larger size device. But a larger device size requires more input DC power which should be avoided. An optimum compromising must thus be reached. Secondly output power can be increased by optimization of the Photonic lattices (PL) patterns by increasing the duty cycle, and minimizing length of the pattern.

The QCL linewidth given by our measurement is 3 MHz which is broader than the targeted linewidth (1 MHz). So next step of this project is adding a feedback loop for the detection system. The absorption peaks of the gas can be used as a frequency reference for the feedback loop, with the reference frequency source for the loop needing to be compact and stable. Microwave frequency multipliers are very competitive since they have already been applied to stabilize QCL radiation successfully [173, 174]. More refinement is though needed as well as use of more stable bias sources and coolers.

Operation temperature and threshold current density aren’t affected significantly by integration of a QCL into a waveguide. And the beam profile is improved significantly by this integration, which is very helpful for coupling the power into Schottky diode detector. But the output power can be improved by optimizing the waveguide design. An open ended waveguide can be changed to a rectangular waveguide and integrated with a feed-horn [175], and the rectangular waveguide can be matched to the QCL emission frequency.

7.2 Schottky diode detector characterization and heterodyne detection

A Schottky diode detector is proposed for heterodyne detection in LOCUS. In this thesis, The Schottky diode detectors have been characterised with THz QCLs, using a direct detection approach. Two neighbouring FP modes of a THz QCL were coupled into a Schottky diode detector, and the output heterodyne signal from a Schottky diode detector was studied.

7.2.1 Direct detection with Schottky diode detectors

Two Schottky diode detectors were characterized, one medium gain and one high gain, and used to replace a commercial bolometer for THz radiation detection. QCLs lasing at 2.22 THz, 2.56 THz, 2.75 THz, 3.05 THz and 3.50 THz were used as the THz radiation source. It was shown that the Schottky diode detectors could replicate the LIV curves measured with a bolometer for all five QCLs. The noise levels of the detectors were measured and the signal-to-noise ratio (SNR) of the medium gain detector is 30 times larger than the high gain detector. This suggests that the biggest noise in the detectors is arising from amplification circuit, and not the detector itself, as the high gain detector had an amplifier embedded within it.

The responsivity of the Schottky diode detectors was also tested. The responsivity of the detectors at different frequencies was measured the detection cut-off frequencies of the detectors determined. The responsivity of the high gain detector has a clear linear roll off with increase of detected frequency, and the cut off frequency of the high gain detector was calculated to be 3.67 THz which is the highest room temperature THz detection based on the Schottky diodes.

The response speeds of the detectors was also measured, and 4.1×10^{-7}s and 3.3×10^{-7}s for switch on and off speeds, respectively of the medium gain detector were determined, and 1.33×10^{-6} s and 1.25×10^{-6} s speeds for switch on and turn off times for the high gain detector were obtained.

7.2.2 Heterodyne mixing of QCL radiation in a Schottky diode detector

Heterodyne detection of a single THz QCL was undertaken by mixing the signal of two neighbouring modes. This is proved to be a very convenient and easy method to measure the linewidth of THz emission. And the heterodyne signal from the Schottky diode mixer also proved to be a very efficient way to investigate thermal equilibrium speed of a QCL. Finally, this study provided a cheap and convenient way to measure the refractive index of THz QCL, with a value of 3.77 being obtained for QCL studied.

7.2.3 Future work of Schottky diode detector needed

The characterised Schottky diodes had a cut-off frequency of 3.67 THz which is enough for the 3.5 THz channel targeting OH, but it is still insufficient for the O detection channel (4.7 THz) in the proposed LOCUS payload. So higher cut-off frequency Schottky diode detectors are needed and the detectors need to be integrated with MM single mode QCLs in a waveguide package.

The Schottky diode detector is also sensitive to the radiation polarization. So the radiation polarization of the waveguide integrated QCL should be studied, to enable the best position of QCL and Schottky diode detector in an integrated waveguide to be obtained.

7.3 Gas spectroscopy with a photomixer and a free running single mode THz QCL

High resolution spectroscopy using heterodyne detection with a THz QCL based LO is proposed in LOCUS. The sensitivity, tuning bandwidth, and the ability to resolve an absorption line are critical for this system. Detection of methanol was thus demonstrated with a single mode THz QCL. This showed the ability to resolve individual absorption lines of gases clearly, and the sensitivity and tuning bandwidth of the system was assed.

7.3.1 THz spectroscopy of methanol with a photomixer

A photomixer was used for spectroscopy at 95 Torr and 20 Torr of methanol at THz frequency. The results were compared with the JPL database good agreement was obtained. Meanwhile, water absorption peaks were also present in the measured methanol absorption peaks due to residual water in the methanol gas cell.

7.3.2 THz spectroscopy of methanol with a free running single mode THz QCL

A free running THz QCL lasing at 2.62 THz was used for spectroscopy. The QCL operated continuous wave and the lasing frequency is increased with bias at 20K and 30K heat sink temperatures, which gives a continuous frequency tuning for spectroscopy. The radiation of the QCL then passed through a 73 cm long gas cell which was filled with methanol.

Different pure methanol pressures from 1 Torr to 5 Torr were used to full the gas cell, and the THz absorptions are analysed. Increase of pressure gave an absorption peak linewidth broadening. Meanwhile, mixtures of methanol and N_2 were also investigated, and the partial pressure of methanol in the 5Torr mixed gas changed from 1Torr to 5 Torr. No pressure broadening was observed, but there was a clear increase of absorbed THz power with increase of methanol partial pressure.

Then the sensitivity of the system was analysed. The noise level of the system was obtained by measuring the power passing through the gas cell. The minimum number of molecules that can be detected in the gas cell was limited by the noise level, and estimated to be is 6.0×10^{18} molecules.

7.3.3 Future work of spectroscopy with THz QCL

Methanol absorption lines have been identified, but it is the OH and O species that are most of interest for the high frequency channels in LOCUS. So new spectroscopy with 3.5 THz and 4.7 THz single mode QCLs need to be carried in the future.

The spectroscopy carried out in this thesis used a direct detection method whilst LOCUS is based on a heterodyne detection to obtain high resolution passive detection of MLT species. So a heterodyne detection system with Schottky diode detectors need to be demonstrated for gas spectroscopy.

References

[1] Thomas M. Lillesand, et al, “Remote sensing and image interpretation 6th edition,” Hoboken, NJ: John Wiley & Sons, 2008.

[2] Jun Takahashi, Seitaro Urakaw, et al, “Near-infrared colors of asteroid 2012 DA^{14} at its closest approach to Earth: Observations with the Nishiharima Infrared Camera (NIC),” Publications of the Astronomical Society of Japan, Vol. 66, No. 3, 2014.

[3] Kidd, C, "Radio frequency interference at passive microwave earth observation frequencies," *International journal of remote sensing*, Vol. 27, No. 18, 2006.

[4] George R. Carruthers and Thornton Page, “Apollo 16 Far-Ultraviolet Camera/Spectrograph: Earth Observations,” American Association for the Advancement of Science, Vol. 177, No. 4051, 1972.

[5] A.E. Hedin, “Extension of the MSIS Thermospheric Model into the Middle and Lower Atmosphere,” J. Geophys. Vol. 96, No. 1159, 1991.

[6] Robert J. States and Chester S. Gardner, “Thermal Structure of the Mesopause Region (80–105 km) at 40°N Latitude. Part I: Seasonal Variations,” J. Atmos. Sci., Vol. 57, 1999.

[7] J. M. C. Plane, W. Feng, et al, “Resolving the strange behavior of extraterrestrial potassium in the upper atmosphere,” Geophys. Res. Lett., Vol. 41, No. 4753–4760, 2014.

[8] Mangalathayil Ali Abdu and Dora Pancheva, “Aeronomy of the Earth's Atmosphere and Ionosphere,” Springer, London, 2011.

[9] Bruce Swinyard, Oliver Auriacombe, et.al, “The Low cost upper atmosphere sounder: the “elegant Breadboard” program,” Millimeter Waves and THz Technology Workshop (UCMMT), 8th UK, Europe, China, 2015.

[10] Dennis Normile, “Tracking CO_2’s Comings and Goings From Space,” Science, Vol. 323, No. 325, 2009.

[11] A. G. Davies, and E. H. Linfield, “Bridge the THz gap,” Phys. World, vol. 17, no. 4, 2004.

[12] https://commons.wikimedia.org/wiki/File:Spectre_Terahertz.svg

[13] Jason, C, Thomas, M, Goyette, et al, “Terahertz imaging of subjects with concealed weapons,” Terahertz for Military and Security Applications IV, Orlando, April 17, 2006.

[14] S. Kawaguchi, “Low-frequency dynamics of biological molecules studied by terahertz time-domain spectroscopy,” Spectroscopy, Vol. 24, p153-158, 2010.

[15] D. G. Allis, “Theoretical analysis of the solid-state terahertz spectrum of the high explosive RDX,” Chem. Phys. Lett., Vol. 463, No. 1–3, pp. 84–89, 2008.

[16] Jackson JB, “Terahertz imaging for non-destructive evaluation of mural paintings,” Opt Communication, Vol. 281 pp. 527–32, 2008.

[17] Jepsen, P.U., D.G. Cooke, and M. Koch, “Terahertz spectroscopy and imaging - Modern techniques and applications,” Laser & Photonics Reviews, Vol. 5, No.1, p. 124-166, 2011.

[18] Jewariya, M., et al, “Fast three-dimensional terahertz computed tomography using real-time line projection of intense terahertz pulse,” Opt. Express, Vol. 21, No. 2, p. 2423-2433, 2013.

[19] J. Federici, L. Moeller, “Review of terahertz and sub-terahertz wireless communications,” J. Appl. Phys. Vol. 107, No. 11, 2010.

[20] A. G. Davies, A. D. Burnett, W. Fan, E. H. Linfield, and J. E. Cunningham, "Terahertz frequency spectroscopy of materials of security relevance," Materials Today, Vol. 11, No. 3, pp. 18-26, March, 2008.

[21] Peter Y. Yu, “Fundamentals of semiconductors- physics and material properties (4th edition),” pp. 17, 2010.

[22] Griffiths, P and de Hasseth, J.A, “Fourier Transform Infrared Spectrometry (2nd ed.),” Wiley-Blackwell, 2007.

[23] Planck, M, “The Theory of Heat Radiation. Masius, M. (transl.) (2nd ed.),” P. Blakiston's Son & Co, 1914.

[24] Charrada K, Zissis G and Aubes M, “Two-temperature, two-dimensional fluid modelling of mercury plasma in high-pressure lamps,” J. Phys. D: Appl. Phys. Vol. 29, No. 9, 1996.

[25] Zolotarev V M, Mamedov R K, Bekhterev A N, et al, “Spectral emissivity of a globar lamp in the 2–50-μm region,” J. Opt. Technol. Vol. 74, No. 6, p, 378–84, 2007.

[26] R. J. Barker, J. H. Booske, N. C. Luhmann, and et al, “Modern Microwave and Millimeter-Wave Power Electron,” Piscataway, NJ: IEEE, 2005.

[27] Bratman V L, Kalynov Y K and Manuilov V N, “Large-orbit gyrotron operation in the terahertz frequency range,” Phys. Rev. Lett. Vol. 102, No. 24, 2012.

[28] Sabchevski S P and Idehara T, “Design of a compact sub-terahertz gyrotron for spectroscopic applications,” J. Infrared Millimetre Terahertz Waves, Vol. 31, No. 9, p. 34–48, 2012.

[29] Alberti S et al, “Experimental study from linear to chaotic regimes on a terahertz-frequency gyrotron oscillator,” Phys. Plasmas, Vol. 19, No. 12, 2012.

[30] Saito T et al, “Generation of high power sub-terahertz radiation from a gyrotron with second harmonic oscillation” Phys. Plasmas, Vol. 19, No. 06, 2012.

[31] Nusinovich G S, Sprangle P, and et al, “On the sensitivity of terahertz gyrotron based systems for remote detection of concealed radioactive materials,” J. Appl. Phys, Vol. 111, No. 12, 2012.

[32] Lewen F, Michael E, and et al, “Terahertz laser sideband spectroscopy with backward wave oscillators,” J. Mol. Spectroscopy, Vol. 183, No. 20, p. 7–9, 2012.

[33] Dobroiu A, Yamashita M, and et al, “Terahertz imaging system based on a backward-wave oscillator,” Appl. Opt. Vol. 43, No.56, p. 37–46, 2012.

[34] Mineo M and Paoloni C, “Corrugated rectangular waveguide tuneable backward wave oscillator for terahertz applications,” IEEE Trans. Electron Devices, Vol. 57, No. 148, p. 1–4, 2010.

[35] Xu X, Wei Y, and et al, “A watt-class 1-THz backward-wave oscillator based on sine waveguide,” Phys. Plasmas, Vol. 19, 2012.

[36] He W, Donaldson C R, and et al, “High power wideband gyrotron backward wave oscillator operating towards the terahertz region,” Phys. Rev. Lett, Vol. 110, No. 16, 2013.

[37] Knyazev B A, Kulipanov G N and et al, “Novosibirsk terahertz free electron laser: instrumentation development and experimental achievements,” Meas. Sci. Technology, Vol. 21, No. 05, 2010.

[38] Qing-Lun Liu, Zi-Cheng Wang, and et al, “A THz Backward-Wave Oscillator Based on a Double-Grating Rectangular Waveguide,” IEEE Transactions on electron devices, vol. 60, No. 4, 2013.

[39] Jun Jian Ma, Xiao Fang Zhu, et. al, “Numerical simulation of two-cavity Gyroklystron amplifier,” International Conference on Microwave and Millimeter Wave Technology (ICMMT), 2012.

[40] Williams G P, “High-power terahertz synchrotron sources,” Phil. Trans. R. Soc. Lond. A, Vol. 362, No. 4, p. 3-14, 2004.

[41] Yang L A, Hao Y, and et al, “Improved negative differential mobility model of GaN and AlGaN for a terahertz Gunn diode,” IEEE Trans. Electron Devices, Vol. 58, No. 4, p. 76–83, 2011.

[42] Yang L A, Long S, and et al, “A comparative investigation on sub-micro-meter InN and GaN Gunn,” J. Phys. D: Appl. Phys, Vol. 47, No. 37, 2014.

[43] Jae-Sung Rieh, Daekeun Yoon and et al, “An Overview of Solid-State Electronic Sources and Detectors for Terahertz Imaging,” ICSICT2014, Guilin, China, 2014.

[44] John Ward, Erich Schlecht and et al, “Capability of THz sources based on Schottky diode frequency multiplier chains,” IEEE MTT-S Digest 2004.

[45] Alain Maestrini, Bertrand Thomas and et al, “Schottky diode-based terahertz frequency multipliers and mixers,” C. R. Physique, Vol. 11, No. 4, p. 80-95, 2010.

[46] V. Drakinskiy, P. Sobis, and et al, “Terahertz GaAs Schottky diode mixer and multiplier MIC’s based on e-beam technology,” The 25th International Conference on Indium Phosphide and Related Materials, Japan, 2013.

[47] K. A. McIntosh, E. R. Brown, and et al, “Terahertz photo-mixing with diode lasers in low-temperature-grown GaAs,” Appl. Phys. Lett, Vol. 67, No. 26, 1995.

[48] Wu X L, Xiong S J, et al, “Green light stimulates terahertz emission from mesocrystal microspheres,” Nature Nano technol. Vol. 6, p. 103–106, 2011.

[49] Auston D H, “Picosecond optoelectronic switching and gating in silicon,” Appl. Phys. Lett., Vol. 26, p. 101, 1975.

[50] Shen Y C, Upadhya P C, et al, “Ultrabroadband terahertz radiation from low-temperature-grown GaAs photoconductive emitters,” Appl. Phys. Lett, Vol. 83, No. 15, 2003.

[51] Shikata J I, Sato M, et al, “Enhancement of terahertz-wave output from $LiNbO_3$ optical parametric oscillators by cryogenic cooling,” Opt. Lett, Vol. 24, No. 4, p. 202–204, 1999.

[52] N.B. Singh, D.R. Suhre, et al, “Far-infrared conversion materials: Gallium selenide for far-infrared conversion applications,” Progress in Crystal Growth and Characterization of Materials, Vol. 37, No.1, p. 47–102, 1998.

[53] K. A. McIntosh, E. R. Brown, and et al, “Terahertz photo-mixing with diode lasers in low-temperature-grown GaAs,” Appl. Phys. Lett., Vol. 67, No. 26, 1995.

[54] S. Preu, et. al, “Tunable, continuous-wave Terahertz photomixer sources and applications,” J. Appl. Phys. Vol. 109, No. 06, 2011.

[55] L. Costa, J.C.S. Moraes, et al, “CH_3OH optically pumped by a $^{13}CO_2$ laser: new laser lines and assignments,” Appl. Phys. B, Vol. 86, p. 703–706, 2007.

[56] J. Farhoomand, and H. M. Pickett, “Stable 1.25 Watts CW Far Infrared Laser Radiation at the 119 mm Methanol Line,” Int. J. of IR & MMW, Vol. 8, No. 5, 1987.

[57] J. C. Petersen, “Laser Lines from CH_3OH Pumped Lasers,” Appl. Phys. B, Vol. 27, No. 19, 1982.

[58] J.C. Petersen, G. Duxbury, “Submillimetre laser lines from CH_3OH pumped by a $^{13}C_{18}O_2$ pump laser: Observations and assignments,” Appl. Phys. B, Vol. 34, No. 17, 1984.

[59] E. R. Mueller, W. E. Robotham, et al, “2.5 THz Laser Local Oscillator for the EOS Chem 1 Satellite,” Proc. Of the Ninth International Symposium on Space Terahertz Technology, 1998.

[60] R. Köhler, A. Tredicucci, et al, “Terahertz semiconductor-heterostructure laser," Nature, Vol. 417, pp. 156-159, 2002.

[61] Cho, A. Y*,* Arthur, J. R, "Molecular beam epitaxy," Prog. Solid State Chem., Vol. 10, p. 157–192, 1975.

[62] Williams B S, “Terahertz quantum-cascade lasers,” Nature Photon, Vol. 1, p. 517–25, 2007.

[63] Lianhe Li, Li Chen, et al, “Terahertz quantum cascade lasers with >1 W output powers,” electronics letters, Vol. 50, No. 4, 2014.

[64] B.S. Williams, S. Kumar, et al “High-power terahertz quantum-cascade lasers,” electronics letters Vol. 42, No. 2, 2006.

[65] Jerome Faist, Federico Capasso, et al, “Quantum Cascade Laser,” Science, Vol. 264, No. 5158, pp. 553-556,1994.

[66] S. Fathololoumi, E. Dupont, et al, “Terahertz quantum cascade lasers operating up to ~ 200 K with optimized oscillator strength and improved injection tunnelling,” optical express, vol. 20, No. 4, 2012.

[67] Williams B S, Kumar S, Hu Q and Reno J L, “Operation of terahertz quantum-cascade lasers at 164K in pulsed mode and at 117K in continuous-wave mode,” Opt. Express, Vol. 13 Vol. 9, p.3331-3339, 2005.

[68] Yamanishi, et al, “Theory of the Intrinsic Linewidth of Quantum-Cascade Lasers: Hidden Reason for the Narrow Linewidth and Line-Broadening by Thermal Photons,” IEEE J. Quantum Electron, Vol. 44, No. 1, p. 12, 2008.

[69] S. Bartalini, et al, “Observing the Intrinsic Linewidth of a Quantum-Cascade Laser: Beyond the Schawlow-Townes Limit,” Phys. Rev. Lett, Vol. 104, No. 08, 2010.

[70] A. Barkan, et al, “Linewidth and tuning characteristics of terahertz quantum cascade lasers,” Opt. Lett, Vol. 29, No. 575, 2004.

[71] F. Sizov, A.Rogalski, “THz detectors,” Progress in Quantum Electronics, Vol. 34 p. 278–347, 2010.

[72] Kaufmann, P. et al., “Continuum Terahertz Radiation Detection Using Membrane Filters”, International Microwave Optoelectronics Conference, SBMO & IEEE-MTT, Nov. 3-6 2009, Belem, Pará, Brazil, 2009.

[73] Bennett, H.E. and Porteus, J. O. “Relation between surface roughness and specular reflectance at normal incidence“, J. Opt. Soc. Am. Vol. 51, p. 123-129, 1961.

[74] D. Klocke, A. Schmitz, et al, "Infrared receptors in pyrophilous ('fire loving') insects as model for new un-cooled infrared sensors," Beilstein Journal of Nanotechnology, Vol. 2, No. 186, 2011.

[75] E. M. Gershenzon, G. N. Goltsman, et al, “Millimeter and submillimeter range mixer based on electron heating of superconducting films in the resistive state,” Sov. Phys. Superconductivity, vol. 3, p. 1582, 1990.

[76] V. Norkus, “Pyroelectric infrared detectors based on lithium tantalate: state of art and prospects.” Proc. of SPIE, Vol. 5251, p. 121–128, 2004.

[77] Hale P. J. et al, “20 THz broadband generation using semi-insulating GaAs interdigitated photoconductive antennas,” Opt. Express, Vol. 22, p. 26358–26364, 2014.

[78] Mark Lee, et. al, “Heterodyne Mixing of Terahertz Quantum Cascade Lasers Using a Planar Schottky Diode,” quantum electronics, Vol. 14, No. 2, 2008.

[79] Alain Maestrini, “Schottky diode based terahertz frequency multipliers and mixers,” C. R. Physique, Vol. 11, p. 480−495, 2010.

[80] Webster, John G, “The measurement, instrumentation, and sensors handbook,” CRC Press LLC, pp. 32–113, 1999.

[81] D. B. Rutledge, D. P. Neikirk, et al, “Integrated circuit antennas,” in Infrared and Millimeter Waves. New York: Academic, vol. 10, pp. 1–90, 1983.

[82] E. M. Gershenzon, G. N. Goltsman, et al, “Millimeter and submillimeter range mixer based on electron heating of superconducting films in the resistive state,” Sov. Phys. Superconductivity, vol. 3, p. 1582, 1990.

[83] E.M. Conwell, “High field transport in semiconductors,” Solid State Physics, Suppl. 9, Academic Press, New York, 1967.

[84] Y. Nakagawa and H. Yoshinaga, “Characteristics of high-sensitivity Ge bolometer”, Jap.J. Appl. Phys. Vol. 9, p. 125–131, 1970.

[85] K. Wang, R. Ramaswamy, et al, “Microwave heterodyne receiver based on AlGaAs/GaAs 2DEG bolometer,” 35th International Conference on Infrared, Millimeter, and Terahertz Waves, 2010.

[86] H. Moseley and D. McCammon, High performance silicon hot electron bolometers, in: Proceedings of the Ninth International Workshop on Low Temperature Detectors, AIP Proc. 605, pp. 103–106, 2002.

[87] Bennett, H.E. and Porteus, J. O. “Relation between surface roughness and specular reflectance at normal incidence“, J. Opt. Soc. Am. Vol. 51, p. 123-129, 1961.

[88] Robert Repas, “Passive infrared (PIR) sensors detect infrared energy radiating from objects within their field of vision,” Machine Design Jul 10, 2008.

[89] Webster, John G, “The measurement, instrumentation, and sensors handbook,” pp. 32–113, 1998.

[90] J. Lehman, A. Sanders, et al, “Very black infrared detector from vertically aligned carbon nanotubes and electric-field poling of lithium tantalate.” Nano letters, Vol. 10, No. 9, p. 3261–3266, 2010.

[91] V. Norkus, “Pyroelectric infrared detectors based on lithium tantalate: state of art and prospects.” Proc. of SPIE, Vol. 5251, p.121–128, 2004.

[92] F. F. Sizov, V. P. Reva, et al, “Uncooled Detectors Challenges for THz/sub-THz Arrays Imaging,” Journal of Infrared, Millimeter, and Terahertz Waves, Vol. 32, No. 10, p. 1192–1206, 2011.

[93] Exter, M, C. Fattinger, et al, “Terahertz time-domain spectroscopy of water vapor,” Optics Letters, Vol. 14, No. 20, p. 1128-1130, 1989.

[94] Hirori, H, et al, “Attenuated total reflection spectroscopy in time domain using terahertz coherent pulses,” J. Appl. Phys, Vol. 43: p. L1287-L1289, 2004.

[95] Hu, B. B. and Nuss, M. C., “Imaging with terahertz waves,” Opt. Lett, Vol. 20, p. 1716–1719, 1995.

[96] Mittleman. D. M, Jacobsen. R. H, et al, “T-ray imaging,” IEEE Sel. Top. Quantum Electron, Vol. 2, p. 679–692, 1996.

[97] Gupta, Shantanu, Whitaker, John F, et al, “Ultrafast carrier dynamics in III-V semiconductors grown by molecular-beam epitaxy at very low substrate temperatures,” Quantum Electronics, 28(10), 2464-72, 1992.

[98] D. T. Young and J. C. Irvin, “Millimeter frequency conversion using Au-n-type GaAs Schottky barrier epitaxial diodes with a novel contacting technique,” Proc. IEEE, vol. 53, no. 12, pp. 2130–2131, Dec. 1965.

[99] J.L. Hesler, T.W. Crowe, “Responsivity and noise measurements of zero-bias Schottky diode detectors,” in: Proceedings of the 18th International Symposium on Space Terahertz Technology, Pasadena, 2007.

[100] E. I. Kolobanov, et al, “ Highly sensitive fast Schottky-diode detectors in experiments on Novosibirsk free electron laser”, Proc. Joint 30th International Conference on Infrared and Millimeter Waves, Williamsburg, USA, p. 154-155, 2005.

[101] Vitaly, V. Kubarev, et al, “Ultra-fast Terahertz Schottky Diode Detector,” Infrared, Millimeter, and Terahertz Waves, 2009.

[102] Bozhkov*,* V. G, *“*Semiconductor detectors, mixers, and frequency multipliers for the terahertz band,” Radio phys*.* Quantum Electron*.* Vol. *46*, p. 631–656*,* 2003.

[103] S. P. Rea, B. N. Ellison, B. Swinyard, et.al, ‘The low cost upper-atmosphere sounder (LOCUS)’, 26th international symposium on space terahertz technology, Cambridge, Ma, 16-18, march, 2015.

[104] https://spec.jpl.nasa.gov/.

[105] A. Barkan, et al, “Linewidth and tuning characteristics of terahertz quantum cascade lasers,” Opt. Lett, Vol. 29, No. 575, 2004.

[106] Sze. S. M, “Physics of Semiconductor Devices,” (New York: Wiley) p 558, November, 2006.

[107] Esaki, L, “Superlattice and Negative Differential Conductivity in Semiconductors,” IBM Journal of Research and Development, Vol. 14, No. 61, 1970.

[108] http://www.teamwavelength.com/info/qclbasics.php.

[109] Bradley J. Frey, Douglas B. Leviton, et.al, “Temperature-dependent refractive index of silicon and germanium,” Proceedings of SPIE - The International Society for Optical Engineering, June 2006.

[110] Christopher Roland and George H. Gilmer, “Epitaxy on surfaces vicinal to Si (001). I. Diffusion of silicon adatoms over the terraces,” physical review B, V. 46, No. 20, 1992.

[111] Jaeger, Richard C, "Lithography Introduction to Microelectronic Fabrication (2nd ed.),” Upper Saddle River: Prentice Hall, 2002.

[112] Willson, C. G., et al, "Photoresist materials: a historical perspective," Advances in Resist Technology and Processing, 1997.

[113] Rizvi, Syed, “The Technology History of Masks,” Handbook of Photomask Manufacturing Technology. CRC Press. p. 728, 2005.

[114] Jaeger, Richard C, "Film Deposition, Introduction to Microelectronic Fabrication (2nd ed.),” Upper Saddle River: Prentice Hall, 2002.

[115] Brünglinghaus, Marion. "Mean free path". European Nuclear Society, Retrieved, 2011.

[116] Kittel, Charles, “Introduction to Solid State Physics, 7th Edition,” Wiley, 2007.

[117] Tobias Gresch, “Gain and waveguide engineering in mid-infrared quantum cascade lasers,” PhD thesis, ETH Zurich, 2009.

[118] M. Heiblum, M. I. Nathan and C.A. Chang, “Characteristics of AuGeNi Ohmic contacts to GaAs,” Solid state electronics Vol. 25, No. 3, pp. 185-195, 1982.

[119] R.E. Williams, "Modern GaAs Processing Methods," Chap. 5, Artech House, 1990.

[120] Ghandhi, Sorab K, “VLSI Fabrication Principles: Silicon and Gallium Arsenide,” New York: John Wiley & Sons, Inc, 1994.

[121] Laura Francoviglia, “Fabrication of Semiconductors by Wet Chemical Etch,” the Journal of undergraduate research, University of Kansas, Summer.2008.

[122] S. H. Jones, D. K. Walker, “Highly Anisotropic Wet Chemical Etching of GaAs Using NH4OH:H202:H20,” J. Electro chem. Soc., Vol. 137, No. 5, May 1990.

[123] Albert G. Baca, Carol I.H. Ashby, “Fabrication of GaAs Devices,” Institute of electrical engineering, London, UK, 2005.

[124] Bragg, W.H., and Bragg, W.L, "The Reflexion of X-rays by Crystals," Proc R. Soc. Lond. A., Vol. 88, No. 605, p. 428–38, 1913.

[125] S. Chakraborty, E. H. Linfield, and A. G. Davies, "Semiconductor Laser with Aperiodic Photonic Lattice," U.S. patent WO 2008/012527 A1, January 31, 2008.

[126] Christopher Kim, “GaAs refractive index dependence on carrier density and optimizing terahertz devices,” Abstract Submitted for the MAR16 Meeting of The American Physical Society, 2016.

[127] L. A. Coldren, S. W. Corzine, and M. L. Masanovic, “Diode Lasers and Photonic Integrated Circuits, Second,” Wiley Series in Microwave and Optical Engineering, John Wiley & Sons, 2012.

[128] Orloff, Jon, "Fundamental limits to imaging resolution for focused ion beams," Journal of Vacuum Science and Technology B, Vol. 14, No. 6, 1996.

[129] Castaldo, V., Hagen, C. W., "Sputtering limits versus signal-to-noise limits in the observation of Sn balls in a Ga+ microscope," Journal of Vacuum Science and Technology B, Vol. 26, No. 6, 2008.

[130] F. Braun, “Uber die stromleitung durch schwefelmetalle,” Annalen der Physik, Vol. 229, No. 12, pp. 556-563, 1857.

[131] W. Schottky, “Deviations from Ohm’s law in semiconductors,” Phys. Z., Vol. 41, p. 570–573, 1940.

[132] Bardeen, J. "Surface States and Rectification at a Metal Semi-Conductor Contact,” Physical Review, Vol. 71, No. 10, p. 717, 1947.

[133] A. Cowley and S.Sze, “surface states and barrier Height of Metal-Semiconductor systems,” Journal of Applied physics, Vol. 36, No. 10, p. 3212, 1965.

[134] S. Sze, C. Crowell, and D. Kahng, “Photoelectric Determination of Image Force Dielectric Constant for Hot Electrons in Schottky Barriers,” Journal of Applied Physics, Vol. 35, No. 8, p. 2534, 1964.

[135] http://www.doitpoms.ac.uk/tlplib/semiconductors/junction.

[136] Brian J. Rizzi, et al, “Varactor diodes for millimeter and sub-millimeter wavelength,” Third International Symposium, Space THz Tech., Ann Arbor, March 1992.

[137] Bart Van Zegbhroeck, “Principles of semiconductor devices, Chapter 3: Metal-Semiconductor Junctions,” 2011.

[138] Heinz K. Henisch, “Rectifying Semi-conductor Contacts,” Clarendon Press, 1957.

[139] A. Carlson, “Principles of Receiving Diodes,” M/A-COM Receiving Diode Handbook, 1980.

[140] R. Fano, “Theoretical limitation on the broadband matching of arbitrary impedances,” J. Franklin Inst., Vol. 249, pp. 57-83, 1950.

[141] R. Zimmermann, R. Zimmermann, and P. Zimmermann, "All Solid-State Radiometers for Environmental Studies to 700 GHz," Third International Symposium on Space THz Tech, Ann Arbor, MI, March 1992.

[142] H. Nett, S. Crewell K. Kunzi, "A 625-650 GHz Heterodyne Receiver for Airborne Operation," 16th Conf. IR and MM Waves, Lausanne, Switzerland, August 1991.

[143] S. Crewel and H. Nett, "Measurements of the Single Sideband Suppression for a 650 GHz Heterodyne Receiver," Third Intl Symp. Space THz Tech., Ann Arbor, MI, March 1992.

[144] K. Hui, “A micro-machined 585 GHz Schottky Mixer,” IEEE Microwave and Guided Wave letters, Vol. 10, No.9, pp. 374-376, 2000.

[145] W.L. Bishop, K. McKinney, “A Novel Whisker less Schottky Diode for Millimeter and Submillimeter Wave Applications,” IEEE MTT-S International Symposium, Las Vegas, Nev., 607-610, June 1987.

[146] W.L. Bishop, “A Micron Thickness, Planar Schottky Diode Chip for Terahertz Applications with Theoretical Minimum Parasitic Capacitance,” IEEE MTT-S International Microwave Symposium, Dallas, TX, pp. 1305-1308, May 1990.

[147] J. L. Hesler, “Planar Schottky Diodes in Submillimeter-Wavelength Waveguide Receivers,” Ph.D. dissertation, School of Engineering and Applied Science, University of Virginia, Charlottesville, United States, 1996.

[148] B. Alderman, H.Sanghera, et.al, “Schottky diode technology at the Rutherford Appleton Laboratory,” IEEE International Conference on Microwave Technology & Computational Electromagnetics, 2011.

[149] http://www.qmcinstruments.co.uk/images/tki/PMETER/manual32.pdf.

[150] A. Scheuring, P. Dean, A. Valavanis, “Transient Analysis of THz-QCL Pulses Using NbN and YBCO Superconducting Detectors,” IEEE Trans. THz Sci. Technol., Vol. 3, No. 2, pp. 172–179, 2013.

[151] A. Valavanis, J. X. Zhu, N. Brewster, L. H. Li, R. Dong, “Mechanically robust waveguide-integration and beam shaping of terahertz quantum cascade lasers,” Electron. Lett, Vol. 51, No. 12, pp. 919–921, 2015.

[152] A. J. L. Adam, “Beam patterns of terahertz quantum cascade lasers with subwavelength cavity dimensions,” Applied Physics Letters, Vol. 88, No. 15, p. 151105–151105–3, 2006.

[153] Michael C. et al, “Monolithically integrated solid-state terahertz transceivers,” Nature Photonics, Vol. 4, No. 8, p. 565–569, 2010.

[154] Amanti, M., et al, “Horn antennas for terahertz quantum cascade lasers,” Electron. Lett, Vol. 43, pp. 573–574, 2007.

[155] Lee, A.W.M., “High-power and high-temperature THz quantum-cascade lasers based on lens-coupled metal-metal waveguides,” Opt. Lett, Vol. 32, pp. 2840–2842, 2007.

[156] B. Thomas, et al, “Integrated Heterodyne Receivers for MM & Sub-millimeter Atmospheric Remote Sensing,” the Institution of Engineering and Technology Seminar on MM-Wave Products and Technologies, 2006.

[157] Scalari, G., “Far-infrared (λ≈87 μm) bound-to-continuum quantum cascade lasers operating up to 90 K,” Appl. Phys. Lett., Vol. 82, pp. 3165–3167, 2003.

[158] Y. Ren, et al, “Frequency locking of single-mode 3.5-THz quantum cascade lasers using a gas cell,” Appl. Phys. Lett. Vol. 100, p. 041111, 2012.

[159] Carslaw, H. S., Jaeger, J. C., “Conduction of Heat in Solids (2nd ed.),” Oxford University Press, 1959.

[160] Miriam S. “Non-equilibrium longitudinal and transverse optical phonons in terahertz quantum cascade lasers,” Applied physics letters, Vol. 100, p. 091101, 2012.

[161] S. R. Kisting, et al, “High precision temperature- and energy dependent refractive index of GaAs determined from excitation of optical waveguide eigen-modes,” Applied Physics Letters, Vol. 57, p. 1328, 1990.

[162] Christian Tanguy, “Temperature dependence of the refractive index of direct band gap semiconductors near the absorption threshold: Application to GaAs,” Journal of Applied Physics, Vol. 80, p. 4626 1996.

[163] Elad Gross, et al, “Measuring the refractive index around intersubband transition resonance in GaN/AlN multi quantum wells,” optics express, vol. 11, No.3, 2013.

[164] Beer, “Determination of the absorption of red light in colored liquids,” Annalen der Physik und Chemie, Vol. 86, pp. 78–88, 1852.

[165] J.H. Lambert, “On the measure and gradations of light, colors, and shade,” Germany: Eberhardt Klett, 1760.

[166] https://en.wikipedia.org/wiki/Full_width_at_half_maximum.

[167] Peach, G. "Theory of the pressure broadening and shift of spectral lines". Advances in Physics, Vol. 30, No. 3, p. 367–474, 1981.

[168] E.F. PliŃski, “Terahertz photo-mixer,” bulletin of the polish academy of sciences technical sciences, Vol. 58, No. 4, 2010.

[169] P.R. Smith, et al, “Sub-picosecond photo-conducting dipole antennas,” IEEE J. Quant. Electron. QE, Vol. 24, No. 2, p. 255–260, 1988.

[170] E.R. Brown, et al, “Coherent millimeter-wave generation by heterodyne conversion in low temperature-grown GaAs photoconductors”, J. Appl. Phys. Vol. 73, p. 1480, 1993.

[171] D. Saeedkia, et al, “The interaction of laser and photoconductor in a continuous-wave terahertz photo-mixer,” IEEE J Quantum Electronics, Vol. 41, p. 1188–1196, 2005.

[172] Christopher R. Webster, “Brewster-plate spoiler: a novel method for reducing the amplitude of interference fringes that limit tuneable-laser absorption sensitivities,” J. Opt. Soc. Am. B, Vol. 2, No. 9, 1985.

[173] A.M. Baryshev, P. Khosropanah, et.al, “Phase-locking of a 2.7-THz quantum cascade laser to a microwave reference,” 20th international symposium on space THz technology, Charlottesville, 20-22 April 2009.

[174] B.T. Bulcha, a J.L. Hesler, et.al, “Phase Locking of a 2.5 THz Quantum Cascade Laser to a Microwave Reference using THz Schottky Mixer,” 40th international conference on Infrared, millimeter, and Terahertz wave, Hong Kong, August, 2015.

[175] A. Valavanis, M. Henry, et.al, “Feedhorn-integrated THz QCL local oscillators for the LOCUS atmospheric sounder,” 41st International Conference on Infrared, Millimeter and Terahertz Waves, Copenhagen, Denmark,25-30 Sep 2016.

[176] H.-W. Hübers, R. Eichholz, et al, “High Resolution Terahertz Spectroscopy with Quantum Cascade Lasers,” Journal of Infrared, Millimeter, and Terahertz Waves, Vol. 34, No. 5,

Appendix I QCL fabrication processing

		1. Sample cleaning
1.	Cleaning	Clean sample in ultra sonic bath with acetone at 10% power for 1 minute.
2.		Rinse sample in acetone in 2 separate beakers.
3.		Rinse sample in IPA in 2 separate beakers.
4.		Blow dry sample with nitrogen.
5.		If the processing is restarted after resist spin coat treat the sample with plasma in the plasma asher at 50W for 5 minutes
		2. Edge Bead Removal
1.	Sample loading	Test the vacuum of the spin chuck.
2.		Check for the “X” mark at the substrate side of the sample.
3.		Place the sample on the spin chuck with the substrate side facing down and switch on the vacuum.
4.		Blow dry sample surface with nitrogen.
5.	Resist coating	Apply 1-2 drops of Shipley®1813 photoresist.
6.		Spin photoresist at 5000 rpm with a step value of 4 for 30 seconds.
7.	Soft baking	Soft bake S-1813 in a temperature controlled hot plate at 115°C for 1 minute.
8.		Ensure ***QCL Mask 1*** is free from residual resist.
9.	Photolithography	Expose the sample to UV radiation under the edge bead removal mask at 3mW/cm^2 for 1 minute 30 seconds.
10.	Development	Develop the sample in MF-319 for 3 minutes in 2 stages (2 min 50 sec. + 10 sec).
11.		Rinse the sample in DI-water.
12.		Blow dry sample with nitrogen.
13.		***Do not check the sample in microscope for the resist development.***

14.		If there are some stray resist at the edge, remove them gently using a cotton swab dipped in acetone. ***Do not touch the resist at the centre with the acetone soaked swab.***
		3. Mesa and ridge etching
1.		Use the photoresist coated sample from step 2 for the processing of this stage.
2.		Ensure ***QCL Mask 1*** is free from residual resist.
3.	Photolithography	Expose the sample to UV radiation under the ridge etch mask at 3mW/cm^2 for 10 seconds.
4.	Development	Develop the sample in MF-319 for 75 seconds in 2 stages (1 min. + 15 sec).
5.		Rinse the sample in DI-water.
6.		Blow dry sample with nitrogen.
7.	Microscope check	Check for the fidelity and pattern transfer in optical microscope.
8.	Hard baking	Hard bake S-1813 in a temperature controlled hot plate at 90°C for 1 minute.
9.	Glass mounting	Blow dry glass slide with nitrogen.
10.		Apply 1-2 drops of Shipley®1813 photoresist.
11.		Spread the photoresist by rotating the glass slide.
12.		Mount the sample on the photoresist coated glass slide,
13.		Place the glass slide on a temperature controlled hot plate at 115°C for 1 minute.
14.	Surface profiling	Measure photoresist thickness using surface profiler.
15.	Etching	Prepare an etchant solution of H_2SO_4:H_2O_2:H_20 mixed at 1:8:40 (etching rate ≈1µm/min.) Prepare 2 x (1:8:40) ml for 1 sample and 5 x (1:8:40) ml for 3 samples.

16.		Etch through the active region (for ≈10µm time approx. 10min., refer to the MBE growth layer data). Agitate the sample in a figure of “8” pattern to ensure uniform etching.
17.		Rinse in DI-water for approx. 1 min.
18.		Blow dry sample with nitrogen.
19.	Surface profiling	Measure the etch depth using the surface profiler. Measure the etch depth in all three ridges and consider the mean etch depth. ***Scan the needle from the ridge to mesa floor, and not vice versa, to prevent damage to the ridge.***
20.		If the etch depth is shallower than intended repeat etching and surface profiling (steps 15-18). ***Do not over etch.***
21.	Glass unloading	Soak the glass mounted sample in acetone to dissolve the photoresist holding sample to glass and coating the sample.
22.	Cleaning	Rinse sample in acetone in 2 separate beakers.
23.		Rinse sample in IPA in 2 separate beakers.
24.		Blow dry sample with nitrogen.
25.		Treat the sample with plasma in the plasma asher at 50W for 5 minutes.
4. Bottom contact metallisation		
1.	Sample loading	Test the vacuum of the spin chuck.
2.		Place the sample on the spin chuck with the substrate side facing down and switch on the vacuum.
3.		Blow dry sample surface with nitrogen.
4.	Resist coating	Apply 1-2 drops of Shipley®1813 photoresist.
5.		Spin photoresist at 5000 rpm with a step value of 4 for 30 seconds.
6.	Soft baking	Soft bake S-1813 in a temperature controlled hot plate at 90°C for 1 minute.

7.		Ensure ***QCL Mask 1*** is free from residual resist.
8.	Photolithography	Expose the sample to UV radiation under the bottom contact mask at 3mW/cm^2 for 10 seconds.
9.	Development	Soak the sample in chlorobenzene for 2 minutes. ***Chlorobenzene is carcinogenic – wear face mask, cover chlorobenzene beaker with a lid at all time.***
10.		Develop the sample in MF-319 for 90 seconds in 2 stages (1 min 15 sec. + 15 sec).
11.		Rinse the sample in DI-water.
12.		Blow dry sample with nitrogen.
13.	Microscope check	Check for the fidelity and pattern transfer in optical microscope.
14.	Resist softening	Expose sample to UV radiation without any mask for 2 minutes. ***Do not develop sample after this step.***
15.	Oxide cleaning	Treat the sample with plasma in the plasma asher at a low power of 25W for 70 seconds.
16.	Metallisation	Deposit 200nm of AuGeNi using the Leybold Thermal Evaporator (Univex 300). Check the boat with continuity tester. AuGeNi weight: 0.60gm; Vacuum pressure (min.): 2x10^{-6}mBar. Evaporate at 0.1Å/second for 5 minutes and then at 1Å/second for the rest.
17.	Lift off	Soak the metal coated sample in acetone and leave it over night.
18.		Use a pipette to blow acetone and remove metal from sample.
19.		Stray metals can be cleaned with a brush in a shallow dish filled with acetone. ***Take extra care not to scratch or damage the ridge.***

20.	Microscope check	Place the sample in a shallow dish filled with IPA and inspect under optical microscope.
21.		Repeat steps 17 & 18 to get rid of stray metal and repeat 19.
22.	Cleaning	Rinse sample in acetone in 2 separate beakers.
23.		Rinse sample in IPA in 2 separate beakers.
24.		Blow dry sample with nitrogen.
25.		Treat the sample with plasma in the plasma asher at 50W for 5 minutes.
26.	Microscope check	Check for the fidelity and pattern transfer in optical microscope.
27.	Annealing	Anneal the bottom contact using RTA at 430°C for 60seconds. ***Recipe: SPK_QCL_ANNEAL_430***
28.	Resistance test	Measure resistance of the bottom contact in the characterisation room. ***Resistance range: 10-20Ω***
5. Top contact metallisation		
1.	Cleaning	Rinse sample in acetone in 2 separate beakers.
2.		Rinse sample in IPA in 2 separate beakers.
3.		Blow dry sample with nitrogen.
4.		Treat the sample with plasma in the plasma asher at 50W for 5 minutes.
5.	Sample loading	Test the vacuum of the spin chuck.
6.		Place the sample on the spin chuck with the substrate side facing down and switch on the vacuum.
7.		Blow dry sample surface with nitrogen.
8.	Resist coating	Apply 1-2 drops of Shipley®1813 photoresist.
9.		Spin photoresist at 5000 rpm with a step value of 4 for 30 seconds.

10.	Soft baking	Soft bake S-1813 in a temperature controlled hot plate at 90°C for 1 minute.
11.		Ensure ***QCL Mask 1*** is free from residual resist.
12.	Photolithography	Expose the sample to UV radiation under the top contact mask at $3mW/cm^2$ for 10 seconds.
13.	Development	Soak the sample in chlorobenzene for 2 minutes. ***Chlorobenzene is carcinogenic – wear face mask, cover chlorobenzene beaker with a lid at all time.***
14.		Develop the sample in MF-319 for 90 seconds in 2 stages (1 min 15 sec. + 15 sec).
15.		Rinse the sample in DI-water.
16.		Blow dry sample with nitrogen.
17.	Microscope check	Check for the fidelity and pattern transfer in optical microscope.
18.	Resist softening	Expose sample to UV radiation without any mask for 2 minutes. ***Do not develop sample after this step.***
19.	Oxide cleaning	Treat the sample with plasma in the plasma asher at a low power of 25W for 70 seconds.
20.	Metallisation	Deposit 100nm of AuGeNi using the Leybold Thermal Evaporator (Univex 300). Check the boat with continuity tester. AuGeNi weight: 0.350gm; Vacuum pressure (min.): $2x10^{-6}$mBar. Evaporate at 0.1Å/second for 5 minutes and then at 1Å/second for the rest.
21.	Lift off	Soak the metal coated sample in acetone and leave it over night.
22.		Use a pipette to blow acetone and remove metal from sample.
23.		Stray metals can be cleaned with a brush in a shallow dish filled with acetone.

		Take extra care not to scratch or damage the ridge.
24.	Microscope check	Place the sample in a shallow dish filled with IPA and inspect under optical microscope.
25.		Repeat steps 21 & 22 to get rid of stray metal and repeat 23.
26.	Cleaning	Rinse sample in acetone in 2 separate beakers.
27.		Rinse sample in IPA in 2 separate beakers.
28.		Blow dry sample with nitrogen.
29.		Treat the sample with plasma in the plasma asher at 50W for 5 minutes.
30.	Microscope check	Check for the fidelity and pattern transfer in optical microscope.
6. Ti/Au Top over layer metallisation		
1.	Sample loading	Test the vacuum of the spin chuck.
2.		Place the sample on the spin chuck with the substrate side facing down and switch on the vacuum.
3.		Blow dry sample surface with nitrogen.
4.	Resist coating	Apply 1-2 drops of Shipley®1813 photoresist.
5.		Spin photoresist at 5000 rpm with a step value of 4 for 30 seconds.
6.	Soft baking	Soft bake S-1813 in a temperature controlled hot plate at 90°C for 1 minute.
7.		Ensure ***QCL Mask 2*** is free from residual resist.
8.	Photolithography	Expose the sample to UV radiation under the overlayer mask at 3mW/cm^2 for 10 seconds.
9.	Development	Soak the sample in chlorobenzene for 2 minutes. ***Chlorobenzene is carcinogenic – wear face mask, cover chlorobenzene beaker with a lid at all time.***
10.		Develop the sample in MF-319 for 90 seconds in 2 stages (1 min 15 sec. + 15 sec).
11.		Rinse the sample in DI-water.

12.		Blow dry sample with nitrogen.
13.	Microscope check	Check for the fidelity and pattern transfer in optical microscope.
14.	Resist softening	Expose sample to UV radiation without any mask for 2 minutes. ***Do not develop sample after this step.***
15.	Oxide cleaning	Treat the sample with plasma in the plasma asher at a low power of 25W for 70 seconds.
16.	Metallisation	Deposit 20nm of Ti & 100-150nm of Au using the Edwards Turbo Evaporator. Check the boat with continuity tester ($R\approx 1\Omega$). Ti: 3-4 wires; Au: 7-8 pcs.; Vacuum pressure (min.): 2x10^{-6}mBar. Evaporate at 0.1nm/second for first 20nm (Ti & Au) and then at 0.2nm/second for the rest (Au only).
17.	Lift off	Soak the metal coated sample in acetone and leave it over night.
18.		Use a pipette to blow acetone and remove metal from sample.
19.		Stray metals can be cleaned with a brush in a shallow dish filled with acetone. ***Take extra care not to scratch or damage the ridge.***
20.	Microscope check	Place the sample in a shallow dish filled with IPA and inspect under optical microscope.
21.		Repeat steps 21 & 22 to get rid of stray metal and repeat 23.
22.	Cleaning	Rinse sample in acetone in 2 separate beakers.
23.		Rinse sample in IPA in 2 separate beakers.
24.		Blow dry sample with nitrogen.
25.		Treat the sample with plasma in the plasma asher at 50W for 5 minutes.

26.	Microscope check	Check for the fidelity and pattern transfer in optical microscope.
	7. Substrate etching	
1.	Glass mounting	Blow dry glass slide with nitrogen.
2.		Apply 1 drop of dry Shipley®1813 photoresist (solvent evaporated) on sample surface.
3.		Bake the sample in a temperature controlled oven at 65°C for 4 minutes.
4.		Apply 2-3 wax balls on glass slide.
5.		Soft bake glass in a temperature controlled hot plate at 90°C to melt the wax
6.		Mount gently the sample on the melted wax glass slide with top surface facing down (ridge buried in wax).
7.		Ensure a quick hardening of wax positioning the glass on a cold metal surface
8.	Micrometer profiling	Measure the thickness with micrometer setup. Set the glass slide surface as a reference point. Measure the thickness of resist covered sample at the 4 corners and at the middle.
9.	Etching	Prepare an etchant solution of H_2SO_4:H_2O_2:H_20 mixed at 1:8:1 (etching rate ≈15µm/min.) Prepare 15 x (1:8:40) ml for 1 sample and 25 x (1:8:40) ml for 3 samples.
10.		Etch through 450µm of substrate (approx. 25-30min). Etch in 4 steps with etching time of approx. 7 minutes. Agitate the sample in a figure of "8" pattern to ensure uniform etching or use the magnetic stirrer (speed 3) to etch the substrate.
11.		Rinse in DI-water for approx. 1-2 min.
12.		Blow dry sample with nitrogen.
13.	Micrometer profiling	Measure the thickness with micrometer setup. Set the glass slide surface as a reference point.

		Measure the etch depth using the micrometer setup at the 5 points (in step 34).
14.		If the etch depth is shallower than intended repeat etching and surface profiling (steps 35-38).
15.	Glass unloading	Soft bake glass in a temperature controlled hotplate at 90°C to melt the wax Gently move the sample in a tetrachloroethylene beaker in order to wash off wax residual The sample is now thinned considerably, ***Handle with care.***
16.	Cleaning	Rinse sample in acetone in 2 separate beakers.
17.		Rinse sample in IPA in 2 separate beakers.
18.		Blow dry sample with nitrogen.
19.		Treat the sample with plasma in the plasma asher at 50W for 5 minutes.
8. Ti/Au Back over layer metallisation & copper block metal coating		
1.	Copper block cleaning	Clean copper block in acetone for 1 minute.
2.		Clean copper block in ultra sonic bath with acetone at 100% power for 10 minutes.
3.		Clean copper block in ultra sonic bath with IPA at 100% power for 10 minutes.
4.		Blow dry copper block with nitrogen.
5.		Dry clean copper blocks in a temperature controlled hot plate at 200°C for 5 minutes.
6.	Oxide cleaning	Treat the substrate side of the sample with plasma in the plasma asher at 50W for 5 minutes.
7.	Metallisation	Deposit 20nm of Ti & 100nm of Au using the Edwards Turbo Evaporator. Check the boat with continuity tester ($R\approx1\Omega$). Ti: 3-4 wires; Au: 7-8 pcs.; Vacuum pressure (min.): $2x10^{-6}$mBar.

		Evaporate metal on both sample and the polished surface of copper block. Evaporate at 0.1nm/second for first 50nm (Ti & Au) and then at 0.2nm/second for the rest (Au only).
8.	Cleaning	Rinse sample in acetone in 2 separate beakers.
9.		Rinse sample in IPA in 2 separate beakers.
10.		Blow dry sample with nitrogen.
9. Sintering		
1.	Sintering	Sinter the top contact and the over-layers using RTA at 270°C for 5minutes. ***Recipe: SPK_QCL_Anneal_TOP***
10. Ridge separation and facet cleaving		
1.	Cleaving	Check the scriber orientation with a scrap sample before ridge separation. Separate laser ridges using a scriber with an applied force of 15-25.
2.	Facet cleaving	Cleave laser facets with a surgical scalpel knife. Check the facets with the angular microscope. ***Do not damage the facet and do not handle sample with the facet side.***